UNIVERSITÉ DE GENÈVE
Département de physique
de la matière condensée

FACULTÉ DES SCIENCES
Professeur D. van der Marel

Spectroscopic signatures of electronic correlations in superconductors and magnets

THÈSE

présentée à la Faculté des sciences de l'Université de Genève
pour obtenir le grade de docteur ès sciences, mention physique

par

Fabrizio CARBONE

de

Novi Ligure (Italie)

Thèse n° 3824

GENÈVE
Atelier de reproduction de la Section de physique
2007

La Faculté des sciences, sur le préavis de Messieurs D. VAN DER MAREL, professeur ordinaire et directeur de thèse (Département de physique de la matière condensée), Ø. FISCHER, professeur ordinaire (Département de physique de la matière condensée), Th. GIAMARCHI, professeur ordinaire (Département de physique de la matière condensée), F. PARMIGIANI, professeur (Istituto Nazionale per la Fisica della Materia, Laboratorio Nazionale Tecnologie Avanzate e nanoscienza, Trieste, Italia) et G. AEPPLI, professeur (University College London, Department of physics and astronomy, London, United Kingdom) autorise l'impression de la présente thèse, sans exprimer d'opinion sur les propositions qui y sont énoncées.

Genève, le 8 janvier 2007

P. Spierer

Thèse - 3824 -

Le Doyen, Pierre SPIERER

Spectroscopic signatures of electronic correlations in superconductors and magnets

Fabrizio Carbone

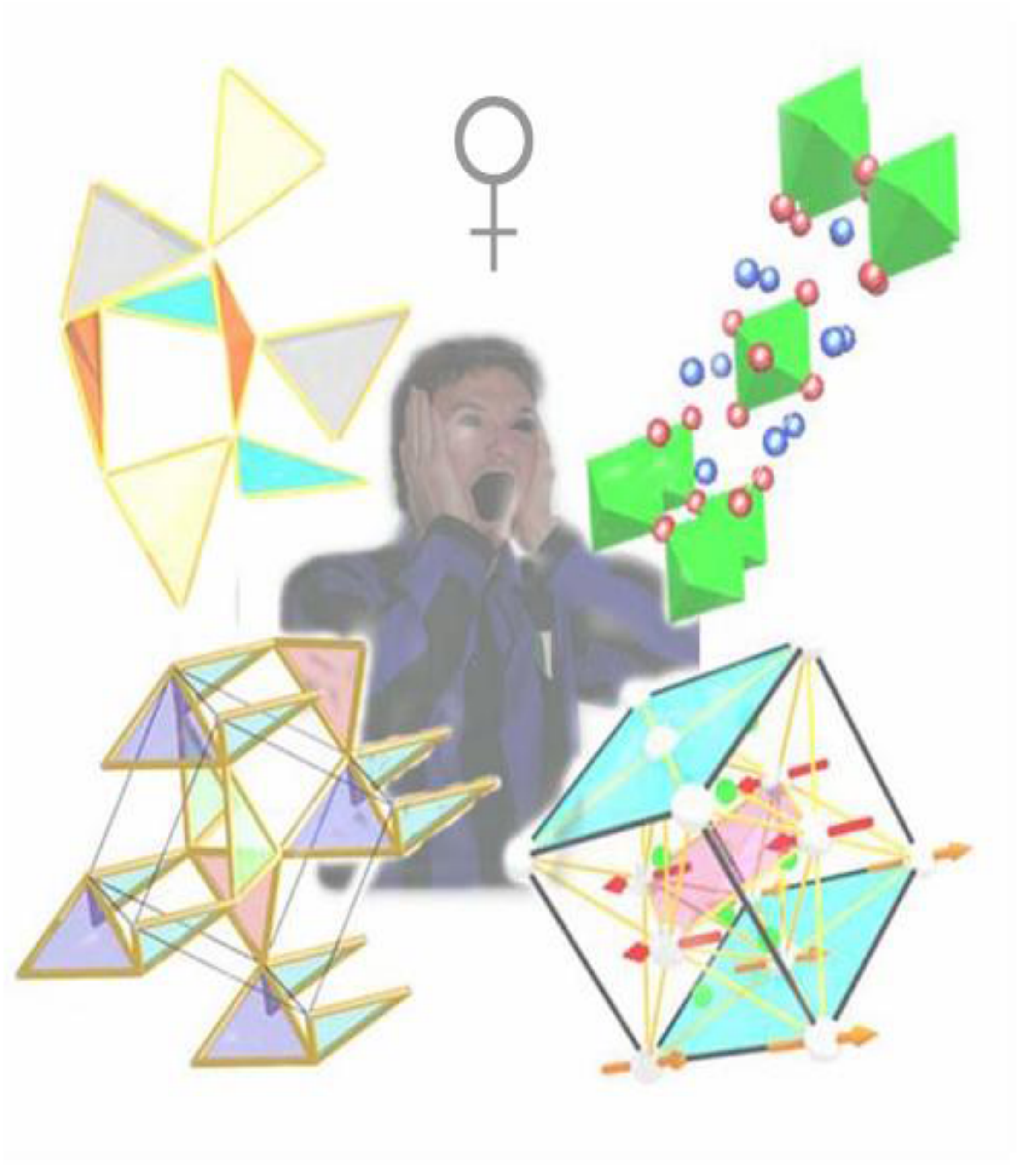

I would like to dedicate this work to Annetta, Giampiero, Katarzyna and Maria, who did something very special for me. You have all an important place in my memories.

. . . Or tutto intorno
una ruina involve,
dove tu siedi, o fior gentile, e quasi
i danni altrui commiserando, al cielo,
di dolcissimo odor mandi un profumo,
che il deserto consola

Giacomo Leopardi. "La Ginestra"

Table of Contents

Résumé en français

Introduction

L'habitude des anthropologistes à utiliser le nom du matériau utilisé par les hommes pour nommer un âge de l'histoire montre l'énorme importance des matériaux dans l'histoire de l'humanité. Comprendre et utiliser les nouveaux matériaux a été une des plus grandes conquêtes de l'humanité. Dans notre siècle, le développement de l'électronique et la photonique a suivi la compréhension microscopique des semiconducteurs et des métaux par la mécanique quantique. La majeure partie des propriétés des solides est déterminée par la portion des électrons participant aux liaisons chimiques. Si ces électrons sont des particules chargées, dans beaucoup de situation, la répulsion coulombienne mutuelle peut être négligée dans la description du solide. Un des enjeux majeurs de la physique moderne est de traiter correctement ces interactions dans les matériaux où les négliger conduits à une mauvaise compréhension des résultats expérimentaux. Ces interactions sont à l'origine de nombreux phénomènes qui ont d'importantes implications dans le magnétisme et la supraconductivité. Si l'observation du magnétisme remonte à la Grèce antique, il n'a été compris que grâce au récent avènement de la mécanique quantique et du concept de "spin électronique". Dans les métaux de transition, la forte répulsion coulombienne ressentie par les électrons d favorise un arrangement magnétique de leurs spins dans leurs orbitales d. La description la plus simple d'un matériau magnétique serait de considérer les moments magnétiques de chaque atome orientés les uns par rapport aux autres. Cette description s'applique aux matériaux dans lesquels les électrons d sont localisés sur leur atome et on peut alors parler d'orbitale atomique et de spins comme dans les oxydes de métaux de transition. Cependant, le magnétisme a été également observé dans des systèmes métalliques où les électrons sont délocalisés dans les liaisons covalentes. Le concept de magnétisme itinérant a été développé pour expliquer ce phénomène. Les électrons formant les bandes électroniques des solides, équivalentes aux orbitales atomiques, peuvent révéler différentes structures entre une direction de leur spin et une autre. Ceci résulte en une polarisation de spin qui crée un moment magnétique au sein du système. Ce scénario représente la limite où les interactions électron-électron sont faibles mais capables de produire du magnétisme et les implications microscopiques sont actuellement l'objet de débats.

MnSi est considéré comme un matériau à ferromagnétisme itinérant (weak itinerant ferromagnet) et peut être décrit par un model de ce type. Une partie de cette thèse s'intéresse à la détermination de la structure électronique de ce matériau, et aux effets des répulsions coulombiennes pour donner une réponse microscopique à son magnétisme.
Une vaste classe de matériaux couvrant une large part de la table périodique a montré qu'ils devenaient supraconducteurs à basse température à cause de la formation de paires assistée par le couplage électron-phonon. Ceci est expliqué dans la théorie de Bardeen, Schriffer, Cooper, BSC. Les interactions de coulomb entre les électrons mobiles (chargés négativement) et les ions (chargés positivement) peuvent déformer le réseau cristallin. Cette déformation peut exciter un mode de phonon particulier du cristal. Il résulte de cette interaction un potentiel attractif autour de l'électron qui favorise la formation d'une paire. Lorsque deux électrons, particules possédant un spin semi-entier, se couplent, ils se comportent comme une particule possédant un spin entier et obéissant par conséquent à la statistique de Bose-Einstein et peuvent condenser dans un état quantique unique. Ce condensat représente l'état fondamental du système, ainsi, dans un supraconducteur le courant peut circuler dans l'état fondamental, et le matériau montre une résistivité nulle. Dans les supraconducteurs BSC, la formation du condensat diminue l'énergie potentielle du système dans une plus grande mesure que son énergie cinétique augmente. L'énergie totale est diminuée et le matériau subit une transition de phase supraconductrice. En 1986, une famille de matériaux possédant des transitions supraconductrices à des températures bien supérieures à celles des matériaux BCS a été découverte. Le composé BCS possédant la plus haute température de transition est MgB2 avec une Tc d'environ 39K alors que le composé $Tl_2Ba_2Ca_2Cu_3O_1$0 devient supraconducteur à 125K. Ces matériaux sont appelés "Cuprates" en raison de la présence de plans CuO2. De nombreux arguments indiquent un mécanisme de couplage "non-BCS" dans ces matériaux, mais malgré un grand nombre de recherches, il n'existe toujours pas de consensus sur le mécanisme de formation de paires. Alors que les matériaux BSC sont des liquides de Fermi où les interactions électron-électron peuvent être traitées comme des perturbations, les cuprates ne sont pas des liquides de Fermi dans l'état normal et les interactions électron-électron jouent un r“le dominant. Dans un tel contexte, de nombreux mécanismes de formation de paires on été proposés, tous relatant une diminution de l'énergie cinétique des électrons, contraire au scénario BSC. Mesurer le changement d'énergie cinétique du système lors de la transition supraconductrice pourrait donc indiquer quel mécanisme de formation de paire est responsable de la supraconductivité dans les Cuprates.

Spectroscopie optique des supraconducteur à haute T_c

Les ondes électromagnétiques sont un bon moyen de sonder le mouvement des particules chargées. La réponse d'un systeme de particules chargées à la lumière est la conductivité optique complexe $\sigma = \sigma_1 + i\sigma_2$, où σ_1 mesure l'absorption de la lumière dans le matériau et σ_2 est la partie réactive de la réponse. Une loi sur la somme existe en spectroscopie optique appelée "sum-rule":

$$SW = \int_0^\infty \sigma_1(\omega\prime) d\omega\prime = \frac{\omega_p^2}{8} \tag{R.1}$$

La quantité SW est appelée poids spectral optique et représente le poids de toutes les transitions dans le spectre de la conductivité. Si on limite cette intégrale à une fréquence de coupure Ω_c, il devient possible de mesurer le poids de la seule bande de conduction, qui représente la réponse des électrons libres, responsables des propriétés électroniques du système. Le poids spectral peut etre relié à l'énergie cinétique par une simple relation de proportionnalité, et dans l'approximation aux premiers voisins des liaisons fortes, l'expression $SW = -K$ (K étant l'énergie cinétique) est valide. La mesure du changement de SW lors de la transition de phase peut permettre de déterminer expérimentalement si l'énergie cinétique augmente ou diminue lorsque le systeme devient supraconducteur. Cet effet a été vu dans des monocrystaux de Bi2212 [1] pour la première fois. Jusqu'à maintenant nous avons implicitement fait des assomptions dont la validité doit être vérifiée:

- Le poids spectral (SW) est une intégrale de zéro à une certaine fréquence de coupure. Evidemment, comme il n'est pas possible de mesurer le spectre optique jusqueà une fréquence nulle, nous devons estimer l'influence de la partie spectrale manquante sur le résultat final.
- L'équation $SW = -K$ n'est strictement valide que lorsque la dispersion de la bande est limitée aux sauts entre premiers voisins.
- Afin d'établir si oui ou non ceci est une propriété commune à tous les Cuprates, nous devons étudier ces effets sur différentes compositions.

Une partie de ce travail consistera à répondre à ces trois points. Nous avons mesuré différents Cuprates avec des composition différentes par refléctivité infrarouge (entre 12 meV et 0.78 eV) et par ellipsométrie spectroscopique (entre 0.78 eV et 4 eV) dans une gamme de températures entre 10K et 300K. Afin de voir les effects induits par la supraconductivité, les données ont été enregistrées avec une résolution en température de 1K. De plus, un rapport signal sur bruit supérieur à 3000 su les constantes optiques mesurées a été atteint dans toute le domaine spectral afin de détecter les

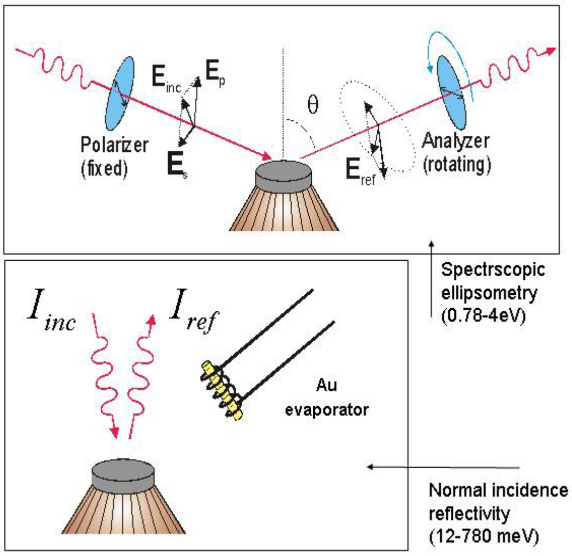

Figure R.1: Représentation schématique des mesures de réflectivité et d'ellipsométrie.

changements les plus subtiles à T_c. Beaucoup de soin a été apporté à ce sujet et grâce particulièrement à l'utilisation d'un cryostat ultra stable nous avons pu mesurer le transfert de poids spectral lors de la transition avec une grande précision sur différents matériaux. La Fig. R1 montre le schéma de l'expérience: La réflectivité est mesurée en illuminant l'échantillon puis une couche d'or est déposée "in-situ" afin de prendre la réflectivité de l'or comme référence. L'ellipsométrie consiste à éclairer l'échantillon avec une lumière linéairement polarisée et à mesurer l'ellipticité de la polarisation émergeante induite par l'échantillon. La combinaison de ces deux techniques donne accès à la conductivité optique complexe dans une large échelle d'énergies. D'apparence simple, cette expérience est complexe en raison de la large gamme spectrale (4 décades) et de température (2 décades) et de la haute résolution nécessaire. Dans les travaux de la référence [1] nous avons mesuré le tenseur diélectrique d'un cristal de Bi2223 dans toutes les directions cristallographiques non-équivalentes. Dans cette publication, nous avons montré que SW peut être déterminé avec une très grande précision même si les mesures ne descendent pas jusqu'à une fréquence nulle grâce à la combinaison de la grande précision dans la connaissance des parties réelles et imaginaires de la conductivité optique dans une grande gamme spectrale. Ceci a été le sujet d'une autre publication où nous avons pu donner des arguments quantitatifs basés sur des approches analytique et numérique des propriétés des fonctions analytiques. Nous avons également discuté les implications théoriques du choix de la fréquence de coupure Ω_c dans l'intégrale du poids spectral montrant qu'en dessous de 1eV, le poids spectral peut être en effet représentatif de la réponse des électrons de conduction dans les Cuprates, donnant accès à la variation

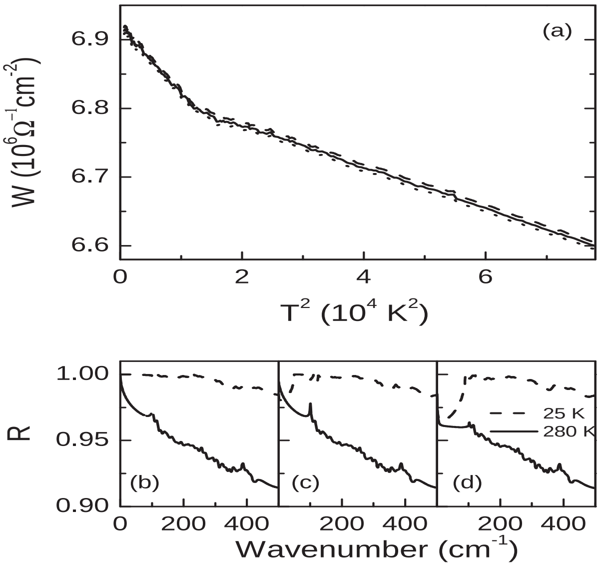

Figure R.2: Le graphique du haut représente le poids spectral en fonction de la température. La transition supraconductrice induit une augmentation de SW en dessous de T_c indiquant une diminution de l'énergie cinétique des porteurs libre ($SW = -K$). Le graphique du bas montre les différentes extrapolations à basse fréquences faites sur les mesures de réflectivités utilisées pour générer les barres d'erreur sur le poids spectral. Il est clair que les détails du spectre en dessous de la dernière fréquence mesurée ne sont pas cruciaux dans la détermination de SW.

de l'énergie cinétique des porteurs libres. Dans la Fig. R.2, nous montrons l'effet des extrapolations à basse fréquences sur le transfert de poids spectral. Dans la référence [3] nous avons étudié la dépendance du transfert de poids spectral avec le dopage en oxygène dans des échantillons de Bi2212. La non stochiométrie en oxygène dans ces matériaux peut faire varier les propriétés supraconductrices en modifiant le nombre de porteurs dans la bande de conduction. Sans dopage, le système est un isolant. Il devient métallique et supraconducteur en ajoutant de l'oxygène puis, passé une certaine quantité, la supraconductivité est supprimée. Dans la Fig. R.3, on peut voir le diagramme de phase des Cuprates supraconducteurs. Le transfert de SW en fonction du dopage a un comportement non trivial qui peut être expliqué théoriquement dans le contexte du modèle t-J partant d'un cluster de 4 atomes de cuivre, Fig. R.4. L'Hamiltonien du modèle t-J est:

$$H = -t\sum_{i,j,\sigma}(b^{\dagger}_{i,\sigma}b_{j,\sigma} + H.c) + J\sum_{i,j} S_i S_j \tag{R.2}$$

$$b_{i,\sigma} = c_{i,\sigma}(1 - n_{i,-\sigma}) \tag{R.3}$$

$$c^{\dagger}_{i,\sigma}c_{i,\sigma} = n_{i,\sigma} \tag{R.4}$$

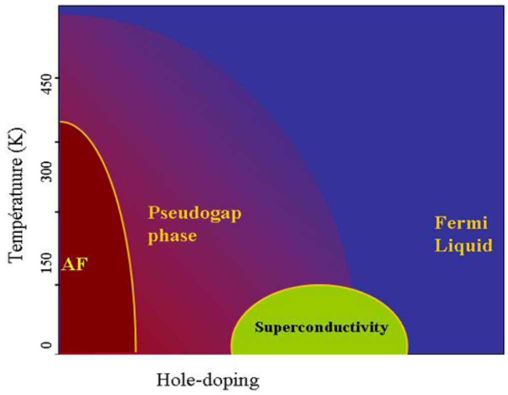

Figure R.3: Diagramme de phase en fonction du dopage en oxygène. Le composé stochiométrique est un isolant de Mott. La plus haute temperature de transition supra est atteinte pour un rapport trou/atome de cuivre de 0.15.

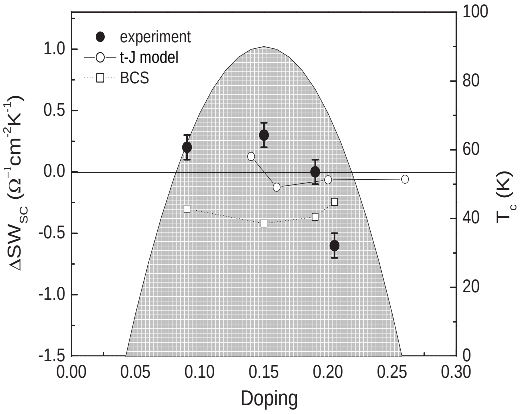

Figure R.4: Comparaison entre les valeurs du changement de poids spectral induit par la supraconductivité expérimentales et les resultats obtenus avec le model t-J.

et représente un système avec un interaction d'échange J entre voisins et où la double occupation d'un site est interdite. Ce modèle décrit assez bien la physique a basse énergie des Cuprates supraconducteurs, comme le confirme nos résultats. Jusque la, nous avons considéré comme admise la relation entre le poids spectral et l'énergie cinétique. Ce point subtil a été traité dans une récente publication. Pour certaines compositions, en effet, le poids spectral peut être très différent de l'énergie cinétique. Nous avons aussi vérifié que pour les compositions que nous avons mesurées expérimentalement, cette relation est une bonne approximation de la réalité.

La structure électronique et le magnétisme de bande de MnSi

Comme nous l'avons mentionné dans l'introduction, le magnétisme de bande prend son origine dans la polarisation de spin des bandes électroniques d'un solide. Afin d'avoir une description microscopique du magnétisme dans MnSi, qui est considéré comme un aimant itinérant, nous devons connaître avec précision sa structure électronique. Lorsque les répulsions colombiennes sont faibles, les calculs de structure de bande donnent une bonne représentation de la structure électronique. Si elles sont fortes, des effets de localisation peuvent apparaêtre et l'image itinérante n'est plus valable. Une estimation précise des répulsions Coulombiennes est cruciale pour les systèmes magnétiques, étant donné qu'elles gouvernent le magnétisme. Nous avons étudié la structure de MnSi en utilisant l'absorption des rayons X (XAS) et la photoémission spectroscopique (XPS) et comparé leur résultats avec des calculs de structure de bande LDA.

En XAS, on excite les électrons profonds à des niveaux inoccupés d'un élément particulier. C'est une technique sensible à l'élément qui peut sonder la densité des états inoccupés d'un matériau. Si la fonction d'onde du trou a une grande interaction avec la fonction d'onde de l'électron excité associé, par exemple une transition 2p-3d dans un métal de transition, des effets de multiplet atomiques peuvent apparaêtre et la forme du spectre d'absorption dépend fortement de la configuration fondamentale du système. Ceci fait de l'absorptions X un moyen idéal pour sonder la valence des matériaux. Dans MnSi, on ne s'attend pas a voir d'effet multiplets, étant donné que les électrons de la bande de conduction sont délocalisés dans un état métallique. Dans ce contexte, on peut s'attendre à ce qu'une simple approche LDA sera suffisante pour représenter les processus d'absorption: en LDA, on calcule la densité d'états inoccupés d'une seule particule d'un élément sondé par les rayons X. En conservant l'effet du trou comme un simple potentiel de Coulomb sur un atome, on est capable de simuler le processus d'absorption X. Cette approche néglige les répulsions Coulombiennes entre porteurs. Nous avons montré que cette procédure échoue lamentablement dans MnSi et FeSi alors qu'elle donne de bonnes prévisions pou CoSi, visible en Fig. R.5. La théorie des multiplets atomiques ne donne également pas des résultats satisfaisants. La raison est que MnSi et FeSi sont des matériaux dans lesquels les répulsions coulombienne ne sont ni négligeables ni dominantes. On pourrait expliquer les spectres XAS dans ces matériaux en proposant que leur état fondamental a un caractère de valence mixte ou les effets de localisation de charge supprime partiellement les fluctuations de valence typiques dans ces systèmes métalliques. L'absorption XAS est une sonde en énergie, en un sens, il n'est pas parfaitement justifié de la considérer comme une sonde du "vrai" état fondamental du système car les rayons X sont eux-mêmes une source de perturbation significative. La même tendance est observée au moyen de la photoémission de la bande de valence; les spectres de MnSi et FeSi ne peuvent pas être reproduits par des calculs LDA alors que pour CoSi un bon accord est observé. Dans MnSi, des expériences d'annihilation de positron qui sondent la densité d'état à la surface de Fermi ont également montré une déviation des prédictions du scénario LDA. Ces observations suggèrent que MnSi est à la limite entre un composant à moment local et itinérant, rendant la compréhension microscopique de son magnétisme une tache difficile. Les aimants itinérants, en fait, on quelques caractéristiques communes avec les aimants localisés, la susceptibilité Curie-Weiss, la dépendance en température du taux de relaxation magnétique (1/T1), mais leurs valeurs absolues sont renormalisées. Un indice microscopique pour comprendre ces observations vient de la théorie de fluctuation de spin de Moryia. En comparant de nouvelle mesures RMN avec des mesures de diffusion de neutrons, nous pouvons estimer avec précision quelques paramètres microscopiques de ce modèles cependant d'importantes déviations sont observées. Le spectre d'excitation magnétique de ce matériau est montre des ondes de spin bien définies en intersection avec le continuum de Stoner a 3 meV.

Ceci en fait un composé idéal pour étudier la diffusion paramagnétique et, en fait, l'observation de l'échange entre les ondes de spin et le continuum a été réalisé sur MnSi. Cependant, l'étude des excitations de Stoner dans MnSi n'est pas allée au-delà d'un transfert d'énergie de 20 meV à cause de difficultés expérimentales et à cause de la présence de phonons optiques entre 20 et 60 meV. Les données à basse énergie ont été interprétées en terme de fluctuation de spin ce qui peut expliquer la loi de Curie-Weiss observée dans la susceptibilité magnétique. Dans ce modèle, la dépendance en température de la magnétisation est essentiellement gouvernée par la dépendance en température des ondes de spin de faibles énergies alors que les excitations de Stoner devraient être indépendantes de la température. Dans nos données de diffusion inélastique de neutrons, nous pourrions étudier les excitations de Stoner jusqu'à une énergie de transfert de 400 meV à température ambiante et 10K. Nous avons trouvé une dépendance en température inattendue des excitations de Stoner qui remet en question l'interprétations microscopique de la loi de Curie-Weiss de la susceptibilité basée sur le model de fluctuation de spin.

Dans une expérience de diffusion de neutrons, la section efficace par unité d'énergie et

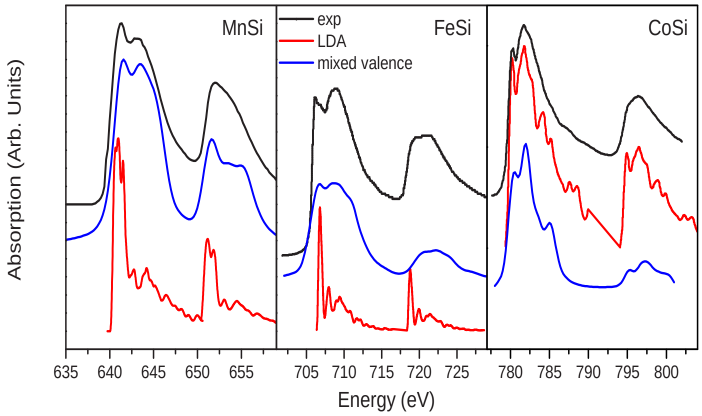

Figure R.5: Spectres XAS de MnSi FeSi et CoSi, On peut voir que le calcul dans l'état de valence mixte peut reproduire le processus d'absorption des trois composés alors que la LDA ne marche que pour CoSi où les répulsions coulombiennes sont négligeables à cause du fait que la bande 3d est presque complètement remplie.

d'angle solide pour une interaction électromagnétique entre le moment magnétique du neutron et les moments magnétiques présents dans un solide est donné par la formule:

$$\frac{d^2\sigma}{d\Omega dE\prime} = \frac{k_f}{k_i}(\gamma r_0)^2 \mid \frac{g}{2}F(Q) \mid^2 \sum_{\alpha,\beta}(\delta_{\alpha,\beta} - Q_\alpha Q_\beta S^{\alpha,\beta}(Q,\omega)) \tag{R.5}$$

Où $Q = k_f - k_i$ et $\hbar\omega = E_f - E_i$ sont les transferts d'impulsion et d'énergie. $\gamma = 1.913$ et $g \sim 2$ sont les g-facteurs spectroscopiques des neutrons et des atomes magnétiques. $F(Q)$ est le facteur de forme magnétique et dépends de l'atome présent dans le solide. Dans l'Eq. R.5. La quantité $S(Q,\omega)$ contient la fonction de correlation de spin:

$$S^{\alpha,\beta}(Q,\omega) = \frac{1}{2\pi\hbar}\int dt e^{i\omega t}\frac{1}{N}\sum_{i,j} < S_i^\alpha(t) S_j^\beta(0) > e^{-iQ(R_i - R_j)} \tag{R.6}$$

En utilisant le théorème de fluctuation-dissipation, on peu relier la fonction de corrélation de spin à la susceptibilité de spin par la formule:

$$S(Q,\omega) = \frac{1}{1 - e^{-\beta\hbar\omega}}\frac{\chi\prime\prime(Q,\omega)}{\pi(g\mu_B)^2} \tag{R.7}$$

Avec $\beta = 1/k_B T$. On peut voir de ces équations qu'avec une expérience de diffusion de neutrons, il est possible d'avoir une information directe sur la partie imaginaire de la susceptibilité de spin en fonction de l'énergie et de l'impulsion. Dans les aimants itinairants, la susceptibilité de spin a été étudiée au moyen de méthodes RPA (random phase approximation). Dans ce model, la partie imaginaire ed la susceptibilité de spin est donnée par:

$$\chi\prime\prime(Q,\omega) = \frac{Im\chi_0(Q,\omega)}{[1 - IRe\chi_0(Q,\omega)]^2 + [IIm\chi_0(Q,\omega)]^2} \tag{R.8}$$

Où I est l'interaction intra-atomique et χ_0 est la susceptibilité du gaz d'électron qui n'interagit pas. χ_0 peut être calculé analytiquement et des ondes de spin bien définies avec une dispersion quadratiques sont prédites par ce model. Une comparaison détaillée à ce model à été réalisée dans la ref. [5]. Dans MnSi, on doit aller à travers cette approche afin d'expliquer la loi de Curie-Weiss de la susceptibilité magnétique et les propriétés particulières de la diffusion paramagnétique. Ceci est fait par la théorie des fluctuations de spin de Moryia, où la susceptibilité de spin est donnée par la formule:

$$\chi(Q,\omega) = \frac{\chi_0(Q,\omega)}{1 - I\chi_0(Q,\omega) + \lambda(Q,\omega)} \tag{R.9}$$

Le terme additionnel produit le comportement Curie-Weiss observé expérimentalement. Avant d'être capable de comparer la susceptibilité mesurée avec des prédictions théoriques, il est nécessaire de séparer la diffusion magnétique de celle des phonons. Comme nous l'avons mentionné précédemment, dans MnSi, plusieurs modes de phonons polluent le spectre entre 20 meV et 60 meV. Un calcul ab-initio LDA de la dispersion de phonon permet de faire une telle distinctions et son ajustement fin nous renseigne également en retour sur la structure électronique. La Fig. R.6 montre la comparaison entre la dispersion de phonons obtenue expérimentalement et le calcul LDA.

Un résultat encourageant a été atteint. Ceci nous permet d'attribuer une part de la diffusion au magnétisme. Dans la Fig. R.7, on note que le spectrum des excitations magnetiques a haute temperature est assez different de celui a 10K, espécialment autour du point R (1,1,1). Cette observation est en contrast avec la théorie de Moryia qui predit que le spectrum des excitations de Stoner soit independent de la temperature. Cette observation suggère que les excitations de Stoner jouent un rôle important dans le magnétisme de MnSi, contrairement aux prédictions de la théorie de fluctuation de spin.

En résumé, nos observations pourrait paretre contrastées sur certains plans: La localisation est mise en évidence au moyen de sondes de haute énergies, les expériences de diffusion de neutron sont interprétées en terme d'un modèle itinérant. Les divergences observées dans les deux approches confirment qu'aucune des deux, purement localisée ou purement itinérant, n'est correct. Si la région limite de formation de moments locaux est une terra incognita d'un point de vue théorique, nos observations

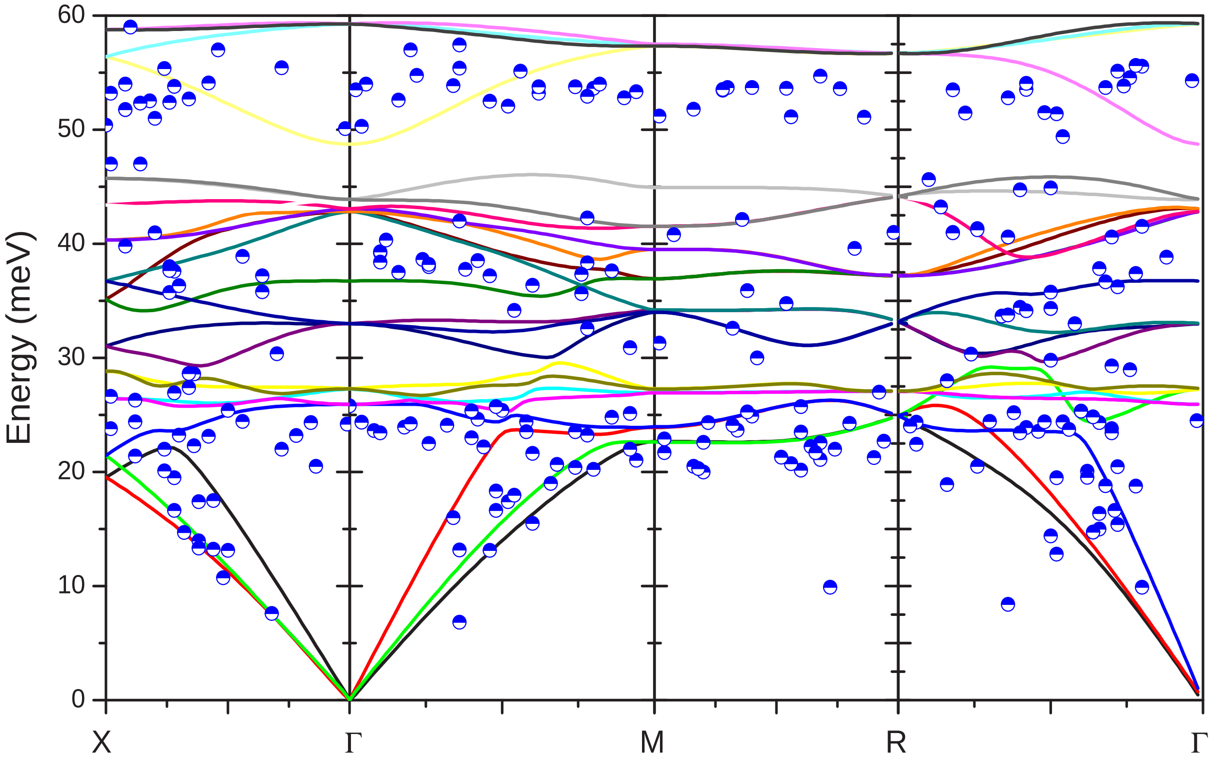

Figure R.6: Position des pics obtenus des scans où l'échantillon et tourné de 90ø affin d'avoir la direction [110] parallèle au rayon incident et les pics obtenus dans d'autres scans et pouvant être attribués aux phonons sont représentés avec la dispersion calculée par LDA sur un cluster de 3x3x3.

expérimentales donne des éléments utiles pour développer un model microscopique pour le magnétisme de band dans MnSi

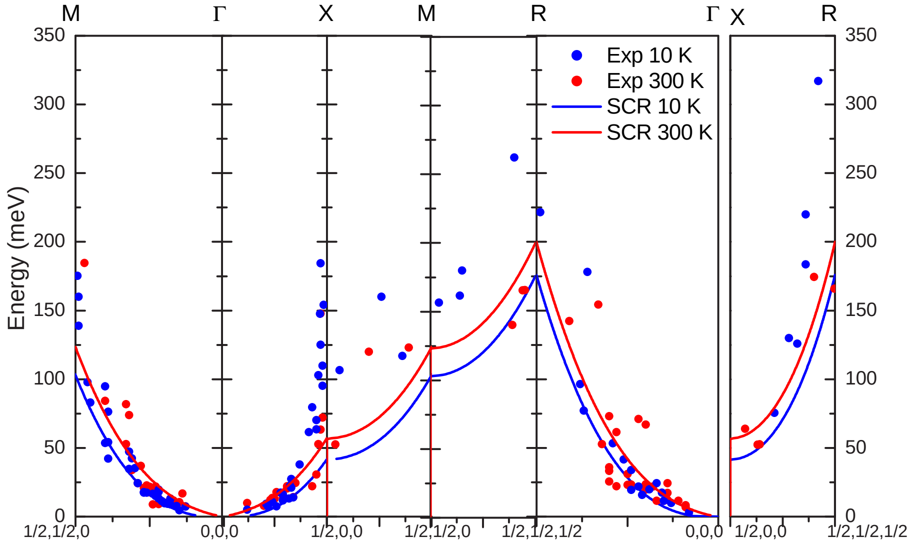

Figure R.7: La dispersion des excitations magnetiques en MnSi est representé. Les lignes representent la prédictione de la théorie de Moriya a deux temperatures: 300K (rouge) et 10 K (bleu). Les points sont les experiments aux mèmes temperatures.

Bibliography

[1] "Temperature-modulation analysis of superconductivity-induced transfer of in-plane spectral weight in $Bi_2Sr_2CaCu_2O_8$" A.B. Kuzmenko, H.J.A. Molegraaf, **F. Carbone**, and D. van der Marel. Phys. Rev. B **72** 144503 (2005).

[2] " In-plane optical spectral weight transfer in optimally doped $Bi_2Sr_2Ca_2Cu_3O_10$" **F. Carbone**, A.B. Kuzmenko, H.J.A. Molegraaf, E. van Heumen, E. Giannini and D. van der Marel. Phys. Rev. B **74** 024502 (2006).

[3] "Model independent sum rule analysis based on limited-range spectral data". A.B. Kuzmenko, D. van der Marel, **F. Carbone**, F. Marsiglio. Submitted to Nature Physics.

[4] "Doping dependence of the redistribution of optical spectral weight in $Bi_2Sr_2CaCu_2O_8$". **F. Carbone**, A.B. Kuzmenko, H.J.A. Molegraaf, V. Lukovac, E. van Heumen, F. Marsiglio, P. Kes, M. Li, S. Corajault, H. Berger, K. Haule and G. Kotliar. Phys. Rev. B **74** 064510 (2006).

[5] "Intraband Optical Spectral Weight in the presence of a van Hove singularity: application to $\mathrm{Bi_2Sr_2CaCu_2O_{8+\delta}}$ ". F. Marsiglio, **F. Carbone**, A.B. Kuzmenko, D. van der Marel. Phys. Rev. B. in press. cond-mat/0606688

[6] Y. Ishikawa, G. Shirane, J.A. Tarvin and M. Khogi Phys. Rev. B **16**, 4956 (1977).

Summary

Introduction

The use of anthropologists to name an era after the material used by mankind in that period suggests the importance that materials have had in the history of man. Understanding and using new materials has been the driving force for many of the technological conquests that human kind made. In our century, the development of electronic and photonics have followed the microscopic understanding of semiconductors and metals thanks to quantum mechanics. Most of the properties of solids are determined by a portion of the electrons composing the single elements which are involved in the chemical bonding that gives to the material its shape. These electrons are electrically charged particle, yet in many situations their mutual Coulomb repulsions can be neglected in the description of the solid. In the modern solid state physics one of the open challenges is to treat these interactions properly in all those materials where neglecting them results in a poor understanding of the experimental observations. These interactions are the cause of several interesting phenomena which have several important applications such as magnetism and superconductivity. Magnetism have been observed since ancient Greece, but only when quantum mechanics was developed and the concept of electron spin became available could be explained. In transition metal elements, the strong Coulomb repulsion felt by the d-electrons favor a magnetic arrangement of their spins in the atomic d-orbital. The easiest description of a magnetic solid would be to think of these magnetic moments of the atoms oriented among each other. This description applies to materials where indeed the d-electrons are localized on their atoms, and one can talk of atomic orbitals and spins, like in transition metal Oxides. However, magnetism has been observed in metallic systems as well, where the electrons of the solid are delocalized in a covalent bonding. The concept of itinerant magnetism has been developed in order to explain this phenomenon. The electrons forming the bands of the solids, which are the equivalent of the atomic orbitals in a "solid-language", can form different band structures for one spin direction or the other in certain situations. This results in a spin polarization which gives a net magnetic moment in the system. This scenario represents the limit where the electron-electron interactions are weak, but still capable of provoke magnetism, and its microscopic implications are a current

subject of debate. MnSi is considered to be a weak itinerant ferromagnet, and should be described by a model of this kind. Part of this thesis deals with the problem of determining the electronic structure of this material, and the effect of the Coulomb repulsions in order to give a microscopic clue to its magnetism.
A vast class of materials spanning large part of the periodic table has been shown to become superconductors at low temperature due to an electron-phonon driven pairing mechanism. This has been explained in BCS theory. The electrons moving in the lattice can deform the lattice itself via the Coulomb interaction between the electron negative charge and the ions positive one; this deformation can excite a particular phonon mode of the crystal. The result of this interaction creates an attractive potential around the electron that favors the pairing mechanism. When two electrons, particles with half integer spin, couple together, they behave as a particle with integer spin and obey the Bose-Einstein statistic and can condensate in a single quantum state. This condensate represents the ground state of the system, therefor in a superconductor current can flow in the ground state, and the material shows a zero resistivity. In BCS superconductors, when the pairs condensate is formed, the system lowers its potential energy by a larger amount then it increases its kinetic energy. The total energy is lowered and the material undergoes a superconducting phase transition. In 1986 a family of material has been discovered which exhibits a superconducting transition temperature much higher than the one of BCS materials. The highest T_c BCS compound known is now MgB_2 with a T_c around 39 K while Hg...CuO_2 becomes superconductor around 150 K under pressure. These materials are so called "Cuprates" because they are all compounds involving CuO_2. Several arguments have pointed toward a non-BCS pairing mechanism in these systems, but despite the large amount of research, a consensus has not be reached yet about the way the electrons pair. While BCS materials are Fermi Liquid systems where electron electron interactions can be treated as a perturbation, cuprates superconductors are non Fermi Liquid in the normal state and electron electron interactions are playing a dominant role. In such a context several pairing mechanisms have been proposed, a common ingredient of these is that the pairing occurs with a lowering of the electronic kinetic energy, opposite to the situation in BCS. Being able to measure the changes in kinetic energy of the system across T_c could then indicate which pairing mechanism is responsible for superconductivity in the Cuprates.

Optical spectroscopy of High T_c superconductors

A common probe of the motion of charged particles are electromagnetic waves. The response function of a system of charged particles to light is the complex optical conductivity $\sigma = \sigma_1 + i \cdot \sigma_2$, where σ_1 measures the absorption of light in the material and σ_2 is the reactive part of the response function. A sum rule is available in optical spectroscopy, the so called f sum-rule:

$$SW = \int_0^\infty \sigma_1(\omega\prime)d\omega\prime = \frac{\omega_p^2}{8} \tag{R.10}$$

The quantity SW is called optical spectral weight and it represents the weight of all optical transitions in the conductivity spectrum. If one limits the integral to a proper cut off Ω_c, it is possible to measure the weight of the only conduction band, which represents the response of the free electrons responsible for the electronic properties of the system. The SW can be related to the kinetic energy via a simple proportionality relation, and in the tight binding nearest neighbor approximation the expression SW = -K (K being the kinetic energy) is valid. being able to measure the changes in SW across the phase transition would allow to experimentally determine if kinetic energy is increasing or decreasing when the system becomes superconductor. This effect has been seen on a single crystal of Bi2212hajo for the first time. Up to this point we implicitly made several assumptions, whose validity needs to be verified:

- The SW is an integral from zero frequency up to a certain cut off. Obviously it is not possible to perform an optical experiment down to zero energy, one has to estimate how the missed spectral information is going to influence the final result.

- The equation SW = -K is strictly valid only when the parametrization of the band dispersion is limited to the nearest neighbor hopping parameter.

- In order to establish weather or not this is a common properties of the cuprates superconductors one has to study this effect for different compositions.

Answering these three points is the subject of part of this work. We measured different cuprates with different compositions by infrared reflectivity (between 12 meV and 0.78 eV) and spectroscopic ellipsometry (between 0.78 eV and 4 eV) in the temperature range between 10 K and 300 K. In order to see the superconductivity induced effect, the data were measured with a 1 K temperature resolution; moreover, a signal to noise ration higher than 3000 on the measured optical constants had to be achieved everywhere in the spectrum in order to detect the subtle changes at T$_c$. Much care has been taken in this respect, and thanks to a state of the art apparatus involving an home made ultra-stable cryostat of special design, we could measure the SW transfer across the phase transition with high accuracy in different materials. In Fig. R1 one can see a schematic of the experiments: reflectivity is measured shining infrared light on the sample and measuring the reflected beam; the sample is then coated with gold in situ and the reflected beam from the gold surface is measured as a reference. In ellipsometry one impinges on the sample with a linearly polarized beam and measures the degree of ellipticity in the polarization that the sample induces in the beam. The combination of these two techniques can provide the complex conductivity in a wide range of energies. Despite the simplicity of the concept, this experiment is very demanding because of the very broad energy (almost 4 decades) and temperature (almost 2 decades) ranges required with high accuracy.

In Ref. [1] we measured the dielectric tensor of a crystal of $Bi_2Sr_2Ca_2Cu_3O_{10}$ in all its non-equivalent crystallographic directions. In this publication we have shown that the SW can be determined with very high accuracy even if the data are not measured down to zero frequency, thanks to the combined accurate knowledge of the real and imaginary part of the optical conductivity in a broad frequency range. This has been the subject of a further publication where we could give quantitative arguments based on an analytical and numerical analysis of the properties of analytical functions [2]. We also discussed the theoretical implications of the choice of the frequency cut off in the SW integral, showing that the SW below 1 eV can indeed be representative of the response of the conduction band electrons in the cuprates giving hints on the changes in Kinetic energy of the free carriers. In Fig. R2 we show the effect of the low frequency extrapolations on the SW transfer.

In Ref. [3] we studied the dependence of the SW transfer on the Oxygen doping in $Bi_2Sr_2CaCu_2O_8$ samples. The Oxygen off stoichiometries in these material can vary their superconducting properties by changing the number of carriers in the conduction band. At zero doping the system is a charge transfer insulator, it becomes metallic and superconductor introducing Oxygen abundance and over a certain Oxygen quantity superconductivity is suppressed. In Fig. R3 one can see the phase diagram for cuprates superconductors. The SW transfer as a function of doping has a non trivial behavior which could be explained theoretically in the context of the t-J model starting from a cluster of 4 Copper atoms, Fig. R4. The t-J model Hamiltonian is:

$$\begin{aligned} H &= -t\sum_{i,j,\sigma}(b^{\dagger}_{i,\sigma}b_{j,\sigma}+H.c)+J\sum_{i,j}S_iS_j && \text{(R.11)}\\ b_{i,\sigma} &= c_{i,\sigma}(1-n_{i,-\sigma}) && \text{(R.12)}\\ c^{\dagger}_{i,\sigma}c_{i,\sigma} &= n_{i,\sigma} && \text{(R.13)} \end{aligned}$$

and represents a system with and exchange interaction J between neighbors and where the double occupation of a site is forbidden. This model can describe fairly well the low energy physics of cuprates superconductors, as confirmed by our results. So far we have been giving for granted the relation between the SW and the kinetic energy. This is a very subtle issue which has been addressed in a recent publication[4]. For certain compositions in fact the SW can behave very differently from the electronic kinetic energy. On the other hand we verified that for the compositions that we experimentally investigated this relation is a good approximation of reality.

The electronic structure and the band magnetism of MnSi

As we mentioned in the introduction, band magnetism originates form a spin polarization of the electronic bands of a solid. In order to have a microscopic description of the magnetism of MnSi, which is believed to be an itinerant magnet, one has to know precisely its electronic structure. When Coulomb repulsions are weak, band structure calculations provide a good representation of the electronic structure. If Coulomb repulsions are strong, localization effects can happen and the itinerant picture starts to break down. An accurate estimate of Coulomb repulsions is crucial for magnetic systems, since magnetism itself is driven by them. We investigated MnSi electronic structure by means of X ray Absorption Spectroscopy and Photoemission Spectroscopy and compared these results to first principle LDA band structure calculations.

In XAS one excites a core electron to the unoccupied states of one particular element. It is an element specific probe which can sense the unoccupied density of states of a material. If the core-hole wave function has a large interaction with the excited electron wave function, for example in a $2p \mapsto 3d$ transition in a transition metal, atomic multiplets effect can occur and the shape of the absorption spectrum heavily depends on the ground state configuration of the system. This makes XAS suitable for studies of the valency of materials. In MnSi though, one would not expect to find atomic multiplets effect, since the electrons in the conduction band are delocalized in a metallic state. In such a context one would expect that a simple Local Density Approximation (LDA) approach would be sufficient to represent the XAS process: in LDA one calculates the single particle unoccupied density of states on the element probed by X rays. Keeping into account the effect of the core-hole as a simple Coulomb potential on the atom one is able to simulate the XAS process. This approach neglects Coulomb repulsions between carriers. We have shown that this procedure miserably fails in MnSi and FeSi while it gives consistent results in CoSi, see Fig. R5. On the other hand, also the atomic multiplet theory does not give satisfactory results. The reason is that MnSi and FeSi are materials where Coulomb repulsions are neither negligible nor dominant. We could explain the XAS spectra in these materials proposing that their ground state has a mixed valence character where charge localization effects partially suppress the valence fluctuations typical of metallic systems. XAS is a high energy probe, in some sense it is not fully justified to say that it is a probe of the true ground state of the system because the x-rays are indeed provoking a significant perturbation. The same trend is observed by means of valence band photoemission; the spectra of MnSi and FeSi cannot be reproduced by LDA calculations, while in CoSi a very good agreement is achieved. Also some deviations form the LDA scenario, in MnSi, are observed by means of Positron Annihilation Spectrosocpy which can probe the density of states at the Fermi surface.

These observations suggest that MnSi is on the edge between a local moment compound and an itinerant one, making the microscopic understanding of its magnetism a difficult task. Itinerant magnets in fact, have several characteristics in common with localized magnets, the Curie-Weiss susceptibility, the temperature dependence of the magnetic relaxation rate (1/T1), but their absolute values are renormalized. A microscopic clue to the understanding of these observations came from Moryia's spin fluctuation theory. By the comparison to some new NMR measurements as well as neutron scattering experiments, we can estimate with precision some important microscopic parameters of this model, however some significant departures are observed. The magnetic excitation spectrum of this material shows well-defined spin waves intersecting the Stoner continuum around 3 meV. This makes it an ideal compound to study the paramagnetic scattering, and in fact the first observation of dumped spin waves within the continuum has been done in MnSi. However, the study of the Stoner excitations in MnSi didn't go further then an energy transfer of 20 meV because of experimental difficulties and because of the presence of the optical phonons in the range between 20 and 60 meV. The low energy data have been interpreted in terms of the spin fluctuation theory, which can explain the Curie-Weiss law observed in the magnetic susceptibility. In this model the behaviour with temperature of the magnetization is mostly governed by the temperature dependence of the low energy spin waves, while the Stoner excitations are expected to be almost temperature independent. In our inelastic neutron scattering data we could study the Stoner excitations up to an energy transfer of 400 meV at room temperature and 10 K. We find an unexpected temperature dependence of the Stoner excitations, which questions the microscopic interpretation of the Curie-Weiss law of the susceptibility based on the spin fluctuation model.

In a neutron scattering experiment, the cross section per unit of energy and solid angle for the electromagnetic interaction between the neutron magnetic moment and the magnetic moments present in a solid is given by the formula:

$$\frac{d^2\sigma}{d\Omega dE\prime} = \frac{k_f}{k_i}(\gamma r_0)^2 \mid \frac{g}{2}F(Q) \mid^2 \sum_{\alpha,\beta}(\delta_{\alpha,\beta} - Q_\alpha Q_\beta S^{\alpha,\beta}(Q,\omega)) \tag{R.14}$$

Where Q $= k_f - k_i$ and $\hbar\omega = E_f - E_i$ are the momentum and energy transfer. $\gamma = 1.913$ and $g \simeq 2$ are the spectroscopic g-factors of the neutron and magnetic atom. F(Q) is the magnetic form factor and depends on the atom present in the solid. In Eq. R.14 the quantity S(Q,ω) contains the spin correlation function:

$$S^{\alpha,\beta}(Q,\omega) = \frac{1}{2\pi\hbar}\int dte^{i\omega t}\frac{1}{N}\sum_{i,j} < S_i^\alpha(t)S_j^\beta(0) > e^{-iQ(R_i - R_j)} \tag{R.15}$$

Using the fluctuation-dissipation theorem one can relate the spin correlation function to the spin susceptibility by the formula:

$$S(Q,\omega) = \frac{1}{1 - e^{-\beta\hbar\omega}}\frac{\chi\prime\prime(Q,\omega)}{\pi(g\mu_B)^2} \tag{R.16}$$

with $\beta = 1/k_B T$. One can see from these equations that with a neutron scattering experiment it is possible to have direct information on the imaginary part of the spin susceptibility as a function on energy and momentum. In itinerant magnets, the spin susceptibility has been investigated by means of the RPA (random phase approximation) method. In this model the imaginary part of the spin susceptibility is given by:

$$\chi''(Q,\omega) = \frac{Im\chi_0(Q,\omega)}{[1 - IRe\chi_0(Q,\omega)]^2 + [IIm\chi_0(Q,\omega)]^2} \tag{R.17}$$

where I is the intra-atomic interaction and χ_0 is the susceptibility of the non interacting electron gas. χ_0 can be calculated analytically and well defined spin-waves with a quadratic dispersion are predicted by this model. A detailed comparison to this model has been performed in Ref.[5]. In MnSi, one needs to go beyond this approach in order to explain the Curie-Weiss law of the magnetic susceptibility and the peculiar properties of the paramagnetic scattering. This is done by Moryia's spin fluctuation theory, where the spin susceptibility is given by the formula:

$$\chi(Q,\omega) = \frac{\chi_0(Q,\omega)}{1 - I\chi_0(Q,\omega) + \lambda(Q,\omega)} \tag{R.18}$$

The additional term with respect to the RPA formula $\lambda(Q,\omega)$ is producing the Curie-Weiss behavior observed experimentally. Before being able to compare the measured susceptibility with the theoretical prediction one has to reliably separate the magnetic scattering form the phonon scattering. As we mentioned before, in MnSi several phonon modes are polluting the spectra between 20 and 60 meV. A precise ab-initio LDA calculation of the phonon dispersion could allow one to make such a distinction and its fine tuning can also give an important feedback on the electronic structure determination. In Fig. R6 one can see a comparison between the experimentally derived phonon dispersion and the LDA calculation. One can see that a very encouraging result is achieved, although some departures are present. This allow us to assign some of the scattering as magnetic in origin. In Fig. R7 we display directly the dispersion of the magnetic excitations at room temperature and 10 K together with the results obtained from the simulation based on eq. R18. One can see that a significant temperature dependence is observed, especially around the R point (1,1,1) in the experiment. The theory however, predicts a weak temperature dependence of the Stoner spectrum, even of the opposite sign of the one observed experimentally. It is remarkable that the strongest temperature dependence is observed around the (1,1,1) point, which is the easy axis of the magnetization in the ordered phase. This observation suggests that the Stoner excitations are playing an important role in the magnetism of MnSi, contrary to the prediction of spin fluctuation theory. Altogether, our observations might look somewhat in contrast in certain respects: evidence for localization is found by means of high energy probes, yet the neutron scattering experiments are interpreted in terms of an itinerant model. However, the departures observed in both approaches actually confirms that none of the two, the purely localized or purely itinerant, is actually correct. The region on the edge of the formation of local moments is terra incognita from the theoretical point of view, our experimental observations provide useful hints for developing a microscopic model for the band magnetism of MnSi.

Bibliography

[1] " In-plane optical spectral weight transfer in optimally doped $Bi_2Sr_2Ca_2Cu_3O_10$" **F. Carbone**, A.B. Kuzmenko, H.J.A. Molegraaf, E. van Heumen, E. Giannini and D. van der Marel. Phys. Rev. B **74** 024502 (2006).

[2] "Model independent sum rule analysis based on limited-range spectral data". A.B. Kuzmenko, D. van der Marel, **F. Carbone**, F. Marsiglio. Submitted to Nature Physics.

[3] "Doping dependence of the redistribution of optical spectral weight in $Bi_2Sr_2CaCu_2O_8$". **F. Carbone**, A.B. Kuzmenko, H.J.A. Molegraaf, V. Lukovac, E. van Heumen, F. Marsiglio, P. Kes, M. Li, S. Corajault, H. Berger, K. Haule and G. Kotliar. Phys. Rev. B **74** 064510 (2006).

[4] "Intraband Optical Spectral Weight in the presence of a van Hove singularity: application to $\mathrm{Bi_2Sr_2CaCu_2O_{8+\delta}}$ ". F. Marsiglio, **F. Carbone**, A.B. Kuzmenko, D. van der Marel. Phys. Rev. B. in press. cond-mat/0606688

[5] Y. Ishikawa, G. Shirane, J.A. Tarvin and M. Khogi Phys. Rev. B **16**, 4956 (1977).

Per i non addetti ai lavori

Quando vi sedete dietro ad un tavolo per giocare a Monopoly, studiate le regole del gioco e poi giocate. Ogni volta che passate dal via ritirate, perdonate ma io sono del '76 e ho ricevuto il monopoly a 5 o 6 anni, venti mila lire. Nessuno credo si sia mai sognato di chiedere perché. Si tratta di una regola del gioco. Cosa c'entra questo con la fisica? Fare il fisico in sostanza si tratta di sedere dietro al tavolo e iniziare a giocare a monopoly senza sapere le regole, cercando di capirle da come evolve il gioco. Immaginate che il monopoly abbia una volontá propria e che faccia fluire il denaro e le carte man mano che voi spostate il vostro simbolo. Capire le regole vi porta poco a poco a capire il gioco. Se non andate in bancarotta prima, analogia tristemente attinente all'uso che l'uomo fa della natura, ad un certo punto avrete una buona idea di come si gioca e la vostra preoccupazione primaria sará qual é la mossa migliore, mentre la preoccupazione principale di filosofi e religiosi sará perché proprio venti mila lire e non cinquanta. In questo breve riassunto io butteró nella mischia molte regole che i fisici hanno scoperto in anni di storia. Il proposito di questa digressione é di pregarvi di fare lo sforzo di non chiedervi il perché di certe regole. Tutto allora fluirá con semplicitá, dando quella effimera illusione di capire la natura.

Dall'osservazione dei fenomeni magnetici ai tempi dell'antica Grecia ad una loro spiegazione microscopica sono trascorsi piú di 2000 anni. Tanto ci ha messo l'uomo a formulare la teoria della meccanica quantistica. I solidi che ci circondano nella vita di tutti i giorni, a livello microscopico, sono formati da un reticolo ordinato di atomi, che sono i tasselli fondamentali del mosaico che ci circonda: la natura. Gli atomi sono costituiti da un nucleo carico positivamente e da particelle cariche negativamente (elettroni) che orbitano a distanze distribuite in modo discontinuo attorno ad esso (orbitali). Gli elettroni che occupano gli orbitali piú esterni sono quelli responsabili della formazione dei legami chimici che tengono insieme molecole e solidi. Ciascun elettrone possiede un momento magnetico (cioé la capacità di esercitare una certa forza magnetica) che puo' essere diretto solamente in due direzioni convenzionalmente chiamate su e giú, per non far politica s'intende. Gli elettroni possono riempire gli orbitali a due a due, a patto che quando occupano lo stesso orbitale abbiano questi momenti magnetici orientati l'uno opposto all'altro. Il risultato di questa regola é che il momento magnetico risultante é nullo e nessun fenomeno di attrazione di altri corpi viene osservato. Alcuni atomi, i metalli di transizione come Ferro, Cobalto, Manganese etc..., hanno degli orbitali chiamati "d" dalla forma molto particolare e compatta. Questo fa si che due elettroni che si trovassero sullo stesso orbitale rimarrebbero molto vicini durante il loro moto. Gli elettroni sono particelle cariche negativamente; la loro tendenza a respingersi fa si che preferiscano occupare un orbitale ciascuno mantenendo i momenti magnetici orientati parallelamente. Questo fa si che il momento magnetico risultante non venga cancellato e il materiale si dice ferromagnetico. Questa descrizione funziona bene in tutti quei materiali nei quali, nonostante la formazione del legame chimico, il movimento degli elettroni é ancora molto simile a quello che avrebbero nei rispettivi atomi isolati. In molti casi invece, quando gli atomi formano un solido, gli elettroni piú lontani dal nucleo percorrono traiettorie diverse che spaziano in tutto il solido e che per semplicitá da qui in poi chiameremo bande. É il caso del legame metallico, che spiega la propagazione della corrente e del calore in questi materiali. Alcuni metalli possono essere magnetici, quasi sempre quando contengono metalli di transizione, grazie ad una diversa forma di magnetismo chiamato magnetismo itinerante. In alcuni casi, gli elettroni che percorrono queste bande per evitarsi il piú possibile si dispongono su bande diverse a seconda della direzione del loro momento magnetico. Il risultato é un momento magnetico non nullo originato da elettroni che sono delocalizzati in tutto il solido. In questa tesi abbiamo studiato uno di questi materiali, composto da Silicio e Manganese, perché la comprensione microscopica di quello che veramente succede in questo tipo di magneti é ancora scarsa. Come é facile capire da quanto detto finora, un ingrediente fondamentale del perché questi fenomeni magnetici avvengano, é la repulsione tra le cariche negative. Mentre la natura di questa repulsione é semplice da studiare negli atomi, perché la forma degli orbitali é conosciuta, in un solido questo é un problema molto complicato. Uno dei risultati di questo lavoro é stata la determinazione sperimentale delle caratteristiche delle bande del solido e la stima delle repulsioni che influenzano il moto degli elettroni che percorrono queste bande. Questo, collegato alle caratteristiche magnetiche del materiale, puó fornire un'idea dettagliata dei meccanismi che a livello microscopico portano un materiale metallico ad esibire comportamenti magnetici.

Un altro fenomeno di grande interesse nella fisica dello stato solido è la superconduttivitá. In un solido, la corrente e il calore sono trasportati dagli elettroni. I loro urti contro il reticolo formato dagli atomi danno luogo alla resistenza elettrica. Nei materiali isolanti la corrente e il calore si propagano molto poco perché gli elettroni sono localizzati sui loro atomi. Questi concetti intuitivi e banali sono la base di molti fenomeni che ci circondano; la stufa elettrica funziona grazie ad una resistenza che si scalda al passaggio della corrente, lo scaldabagno idem e cosí via. In generale, la resistenza di un materiale é piú bassa tanto piú bassa é la sua temperatura. L'idea é che piú bassa é la temperatura, minore l'agitazione termica, gli urti contro il reticolo, e di conseguenza la resistenza. Agli inizi del secolo due fisici olandesi volevano verificare questo fenomeno fino alle piú basse temperature possibili. Raffreddando del Mercurio si sono accorti che sotto qualche grado Kelvin (gradi K = gradi C + 273) la resistenza del mercurio non era piccola, ma nulla. In seguito lo stesso comportamento fu osservato in molti altri elementi della tavola periodica. Il fenomeno consiste nell'azzeramento della resistenza elettrica. Si sente sempre dire che lo zero esatto é un concetto che non si puó misurare in fisica, ecco, forse la resistenza di un superconduttore é quanto di piú vicino allo zero l'uomo abbia mai misurato. La comprensione di questo fenomeno avvenne quasi 50 anni dopo, quanto Bardden Schriffer e Cooper svilupparono la teoria BCS che valse loro il premio Nobel per la fisica. A questo punto entra in gioco un'altra regola del monopoly che dice che tutte le particelle del creato possono essere catalogate in due grandi gruppi: i fermioni e i bosoni. I fermioni obbediscono al principio di esculsione di Pauli e portano "magliette" con numeri semi-interi, altra regola del monopoly, mentre i bosoni non obbediscono al principio di esclusione e portano magliette con numeri interi. Per farsi un'idea di cosa sia il principio di esclusione faró un esempio rigorosamente sbagliato, ma utile per capire. Immaginate di avere una pista di atletica con dei corridori che stanno gareggiando, se questi corridori fossero fermioni, (magliette con numeri 1/2, 3/2, 5/2....) secondo il principio di esclusione di Pauli non ci dovrebbero essere due corridori che fanno la stessa velocitá. Se fossero bosoni, anche tutti potrebbero correre alla stessa velocitá. L'ingrediente fondamentale della teoria BCS della superconduttivitá è che sotto una certa temperatura in alcuni solidi gli elettroni, che normalmente sono fermioni, formano delle coppie (dette coppie di Cooper) e viaggiano a due a due. Siccome viaggiano in coppie e hanno numeri semi-interi sulla maglia, che sommati danno un numero intero, si comportano come dei bosoni e acquistano la capacitá di viaggiare tutti alla stessa velocità. Per vedere perché questo porta alla superconduttivitá ci serve un'altra astrazione: supponete di correre sui merletti di un castello, ogni tanto dovrete saltare per passare sul merletto successivo. Se immaginate di correre a velocitá costante e che la lunghezza del vostro salto dipenda solo dalla vostra velocitá, ci sará una velocitá che vi permette di saltare di merletto in merletto senza mai cadere nei buchi. Se ora invece che uno solo foste un gruppo di persone, e se solo uno potesse viaggiare a questa velocitá magica, gli altri inevitabilmente cadrebbero nei buchi e questo rallenterebbe la loro corsa. Se peró tutti potessero viaggiare alla velocitá magica, nessuno cadrebbe nei buchi. Se facciamo un parallelo tra la corsa sui merletti e la corsa degli elettroni in un solido possiamo dire che quando si accoppiano, grazie al fatto che possono comportarsi da bosoni, possono tutti viaggiare alla velocitá giusta ed evitare gli urti con il reticolo. Il risultato é l'assenza di resistenza elettrica. Resta da capire cosa spinge gli elettroni a formare le coppie di Cooper sotto una certa temperatura. Nei superconduttori convenzionali, l'attrazione capace di vincere la repulsione tra due cariche negative é dovuta all'interazione tra gli elettroni stessi e il reticolo. Immaginiamo due trattori che scavino due solchi nella terra dove passano, se questi solchi fossero cosí vicini da toccarsi, ad un certo punto un trattore si troverebbe nella discesa creata dal solco dell'altro trattore e i due trattori inizierebbero a percorrere insieme lo stesso solco. La stessa cosa avviene in un solido, dove ,sotto una certa temperatura in alcuni materiali, l'altezza del solco richiede un'energia maggiore della repulsione tra le due cariche negative per essere superata e i due elettroni iniziano a viaggiare insieme. Questo meccanismo rappresenta un buon modello per i superconduttori convenzionali, detti BCS, nei quali la resistenza elettrica si azzera al di sotto di qualche grado Kelvin. A metá degli anni ottanta una nuova classe di materiali, tutti comprendenti l'ossido di Rame, é stata individuata nella quale la superconduttivitá si manifesta a temperature molto piú alte, nell'ordine dei cento Kelvin. Quello che non é ancora chiaro dopo venti anni di ricerca é il meccanismo che forza gli elettroni a stare a coppie in questi solidi. Nei superconduttori BCS, la coppia di Cooper si forma spendendo dell'energia cinetica (gli elettroni vanno un po' piú veloci), e guadagnando una quantitá maggiore di energia potenziale (gli elettroni diminuiscono le repulsioni dovute al fatto che sono ambedue cariche negative). L'energia cinetica degli elettroni in un solido é intimamente collegata al colore del solido stesso, altra regola del monopoly. Quindi studiando i cambi di colore del solido quando diventa superconduttore si puó scoprire se le coppie di Cooper si formano guadagnando o perdendo energia cinetica. In questa tesi abbiamo dimostrato che nei superconduttori ad alta temperatura la formazione delle coppie di Cooper avviene tramite un guadagno di energia cinetica. Al contrario di quello che succede nei superconduttori convenzionali. Questi risultati ci hanno permesso di verificare sperimentalmente la veridicitá di un modello teorico che descrive la formazione delle coppie di Cooper che si basa su meccanismi diversi dalla deformazione del cristallo che ho descritto in precedenza. In queste righe la quantitá di cose sbagliate che ho scritto é spaventosa, e spero che essendo in italiano nessuno o quasi dei fisici con i quali lavoro riesca a leggerle. Tuttavia, non mi avventuro a cercare di dare una visione intuitiva dei modelli teorici per i superconduttori ad alta temperatura perché il livello di corbellerie potrebbe sorpassare anche il mio senso della decenza. Lo scopo di questo riassunto non era di spiegare la fisica contenuta in questa tesi in modo rigoroso per soddisfare chi la fisica la sa, ma di dare un'idea il piú comprensibile possibile a chi la fisica non la sa, ma si chiede perché mi pagano e cosa faccio tutto il giorno. Infine, circa la rilevanza di questi studi, bisogna considerare che i materiali magnetici sono alla base della gran parte delle memorie utilizzate al giorno d'oggi per lo stoccaggio delle informazioni e la domanda di memorie sempre piú efficaci e piccole non si arresta mai. La comprensione dei materiali magnetici ha dunque un ruolo chiave nello sviluppo della tecnologia per l'informazione. Per quel che concerne i superconduttori invece, la possibilitá di trasportare corrente senza perdite dovute alla resistenza del cavo, solo per fare il piú banale degli esempi, rappresenta una grossa potenzialitá soprattutto in tempi nei quali il risparmio energetico é di grande attualitá. Nella nostra analogia col monopoly diciamo che chi riuscisse a fabbricare un superconduttore che avesse zero resistenza a temperatura ambiente piazzerebbe un bell'albergo su parco della Vittoria......

Chapter 1

Introduction: The role of the Coulomb repulsion between electrons in solids

Often in this thesis the reader will encounter the following statement: "this is an effect of electron-electron correlations" The purpose of this chapter is to give a simple physical explanation to this sentence. The idea is that whenever the reader finds that electron-electron correlations are blamed in the thesis he can find an explanation in this chapter.

1.1 The Coulomb repulsions in solids: the Hartree-Fock approximation

If we consider the Schrodinger equation of a single electron:

$$-\frac{\hbar^2}{2m}\nabla^2\psi(r) + U(r)\psi(r) = \epsilon\psi(r) \tag{1.1}$$

The term U(r) represents the potential that the electron feels and should contain the lattice and the Coulomb repulsions among electrons. To describe the motion of electrons in solids by this equation is virtually impossible because of the very complicated effect of the interaction between electrons. To be strict, one should use an equation for the N particles present in the system:

$$H\Psi = \sum_{i=1}^{N}(-\frac{\hbar^2}{2m}\nabla_i^2\Psi - Ze^2\sum_{R_{i,j}}\frac{1}{r_i - R_j}\Psi) + 1/2\sum_{i\neq j}\frac{e^2}{\mid r_i - r_j \mid}\Psi = E\Psi \tag{1.2}$$

Where the first term represents the kinetic energy of the particles, the second their attraction to the nuclei with position R_j and the third the Coulomb repulsions between the electrons. I introduced this equation here to clarify what one is aiming at. However, no way to get there. Simplifications have to be made in order to solve this problem. One possibility is the Hartree-Fock method. This approximation consists of considering the effect of the electron repulsion as an average perturbation of the single particle motion. In this way one can write the equation 1.2 for the single particle problem in the form:

$$-\frac{\hbar^2}{2m}\nabla\psi_i(r)+U^{ion}(r)\psi_i(r)+[e^2\sum_j\int dr\prime \mid \psi_j(r\prime) \mid^2 \frac{1}{r-r\prime}]\psi_i(r)=\epsilon_i\psi_i(r) \quad (1.3)$$

where we considered the effect of the lattice in the potential $U^{ion}(r) = -Ze^2\sum_{R_j} 1/\mid r - R_j \mid$ and the potential energy given by the electron-electron repulsions as $U^{el}(r) = -e\int dr\prime\rho(r\prime)\frac{1}{r-r\prime}$. In this equation the density of charge ρ contains another approximation: we use the single particle knowledge that the contribution of the electron with wave-function ψ_i to the density of charge is $-e \mid \psi_i(r) \mid^2$ and therefore $\rho(r) = -e\sum_i \mid \psi_i(r) \mid^2$. This is called the Hartree equation and contains a non obvious problem which is solved in the Hartree-Fock approach. Eq.1.3 implies that the possible wavefunctions ψ_i have the form:

$$\Psi(r_1s_1, r_2s_2, ...r_n, s_n) = \psi_1(r_1s_1)\psi_2(r_2s_2)....\psi_n(r_ns_n) \quad (1.4)$$

This wavefunction does not satisfy the Pauli principle, which requires the following antisymmetric condition:

$$\Psi(r_1s_1, r_is_i, r_js_j, ...r_n, s_n) = -\Psi(r_1s_1, r_js_j, r_is_i, ..., r_ns_n) \quad (1.5)$$

This is obtained by substituting Eq.1.4 with a Slater determinant of the one electron wavefunction, which is a linear combination of the product in Eq. 1.4 and all other possible combinations of the permutations of r_js_j. The Hartree equation becomes:

$$-\frac{\hbar^2}{2m}\nabla\psi_i(r)+U^{ion}(r)\psi_i(r)+U^{el}(r)\psi_i(r)-\sum_j\int dr\prime\frac{e^2}{r-r\prime}\psi_j^*(r\prime)\psi_j(r)\delta_{s_i,s_j} = \epsilon_i\psi_i(r) \quad (1.6)$$

After all these manipulations and simplifications, lo and behold, this equation cannot be solved. Unless of course further approximations are done. I am not going to mention all of those since there are many and they depend on the problem one wants to treat. The important point is to realize that starting from the Hartree Fock equation one can address some very important effects due to the Coulomb repulsions, such as the exchange interaction, which is very important for the magnetism of transition metals and the screening that the conduction electrons can do to an externally imposed charge distribution[18].

1.2 The Coulomb repulsions in solids: the Landau Fermi liquid

Using the Hartree-Fock treatment of the electron-electron correlations, in the end we still describe the electronic properties of a system as a consequence of the occupation of a certain set of single particle states. Clearly such a description cannot be satisfying in all situations where electron-electron correlations may lead to very complicated many-body effects. However, the remarkable success of the single particle approximation in describing several properties of solids has a profound reason, which is explained by the Landau Fermi liquid theory. Starting from the single particle scenario, imagine that one has a set of well defined single particle stationary states. If one perturbs these states adding correlations, two things might happen: (i) the energy of the single particle states shifts (which is true also in the Hartree-Fock approximation), (ii) the particles can evolve as a cascade of particle-hole excitations, meaning that these states are no longer stationary (this possibility is neglected in the Hartree-Fock scenario). Clearly the last phenomenon could invalidate the single particle approach if the rate of this scattering is so high that the electron-electron scattering dominates all other scattering events. Even in the presence of screening, Coulomb repulsion would be strong enough to dominate other sources of scattering. In the end the single particle scenario more or less holds thanks to the Pauli exclusion principle.

Imagine a system filled up to the Fermi energy (E_F) and one electron occupying one level above E_F with an energy E_1; this electron can scatter onto another electron with energy E_2 below E_F (because only these states are occupied). The energy levels E_3 and E_4 where the two particles can scatter to must be above E_F (unoccupied states). Moreover, in whatever scattering process the energy must be conserved, meaning that the summation of the energies before the scattering event and after must be the same ($E_1+E_2=E_3+E_4$). If the particle 1 is exactly at the Fermi level one can see that in order to satisfy the energy conservation the scattered particles must end up also on the Fermi surface (E_2,E_3,$E_4=E_F$). However, these states are already occupied, this means that such a scattering event simply cannot take place and at T=0 K the states at E_F are stationary, their lifetime is infinite. The condition T=0K in this description is crucial. In fact, if instead of putting the excited state, particle 1, on top of a completely filled phase space, as would be the case at zero temperature, we put it on top of a thermally distributed set of levels, some levels will be available for the described scattering process. The scattering rate in this scenario will depend on the distance from E_F of the excited state and on the temperature of the system:

$$\frac{1}{\tau} = a(\epsilon_1 - \epsilon_F)^2 + b(k_B T)^2 \tag{1.7}$$

A crude estimate of the scattering time for the electron-electron process gives a lifetime around 10^{-10} sec, while the electron-lattice scattering processes give lifetimes around 10^{-14} sec. These numbers have not to be taken as accurate, however they give a crude reason why most likely the electron-electron scattering can be much slower than other scattering events, and therefore why the effect of Coulomb repulsion could be a minor correction to the single particle picture in metals.

One should realize that the above argument is valid only with the starting point that the system can be represented fairly well by a set of single particle states. To resume, I have shown that in the case in which a set of single particle states is a good starting point for the description of the electronic structure of a solid, then Coulomb repulsions are not likely to play an important role close to E_F. The main idea of Fermi liquid theory is the following: if the Coulomb repulsions are strong enough to invalidate the single particle scenario, one can hope that a set of states obeying the Pauli principle whose structure is similar to that of a set of single particles state describes the system. These states are no longer single particle states, but are called quasi-particle states and they are the result of the complex many body effects due to Coulomb repulsions. A detailed microscopic description of the quasi particle is very difficult and goes beyond the scope of thesis. The consequence of this description is very important and clear. Experimentally, quasiparticles should behave as well defined single particles states, with the only difference that their characteristics should be renormalized by the interactions[18]. When this is not the case, so called non Fermi liquid behaviors, it means that the above picture is not valid, wether the blame should be on the assumption on the scattering rate or on the equivalence between single particles states and many body states or on a combination of the two is the challenge of modern solid state physics and is the motivation of this thesis. I will now discuss what are the consequences of electron-electron correlations onto an experimental observable.

1.3 Manifestations of the Coulomb repulsion in experiments

1.3.1 Coulomb repulsion in Photoemission and X-ray Absorption Spectroscopy

Photoelectron spectroscopy is based on the photoelectric effect discovered by Einstein at the beginning of the XXth century. In these experiments light is used to emit electrons from a solid. The velocity of the outcoming electron contains information on the energy that the electron had in the solid, because of the energy conservation law which implies that the energy of the photoemitted electron is equal to the energy of the photon plus the energy that the electron had in the crystal. Recently it became possible to measure also the angle of photoemitted electrons gaining information also on the momentum that the electrons have in the solid, via the conservation of momentum rule. Such probes are measuring the occupied density of states of a solid. It has been shown[1] via a combination of photoemission and inverse photoemission that in transition metals and rare earths, the occupied d(f) states and the unoccupied d(f) states are split by the energy of the Coulomb repulsion which can be as high as 5 eV for Mn for example. These experiments have shown that Coulomb repulsions can push away electronic states from the Fermi energy, and this effect can manifest itself by giving rise to satellites in the photoemission spectra. In the presence of strong interactions, if two electronic states have a large spatial overlap, Coulomb repulsions can separate them in energy and they can be found in very different positions than one would expect in the absence of correlations[1]. Since I will discuss the electronic structure of cuprate superconductors later on, I will use one of these materials as an example. In Fig.1.1[2] valence band photoemission data on La_2SrCuO_4 are presented and compared to standard band structure calculations and cluster calculations including the effect of Coulomb repulsions. In a single particle band structure calculation one would expect to have the spectral weight of the valence band mostly due to Cu 3d states and O 2p states concentrated around the first 4-5 eV below the Fermi level. Experimentally one finds that the valence band has a rather different shape, where some weight is observed at energies as high as 12 eV from the Fermi level. Performing a cluster calculation that includes the effect of the Coulomb repulsions, one finds that the $3d^9$ and the $3d^{10}$ states are split by 3eV and that the $3d^8$ configuration is pushed away 12 eV from the Fermi energy. Because of Coulomb repulsion the spectral weight in the valence band is thus distributed into a main peak and other components at higher energies which are still due to $3d$ states, and are called satellites. One should realize in Fig.1.1 that the $3d^8$ satellite predicted by the cluster calculation is not visible in the photoemission experiment, but could be observed in a resonant photoemission experiment as discussed in section 3.1.2.

Another popular technique for probing the electronic structure of molecules and solids is X-ray Absorption Spectroscopy [3, 4]. In a single particle scenario, an XAS experiment probes the unoccupied density of states above the Fermi energy. An electron is excited from a core level into an unoccupied state. Since the absorption for a single wavelength is proportional to the unoccupied density of states at that energy, one can measure the spectrum of the unoccupied density of states by tuning the energy. However, this simple picture brakes down spectacularly in the $2p \rightarrow 3d$ absorption spectra of transition metals, where Coulomb repulsions manifest themselves giving rise to atomic multiplet effects. The atomic multiplet theory is often

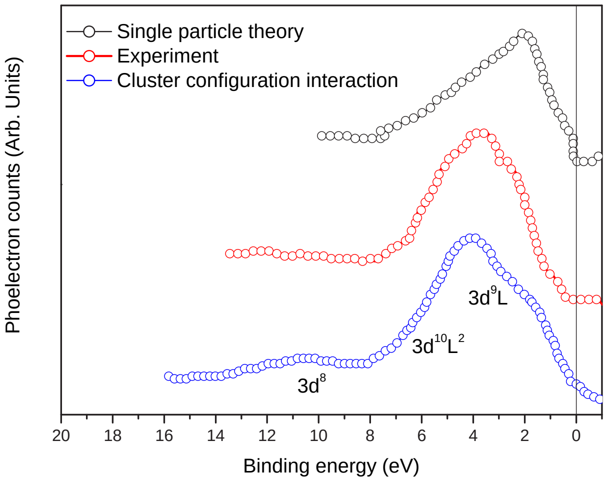

Figure 1.1: Valence band photoemission of La_2SrCuO_4 together with single particle approximation calculation and configuration interaction calculations spectra obtained from Ref. [2].

a good approximation of what goes on in a solid, and represents the extreme case where Coulomb repulsion is so strong that the electrons are localized on their ions and therefor the atomic orbitals are a good approximation of the solid. This applies in particular to transition metals oxides and rare earth compounds. The starting point for the atomic multiplet theory is the atomic Hamiltonian:

$$H = -\sum_N \frac{p_i^2}{2m} + \sum_N \frac{-Ze^2}{r_i} + \sum_{i \neq j} \frac{e^2}{r_{ij}} + \sum_N \zeta(r_i) l_i s_i \tag{1.8}$$

The first term in the Hamiltonian is the kinetic energy of the particles, the second the Coulomb interaction with the nucleus, the third the Coulomb interaction between electrons and the last is the spin orbit coupling. This equation cannot be solved analytically; one should realize that the kinetic energy term and the interaction with the nucleus is going to be the same for all electrons in a certain atomic configuration, therefore the important terms are the Coulomb repulsion and the spin orbit coupling. The Coulomb repulsion term is too large to be treated as a perturbation, therefore we use the central field approximation. This consists in splitting the interaction term into one with a spherical symmetry and one with a generic one. The spherical term is treated as an average Coulomb potential and is subtracted from the total interaction term. This leads to a Hamiltonian for the Coulomb repulsion that reads:

$$H_{ee} = \sum_{pairs} \frac{e^2}{r_{ij}} - < \sum_{pairs} \frac{e^2}{r_{ij}} > \tag{1.9}$$

This interaction, together with the spin-orbit interaction, determines the energy of each electronic configuration. Each of these configurations will be labeled with a symbol of the type ${}^{2S+1}L_J$ where S is the spin of the configuration, (2S+1) is called the multiplicity, L is the total angular momentum of the configuration and J is the total momentum $\mid L{+}S \mid$. The result of Coulomb repulsions is to spread the different atomic configurations over several eV, as we can see in the example in Fig. 1.2 where the energy of all the configurations for the transition metal serie is plotted versus the orbital occupancy; their different contributions, weighted with matrix elements, in the optical absorption spectrum give rise to atomic multiplets peaks, as shown in Fig. 1.3. Seeing multiplet effects in the XAS spectrum of a solid is indeed a strong signature of electron-electron correlations. However, one shouldn't forget that this is a very crude approximation that neglects completely the presence of the solid and its crystal structure. The effect of the solid is to hybridize the ligand orbitals, this effect tends to mix in different configurations, as we will discuss in Chapter 5. The effect of the solid can be taken into account in an approximate way considering that the atom is feeling a potential given by a charge distribution that mimics the symmetry of

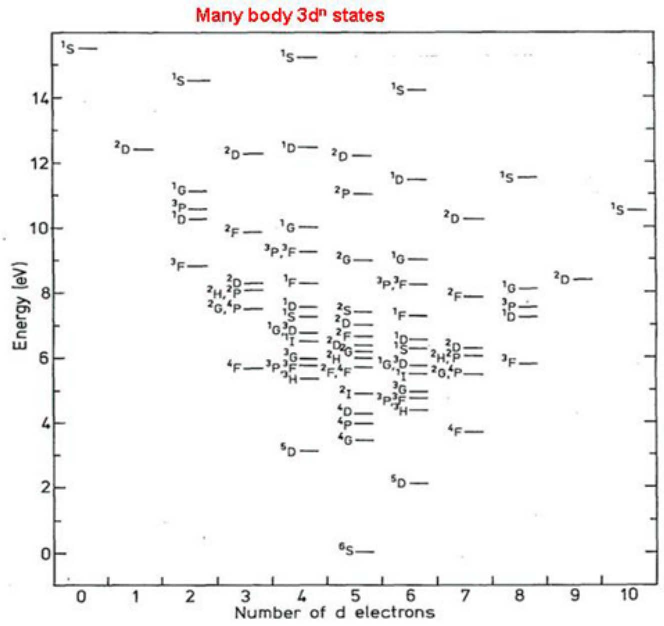

Figure 1.2: Energy distribution of the many body states of 3d orbitals in transition metal as a function of the orbital occupancy. Graph taken from Ref. [1].

the solid. This approach is developed in the so called crystal field theory. In Fig.1.3 I show an XAS spectrum for MnF_2 together with the atomic multiplet calculation where the effect of the crystal field has been taken into account.

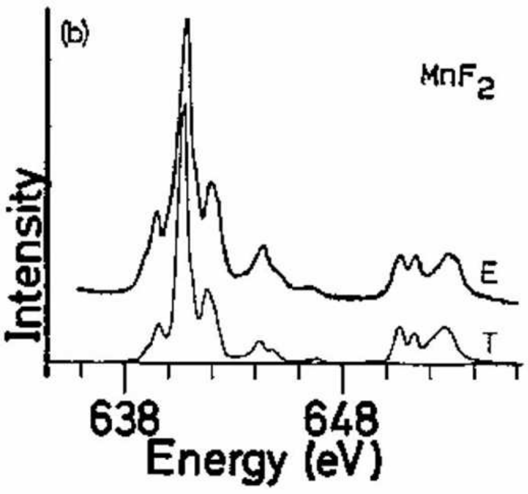

Figure 1.3: XAS of MnF_2 together with the crystal field atomic multiplet calculation. Graph taken from Ref. [4].

1.3.2 Coulomb repulsions in optical spectroscopy, non Drude conductivity and anomalous SW transfer.

In my previous discussion of the Fermi liquid theory I made the statement that in such a context, quasi particles should behave as well defined single particle states with renormalized properties. The optical conductivity of a wide band metal is known to have a Drude behavior, see section 2.2. In section 2.2 I describe the general idea behind the Drude model. For the sake of the current discussion one should keep in mind that this simple model describes the absorption of light by matter assuming that an average relaxation time τ describes the motion of the conduction band electrons which are treated as a free electron gas. This description, very similar to the description of ideal gases, leads to an optical conductivity with the form:

$$\sigma(\omega) = \frac{Ne^2\tau}{m}\frac{1+i\omega\tau}{1+\omega^2\tau^2} \tag{1.10}$$

where τ is the relaxation rate and N the total number of electrons. Clearly in this context of non interacting electrons, the scattering rate is a constant, *i.e.* frequency independent, number. As a consequence of interactions of any kind, electron-electron, electron-phonon, or electron to any other boson (one might think of spin fluctuations for example), one could find at low energy a frequency dependent scattering rate. This possibility is treated in the generalized Drude model [5] and gives an optical conductivity of the form:

$$\sigma(\omega) = \frac{\omega_p^2}{4\pi[1+\frac{\Gamma_2(\omega)}{\omega}]} \cdot \frac{1}{\frac{\Gamma_1(\omega)}{1+\frac{\Gamma_2(\omega)}{\omega}} - i\omega} \tag{1.11}$$

where $\Gamma(\omega) = \Gamma_1(\omega) + i\Gamma_2(\omega)$ is the frequency dependent relaxation rate. One can see that this expression still gives a Drude-like shape of the optical conductivity with renormalized parameters. In this context the scattering rate is no longer a constant and becomes:

$$\Gamma_1(\omega) = \frac{\omega_p^2}{4\pi} \frac{\sigma_1(\omega)}{\mid \sigma(\omega) \mid^2} \tag{1.12}$$

The equation for the optical conductivity at low frequency can be written in the more popular form:

$$\sigma(\omega) = \frac{Ne^2}{m^*} \cdot \frac{\tau*}{1 - i\omega\tau*} \tag{1.13}$$

Where $\frac{1}{\tau^*} = \frac{\Gamma_1(\omega)}{1+\lambda(\omega)}$, with $\lambda = -\Gamma_2/\omega$, has the meaning of the frequency dependent scattering rate and m^* the frequency dependent effective mass. In Fermi liquid theory one can predict the frequency and temperature dependence of the scattering rate, and this formula holds:

$$\frac{1}{\tau^*(\omega, T)} \sim [(2\pi k_B T)^2 + (\hbar\omega)^2] \tag{1.14}$$

As a consequence of this one has for example that, at least at very low energy, where the Fermi liquid theory is expected to hold better, the optical conductivity should have the usual Drude shape expected for metals. Correlation effects can manifest themselves in Fermi liquids by the aforementioned frequency dependent scattering rate[6, 7], or in more exotic behavior in non fermi liquids[8, 9]. The exact nature of the correlation effects leading to such renormalizations is a tough microscopic problem which depends on the knowledge of the spectrum of the bosons on which the electrons scatter, detailed discussions on how to extract this from the optical spectra are currently going on in literature[10].

Strong electron correlations can have another effect on the optical spectra. In section 2.2 I discuss the optical sum rule which relates the integral of the optical conductivity to the total number of carriers. The weight of the optical conductivity in the conduction band can in principle give information about the effective number of carriers and their kinetic energy. It has been shown both theoretically[11, 12, 13, 14] and experimentally[15, 16] that changes of the high frequency optical response can happen because of strong electron-electron repulsion. I will try to give an intuitive idea of why this happens. In the presence of strong electron-electron repulsion the many-body effects could give rise to satellites of the valence band which can be pushed to rather high energies by the Coulomb repulsion. This has been discussed already for photoemission experiments, but it has been shown also theoretically that the optical conductivity of a single band $t-J$ model can show satellite peaks at higher energy. For the sake of clarity, one should know at this point that the $t-J$ model is a simplified version of the Hubbard model, in which Coulomb repulsion is the largest term of the Hamiltonian. In the case of cuprate superconductors these satellites of the optical conductivity have been associated to the spectral weight in the mid-infrared region, which could not be justified by any interband transition. In Fig. 1.4 I show the calculated optical conductivity of a 4×4 cluster within the $t-J$ model. One can see the "Drude" absorption at zero frequency followed by a marked peak and other weaker contributions. These high energy "satellites" have been shown to change upon doping and temperature[12, 13, 14] and give rise to changes in the integral of the conductivity, the spectral weight. The changes in spectral weight at

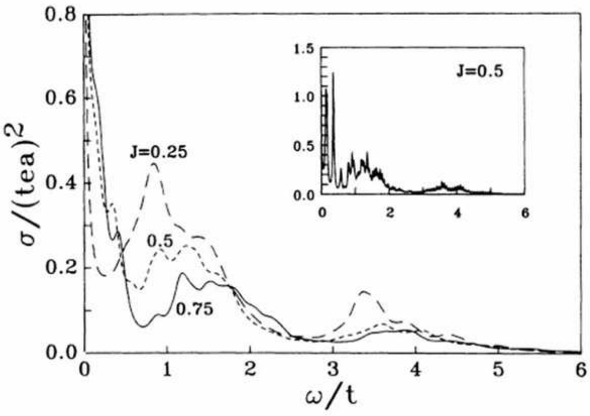

Figure 1.4: The optical conductivity in the $t-J$ model. The calculation was performed on a 4x4 cluster with open boundary condition. The curves are broadened, a high resolution spectrum is shown in the caption. Graph taken from Ref.[12].

high frequency due to strong correlations are a subtle effect, both for theoretical and experimental issues[1]

---

[1] One should keep in mind in the following of this thesis where extensive comparison between the optical SW transfer and $t-J$ model calculations are made, that when referring to the low frequency

---

SW we are using a hard cut-off in the integral which might leave out some of the aforementioned high energy satellites. This would mean that the physical interpretation of the integral becomes somewhat ill defined. What may come to rescue is the fact that at 1 eV one expects that most of the weight of the mid infrared band is already captured; moreover, when the integral is compared to the theoretically obtained integral of the calculated conductivity, the same problem is faced by the calculation and one can hope that theory and experiments are neglecting the same contributions. Indeed when the comparison is based on the definition of kinetic energy this problem might be more severe.

Bibliography

[1] D. van der Marel. "The electronic structure of embedded transition metal atoms". PhD thesis, University of groningen (1985).

[2] A. Fujimori *et al* Phys. Rev. B **35**, 8814 (1987).

[3] B. T. Thole, R.D. Cowan, G.A. Sawatzky, J. Fink, and J.C. Fuggle, Phys. Rev. B **31**, 10 (1985).

[4] F.M.F. de Groot. Chem. Review 101, 1779 (2001).

[5] M. Dressel and G. Grüner. "Electrodynamics of solids" Cambridge University Press, Cambridge (2002).

[6] N. Grewe and F. Steglich. "Heavy Fermions, in: Handbook of physics and chemistry of rare earths" 14, edited by K.A. Gschneider and L. Eyring.

[7] H.R. Ott and Z. Fisk. "in Handbook of physics and chemistry of actinides" 5, edited by A.J. Freeman and G.H. Lander (North-Holland, Amsterdam, 1987), p. 85.

[8] J. Wang, T. Timusk, G.D Dung. Nature **427** 714 (2004)

[9] F.P. Mena,D. van der Marel, A. Damascelli, M. Faeth, A.A. Menovsky, J.A. Mydosh, Phys. Rev. B **67**, 241101 (2003)

[10] L. Benfatto, J.P. Carbotte and F. Marsiglio. Phys. Rev. B **74**, 155115 (2006).

[11] P.F. Maldague, Phys. Rev. B **16**, 2437 (1977).

[12] W. Stephan and P. Horsch. Phys. Rev. B **42** 8736 (1990).

[13] I. Sega and P. Prelovsek. Phys. Rev. B **42** 892 (1990).

[14] A. Moreo and E. Dagotto. Phys. Rev. B **42** 4786 (1990).

[15] H. J. A. Molegraaf, C. Presura, D. van der Marel, P. H. Kes, and M. Li, Science **295**, 2239 (2002).

[16] A.Toschi, M. Capone, M. Ortolani, P. Calvani, S. Lupi, C. Castellani. Phys. Rev. Lett. **95** 097002 (2005)

[17] S. Uchida *et al*, Phys. Rev. B**43**, 7942 (1991).

[18] N.W. Ashcroft and N.D. Mermin, In: *Solid State Physics* (Saunders College Publishing, New York 1976).

Chapter 2

A brief introduction to optical spectroscopy

2.1 The microscopic description of the absorption of light from matter

A thorough description of the interaction between radiation and matter is carried out in several books [1] and is beyond the scope of this work. The purpose of this introduction is therefore to give an intuitive description of optical spectroscopy. The motion of charged particles (electrons) in a solid can be described by the following Hamiltonian:

$$H = \frac{1}{2m}\sum_{i=1}^{N}(p_i + \frac{e}{c}A(r_i))^2 + \sum_{i=1,j=1}^{N,M} V_j^0(r_i - R_j) + \frac{1}{2}\sum_{i=1,i'=1}^{N,M,i\neq i'}\frac{e^2}{|r_i - r_{i'}|} - \sum_{i=1}^{N} e\Phi(r_i) \quad (2.1)$$

The Hamiltonian describes the energy of the particles in a certain position and time, and contains: (i) the kinetic energy of the particles (1st term), due to their proper motion (p) plus the motion caused by the field (A(r)), where r is the position; (ii) the interaction of the electrons with the ions lattice. $V_j^0(r_i - R_j)$ is a periodic function that represents the Coulomb potential due to the positive charge of the nuclei; (iii) the Coulomb repulsion of the electrons between each other (3rd term); (iiii) a scalar potential as produced by an external charge (last term). In this description we neglect the spin orbit coupling, and electron-phonon coupling. The microscopic version of Ohm's law says that:

$$J(\omega) = \sigma(\omega)E(\omega) \quad (2.2)$$

where J is the current density, σ is the conductivity, and E is the electric field (which integrated along a path gives a potential V). The frequency dependence in Eq. 2.2 takes into account the possibility that the field applied to the material is time varying. Once we know the current induced in the solid (measurable) by the external applied field (known) we can extract the conductivity with all its useful microscopic information, because the conductivity reflects the electrical properties of the system. In order to do that, we need to express the density of current J in terms of a microscopic model. In general, the current density can be written as:

$$J = n \cdot q \cdot v \tag{2.3}$$

where n is the number of electrons, q is their charge and v their velocity. The velocity of the particles is something that one can extract from the Hamiltonian, equation 2.1, thus one can relate the microscopic model with the quantity J. The quantum mechanical operator for the current density is:

$$J(r) = -\frac{e}{2}\sum_{i=1}^{N}[v_i\delta(r-r_i) + \delta(r-r_i)v_i] \tag{2.4}$$

where v_i is the velocity of the particles at the position r_i. A charged particle in a field has a speed $v = p/m + eA/mc$, therefor

$$J(r) = -\frac{e}{2m}\sum_{i=1}^{N}[p_i\delta(r-r_i) + \delta(r-r_i)p_i] - \frac{e^2}{mc}\sum_{i=1}^{N}A(r_i)\delta(r-r_i) \tag{2.5}$$

With some fantasy, one can call the first term of this expression the paramagnetic current operator and the second the diamagnetic current operator. The hamiltonian in eq. 2.1, can be written as a sum of two terms, $H = H_0 + H_{int}$, where H_0 is the unperturbed term in the presence of light and H_{int} is the term containing the interaction between light and matter. This interaction term can be written as:

$$H_{int} = \frac{e}{2mc}\sum_{i=1}^{N}[p_i \cdot A(r_i) + A(r_i) \cdot p_i] - e\sum_{i=1}^{N}\Phi(r_i) \tag{2.6}$$

Using eq. 2.5 one can write the interaction term in terms of the current density

$$H_{int} = -\frac{1}{c}\int J(r) \cdot A(r)dr \tag{2.7}$$

Bearing in mind that we want to derive an expression for the optical conductivity, namely the absorption rate of light in matter, we assume that this absorption takes place exciting a transition from a certain initial state $\mid s>$ to a final state $\mid s\prime>$. In a system, the number of transitions per unit time and per unit volume is given by Fermi golden rule:

$$W_{s\mapsto s\prime} = \frac{2\pi}{\hbar^2}\mid< s\prime \mid H_{int} \mid s>\mid^2 \delta[\omega - (\omega_{s\prime} - \omega_s)] \tag{2.8}$$

One can find the matrix elements for this transition using eq. 2.7 and after some further manipulations one can obtain the final expression for the optical conductivity (the so called Kubo formula):

$$\sigma_{\alpha\beta}(q,\omega) = \frac{1}{\omega\nu}\int_{-\infty}^{t} dt\prime e^{-i\omega t - t\prime} < \psi \mid [J_{\alpha}^{+}(q,t), J_{\beta}(q,t\prime) \mid \psi > + \frac{n_0 e^2}{m\omega} i\delta_{\alpha\beta} \quad (2.9)$$

This expression relates the absorption of light due to all the electronic transitions from occupied initial states to unoccupied final states to the current-current correlation function and it is a very general expression often used in condensed matter physics.

2.2 The Drude model and the f-sum rule

The optical spectroscopy of materials started obviously much earlier than the concepts used to derive the Kubo formula were available. Different materials show different colors to the naked eye, some materials even change colors after long exposure to air or water. Already from the first classifications of such color changes done by middle-age alchemists using the not very microscopic idea of putrefaction it is clear that it is possible to say something about the state of matter from its response to light. Once the idea of charged particles circulating in solids was spread, mankind made the first attempt to describe microscopically the interaction of light with matter. In this chapter we will try to connect the first and simplest microscopic model for the optical response of metals (the Drude model) to the sophisticated Kubo formula described above. From this comparison I will extract a very powerful property of the optical conductivity, which is the f-sum rule. What the f-sum rule says is: the number of particles reacting to the light has to be conserved. The Drude model is based on the assumption that a metal is representable as a gas of electrons moving and carrying current and heat. Like in an ideal gas, the relaxation of the system to equilibrium can be described by an average relaxation time τ. This means that the changes in momentum of the electrons are related to the relaxation of the momentum itself and the acceleration of the charges induced by an external field. In an equation:

$$\frac{dp}{dt} = -\frac{p}{\tau} - eE \quad (2.10)$$

The current density is $J = -N \cdot e \cdot v$ and the conductivity $\sigma_1 = J/E$, thus if the electric field is time-dependent, $E(t) = E_0 e^{-i\omega t}$ the solution of the differential equation of motion gives for the frequency dependent conductivity the expression:

$$\sigma(\omega) = \frac{Ne^2\tau}{m}\frac{1+i\omega\tau}{1+\omega^2\tau^2} \quad (2.11)$$

This description is very crude and neglects several concepts developed in the framework of quantum mechanics, although it can be a reasonable picture in several circumstances where the many assumptions made are more or less valid. It is remarkable anyway that such a simple model has a great success in describing the low frequency experimental response of most simple metals. If one integrates over frequency the real part of the equation 2.11

$$\int_0^\infty \sigma_1(\omega\prime)d\omega\prime = \frac{Ne^2}{m}\int_0^\infty \frac{\tau}{1+\omega\prime^2\tau^2}d\omega\prime = \omega_p^2/8 \tag{2.12}$$

where $\omega_p = (\frac{4\pi Ne^2}{m})^{1/2}$ is the plasma frequency. In this context, this expression is derived for a free electron gas. Now I want to derive the very same Drude expression starting from the Kubo formula, this allows one to understand, given the modern knowledge of the microscopic theory, where the assumptions are that lead to such a result. The starting point is equation 2.9; we assume that the current-current correlation function decays following this expression:

$$J(q,t) = J(q,0)e^{-t/\tau} \tag{2.13}$$

This is equivalent to assume that all the final states will relax to the ground state in the same time τ. If we insert this in equation 2.9 we obtain

$$\sigma(q,\omega) = \frac{1}{\hbar\omega}\sum_s \int dt[e^{-i\omega t-|t|/\tau} < s \mid J^2(q) \mid s >] \tag{2.14}$$

If we introduce a full set of states with the property

$$\sum_{s\prime} \mid s\prime >< s\prime \mid = 1 \tag{2.15}$$

we have

$$< s \mid J^2 \mid s > = \sum_{s\prime} |< s \mid J \mid s\prime >|^2 \tag{2.16}$$

If one considers the equation 2.4 for the density of current and calculate its Fourier transform, since we want to obtain an expression in the frequency space, one obtains:

$$J = \int J(r)e^{-iq\cdot r}dr = -e/m\sum_j p_j \tag{2.17}$$

This is true in the dipole approximation, which means that we consider q small as such that $e^{iqr} \approx 1$. The expression for the optical conductivity becomes:

$$\sigma(\omega) = \frac{e^2}{\hbar\omega m^2}\int dte^{-i\omega t-|t|/\tau}\sum_{s,s\prime,j} |< s\prime \mid p_j \mid s >|^2 \tag{2.18}$$

In this formula the quantity $|< s\prime \mid p_j \mid s >|^2$ can be thought of as the probability of the transition from the state s to the state $s\prime$. If we define the oscillator strength as: $2\sum_{s,s\prime,j} \frac{|<s\prime|p_j|s>|^2}{m\hbar\omega_{s,s\prime}} = f_{s,s\prime}$ after integrating equation 2.18 we obtain:

$$\sigma(\omega) = \frac{e^2\tau}{m}\frac{f_{s,s\prime}}{1+i\omega\tau} \tag{2.19}$$

Given the definition of the oscillator strength, it is easy to show that for free electrons $f_{s,s\prime} = N$ where N is the density of electrons. One can see that under certain approximations it is possible to calculate the Drude formula for the conductivity of a metal. Let's briefly discuss which are these approximations. At the very beginning we postulated that the relaxation time of all the final states is the same. It is remarkable that this approximation, that looks very crude at first glance, is actually very robust and holds for the coherent response of all Fermi Liquid materials. This shows that the idea that the electrons in the conduction band of a metal are like a gas of free charged particles for which an average description of their motion is sufficient is not so far from reality. The other important approximation we made is the dipole approximation. Assuming q very small, the so called local limit, one neglects all the possible processes that happen exchanging a momentum, such as electron-lattice and electron-electron interaction. In many cases this leads to a frequency dependent τ, as discussed in more detail in the generalized Drude model [1].

2.3 The experimental path to the determination of the optical spectral weight

So far we discussed the theory that relates the optical conductivity to the microscopic properties of matter. We have shown that the absorption of light by a solid can tell us something about its microscopic properties. In practical terms the absorption of light is a very straightforward concept. In fact, it is related to the ratio between the light that can pass through a material and the light that impinges on the material. This means that a transmission experiment is ideal if one wants to measure the optical conductivity. Sometimes, such an experiment is not possible, or very difficult (for example in metallic systems where the transmission in the infrared is almost zero) and other ways have to be used. In this paragraph we give a brief description of two very popular approaches, spectroscopic reflectivity and ellipsometry, and we discuss the possibility of using a combination of these two methods.

2.3.1 Reflectivity and Kramers-Kronig transformation

A standard technique used to extract the optical conductivity, $\sigma_1(\omega)$ is to measure the normal incidence reflectivity over a broad range of frequencies. Since reflectivity is a combination of the real and imaginary part of the dielectric function

$$r(\omega) = \left(\frac{1 - \sqrt{\epsilon_1(\omega) + i\epsilon_2(\omega)}}{1 + \sqrt{\epsilon_1(\omega) + i\epsilon_2(\omega)}} \right)^2 \tag{2.20}$$

in principle it contains information about both. However, as one can see, one has one equation and two unknowns. One can obtain the second equation imposing the causality condition to the reflectivity signal. Causality implies that the real and imaginary parts of a given response function are Kramers-Kronig related. One can write the complex reflectivity as

$$\begin{aligned} r &=\mid r \mid e^{i\phi} \\ ln(r) &= ln \mid r \mid + i\phi \end{aligned} \tag{2.21}$$

The Kramers-Kronig relation between the modulus and the phase is

$$\begin{aligned} ln \mid r(\omega) \mid &= 1/\pi \wp \int_{-\infty}^{\infty} \frac{\phi(\omega\prime)}{\omega\prime - \omega} d\omega\prime \\ \phi(\omega) &= -1/\pi \wp \int_{-\infty}^{\infty} \frac{ln \mid r(\omega\prime) \mid}{\omega\prime - \omega} d\omega\prime \end{aligned} \tag{2.22}$$

Having the quantity $r(\omega)$ allows to calculate the phase $\phi(\omega)$, the complex reflectivity is then related to the complex dielectric function, Eq. 2.20. It is important to notice that this approach implies the knowledge of the normal incidence reflectivity in the entire energy spectrum, as is clear from the integral in Eq. 2.22. Since this is not experimentally possible, in practice one measures reflectivity over the broadest possible range and than uses suitable extrapolations to get the complete $r(\omega)$ function to use in the Kramers Kronig integral. It is intuitive that a source of error in the extracted quantities is the extrapolation procedure. Several methods have been proposed in order to improve the accuracy of this method, an exhaustive discussion of these approaches is going to be to cumbersome for this thesis, so for whom is interested in knowing more about this procedure I recommend the references [1, 2].

2.3.2 Ellipsometry

One can avoid the aforementioned problem of the extrapolations measuring the complex dielectric function with spectroscopic ellipsometry. The light reflected from a sample is composed of a part polarized parallel to the plane of the sample ($r_{\|}$, s wave) and a part polarized perpendicular to this plane ($r_{\perp}$, p wave). Ellipsometry measures the complex ratio between the reflection coefficients of these two components:

$$\rho = \frac{r_{\|}}{r_{\perp}} = tan(\Psi)e^{i\Delta} \tag{2.23}$$

Where Ψ is related to the amplitude ratio, and Δ to the phase difference of the s and p waves. Knowing the angle of incidence (θ) of the beam one can calculate the complex dielectric constant from the measured quantities Ψ and Δ:

$$\begin{aligned} \epsilon_1 &= sin^2(\theta)[1 + \frac{tan^2(\theta)(cos^2(2\Psi) - sin^2(\Delta)sin^2(2\Psi)))}{(1 + sin(2\Psi)cos(\Delta))^2}] \\ \epsilon_2 &= sin^2(\theta)\frac{tan^2(\theta)sin(4\Psi)sin(\Delta)}{(1 + sin(2\Psi)cos(\Delta))^2} \end{aligned} \tag{2.24}$$

This approach has several advantages over the measurement of reflectivity: (i) it doesn't require extrapolations and Kramers Kronig analysis to get the complex optical constants, (ii) since the intensity of the light does not enter the analysis, a calibration for the absolute value of the reflected beam is not needed, (iii) in the ultraviolet region this technique is less sensitive to the surface roughness than normal incidence reflectivity. The main drawback is that ellipsometry is experimentally more demanding than reflectivity, especially in the infrared region where high quality polarizers operating in a broad region of frequency are not available. The principle of ellipsometry is very simple. On the other hand there are many complications whose discussion is beyond the scope of this thesis. Details can be found in the literature[3, 4, 5]. The important message that this brief introduction wants to stress is that ellipsometry provides an independent determination of the real and imaginary part of the optical constants, in contrast to reflectivity where a further condition has to be imposed in order to separate them.

2.3.3 Drude-Lorentz analysis of reflectivity and ellipsometry

The two approaches discussed before have both positive and negative aspects. More importantly, one should realize that depending on the spectral region, one approach could present important advantages over the other. For example, while ellipsometry is a very well established technique in the visible region of the spectrum, and is still under development in the infrared region, infrared reflectivity has been used already for several decades to investigate the electronic properties of solids. For this reason it is particulary appealing to combine the two techniques in order to cover the whole spectrum and get a better determination of the complex dielectric function. A possible approach that allows to combine these two techniques, reflectivity and ellipsometry, is to fit simultaneously all the data with a model from which, knowing the model parameters, it is possible to calculate all the optical constants. A simple phenomenological description of the optical spectra is given by the Drude-Lorentz model. The dielectric function of this model is given by the formula:

$$\epsilon(\omega) = \epsilon_{\infty} + \sum_i \frac{\omega_{pi}^2}{\omega_{0i}^2 - \omega^2 - i\gamma_i\omega} \tag{2.25}$$

Basically this model describes the optical transitions as lorentzian oscillators with a strength, ω_p, and width, γ. In a metal an oscillator centered at zero frequency mimics the response of the free charges and is referred to as the Drude oscillator. It has been shown that simultaneously fitting the infrared reflectivity and the visible light ellipsometry gives a better determination of the complex dielectric function then the usual reflectivity and KK approach, because of the additional information given by the ellipsometric data [6]. In order to preserve all the spectral information that one measures, one has to use a very large number of oscillators. This approach has been developed in our group and we have shown that it can improve significantly the standard Kramers-Kronig analysis. In order to obtain the optical constants in the whole frequency range, we use a variational procedure described in Ref. [2]. In the first stage, the infrared reflectivity and the ellipsometrically measured complex dielectric function in the visible and UV-range are fitted simultaneously with a Drude-Lorentz model. In the second stage, the fit is refined with a variational dielectric function added on top of the Drude-Lorentz model. The former is essentially a set of a large number of narrow oscillators, each corresponding to one or two spectral datapoints. This yields the Kramers-Kronig consistent dielectric function which reproduces all the fine details of the infrared reflectivity spectra while simultaneously fitting to the measured complex dielectric function at high frequencies. In contrast to the "conventional" KK reflectivity transformation this procedure anchors the phase of the complex reflectivity to the one at high energies measured directly with ellipsometry[6].

2.4 The calculation of the Spectral Weight integral

2.4.1 Why do we bother?

We now focus on a property of the optical conductivity: the f-sum rule. As I discussed in section 1.2, a sum rule can be derived for the optical conductivity:

$$N_{eff}(\omega) = \frac{emV}{\pi e^2} \int_0^{\infty} \sigma(\omega\prime) d\omega\prime \tag{2.26}$$

This equation emphasizes the fact that it is possible to calculate the number of carriers integrating the optical conductivity. Thus, it is intuitive that evaluating the integral of the optical conductivity up to a certain energy, Ω_{cutoff}, it is possible to calculate how many charge carriers are absorbing the electromagnetic radiation in the energy range between zero and the aforementioned energy cut-off. Furthermore, plotting the integral as a function of the frequency cutoff in a material in principle could display its electronic structure. In order to clarify this very important point we show the example of the spectral weight of pure aluminium in Fig. 2.1. The effective

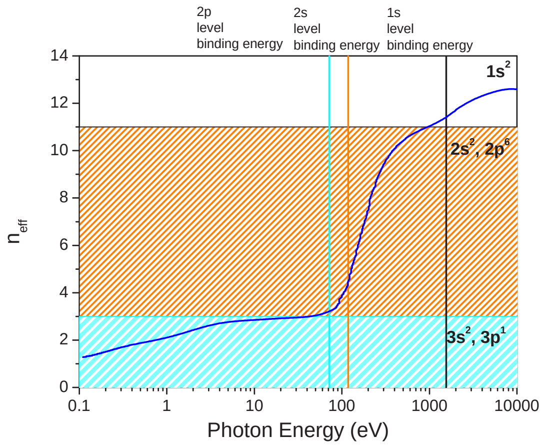

Figure 2.1: The sum rule as a function of the energy cutoff for the ab-initio calculated optical conductivity of aluminum. The data are taken from the literature[7]

number of carriers as a function of energy shows three marked slope changes which, as indicated by the vertical lines, correspond to the electronic levels of aluminium. The low energy plateau represents the conduction band of aluminium, which has a valency of 3 given by the electrons in the 3rd energy level; higher in energy one can see the second level, the effective index rises from 3 to 11 meaning that the 8 electrons of the second level (2 on the s orbital and 6 on the p one) have been added to the 3 third level electrons. Eventually when the electromagnetic wave has sufficient energy to excite the electrons of the 1st level the effective index reaches 13, the total number of electrons in aluminium. The total number of electrons of course is a conserved quantity, meaning that at sufficiently high energy the effective index should be temperature independent. On the other hand, redistributions of spectral weight can occur at lower energies, due to changes of the occupation numbers or of the effective masses as a function of temperature; in this case the partial sum rule, the integral up to a low energy cutoff, can be temperature dependent. For common metals this happens only at very low energy, below 1 eV, while it often happens that in strongly correlated electron systems a violation of the partial sum rule is observable at energies even higher than 2 or 3 eV [8]. This simple example provides an intuitive picture of the f-sum rule which will be largely used in this thesis. One should notice that since the integral in Eq. 2.26 starts from zero energy, a part of experimental information will always be missing since one cannot measure down to zero frequency for practical reasons. In simple cases, such as aluminium, this is not a problem since the spectrum from the optical frequencies extrapolates to the dc conductivity in a Drude-like fashion; in more complicated materials, such as superconductors, where a gap opens and at low temperature a condensate peak is sitting at zero energy a trivial extrapolation of the optical data is less obvious. We derived a number of different approaches in order to evaluate this integral with high precision, in the following section I will describe the main concept which is behind all of these approaches.

2.4.2 Integrating the unknown with precision

The usual equation for the optical spectral weight includes the integral of the optical conductivity from zero up to a certain frequency cutoff. If we take advantage of the Kramers Kronig relations (KK) we can write the following equations for the complex conductivity:

$$\sigma_1(\omega) = \wp \int_0^\infty K(\omega\prime, \omega)\sigma_2(\omega\prime)d\omega\prime \tag{2.27}$$

$$\sigma_2(\omega) = \wp \int_0^\infty K(\omega\prime, \omega)\sigma_1(\omega\prime)d\omega\prime \tag{2.28}$$

$K(\omega, \omega\prime)$ is the kernel $(2\omega/\pi)(\omega^2 - \omega\prime^2)^{-1}$. Given the usual formula for the spectral weight (SW):

$$W(\omega) = \int_0^\infty \sigma_1(\omega\prime)d\omega\prime \tag{2.29}$$

One can express σ_1 in terms of its Kramers Kronig transform and then apply iteratively the truncated Hilbert transform. If we split the integral from zero to infinity into a contribution that we will call internal ($\int_{Int} = \int_{\omega_{min}}^{\omega_{max}}$) and another one called external ($\int_{ext} = \int_0^{\omega_{min}} + \int_{\omega_{max}}^\infty$), KK transform σ_2 in the external integral, split the integration range again and iterate this procedure n times, we can write the SW as a combination of σ_1 and σ_2 in a limited energy range.

$$\begin{aligned}
\int_0^\infty \sigma_1 &= lim_{n\to\infty}\int_{\omega_c}^\infty [\sigma_1 u_1^{(n)} + \sigma_2 u_2^{(n)}]d\omega && (2.30)\\
u_1^{(n)} &= Q_{2n}[1/\pi ln(\frac{\omega+\omega_c}{\omega-\omega_c})] && (2.31)\\
u_2^{(n)} &= Q_{2n+1}[1/\pi ln(\frac{\omega+\omega_c}{\omega-\omega_c})] && (2.32)\\
Q_0 &= 1 && (2.33)\\
Q_1 &= x && (2.34)\\
Q_2 &= -1/2x^2 && (2.35)\\
&.....
\end{aligned}$$

The above solution is analytic and applies only under the assumption that σ_1 and σ_2 are known with infinite precision in the given interval and that the upper limit of this interval tends to infinity. It is possible to extend this treatment to the realistic case where the data have a finite resolution, a certain noise is present and the upper limit of the interval is not infinity. In this case the derivation becomes rather cumbersome, the details of this procedure are described in Ref. [9]. More importantly we can demonstrate that thanks to this approach we can build a routine which is capable of calculating the SW given σ_1 and σ_2 in a limited frequency range in experimental conditions. We show a demonstration of this routine, called Devin, in Fig. 2.2,2.3,2.4. We generate several random sets of Durde-Lorentz models, where the strength, the position and the width of the oscillators is arbitrary, then we calculate ϵ_1 and ϵ_2 for these models and we provide these two quantities to Devin. In the first test we vary the noise level that we superimpose on the data. In Fig. 2.2 one can see one of the many Drude-Lorentz models (lower panels) with two different noise levels. The upper panel of the figure shows the correspondence between the true SW of the models (which we know) and the SW calculated by Devin. It is important to notice that each of the symbols in the upper graphs correspond to a different Drude-Lorentz model, while for obvious reasons in the lower graphs we display only one of these models as an example. It is evident and expected that adding more noise to the data gives larger errors in the determination of the SW, on the other hand the correspondence between the calculated SW and the real one is very good even for rather noisy data, showing that the algorithm works very well. The next test is to vary the width of the interval in which the data are provided to Devin, in Fig. 2.3 one can see that the SW is better determined when a larger interval of data is provided. Finally, we see what the effect of the frequency cutoff is. From Fig. 2.4 one can see that when the cutoff is set inside the interval of the given data the SW is very well determined, while when the cutoff is outside the error bars explode.

In this paragraph we have shown that for very fundamental reasons related to the

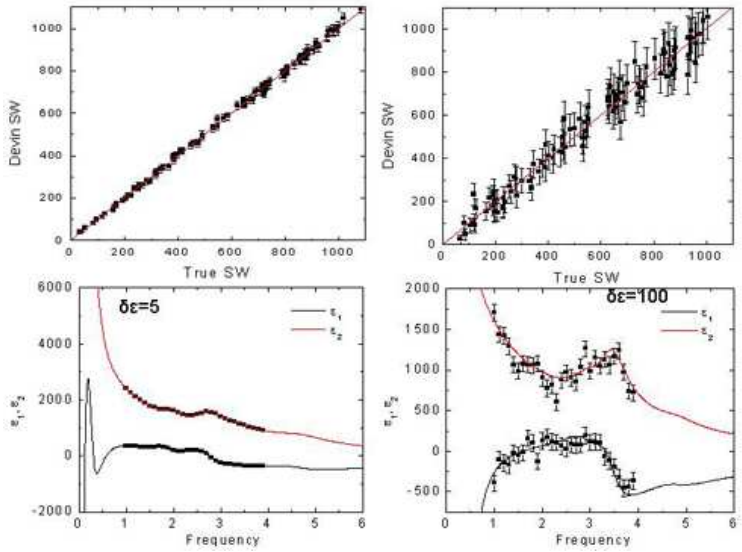

Figure 2.2: The integrated SW for a frequency cut off of Ω= 2 for different Drude-Lorentz models with different noise level.

KK properties of the optical constants, it is not necessary to know the optical conductivity down to zero frequency in order to determine the partial sum rule integral. This is due to the fact that knowing also the imaginary part of the optical conductivity, provides a further constraint to the value of the SW through the KK relation. In principle one can use this approach to determine the SW value, given the possibility of having the complex dielectric function measured. On the other hand, this result shows equally that also the knowledge of the reflectivity can anchor the value of the SW because reflectivity is a function of both the real and imaginary part of the optical conductivity. We will discuss this point later in a practical case, showing that the SW of a Drude-Lorentz model with a large number of oscillators, therefore a function with a lot of spectral degrees of freedom, can be sufficiently constrained by an experimental data set composed of infrared reflectivity and visible light ellipsometry.

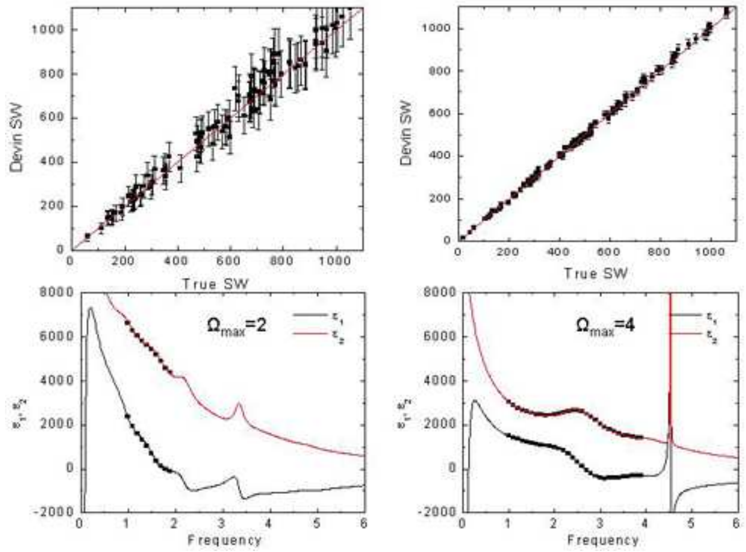

Figure 2.3: The Integrated SW for a frequency cut off of 1.5 for different Drude-Lorentz models for two different width of the "measured" interval

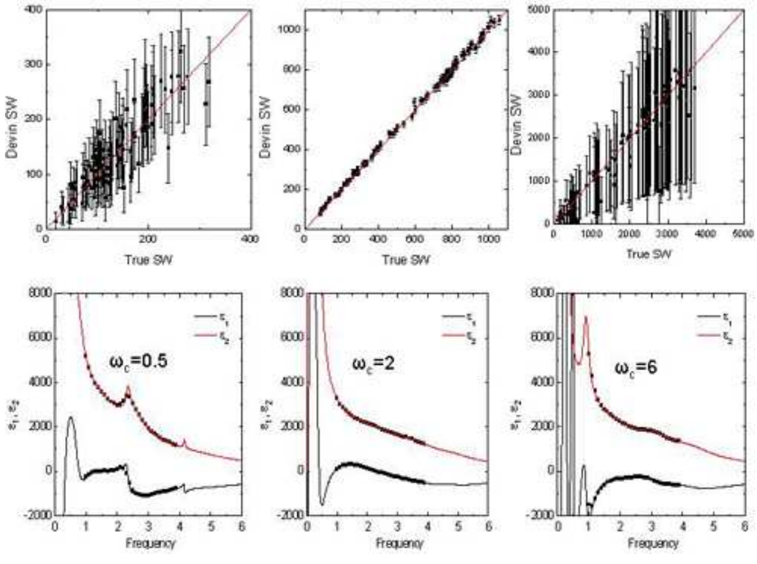

Figure 2.4: The integrated SW for different Drude-Lorentz models and different frequency cut offs

Bibliography

[1] M. Dressel and G. Grüner. "Electrodynamics of solids" Cambridge University Press, Cambridge (2002).

[2] A.B. Kuzmenko, Rev. Sci. Instrum. **76**, 083108 (2005).

[3] R.M.A. Azzam and N.M. Bashara. "Ellipsometry and Polarized Light" (North Holland, Amsterdam, 1987).

[4] A. Röseler, "Infrared and Spectroscopic Ellipsometry" (Akademie-Verlag, Berlin, 1990).

[5] H.G. Tompkins. "A User's Guide to Ellipsometry" (Academic press, Boston, MA, 1993).

[6] I. Bozovic, Phys. Rev. B **42**, 1969 (1990).

[7] E. Shiles *et al*, Phys. Rev. B **22**, 1612 (1980).

[8] P.F. Maldague, Phys. Rev. B **16**, 2437 (1977).

[9] A.B. Kuzmenko, D. van der Marel, F. Carbone and F. Marsiglio. In preparation.

Chapter 3

The spectral weight transfer in cuprate superconductors

"It is necessary to deprive matter of its qualities in order to draw out its soul.....Copper is like a man; it has a soul and a body....the soul is the most subtle part...that is to say, the tinctorial spirit. The body is the ponderable, material, terrestrial thing, endowed with a shadow....After a series of subtle treatments copper becomes without shadow and better than gold...The elements grow and are transmuted, because it is their qualities, not their substances which are contrary." (Stephanus of Alexandria, 620 A.D.). Anyone measuring the infrared reflectivity of cuprates knows that in the superconducting state they can reflect more than gold......

3.1 Overview on the properties of cuprate superconductors

3.1.1 crystal structure

The cuprate superconductors belong to a class of materials which has the perovskite-like crystal structure, shown in Fig. 3.1. Among them the bismuth based family, $Bi_2Sr_2CuO_6$, $Bi_2Sr_2CaCu_2O_8$, $Bi_2Sr_2Ca_2Cu_3O_{10}$, is one of the most studied because large single crystals of good quality are available and because these crystals cleave along the Bi-O planes giving a fairly flat surface. In this thesis I will show experimental results obtained on $Bi_2Sr_2CaCu_2O_8$, and $Bi_2Sr_2Ca_2Cu_3O_{10}$. Since most of the crystallographic features are common to all cuprate superconductors I comment for simplicity on the case of $Bi_2Sr_2Ca_2Cu_3O_{10}$. copper oxide based superconductors can be thought of as a layered structure: in the stoichiometric compound, the Cu-O planes show antiferromagnetism and the material is a charge transfer insulator. In the case of Bi-based cuprates, oxygen can occupy some vacancies in the

Bi-O plane and oxygen in excess can be introduced in the crystal. The Bi-O planes function as charge reservoirs and can induce charge in the CuO_2 planes, doping the system, which thereafter shows a metallic behavior. As a consequence of this, distortions can take place in the structure giving a modulation of the crystal structure. This modulation has been shown to have an impact on the capability of doping the system[1]. From this point on I will refer to the ab plane as the plane defined by the Cu-O checkerboard and to the c-axis as the direction perpendicular to this plane.

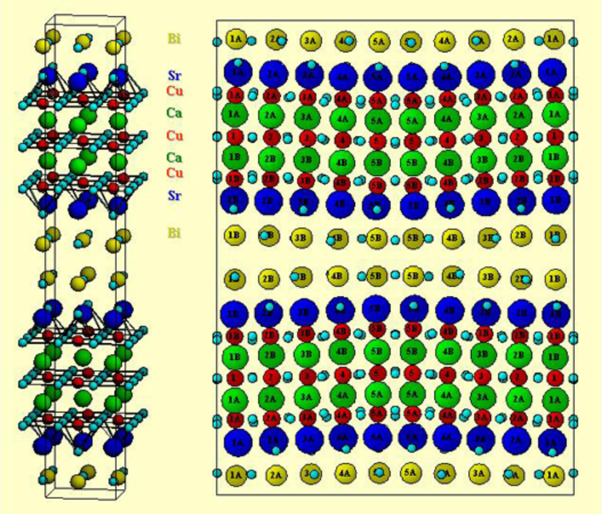

Figure 3.1: $Bi_2Sr_2Ca_2Cu_3O_{10}$ unit cell and the modulated crystal structure.

3.1.2 Cuprates electronic structure

In introducing the electronic structure of cuprate superconductors we will use the unpopular concept that "everything happens in the Cu-O planes". There are several arguments against such a statement, most of them make perfect sense. The fact that depending on the composition, the superconducting transition temperature can vary even by a factor of 10 is the strongest argument in my view. Some effects have also been seen upon oxygen isotope substitution. The reason to use such a simplification is that from the general point of view, the main properties of these materials are undoubtedly given by the Cu-O planes; these planes in fact are the only common building block of all high temperature superconductors. In the undoped (parent) compound, all the atomic shells are filled but the Cu^{++} $3d$ one. As a result of the crystal field, which lifts the degeneracy of the 3d bands, the system ends up with one single hole in the $d_{x^2-y^2}$ orbital, which gives a half filled band. In Fig. 3.2 we show the Cu-O planes with the $d_{x^2-y^2}$ copper orbital together with the oxygen $2p_{x,y}$ ones. In a system where electron-electron correlations are negligible, the Cu $d_{x^2-y^2}$ orbital and the O $2p_{x,y}$ ones form bonding, non-bonding and anti-bonding bands,

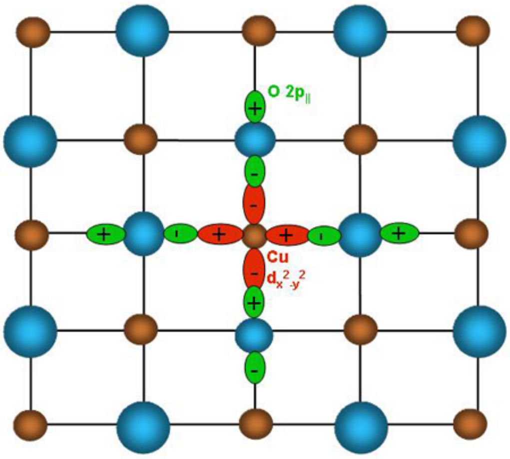

Figure 3.2: The important orbitals in the copper-oxygen plane.

as displayed in the top left graph of Fig. 3.3; the anti-bonding band is half filled and band theory would predict a non magnetic metallic ground state, while a gap of 1.5 eV is observed experimentally and the system is an insulator [2]. Such a failure of band theory is due to the Coulomb repulsion, which causes the electrons to localize on the ions and form an antiferromagnetic lattice, in order to minimize the spatial overlap of their wavefunctions. In the top right graph of Fig. 3.3 one can see that when the Coulomb repulsion U exceeds the width of the conduction band the last splits into a lower Hubbard band (LHB) completely occupied and an upper Hubbard band (UHB) completely empty and the system is a Mott-Hubbard insulator. In a more extreme situation, when the Coulomb repulsion is larger than the copper oxygen charge transfer energy, the system turns into a charge transfer insulator, as visible in the bottom left scheme of Fig. 3.3. The hybridization between the UHB and the bonding band splits the latter into singlet and triplet states, where the singlet state is called Zhang-Rice singlet[3]. More discussions on the nature of this singlet states are in Ref. [4].

It has been proposed [6] that the single band Hubbard Hamiltonian describes the physics of the cuprates:

$$H = -t \sum_{<i,j>,\sigma} (c^{\dagger}_{i,\sigma} c_{j,\sigma} + H.c.) + U \sum_{i} n_{i,\downarrow} n_{i,\uparrow} \tag{3.1}$$

Where the sum in the first term is carried out on the nearest neighbors only. This Hamiltonian can be simplified if one assumes that $U >> t$. The model then reduces to the $t - J$ model. In the $t - J$ model the double occupancy of a site is projected

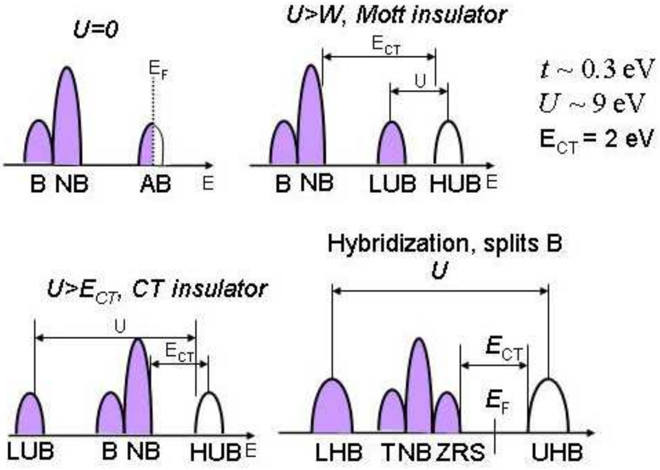

Figure 3.3: Zaanen-Sawatzky-Allen scheme taken from Ref. [5].

out and the Hamiltonian reads:

$$H = -t\sum_{i,j,\sigma}(b^{\dagger}_{i,\sigma}b_{j,\sigma} + H.c) + J\sum_{i,j} S_iS_j \quad (3.2)$$

$$b_{i,\sigma} = c_{i,\sigma}(1 - n_{i,-\sigma}) \quad (3.3)$$

$$n_{i,\sigma} = c^{\dagger}_{i,\sigma}c_{i,\sigma} \quad (3.4)$$

This model is considered to represent the low energy excitations of the cuprates, and we will show a comparison between the experiments and the theoretical predictions based on this model for the low frequency optical spectral weight transfer. One of the key differences between low T_c superconductors and high T_c cuprates is the fact that in the latter the Cooper pair coherence length is much smaller than in BCS theory, of the order of the lattice spacing. In this context several theories have predicted that superconductivity takes place with a lowering of the electronic kinetic energy, opposite to what happens in a conventional BCS superconductor. This can be measured with optics and will be the subject of this chapter. Before going into the details of this problem though, we want to make an experimental connection to the theoretical aspects we discussed concerning the electronic structure of the cuprates. The parent compounds are experimentally found in optical experiments to be insulators with a gap of 1.5 eV[2]. Doping the system results in a metal, in fact a Drude peak grows in the optical conductivity spectrum; moreover one can verify that the effective number of carriers in the conduction band corresponds to the doping. In Fig. 3.4 one can see the optical conductivity for an optimally doped ($\delta = 0.15$, 0.15 holes/Cu atom) sample of $Bi_2Sr_2Ca_2Cu_3O_{10}$. One can see a Drude peak and around 1.5 eV the first peak, interpreted as a charge transfer excitation. At higher energies one has contributions from Bi, O, Sr and Ca bands and a straightforward summation of the number of carriers as we carried out in the case of Aluminum, Fig. 2.1, is not possible. On the other hand one can see that the weight of the conduction band gives roughly the expected number for the effective number of carriers, in fact, if the nominal doping is 0.15 holes/Cu atom, and we consider a formula unit of $Bi_2Sr_2Ca_2Cu_3O_{10}$ which contains 3 Cu atoms, we should expect 0.45 carriers in the conduction band. The SW integral is representative of the conduction band in the energy range between 0.7 and 1.2 eV, where the value of N_{eff} varies between 0.4 and 0.6, indeed in agreement with what one expects. We can therefor experimentally see that the conduction band is filled by the doping carriers. One would also like to see that indeed copper has a $3d^9$ configuration and that indeed the large Coulomb repulsion is manifesting itself in the copper states. X-ray Absorption Spectroscopy (XAS) has been shown to be successful in determining the valence of oxide materials. In the presence of strong electron-electron correlations in fact, the interaction between a 2p core-hole and the 3d valence electrons in transition metals gives rise to atomic multiplet effects which can identify different ground state configurations[7]. A more exhaustive description of this technique will be given in Chapter 5. For the moment one can see, in the topmost panel of Fig. 3.5, that the XAS spectra of $Bi_2Sr_2CaCu_2O_8$ and $Bi_2Sr_2Ca_2Cu_3O_{10}$ is very similar to the simulated spectrum of Cu $3d^9$, supporting the claim that the Cu-O planes are composed by Cu^{++} ions. In the lowest panel of Fig. 3.5 one can see the valence band photoemission spectrum of $Bi_2Sr_2CaCu_2O_8$ and $Bi_2Sr_2Ca_2Cu_3O_{10}$; these spectra have been theoretically reproduced by including into the standard band calculations the effects of Coulomb repulsions by performing a configuration interaction cluster calculation [8]. Moreover, these calculations predicted the presence of a valence band satellite at around 12 eV from the Fermi energy. Such a satellite would be the Cu $3d^8$ electronic state

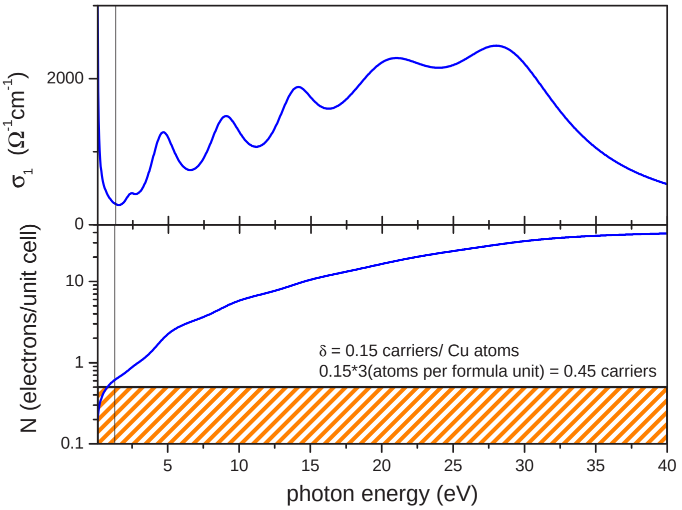

Figure 3.4: Topmost panel: The optical conductivity of Bi2223. Lowest panel: The effective number of carriers versus energy obtained by the f sum-rule in Bi2223.

pushed away from the valence band by an on site Coulomb repulsion larger than 8 eV. In a resonant photoemission experiment the satellite structures of copper are strongly enhanced when the photon energy is tuned at the $2p \mapsto 3d$ transition[9], providing a unique tool to check the impact of Coulomb repulsions on the electronic structure of cuprates. Indeed this satellite has been observed in resonant photoemission on $Bi_2Sr_2CuO_6$ and $Bi_2Sr_2CaCu_2O_8$ samples[10], and in the lower panel of Fig. 3.5 we show new measurements on Y-doped $Bi_2Sr_2CaCu_2O_8$ and $Bi_2Sr_2Ca_2Cu_3O_{10}$ samples which also show the strong resonant $3d^8$ states 12 eV away from the Fermi energy. In these photoemission experiments one can also identify the different electronic states of the elements and compare their position with the peaks observed in the optical spectra, keeping in mind that the selection rules for optics and photoemission are different. To summarize this paragraph, we have discussed the electronic structure of the cuprates, in particular of the Cu-O planes, and we have shown some experimental examples where one can directly see manifestations of the theoretical concepts described above.

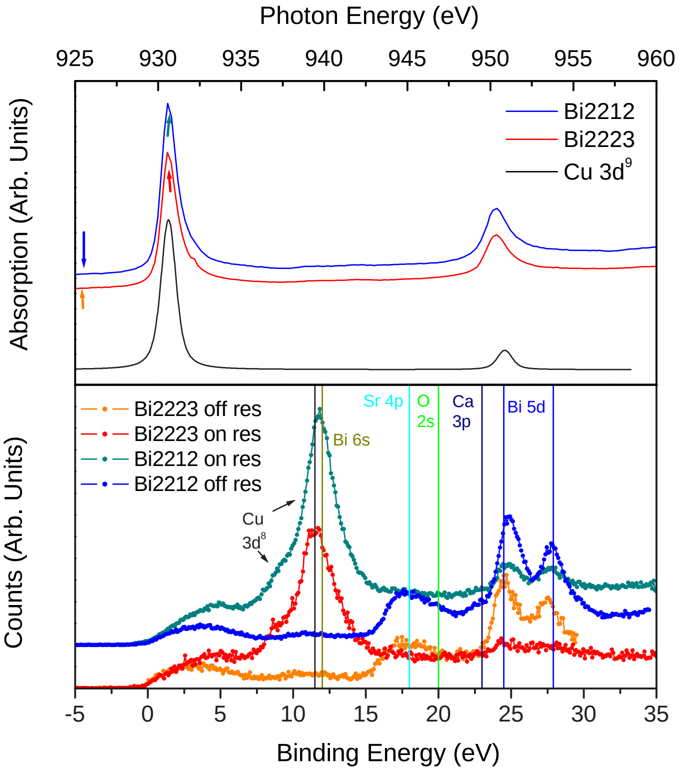

Figure 3.5: Topmost panel: the XAS spectra of Bi2212 and Bi2223 together with $3d^9$ atomic multiplet calculations. Bottom panel: the photoemission and resonant photoemission spectra of Bi2212 and Bi2223.

3.2 The optical spectral weight and the pairing mechanism

A vast class of materials spanning a large part of the periodic table has been shown to become superconducting at low temperature due to an electron-phonon driven pairing mechanism. This has been explained by the BCS theory: the electrons moving in the lattice can deform the lattice itself via the Coulomb interaction between the negative electron charge and the positive ions one; this deformation can excite a particular phonon mode of the crystal. The result of this interaction creates an attractive potential around the electron that favors the pairing mechanism. When two electrons, particles with half integer spin, couple together, they behave as a particle with integer spin, which obeys the Bose-Einstein statistic and can condense in a single quantum state. This condensate represents the ground state of the system, therefor in a superconductor current can flow in the ground state, and the material shows a null resistivity. In the BCS model, when the pair condensate is formed, the system lowers its potential energy by a larger amount than it increases its kinetic energy. The total energy is lowered and the material undergoes a superconducting phase transition. In 1986 a family of materials has been discovered which exhibits a superconducting transition temperature much higher then the one of BCS materials. The intermetallic compound with the highest T_c is MgB_2 with a T_c around 39 K while $\mathrm{Bi}_2\mathrm{Sr}_2\mathrm{Ca}_2\mathrm{Cu}_3\mathrm{O}_{10}$ becomes superconducting around 110 K. The latter are so called "Cuprates" because they are all compounds involving CuO_2 planes. Several alternative models have been proposed for the pairing mechanism of high T_c cuprate [6, 11, 12], many of them predict a decrease of kinetic energy in the superconducting state [6, 11, 12, 13, 14] , but despite the large amount of research, a consensus has not been reached yet about the way the electrons pair. While BCS materials are Fermi Liquid systems where electron-electron interactions can be treated as a perturbation, cuprate superconductors are believed to be non Fermi Liquid in the normal state and electron-electron interactions are playing a dominant role, as discussed in the previous paragraph. Moreover the pseudogap phase [15, 16, 17], and the d-wave symmetry of the superconducting gap [18] are difficult to understand in terms of the standard BCS mechanism based on the electron-phonon interaction. Another indication for an unconventional pairing mechanism came from the experimental temperature dependence of the low energy spectral weight of optimally doped and underdoped Bi2212[19, 20], which behaves opposite to the prediction from BCS theory[21]. On the other hand, it has been shown that in the overdoped region of the phase diagram the system has a more conventional Fermi-liquid behavior[22, 23, 24, 25]. This issue can be addressed by optical techniques[19, 20], taking advantage of the relation between the intraband spectral weight and the energy momentum dispersion of the conduction electrons [26]

$$W(\Omega_c) \equiv \int_0^{\Omega_c} \sigma_1(\omega) d\omega = \frac{\pi e^2 a^2}{2\hbar^2 V} < -\hat{T} >, \tag{3.5}$$

where $\sigma_1(\omega)$ is the real part of the optical conductivity, Ω_c is a cutoff frequency, a is the in-plane lattice constant, V is the volume of the unit cell, and $\hat{T} \equiv -a^{-2}\sum_k \hat{n}_k \partial^2\epsilon_k/\partial k^2$. In the superconducting state, the integration must include the δ-peak at zero frequency due to the condensate. In the nearest neighbor tight-binding approximation $\hat{T}$ is exactly the kinetic energy of the conduction band electrons. In this case the lowering of $W(\Omega_c)$ implies an increase of the electronic kinetic energy and vice-versa. The value of Ω_c has to be chosen as to cut off the region of the interband transitions. In the presence of strong electron correlations the intraband energy region becomes very broad as it includes the high-frequency peaks due to the electronic transitions leading to the double occupancy. Recently Wrobel *et al.* [14] pointed out that $W(\Omega_c)$ is representative of the kinetic energy within the t-J model, if Ω_c is chosen between the values of exchange integral $J \sim 0.1$ eV and hopping $t \sim 0.4$ eV, while it corresponds to the kinetic energy of the Hubbard model when the cutoff energy is above $U \sim 2$ eV.

While the physical meaning of the temperature dependent W(Ω_c) is a matter of theoretical interpretations, it can be, in fact, experimentally determined without model assumptions, as discussed in section 2.4.2. The latter is non-trivial, since the integration in Eq.3.5 requires, at first glance, the knowledge of $\sigma_1(\omega)$ down to zero frequency and a separate determination of the superfluid density. Fortunately, additional information about the real part of the dielectric function $\epsilon_1(\omega)$, which is independently obtained from ellipsometry as well as reflectivity measurement (since reflectivity depends on both ϵ_1 and ϵ_2), allows one to determine accurately $W(\Omega_c)$ and its temperature dependence without low-frequency data extrapolations.

3.3 The relation between SW and kinetic energy

In order to draw conclusions about the kinetic energy of the carriers based on optical experiments, one has to investigate the validity of the relation between SW and kinetic energy, given the real band structure of the material under investigation. It is important to do this, since our intuition is based on the behaviour of the kinetic energy (which, as we illustrate below) always increases in the superconducting state, in a BCS scenario. However, the optical spectral weight for a single band is given by [27, 26]

$$W(T) = \frac{2\hbar^2}{\pi e^2}\int_0^{+\infty} d\nu Re\left[\sigma_{xx}(\nu)\right] = \frac{2}{N}\sum_k \frac{\partial^2\epsilon_k}{\partial k_x^2} n_k, \tag{3.6}$$

whereas the negative of the band kinetic energy is given by a somewhat different expression; in the simplest case it is given by

$$-<K>=-\frac{2}{N}\sum_k \epsilon_k n_k, \tag{3.7}$$

where ϵ_k is the tight-binding dispersion (that takes into account already Hartree-Fock-type corrections) and n_k is the single spin momentum distribution function (we take the lattice spacing to be unity). The sum over k is over the first Brillouin zone, and in the case with bilayer splitting (see below), includes a summation over the two split bands. Note that this is *not* the total kinetic energy of all the electrons, but just the kinetic energy of the electrons in the given tight-binding band(s); furthermore, *only* in the case of nearest neighbour hopping is W proportional to $-<K>$. In the presence of more complicated band dispersion, the expectation value of the kinetic energy has a more expression.

We first review the expectation for the kinetic energy, based on Eq. (3.7), since this correspondence has been used to build intuition concerning the optical spectral weight. First, what happens when the system goes superconducting? The momentum distribution function changes as discussed previously [29]— it goes from a Fermi-like distribution function (in the absence of strong correlations) to a distribution smeared by the presence of a superconducting order parameter. For an order parameter with d-wave symmetry, the momentum distribution is no longer a function of the band structure energy, ϵ_k alone. For example, for a BCS order parameter with simple nearest neighbour pairing form, $\Delta_k = \Delta(\cos k_x - \cos k_y)/2$, then, as k varies from $(0,0)$ to $(\pi,0)$, the magnitude of the order parameter changes from zero to Δ. On the other hand, as k varies along the diagonal (from the bottom of the band to the top), the order parameter is zero (and constant). In any event, even at zero temperature, BCS-like superconductivity *raises* the kinetic energy of the electrons (see Fig. 3 of Ref. [29]). This is as expected, since for non-interacting electrons the normal state at zero temperature corresponds to a state with the lowest possible kinetic energy. Therefore, any modification to this state (for example, because of a superconducting instability) can only increase the kinetic energy expectation value.

The question, partially answered in Refs. [29, 37] is: does this behaviour remain at all electron densities? Furthermore, with further than nearest neighbour hopping, does the spectral weight (given by Eq. (3.6)) also follow the same trend as the negative of the kinetic energy? Perhaps not surprisingly, we find that the spectral weight does not qualitatively follow the kinetic energy near a van Hove singularity. However, as will be discussed further below, we find that for the band structure and doping regime thought to be applicable in $Bi_2Sr_2CaCu_2O_{8+\delta}$ (BSCCO) [28], the spectral weight should decrease in the superconducting state relative to the normal state. That is, correlations, phase fluctuations, scattering rate collapse, or some other scenario is required to understand the "anomalous" behaviour. We will also address the temperature dependence in the normal state; in some ways this is a more easily measured quantity than the change below T_c.

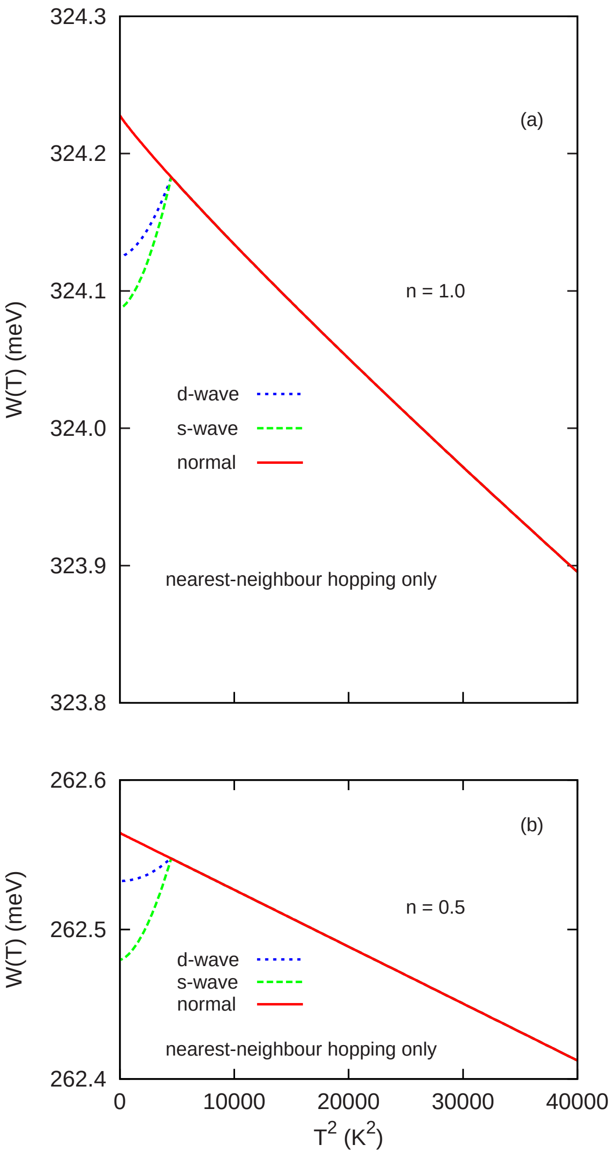

Figure 3.6: Spectral Weight vs. T^2 for (a) half-filling, and (b) $n = 0.5$. The normal state is given by the solid red curve, and the superconducting state with d-wave (s-wave) symmetry by the short-dashed blue (dashed green) curve. In both cases the normal state result is almost linear in T^2, and the superconducting state shows a decrease in the spectral weight (increase in the kinetic energy) as expected. We used $t = 0.4$ eV, and BCS values for order parameters, etc. with $T_c = 69$ K.

In the next section we examine the optical spectral weight for a model with nearest neighbour hopping only. This simple band structure yields an optical spectral weight which is directly proportional to the expectation value of the negative of the kinetic energy. We examine the behaviour of the optical spectral weight as a function of electron density. Note that we will use the symbol n to denote electron density; for a single band this quantity will span values from 0 to 2. It will be used when systematic investigations of the spectral weight for a given band structure are carried out. When comparing with experiments in the cuprate, we will use the symbol δ to denote doping away from half-filling, i.e. $n = 1$. Thus, $\delta = 1 - n$, and the regime of experimental interest is roughly $0 < \delta < 0.25$. We use the phrase "hole doping" to refer specifically to the value of δ.

Following this section we introduce next-nearest neighbour hopping into the band structure ($t - t'$ model). This moves the van Hove singularity away from half filling and also causes the spectral weight to deviate from the kinetic energy; hence both will be plotted in the ensuing plots. We find already in this simple extension significant departures from the "standard BCS" description based solely on the kinetic energy.

Finally, following Ref. [28], we also introduce a next-next-nearest neighbour hopping and a bi-layer splitting term; these are required for a quantitatively accurate description of the ARPES (Angle-Resolved PhotoEmission Spectroscopy) results. We find that these terms have significant effects on the optical sum rule. First, the van Hove singularity is split into two singularities, secondly the first of these occurs at a much lower hole doping level than in the $t - t'$ model.

As discussed in the summary, the end result is that (i) the change in the optical spectral weight due to superconductivity can be either positive or negative, depending on the band structure and electron density, and (ii) if a parametrization of the band structure is adopted from ARPES studies, then the optical spectral weight *decreases* in the superconducting state. The observed *increase* for optimal and underdoped samples then requires additional ingredients. Some possibilities are briefly mentioned.

3.3.1 nearest neighbour hopping only

For nearest neighbour hopping only, the band structure is given by

$$\epsilon_k^{nn} = -2t(\cos k_x + \cos k_y) \tag{3.8}$$

and we have that $2W = - < K >$ in two dimensions. In Fig. 3.6 we show plots of the spectral weight vs. T^2 for two representative electron densities, $n = 1$ and $n = 0.5$. The first places the Fermi level right on the van Hove singularity, while the second is well removed from all van Hove singularities. These are computed through the usual procedure: first, even in the normal state, the chemical potential must be determined at each temperature to ensure that the electron density remains constant as a function of temperature. This is the common procedure, though it is true that in complicated systems for which one is using some "low energy" tight-binding Hamiltonian to describe the excitations that it is not immediately obvious that the electron number density should remain fixed as a function of temperature; nonetheless, we adopt this procedure here. In Eq. (3.6) the chemical potential enters the momentum distribution function, which, in the normal state, is replaced by the Fermi-Dirac distribution function, $n_k \rightarrow f(\epsilon_k - \mu)$. In the superconducting state, we simply adopt a model temperature dependence for the order parameter, following Ref. [29]. This has been tested for both s-wave and d-wave symmetries by comparing to fully self-consistent solutions to BCS equations with separable potentials [29]. One still has to determine the chemical potential self-consistently for each temperature, which is done by solving the number equation in the superconducting state for a fixed chemical potential and order parameter, and iterating until the desired number density is achieved. The value of the zero temperature order parameter is fixed by the weak coupling BCS values, $2\Delta_0 = \eta k_B T_c$ where $\eta = 4.2(3.5)$ for the d-wave (s-wave) case. Further details are provided in Ref. [29]. For the electron densities studied in the first part of this section, we simply take $T_c = 69$ K for all electron densities. In section IV we will adopt T_c values as observed from experiment.

Both plots in Fig. 3.6 show somewhat linear behaviour with T^2, though in Fig. 3.6 there is some noticeable upward curvature due to the van Hove singularity which is present at the Fermi level for this electron density. The decrease in spectral weight at the transition is more pronounced for s-wave symmetry (dashed green curves) than for d-wave symmetry (dotted blue curves). The normal state results show a decreasing value with increasing temperature, indicative of an increasing kinetic energy. This is the 'textbook' example of the temperature dependence of the spectral weight through a superconducting transition [21, 30, 29].

In Fig. 3.7 we examine both the spectral weight difference ($W_s - W_N$ and $W_d - W_N$ for s- and d-wave symmetry, respectively — 'N' here stands for 'normal') at zero temperature, and the slope of $W(T)$ with respect to T^2 at T_c, vs. electron density, n. These plots make evident several important points. First, the van Hove singularity clearly plays a role; it enhances the overall magnitude of the effect, whether we examine the difference between the superconducting and normal state at zero temperature, or the slope at T_c. In fact the latter tracks the former, indicating that both are related to one another. One can understand this qualitatively by the observation that in both cases (warming up or going superconducting) the momentum distribution function broadens, though for different reasons [29]. The most important point to learn from this plot is that the difference is always negative, indicating that, for nearest neighbour hopping only, the opening of a gap does indeed increase the kinetic energy and decrease the spectral weight in a superconductor.

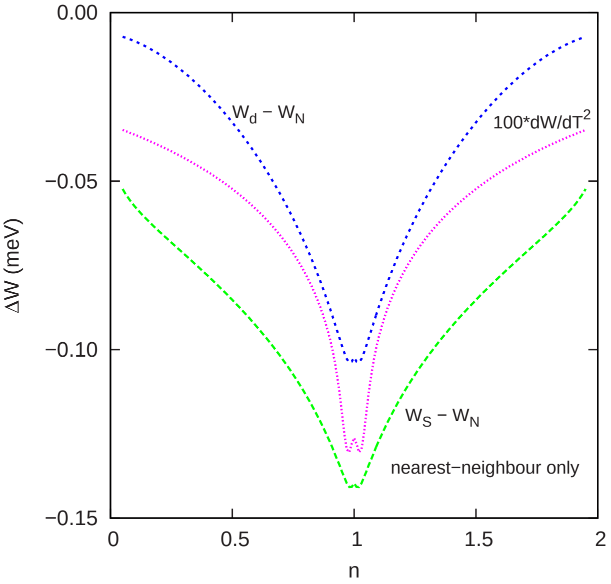

Figure 3.7: The difference $(W_d - W_N)$ in the spectral weight between the superconducting state with d-wave symmetry and the normal state at zero temperature vs. doping (dotted blue curve). The dashed green curve shows the same quantity for s-wave symmetry, and the pink points indicate the slope (with respect to T^2) of the spectral weight near T_c. All three quantities are always negative, and show an enhancement near half-filling due to the van Hove singularity. In fact, the pink points are almost a perfect inverted image of the density of states (see the minus sign in Eq. (3.12)), except for the small density regime near half-filling, where the van Hove singularity makes the Sommerfeld expansion invalid.

3.3.2 next-nearest neighbour hopping

When next-nearest neighbour hopping is included in the band structure, one obtains the so-called $t - t'$ model. This model has band structure

$$\epsilon_k^{nnn} = -2t(\cos k_x + \cos k_y) + 4t' \cos k_x \cos k_y, \tag{3.9}$$

and goes a long way towards understanding the Fermi surface for $\mathrm{Bi_2Sr_2CaCu_2O_{8+\delta}}$ (BSCCO), as determined by ARPES [31, 28], at least for the doping levels studied. On the theoretical side, the presence of t' shifts the van Hove singularity to an energy given by $\mu = -4t'$. For the sake of this study one can study all electron densities; however, one must bare in mind that most experiments on BSCCO are at doping levels such that the van Hove singularity is not crossed, i.e. the Fermi surfaces are always hole-like. We will also study (see next section) a band structure more pertinent to BSCCO [31, 28], which uses a next-next-nearest neighbour hopping amplitude in addition:

$$\epsilon_{k\pm} = \epsilon_k^{nnn} - 2t''(\cos 2k_x + \cos 2k_y) \pm t_\perp(\cos k_x - \cos k_y)^2/4, \tag{3.10}$$

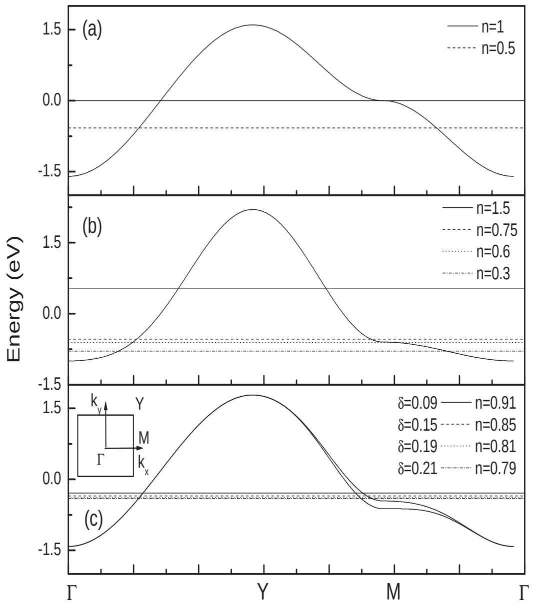

Figure 3.8: Illustrative plots of the band structure for (a) nearest neighbour hopping only, (b) the $t - t'$ model, and (c) the Kordyuk et al. [28] parametrization of the band structure with bilayer splitting. The van Hove singularities occur where the band dispersion flattens.

which we will refer to as the $t - t' - t''$ model. Note that we allow for a bilayer splitting term as well, following Kordyuk et al. [28]. However, they actually adjust hopping parameters for each doping, while we simply adopt the ones used for their overdoped sample: $t = 0.40$ eV, $t' = 0.090$ eV, $t'' = 0.045$ eV, and $t_\perp = 0.082$ eV. Illustrative plots of the band structures are shown in Fig. 3.8.

Returning now to the $t - t'$ model, the van Hove singularity occurs at an electron density $n = 0.60$, i.e. a hole doping (away from half-filling) of $\delta = 1 - n = 0.4$. As mentioned above, this high level of doping is never realized in samples of BSCCO [32]. In any event, we are interested in the more generic behaviour of the spectral weight, given a reasonably representative band structure for the cuprate.

In Fig. 3.9 we show a summary of the doping dependence of the various quantities with the $t - t'$ band structure. In both Fig. 3.9 (a) and (b) we have plotted the density of states at the Fermi level as a function of doping (this is possible for a doping-independent band) to illustrate where the van Hove singularity is. The remarkable feature in Fig. 3.9 (a), for electron densities below (i.e. hole doping away from half filling "above") the van Hove singularity, is that the spectral weight change in the superconducting state is positive ! Similarly in Fig. 3.9 (b) the actual slope of the spectral weight above T_c is positive. Note that our intuition about the kinetic energy change remains correct; it is indeed negative, for all electron densities, for

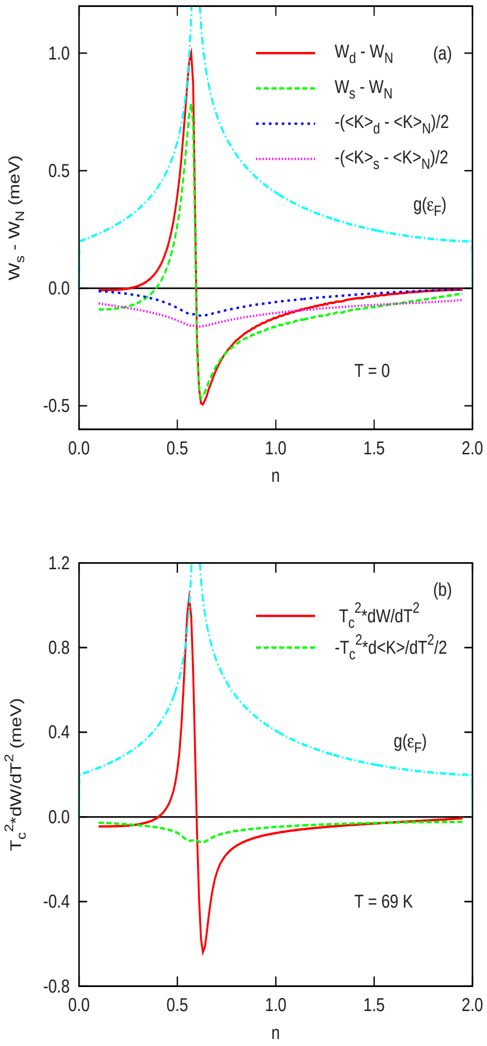

Figure 3.9: (a) The difference $(W_d - W_N)$ in the spectral weight between the superconducting state with d-wave symmetry and the normal state at zero temperature vs. doping (solid red curve), for the $t - t'$ band structure, with $t = 0.4$ eV and $t' = 0.09$ eV. The dashed green curve shows the same quantity for s-wave symmetry. Both exhibit positive values to the left of the van Hove singularity (the density of states at the Fermi level is indicated, as a function of doping, by the dot-dashed cyan curve). The negative of the kinetic energy for d-wave (blue short-dashed curve) and for s-wave (dotted pink curve) behaves as expected, always negative, and peaks (in absolute value) at the van Hove singularity. (b) The normal state slope (taken at $T_c = 69$ K) of the spectral weight vs. doping (solid red curve). The dashed green curve shows the same quantity for the negative of the kinetic energy. These behave in very similar fashion to the differences (taken at zero temperature) shown in (a).

both s-wave and d-wave symmetries. Moreover, the slope is also everywhere negative, which establishes a definite correlation between the slope above T_c and the change at $T = 0$. Note that in Ref. [29] (see Fig. 3 of that reference) the doping parameters were such that the optical sum rule and the negative of the kinetic energy were qualitatively (and even quantitatively) similar [33]. Here, in the vicinity of the van Hove singularity we encounter a regime where these two properties are markedly different from one another.

How do we understand this strange dependence near the van Hove singularity ? It is easiest to focus on the temperature dependence in the normal state. One should first review the simple argument for why the slope for the negative of the kinetic energy is expected to *always* be negative, no matter what the band structure. This quantity is defined as

$$- < K > = - \int_{-\infty}^{+\infty} d\epsilon \ \epsilon \ g(\epsilon) f(\epsilon - \mu) \tag{3.11}$$

where $g(\epsilon) \equiv \frac{1}{N}\sum_k \delta(\epsilon - \epsilon_k)$ is the single spin, single particle density of states for electrons with band dispersion ϵ_k. One can perform a Sommerfeld expansion, which yields two terms, one of which is eliminated by performing the analogous expansion for the electron density, with the requirement that the density remains constant as a function of temperature [34]. The result is [34]

$$- < K > = - < K >_{T=0} - \frac{\pi^2}{3}(k_B T)^2 g(\epsilon_F), \tag{3.12}$$

where, it is now clear that, regardless of the Fermi level, the temperature correction is always negative. This means that the kinetic energy ($< K >$) always increases as the temperature increases, a statement which is physically obvious.

With the spectral weight,

$$W \equiv \frac{2}{N}\sum_k \frac{\partial^2 \epsilon_k}{\partial k_x^2} f(\epsilon_k - \mu), \tag{3.13}$$

there is no simple cancelation, as occurs in the kinetic energy. If one defines the quantity,

$$g_{xx}(\epsilon) \equiv \frac{1}{N}\sum_k \frac{\partial^2 \epsilon_k}{\partial k_x^2} \delta(\epsilon - \epsilon_k), \tag{3.14}$$

then the Sommerfeld expansion can be applied to $W(T)$ as was done for the kinetic energy. The result is

$$W(T) = W(0) + \frac{\pi^2}{3}\frac{(k_B T)^2}{8t}\phi(\epsilon_F), \tag{3.15}$$

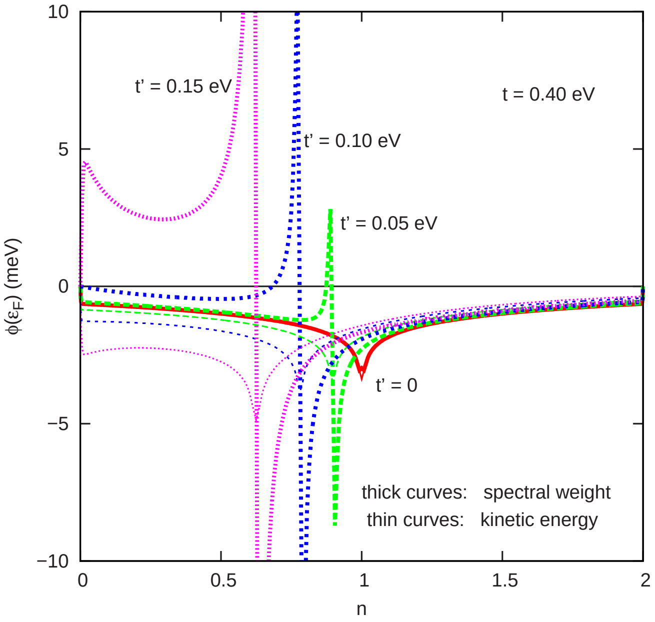

Figure 3.10: The finite temperature correction to the optical spectral weight (thick curves), for various values of t', as indicated. Also plotted is the analogous quantity for the kinetic energy (which, by Eq. (3.12) is just $-8tg(\epsilon_F)$). Note that the latter is always negative, while the spectral weight becomes positive for a finite electron concentration for electron (hole) densities below (above) the van Hove singularity. The magnitude of the anomalous region increases with increasing t'.

where

$$\phi(\epsilon_F) = 8t\left\{\frac{g'_{xx}(\epsilon_F)g(\epsilon_F) - g'(\epsilon_F)g_{xx}(\epsilon_F)}{g(\epsilon_F)}\right\}. \tag{3.16}$$

Using $g_{xx}(\epsilon_F) = -\epsilon_F g(\epsilon_F)$, which is correct for nearest neighbour hopping only, one finds $\phi(\epsilon_F) = -8tg(\epsilon_F)$ and one recovers the previous result, given by Eq. (3.12) for the optical spectral weight as well as for the kinetic energy. Otherwise, the sign of the correction is dependent on the quantity within the braces. This quantity involves a difference between two quantities, both of which contain singularities. This quantity is plotted in Fig. 3.10 for the $t - t'$ model for various values of t', along with the corresponding quantity for the kinetic energy, which, by Eq. (3.12), is $-8tg(\epsilon_F)$. It is evident that as t' increases, a larger anomaly over a wider range of electron densities is expected. For more complicated band structures, an assortment of Fermi energies (i.e. electron concentrations) will exist for which the slope (and the change in the superconducting state) is "anomalous", i.e. positive.

In Fig. 3.11 we show some specific examples of the temperature dependence of the optical spectral weight for a variety of electron concentrations. These results clearly show the progression from the 'standard' result shown for $n = 1.5$ (top

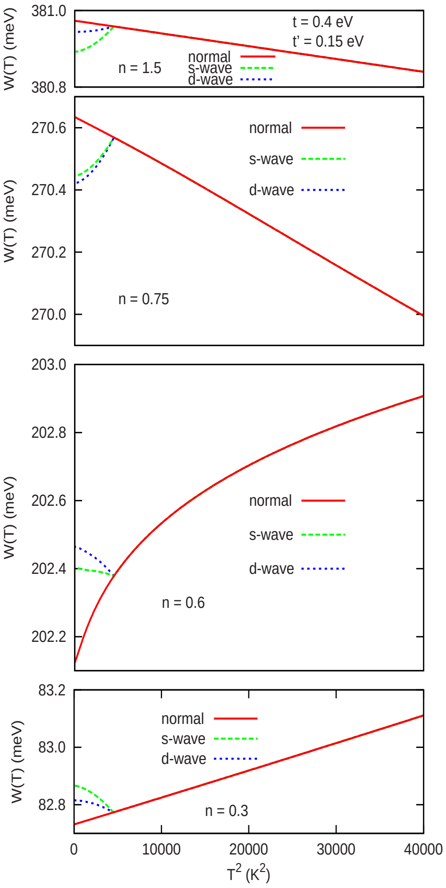

Figure 3.11: Spectral weight for four representative densities for the $t-t'$ model (see Fig. 3.10). The progression from top to bottom is from high electron concentration to low electron concentration. Note the qualitative change from negative slope (lower superconducting vs. normal state difference) to positive slope (higher superconducting vs. normal state difference) as the electron concentration changes such that the chemical potential sweeps through the van Hove singularity.

frame) to the highly anomalous result shown for $n = 0.6$ (third frame). Note the variation of the vertical scale: there is the obvious progression of lower spectral weight with decreasing electron density. However, the magnitude of both the slope and the change due to superconductivity also experiences a large increase for the two electron densities near the van Hove singularity ($n = 0.75$ and $n = 0.6$). For example, the absolute value of the slope in the second frame ($n = 0.75$ is approximately a factor of 5 higher than that in the first frame ($n = 1.5$). Similarly at $n = 0.6$ the slope is much higher than at $n = 0.3$, particularly at low temperatures. The reason is evident from Fig. 3.10: this enhancement occurs in the vicinity of the van Hove singularity. Note that the results of Fig. 3.11 are displayed for $t' = 0.15$ eV. In this case, Fig. 3.10 shows that there is an extended range of electron densities for which a positive slope (and positive change below T_c) occurs. Using $t' = 0.10$ eV, for example, would result in a very narrow range of electron densities for which the optical spectral weight has behaviour opposite to that of the negative of the kinetic energy (see Fig. 3.10, blue dashed curves).

In summary, in the case of the simple next-nearest neighbour model considered, the anomalous region always occurs at electron concentrations *below* the van Hove singularity. In many of the high temperature superconducting cuprate, this electron concentration is not experimentally achieved. Certainly in the experiments that report a positive ("anomalous") optical spectral weight change in BSCCO, this regime is believed to be irrelevant. Hence, while this investigation of the behaviour of the optical spectral weight using the $t - t'$ model certainly plays havoc with our intuition (which motivated the experiments in the first place), it apparently does not provide an explanation of the experimental results [35]. This is further explored in the next section.

3.3.3 bi-layer splitting

It is evident that the characteristics of the optical spectral weight will be very dependent on the band structure and the doping level. A complete investigation of parameter space, with an accompanying catalogue of optical spectral weight behaviour would undoubtedly reveal a wide assortment of results. Perhaps a more useful procedure at this point would be to adopt the band structure proposed for a particular compound (BSCCO), as prescribed by some other experiment (ARPES), and determine the behaviour of the optical spectral weight in this case. As discussed in the previous section, we will adopt the parameters used in Ref. ([28]) to fit their ARPES results; these include a bilayer splitting term, which, as will now be discussed, can result in even more unusual doping dependence. Their determined structure was given in the previous section by Eq. (3.10) with parameters listed below this equation. They also used $t_\perp = 0.082$ eV; we will adopt these parameters for all electron concentrations (i.e. hole doping) for simplicity.

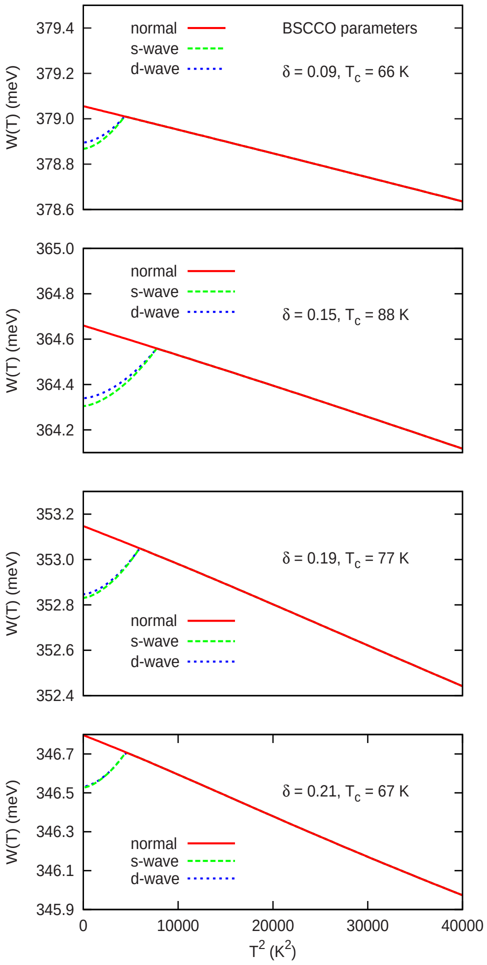

Figure 3.12: Spectral weight for the four hole doping concentrations considered in the experiments [37]. These calculations use the ARPES-determined band structure parameters from Ref. [28], including the bilayer splitting. Slopes are always negative, and the change at T_c is also always negative. Note that in this case the s-wave order parameter gives roughly the same value as the d-wave parameter.

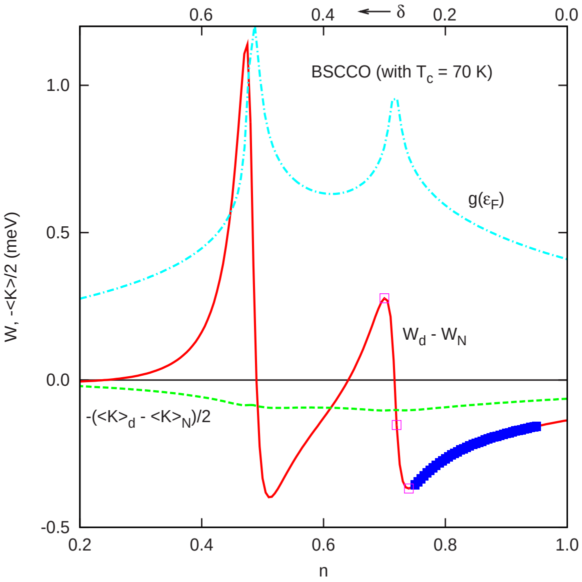

Figure 3.13: Spectral weight difference (solid red curve) as a function of electron concentration for the band structure determined by ARPES [28]. For simplicity we put $T_c = 70$ K for all electron densities. The normal state slope shows very similar behaviour. Also plotted is the negative of the change in the kinetic energy (dashed green curve), and the density of states at the Fermi level (dot-dashed cyan curve), for reference. Note that 'anomalies' in the spectral weight occur at the two van Hove singularities, while the change in kinetic energy is simply gently modulated by the density of states. Also shown with solid blue symbols is the hole doping regime of relevance to the BSCCO experiments in Ref. [37], and considered in the previous figure. For clarity only d-wave results are shown. The three open squares show the doping concentrations considered in the next figure, of possible relevance for overdoped samples with chemical potential that crosses the van Hove singularity [38].

Fig. 3.12 shows the optical spectral weight as a function of temperature for the four doping levels considered in the experiments [37, 36]. For these band structures, BCS would always show a decrease of SW below T_c.

However, very recently, very overdoped BSCCO samples have been produced [38]; ARPES measurements [38] have determined that the chemical potential moves through the first van Hove singularity. Thus, it is instructive to examine the consequences of this BCS model for higher hole doping concentrations (lower electron densities). In Fig. 3.13 the doping dependence of the optical spectral weight slope is shown as a function of electron concentration, n for the hole doped region (with respect to half-filling). This figure uses the band structure parameters from Kordyuk et al. [28], so the crossing of the first van Hove singularity occurs at a higher hole doping (about $\delta \approx 0.28$) than reported in Ref. [38]. Leaving this detail aside for the moment, it is clear from Fig. 3.13 that a dramatic change is expected in the optical spectral weight anomaly for this doping. In Fig.3.14 we show the temperature dependence for some hole doping concentrations near this region, as indicated by the open squares in Fig. 3.13. Both the normal state and superconducting state behaviours show a transition as one crosses the van Hove singularity. It would be most interesting to measure the optical spectral weight in this doping regime. Such measurements would provide a good indication of whether or not the van Hove singularity is relevant in these materials.

3.4 The optical properties of Bi2223

3.4.1 The ab-plane response

Two large single crystals of $Bi_2Sr_2Ca_2Cu_3O_{10}$ with $T_c = 110$ K and transition width $\Delta T_c \sim 1$ K were prepared as described in Ref. [1]. The samples had dimensions $(a \times b \times c)$ of $4 \times 1.5 \times 0.2$ mm^3 and of $3 \times 0.8 \times 3$ mm^3 respectively. The first crystal has been used to measure the in-plane optical properties and was cleaved within minutes before being inserted into the cryostat. We measured the normal-incidence reflectivity from 100 and 7000 cm^{-1} (12.5 meV - 0.87 eV) using a Fourier transform spectrometer, evaporating gold *in situ* on the crystal surface as a reference. The reflectivity curves for selected temperatures are displayed in Fig. 3.15. The ellipsometric measurements were made on the same sample surface in the frequency range between 6000 and 36000 cm^{-1} (0.75 - 4.5 eV) at an angle of incidence of 74°. The ellipsometrically measured pseudo-dielectric function was numerically corrected for the admixture of the c-axis component which provided the true ab-plane dielectric function, whose real and imaginary parts are shown in Fig. 3.16. The c-axis dielectric function that is required for this correction was measured independently on the ac-oriented surface of the second crystal as described in the next section. The superconductivity induced changes of the optical properties at photon energies above

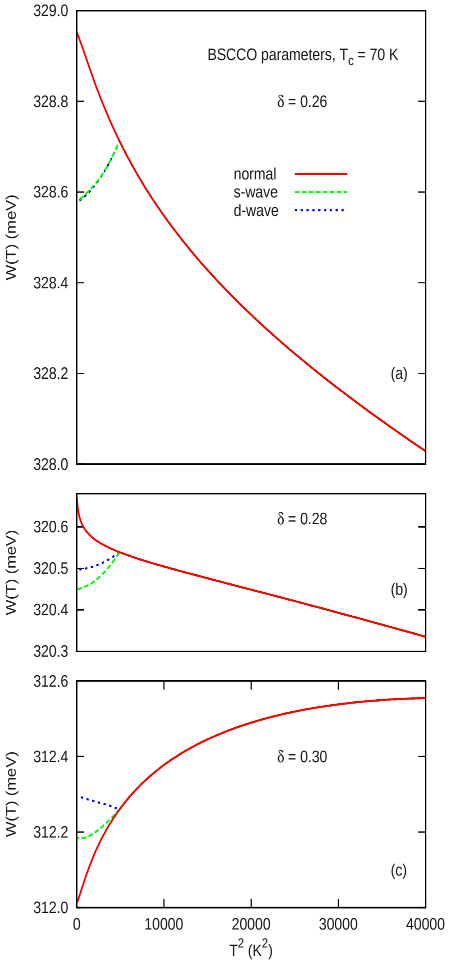

Figure 3.14: Spectral weight for three hole doping concentrations that move the chemical potential across the first van Hove singularity (see Fig. 3.13). Note the dramatic change that occurs as one dopes across the van Hove singularity (see text).

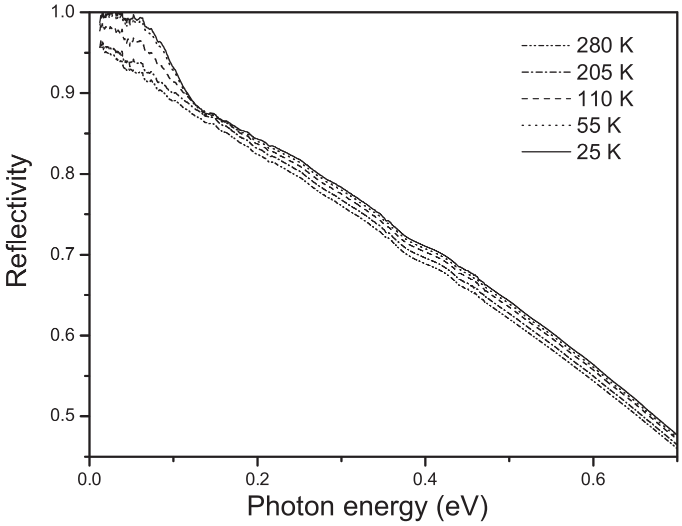

Figure 3.15: In-plane reflectivity spectra of optimally doped Bi2223 for selected temperatures.

the superconducting gap (in the mid-infrared and higher frequencies), are rather small but their reliable detection is crucial to determine to correct sign and magnitude of the spectral weight transfer. We used home-made optical cryostats, whose special design preserves the sample alignment during thermal cycling. In the visible - ultraviolet (UV) region, in order to avoid spurious temperature dependencies of the optical constants due to adsorbed gases at the sample surface, an ultra high vacuum cryostat was used, operating at a pressure in the 10^{-10} mbar range. All data were acquired in the regime of continuous temperature scans at a rate of about 1 K/minute between 20 K and 300 K with a resolution of 1 K. The signal to noise ratio of the temperature dependent reflectivity in the mid-infrared is about 2000.

In order to obtain the optical conductivity $\sigma_1(\omega)$ in the whole frequency range, we used a variational procedure described in Ref. [39]. In the first stage, the infrared reflectivity and the ellipsometrically measured complex dielectric function in the visible and UV-range were fitted simultaneously with a Drude-Lorentz model. The corresponding parameters at selected temperatures are listed in Table 3.1. We found that one Drude and four Lorentz terms form a minimal set of oscillators fitting data well enough at all temperatures. The Drude peak narrows with cooling down and transforms to a condensate δ-peak below T_c. The two lowest frequency oscillators which mostly describe the mid-infrared absorption, show dramatic changes below T_c, mimicking the formation of the superconducting gap. The high-frequency Lorentzians corresponding to the interband transitions, show very little temperature dependence. In the second stage, the fitting was refined with a variational dielectric function added on top of the Drude-Lorentz model. The former is essentially a set of a large number of narrow oscillators, each corresponding to one or two spectral

Table 3.1: Fit of the measured reflectivity and ellipsometry data with one Drude and four Lorentz oscillators: $\epsilon(\omega) = \epsilon_\infty + \sum_k \omega_{p,k}^2/(\omega_{0,k}^2 - \omega^2 - i\gamma_k\omega)$ at selected temperatures. All parameters, except ϵ_∞, are given in cm^{-1}, *i.e.* they should be multiplied by $2\pi c$ to convert to angular frequencies in units of s^{-1}.

ϵ_∞	$\omega_{0,k}$	$\omega_{p,k}$	γ_k	ϵ_∞	$\omega_{0,k}$	$\omega_{p,k}$	γ_k
280 K				55 K			
2.53	0	7184	160	2.46	0	10145	0
	201	8598	706		1113	9997	1866
	1607	15472	6670		4260	12460	7928
	18553	12211	11911		18812	11655	11436
	37110	39368	20474		37550	40829	21353
205 K				25 K			
2.52	0	8497	152	2.45	0	10295	0
	178	7768	787		1149	9730	1797
	1759	15287	6750		4232	12583	7914
	18647	11733	11390		18815	11580	11410
	37190	39761	20750		37622	41095	21582
110 K							
2.47	0	9872	82				
	943	11944	2636				
	5147	10490	8143				
	18757	12162	11992				
	37500	40563	21161				

datapoints. This yields the Kramers-Kronig consistent dielectric function which reproduces all the fine details of the infrared reflectivity spectra while simultaneously fitting to the measured complex dielectric function at high frequencies. In contrast to the "conventional" KK reflectivity transformation this procedure anchors the phase of the complex reflectivity to the one at high energies measured directly with ellipsometry[40].

In Fig. 3.17 we show the optical conductivity at selected temperatures. The spectral and temperature dependence of $\sigma_1(\omega)$ of Bi2223 is very similar to the one of Bi2212[41, 19], although the conductivity of Bi2223 is slightly larger, likely due to a higher volume density of the $\mathrm{CuO_2}$ planes in the tri-layer compound. The strongest changes as a function of temperature occur at low frequencies. In the normal state the dominant trend is the narrowing of the Drude peak. The onset of superconductivity is marked by the opening of the superconducting gap which suppresses $\sigma_1(\omega)$ below about 120-140 meV, slightly higher than in Bi2212. Such a large scale is apparently caused by a large gap value in Bi2223, which amounts up to 60 meV, as shown by tunnelling measurements [42].

The much smaller absolute conductivity changes at higher energies, which are not

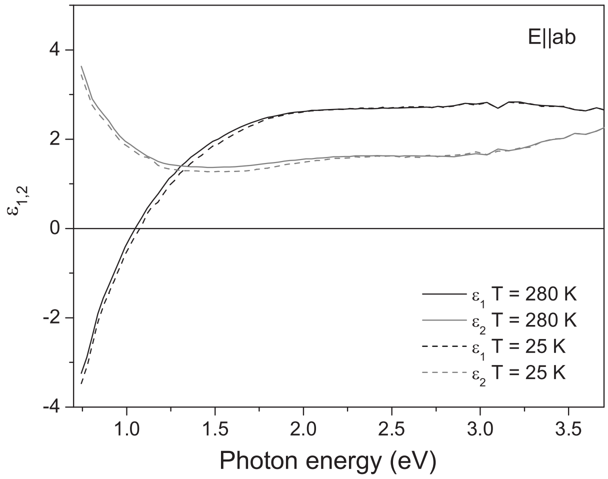

Figure 3.16: Bi2223 ab-plane dielectric function at selected temperature.

discernible at this scale, can be better seen in Fig. 3.18 where we show the temperature dependent optical constants taken at selected photon energies. The change induced by superconductivity in the optical constant is clearly visible as a kink at T_c for energies up to at least 2 eV, which tells that the energy range where the redistribution of spectral weight takes place is very large.

3.4.2 Determination of the c-axis dielectric function

In order to properly convert the pseudodielectric function measured ellipsometrically on the ab-crystal surface to the true dielectric function along the ab-plane, we additionally measured the c-axis dielectric function using another crystal of Bi2223 grown under the same conditions.

We did spectroscopic ellipsometry from 6000 and 36000 cm^{-1} on an ac surface of dimensions ($a \times c$) 3×0.8 mm^2 which we cut and polished with a diamond paper of 0.1 μm grain size. The surface image is shown in Fig. 3.19. Two orthogonal orientations of the sample were used, designated as (ac) and (ca), as shown in Fig.3.19 which provided four ellipsometric parameters $\psi_{ac}, \Delta_{ac}, \psi_{ca}, \Delta_{ca}$ at each frequency. Assuming that $\epsilon_a \approx \epsilon_b$ we inverted four corresponding expressions based on the Fresnel equations in order to obtain four unknown variables ϵ_1^{ab}, ϵ_2^{ab}, ϵ_1^c ϵ_2^c. We applied this procedure for three angles of incidence 65°, 70° and 75° simultaneously in order to improve the accuracy of the inversion. We also measured the normal incidence reflectivity between 450 and 8000 cm^{-1} on the same crystal plane for the electric field parallel to the c-axis. This measurement agrees well with the ellipsometrically determined $\epsilon_c(\omega)$, which confirms the validity of the described inversion procedure. Finally, the reflectivity and ellipsometry output were all fitted simultaneously with a variational KK consistent function [39] in order to extend the frequency dependence

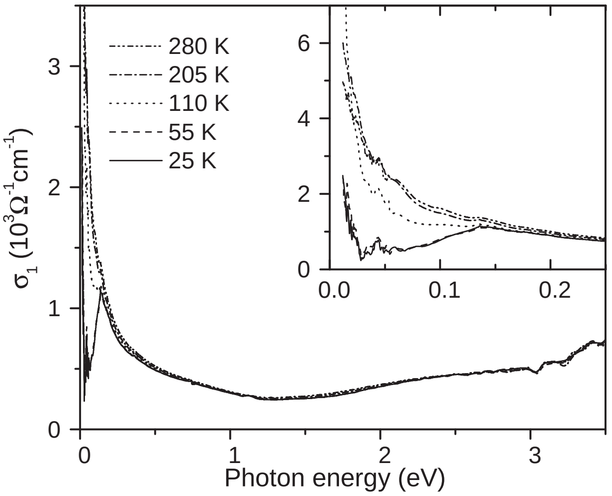

Figure 3.17: In-plane optical conductivity of Bi2223 at selected temperatures. The inset displays the low energy part of the spectrum.

of $\epsilon_c(\omega)$ down to 450 cm^{-1} while anchoring the unknown phase of the reflectivity by the ellipsometric data.

The c-axis reflectivity $R_c(\omega)$, optical conductivity $\sigma_{1c}(\omega)$ and the real part of the dielectric function $\epsilon_{1c}(\omega)$ are displayed in Fig. 3.20. We observe a weak wavelength dependence for $\epsilon_{1c}(\omega)$, which is in a good agreement with with a previous report by Petit *et al* [43]. However, we found a rather different $\sigma_{1c}(\omega)$ which is likely due to the fact in that in Ref.[43] the reflectivity was measured on a textured polycrystalline sample of Bi2223 and the conductivity was obtained by a conventional Kramers-Kronig transform. As it was pointed in Ref.[43], the misalignment of the grains of the oriented ceramic can have a considerable impact on the final result. The main advance compared to these earlier results is that our samples were single crystals, and we determined the real and imaginary part of the dielectric tensor in a direct way using ellipsometry, without the need of a Kramers-Kronig transformation.

3.4.3 The sensitivity of the in-plane dielectric function to the c-axis correction

The pseudodielectric function measured on the ab oriented crystal surface depends on both components of the dielectric tensor and the angle of incidence θ: $\epsilon_{pseudo} = f(\epsilon_{ab}, \epsilon_c, \theta)$. It was shown by Aspnes[44] that in this case the pseudodielectric function should be much more sensitive to the ab-plane component, which lies along the crossing line of the plane of incidence and the sample surface, than to the c-axis one. In order to verify that this is the case, we show in Fig. 3.21 the "sensitivity functions" $\partial\epsilon_{pseudo}/\partial\epsilon_{ab}$ and $\equiv \partial\epsilon_{pseudo}/\partial\epsilon_c$ calculated for the actual angle

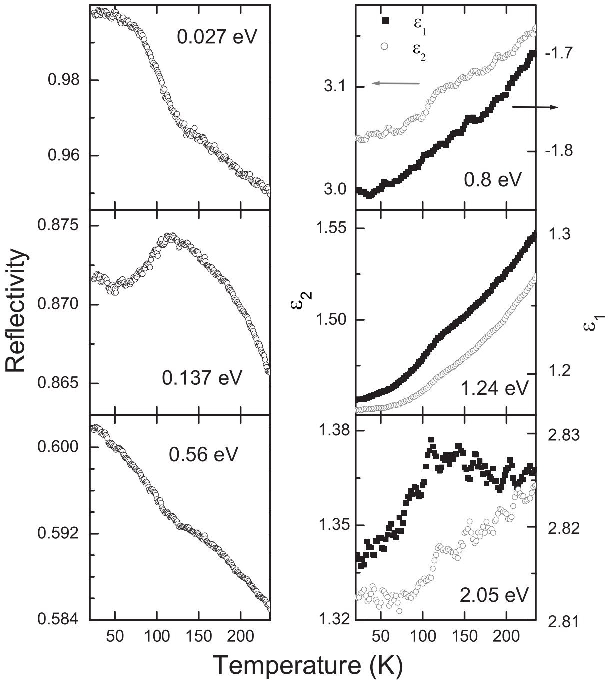

Figure 3.18: Optical constants of Bi2223 at selected photon energies as a function of temperature. Left panel: normal incidence reflectivity at 0.027, 0.14 and 0.56 eV. Right panel: real and imaginary parts of the complex dielectric function at 0.8 1.24 2.05 eV. The photon energies are chosen close to the borders and in the middle of the experimental range.

of incidence (in our case 74°) on the base of described above ac-plane ellipsometry results.

One can see that the pseudodielectric function is indeed much less sensitive to the c-axis component since $\partial\epsilon_{pseudo}/\partial\epsilon_c$ is about 4-5 times smaller than $\partial\epsilon_{pseudo}/\partial\epsilon_{ab}$. For this reason, the temperature dependence of the c-axis dielectric function is expected to have only a minor effect on that of the measured pseudodielectric function. In order to verify this, we performed the c-axis correction of the ab-plane pseudodielectric function and calculated the spectral weight integral $W(\Omega_c = 1eV)$ using in the first case the temperature dependent c-axis dielectric function and in the second case a constant, temperature-averaged one. The resulting temperature dependence of $W(\Omega_c)$ in the former case is shown in Fig. 3.22, while the one in the latter case is shown in Fig.3.23. One can see that accounting for the temperature dependence of the c-axis dielectric function does not have any significant influence on temperature dependence of $W(\Omega_c)$, except for a stronger scatter of the datapoints as a result of the inevitable noise introduced by extra measurement on a small crystal surface. Therefore we used the temperature averaged c-axis data to correct the ab-plane pseudodielectric function in the main part of this work.

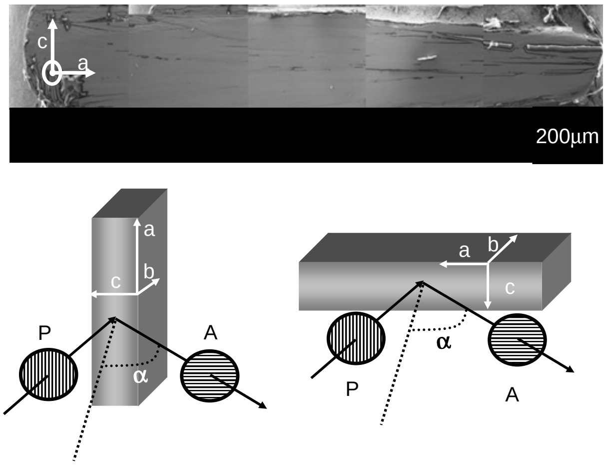

Figure 3.19: Top: the image of the ac plane after polishing. Bottom: two geometries of the ellipsometry experiment.

3.5 The SW transfer in Bi2223

3.5.1 Experimental determination of $W(\Omega_c)$

The extraction of the spectral weight $W(\Omega_c)$ from the measured spectra is a delicate issue. Formally, one has to integrate the optical conductivity over a broad frequency range, including the region below the low-frequency experimental cutoff Ω_{min} (in our case about 100 cm^{-1}) containing the condensate δ-peak (below T_c) at $\omega = 0$ and a narrow quasiparticle peak. According to a frequently occurring misconception the existence of such a cutoff inhibits the calculation of this integral. Indeed if only the real part of the optical conductivity in some finite frequency interval was available, clearly an essential piece of information needed to calculate $W(\Omega_c)$ would be missing, namely $\sigma_1(\omega)$ below Ω_{min}. However, due to the fact that the real and imaginary part of the dielectric constant are related non-locally via the Kramers-Kronig transformation, any change in one of them will affect the other in a broad region of the spectrum. In particular, any change of $\sigma_1(\omega)$ below Ω_{min} must influence $\epsilon_1(\omega)$ at higher frequencies. Since the latter is measured independently (directly by the ellipsometry above 0.75 eV cm^{-1} and indirectly via the reflectivity in the infrared), it puts constraints on the possible values of $\sigma_1(\omega)$ below Ω_{min} and $W(\Omega_c)$. Obviously, these constraints are going to be the more tight the more accurately the optical constants are determined in the accessible interval.

According to the KK relation

$$\epsilon_1(\omega) = 1 + 8\wp \int_0^\infty \frac{\sigma_1(\omega')d\omega'}{\omega'^2 - \omega^2} \tag{3.17}$$

the leading contribution of $\sigma_1(\omega)$ below Ω_{min} to $\epsilon_1(\omega)$ above Ω_{min} is proportional

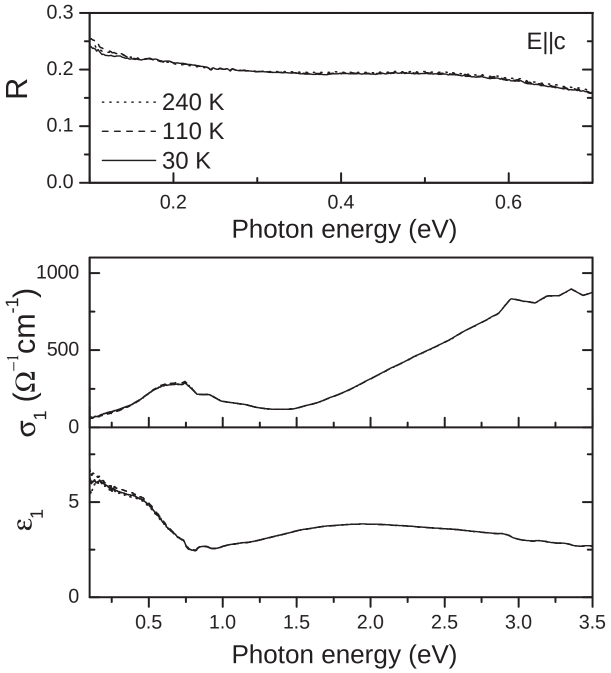

Figure 3.20: c-axis optical spectra of Bi2223 at selected temperatures. Top panel: normal incidence reflectivity, middle panel: $\sigma_1(\omega)$, bottom panel: $\epsilon_1(\omega)$.

to the integral $\int_0^{\Omega_{min}} \sigma_1(\omega)d\omega$ whereas $\epsilon_1(\omega)$ is much less sensitive to the spectral details of $\sigma_1(\omega)$ below Ω_{min}[40, 45]. For example, the contributions of the superfluid condensate and of a narrow quasiparticle peak (provided that its width $\gamma \ll \Omega_{min}$) to ϵ_1 (and thus to the reflectivity) at high frequencies are almost indistinguishable. Therefore the value of the integral of $W(\Omega_c)$ can be model-independently determined from our experimental data, while resolving the details of $\sigma_1(\omega)$ below 100 cm^{-1}, for example the separation of the superfluid density and quasiparticle spectral weight, is not possible. In practice, the realization of the extra bounds on the value of $W(\Omega_c)$ using the additional information contained in the real part of the dielectric function can be done via the aforementioned procedure of variational Kramers-Kronig constrained fitting[39]. Essentially, this is a modeling of the data with a very large number of narrow oscillators, which are added to the model dielectric function until all the fine details of the measured spectra are reproduced. Importantly, the model function always satisfies the KK relations. Once a satisfactory fit of both reflectivity in the infrared region and $\epsilon_1(\omega)$ and $\epsilon_2(\omega)$ above 0.75 eV is obtained, we use the integral of $\sigma_1(\omega)$ generated analytically by this multi-oscillator model as an estimate of the spectral weight. Since the number of oscillators is very large and their parameters are all automatically adjustable, this procedure is essentially model independent. The spectral weight as a function of temperature is shown in Fig. 3.23, for different cut off frequencies.

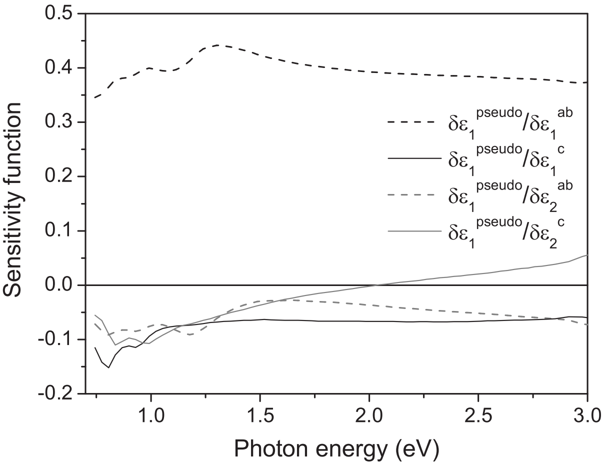

Figure 3.21: Real and imaginary parts of the sensitivity functions $\partial\epsilon_{pseudo}/\partial\epsilon_{ab}$ and $\partial\epsilon_{pseudo}/\partial\epsilon_{c}$ defined in the text.

In order to illustrate that the measured spectra can indeed anchor the value of the low frequency spectral weight without the need of the low-frequency extrapolations of reflectivity (as it would be the case in the conventional KK transform of reflectivity), we performed the following numerical test. In the superconducting state, the model contains a narrow oscillator centered at zero frequency which accounts for the spectral weight of the condensate and a narrow quasiparticle peak. We artificially displaced this oscillator from the origin to a finite frequency, yet below Ω_{min}. The least mean square routine then readjusted all the other parameters in order to produce a new best fit. After that the overall fitting quality (the mean-squared error χ^2) and the low frequency spectral weight remained almost unchanged with respect to the initial values, which is indicated by the errorbar in Fig. 3.24, while the reflectivity below 100 cm^{-1} now shows a very different behavior, as it is shown in Fig. 3.25. This demonstrates that the details of $\sigma_1(\omega)$ and $R(\omega)$ below 100 cm^{-1} are not essential for the determination of $W(\Omega_c)$. In Fig. 3.26 we show an estimation of the errorbars on the SW for a cut off frequency of 8000 cm^{-1} performed with the program Devin2 described in section 2.4.1. We use a set of data which spans the frequency interval between 100 cm^{-1} and 20000 cm^{-1} with a resolution of 100 cm^{-1}. These data have been been obtained via a combination of normal incidence reflectivity and ellipsometry. In the inset of the figure one can see a portion of the spectrum with the estimated error-bars. In the main figure weshow the SW(Ω_c=8000 cm^{-1}) as a function of the frequency interval provided to the program. In the topmost panel one can see the SW as a function of the lowest frequency data-point given to the program. It is clear from this graph that as one provides to Devin2 a data-set in which the lowest frequency point is above the frequency cut off of the integral, the error-bars immediately explode, as expected from the previous examples with generated data. Similarly, in the bottom panels, when the highest frequency point is

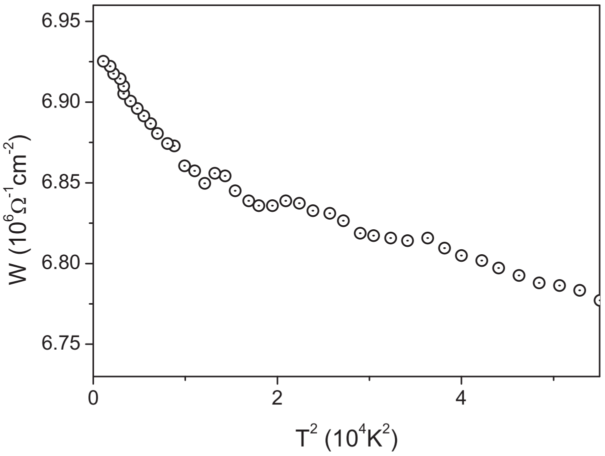

Figure 3.22: Spectral weight as a function of temperature (for the cutoff of 1 eV) obtained when a temperature dependent c-axis data were used to correct the ab-plane pseudodielectric function for the admixture of the c-axis component. The temperature resolution in this plot is lower than in Fig.3.23 because the c-axis temperature dependent data have a resolution of 5 K.

below the frequency cut off, the error-bars tend to diverge. It is important to notice that, a bit surprisingly, the most severe impact on the error-bars does not come from the lowest frequency limit of the data-set, where the conductivity is the highest in a metallic sample. In fact one can see in the figure that estimating the integral to a cut off frequency which is above the measured data-range gives much larger error-bars. This strengthen the idea described above, that any Kramers-Kronig consistent multioscillator model that fits the entire data-set, can give very different low frequency extrapolations below the lowest measured data-point without large changes of the SW. The analysis we provide in this section confirms and gives a quantitative clue to this observation. The reason is that while the value of the integral of σ_1 is anchored by the knowledge of both σ_1 and σ_2 because of the Kramers-Kronig relation, the details of the integrand function outside the measured interval are not.

3.5.2 Superfluid density

Even though the described above procedure does not involve a separate determination of the condensate spectral weight, it is nevertheless interesting to estimate the superfluid density and the penetration depth of Bi2223 as compared to other cuprate. This is approximately given by the spectral weight of the δ-peak in the Drude-Lorentz model (see Table 3.1). The condensate plasma frequency ω_{ps} is about 10300 cm^{-1} ($\sim$ 1.3 eV), which corresponds to the penetration depth $\lambda \approx$ 0.15-0.16 μm. For comparison, the same procedure applied to our previous data on Bi2212 [19] gives ω_{ps}=9500 cm^{-1} and $\lambda \approx$ 0.17 μm. The stronger superfluid component of

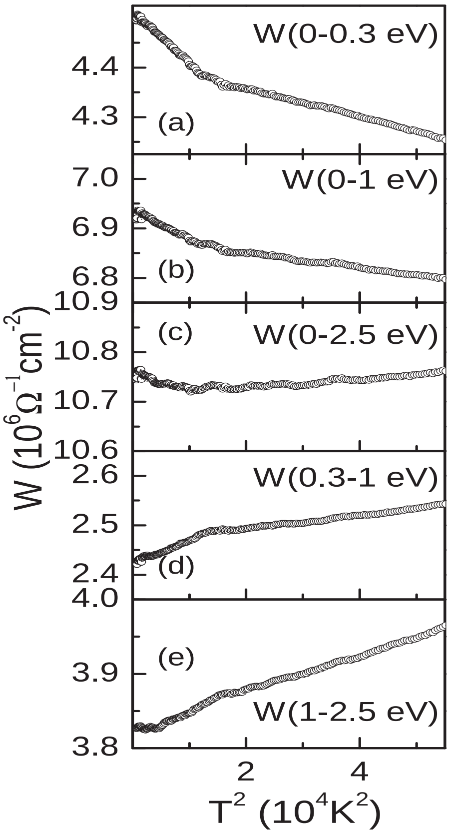

Figure 3.23: Integrated spectral weight as a function of temperature (plotted vs. T^2 for the reasons described in the text. The results corresponding to different ranges of integration are shown: (a) from 0 to 0.3 eV, (b) from 0 to 1 eV, (c) from 0 to 2.5, (d) from 0.3 to 1 (e) from 1 to 2.5 eV.

Bi2223 as compared to Bi2212 correlates with a slightly higher plasma frequency of the former. One should note that in Ref.[41] a smaller value ω_{ps}=9250 (8890) cm^{-1} was found along the a (b)-axis.

Another way to extract the superfluid density is to plot the value of $(\pi/2)\sigma_2(\omega)\omega$ plotted as a function of frequency (Fig.3.27). The zero energy extrapolation of this value represents the spectral weight of the condensate. This value is about $2.7 \pm 0.2 \cdot 10^6$ Ω^{-1}cm^{-2}. After multiplying with the usual factor $120/\pi$ to make the conversion to plasma-frequency squared, we obtain $\omega_{ps}/2\pi c = 1030 \pm 40$ cm$-^1$, in good agreement with the value extracted from the Drude-Lorentz fitting. Importantly, the reactive response of the low-lying quasiparticle peak cannot be separated from the condensate using only optical data down to a few meV.

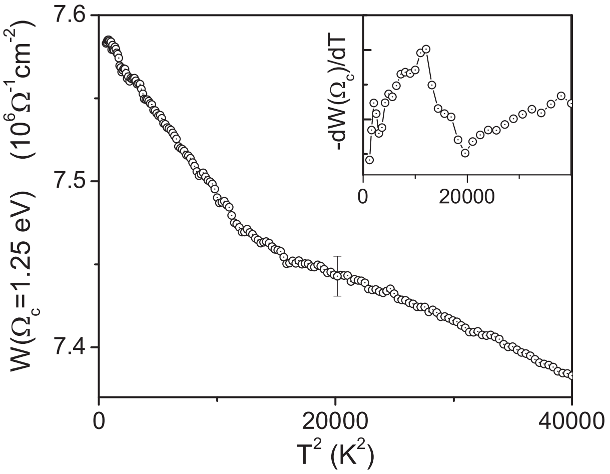

Figure 3.24: Spectral weight $W(\Omega_c, T)$ at cut of frequency of 1.25 eV plotted as a function of T^2. The errorbar is the maximum spread of the values of $W(\Omega_c, T)$, obtained using three different low energy extrapolations shown in the panels of Fig.3.25.

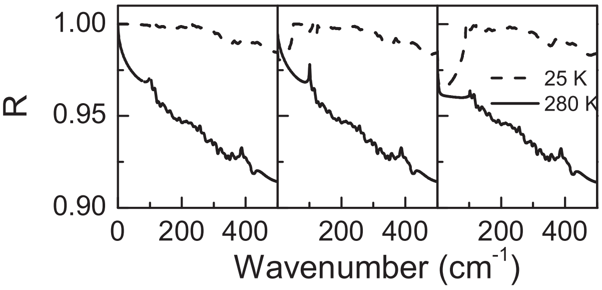

Figure 3.25: Illustration of the numerical test described in the text: reflectivity curves down to zero frequency for different positions of the low energy peak, from left to right 0, 60 and 90 cm^{-1}.

3.5.3 Temperature dependent redistribution of spectral weight

It is important to establish the relevant cutoff energy in the spectral weight integral. The optical conductivity of Bi2223 (see Fig.3.17) as well as the one of Bi2212[41, 19] shows a minimum around 1 eV separating the Drude peak from the lowest-energy interband transition, which is believed to be a charge transfer excitation. It is interesting that such a separation is even more pronounced if wewe plot the difference between conductivity spectra at T_c and a high temperature: $\sigma_1(\omega, 110K) - \sigma_1(\omega, 280K)$ (see upper panel of Fig. 3.28). A sharp upturn below 20 meV, a dip at around 50 meV and a slow approaching of this difference to zero (while being negative) as the energy increases can be attributed to the narrowing of the Drude peak [45]. How-

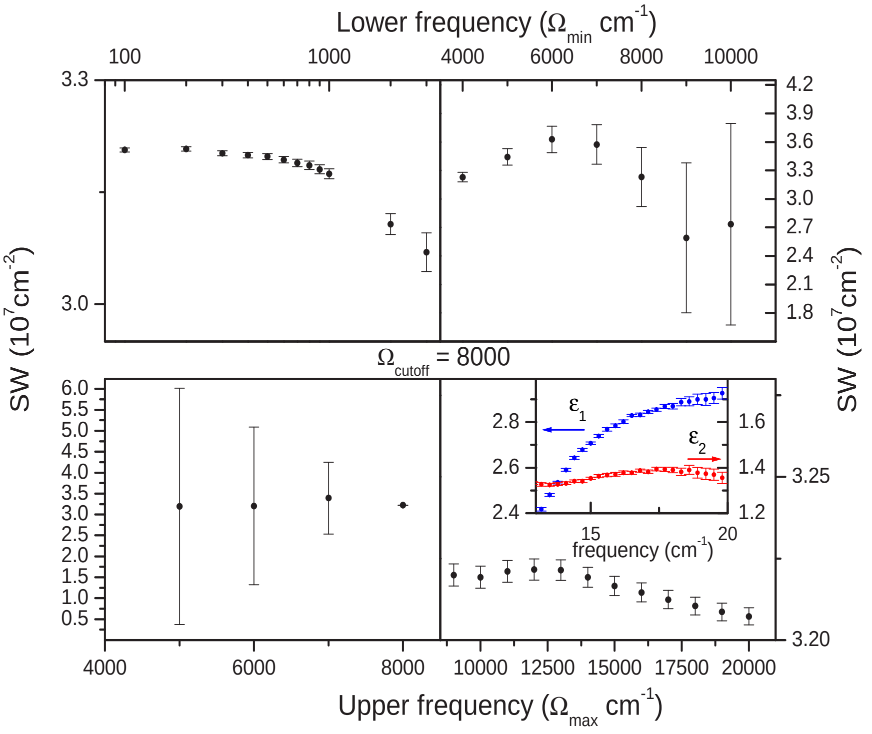

Figure 3.26: Devin2 test on Bi2223: In the top panels we display the value of the integral $\int_0^{8000}\sigma_1(\omega)d\omega$ as a function of Ω_{min}, where Ω_{min} is the lowest measured data-point, while Ω_{max} is kept constant. One can see that when the lowest measured data-point is above the cut-off of the integral the errorbar explodes. The same test is performed varying the highest measured frequency, in the bottom panel. The inset shows the actual data with their error-bar.

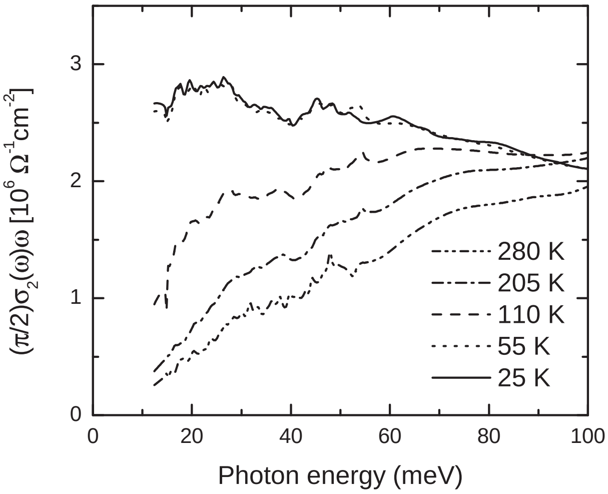

Figure 3.27: The value of $(\pi/2)\sigma_2(\omega)\omega$ plotted vs. frequency. The zero energy extrapolation of this value represents the joint spectral weight of the condensate and the low-lying quasiparticle peak.

ever, above the same characteristic energy of about 1 eV this monotonic trend totally disappears. Instead, $\sigma_1(\omega, 110K) - \sigma_1(\omega, 280K)$ shows a dip at 1.5-2 eV, which corresponds to the removal of spectral weight from this region, as the system is cooled down. The difference $\sigma_1(\omega, 25K) - \sigma_1(\omega, 110K)$ between the two spectra in the superconducting state also shows that the effect of the narrowing of the Drude peak does not noticeably extend above 1 eV (Fig. 3.28). We can learn more from the corresponding differences of the integrated spectral weight $W(\omega, 110K) - W(\omega, 280K)$ and $W(\omega, 25K) - W(\omega, 110K)$ which are displayed in the lower panel of Fig. 3.28. In order to separate the effect of the superconducting transition from the temperature dependence already present in the normal state, we additionally plot the 'normal-state corrected' spectral weight difference of the superconducting state relative to the normal state $W_{SC} - W_N$ calculated according to the procedure described in Section 3.5.4. Not surprisingly, all curves show an intense spectral structure below ~ 0.3 eV as a result of strong changes of the shape of the Drude peak with temperature. However between 0.3-0.5 and 1.0-1.5 eV the spectral variation is weak and, importantly, both normal- and superconducting-state differences remain positive in this 'plateau' region. This indicates an increase of the intraband spectral weight as the sample is cooled down and an extra increase in the superconducting state. Above 1.5-2 eV, the normal-state difference $W(\omega, 110K) - W(\omega, 280K)$ decreases rapidly and becomes negative, which suggests that spectral weight is transferred between the charge-transfer and the intraband regions. In contrast, the superconducting state differences (both normal-state corrected and not) continue decreasing slowly and remain positive up to at least 2.5 eV, which means that the Ferrell-Glover-Tinkham sum rule is not yet recovered at this energy.

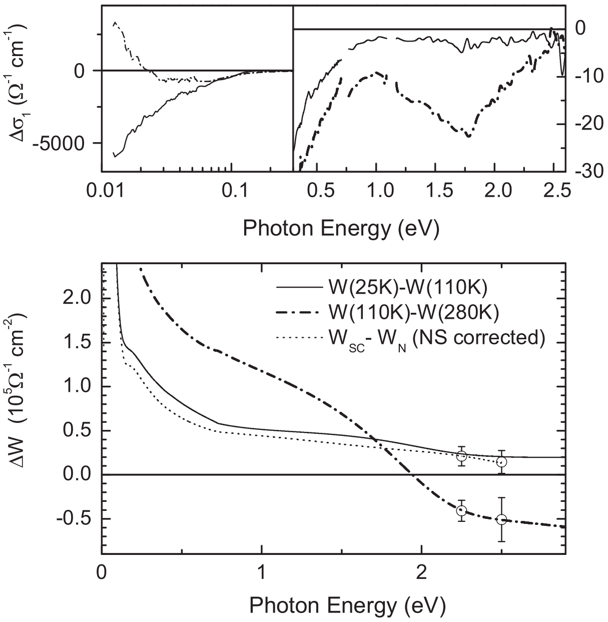

Figure 3.28: Difference spectra of the in-plane optical conductivity and of the integrated spectral weight. Top panel: $\sigma_1(\omega, 25K)$-$\sigma_1(\omega, 110K)$ (solid line) and $\sigma_1(\omega, 110K)$-$\sigma_1(\omega, 280K)$ (dashed-dotted line). Bottom panel: $W(\omega, 25K)$-$W(\omega, 110K)$ (solid line), $W(\omega, 110K)$-$W(\omega, 280K)$(dashed-dotted line) and $W_{SC} - W_N$, corrected for the normal state temperature dependence as descibed in the text (dotted line).

Another way to visualize the spectral weight transfer is to plot $W(\Omega_c)$ as a function of temperature for different cutoff energies. In Fig. 3.23(a-c) we present such curves for $\Omega_c = 0.3$, 1 and 2.5 eV.

One can immediately notice that the curves $W(0.3eV, T)$ and $W(1eV, T)$, apart from different absolute values, have almost identical temperature dependencies; accordingly, the integrated spectral weight between 0.3 and 1 eV (Fig. 3.23d) shows a very little variation with temperature. This is, of course, a manifestation of the existence of the discussed above 'plateau' region in the frequency dependent spectral weight differences (Fig. 3.28). This observation is in line with the theoretical findings of Wrobel *et al*[14] who pointed out that spectral weight integrated to the hopping parameter $t \sim$ 0.3-0.4 eV is representative of the kinetic energy of the t-J model.

Above T_c, the spectral weight $W(T)$ for the cutoff of 1 eV increases gradually with cooling down in a virtually T^2 fashion, which is most clearly seen when $W(\Omega_c)$ is plotted versus T^2 (Fig. 3.23a,b). A similar normal state behavior was observed in optimally and underdoped Bi2212[19] and in La_2CuO_4[46]. Although a T^2 term follows trivially from the Sommerfeld expansion for the temperature broadening of the Fermi-Dirac distribution, the absolute value of this term turns out to be several times larger than what one expects from this expansion[30, 47]. The DMFT calculations within the Hubbard model [47] showed that this may be caused by strong correlation effects. On the other hand, it was recently pointed out[48, 49] that the temperature dependence of the one-electron spectral function due to inelastic electron-boson scattering contributes to the overall temperature dependence of the optical sum rule much stronger than the Sommerfeld term. The extra contribution though is predominantly T-linear if the boson energy is small[49].

At the superconducting transition the curve $W(T)$ shows a sharp *upward* kink (slope change) close to $T_c = 110$ K. The same effect was observed in optimally and underdoped Bi2212 [19]. In order to directly compare these data to the results of Ref. [19], we plot in Fig. 3.24 the $W(\Omega_c, T)$ for Ω=1.25 eV together with the temperature derivative. One should stress that the corresponding kinks are already observed on the temperature dependence of directly measured optical constants (see Fig.3.18). By extrapolating the normal state trend to T = 0 K, we can estimate the size of the superconductivity induced spectral weight transfer in the intraband region: $\Delta W \approx 0.8 \times 10^5\ \Omega^{-1}\text{cm}^{-2}$, which is about 1% of the total intraband spectral weight (as shown by Fig.3.23).

Remarkably, the upward kink of $W(\Omega_c, T)$ at T_c is still observed for the cutoff of 2.5 eV (Fig. 3.23c) suggesting that superconductivity induced spectral weight transfer involves energies above the charge transfer gap, as we could already see from Fig. 3.28. In the context of the Hubbard model, the integrated spectral weight corresponds to the kinetic energy of the Hubbard hamiltonian [14] when the cut off frequency is set much higher than the U. One would be tempted conclude from the superconductivity-induced increase of W(2.5eV) that also the total kinetic energy of the Hubbard model is lowered below T_c, as observed in the cluster DMFT calculations [50]. Westress, however, that in order to make a definitive statement about the kinetic energy in the Hubbard model one should extend the cutoff frequency much higher than 2.5 eV. Unfortunately, the noise level at higher energies precludes the observation of the small superconductivity-induced effects. Another problem is that this range overlaps with strong absorption range due to charge transfer from oxygen to copper and that those transitions may have temperature dependencies for a variety of reasons which are not related to the kinetic energy lowering of the charge carriers.

3.5.4 Temperature modulation analysis at T_c

The existence of relatively sharp kinks (slope discontinuities) at T_c on the curves of the temperature dependence of various optical functions (see Fig.3.18) enables an alternative way to quantify the superconductivity-induced spectral weight changes which gives perhaps a better feeling of the error bars involved [51]. We recently applied this procedure, which is essentially a temperature-modulation method, to a similar set of data on optimally doped Bi2212 [45].

In order to separate the superconductivity-induced effect from the large temperature dependence in the normal state not related to the onset of superconductivity we apply the 'slope-difference operator' Δ_s defined as [51]:

$$\Delta_s f(\omega) \equiv \left.\frac{\partial f(\omega,T)}{\partial T}\right|_{T_c+\delta} - \left.\frac{\partial f(\omega,T)}{\partial T}\right|_{T_c-\delta}, \tag{3.18}$$

where f stands for any temperature dependent function. In Fig.3.29 the slope-difference spectra $\Delta_s R(\omega)$, $\Delta_s \epsilon_1(\omega)$ and $\Delta_s \sigma_1(\omega)$ are displayed with the error bars, which we determined from the temperature dependent curves such as shown in Fig.3.18, using a numerical procedure, described in Ref.[45]. Since Δ_s is a linear operator, the KK relation between ϵ_1 and ϵ_2 holds also for the slope-difference spectra $\Delta_s \epsilon_1(\omega)$ and $\Delta_s \epsilon_2(\omega)$. Thus we can fit the latter spectra with a multi-oscillator Drude-Lorentz model, which automatically satisfies the KK relations. If the number of oscillators is large enough, the procedure becomes essentially model-independent. Using the same dielectric function we can additionally calculate the slope-difference spectrum of reflectivity as it is related to $\Delta_s \epsilon_1(\omega)$ and $\Delta_s \epsilon_2(\omega)$:

$$\Delta_s R(\omega) = \frac{\partial R}{\partial \epsilon_1}(\omega, T_c)\Delta_s \epsilon_1(\omega) + \frac{\partial R}{\partial \epsilon_2}(\omega, T_c)\Delta_s \epsilon_2(\omega). \tag{3.19}$$

The functions $\frac{\partial R}{\partial \epsilon_1}(\omega, T_c)$ and $\frac{\partial R}{\partial \epsilon_2}(\omega, T_c)$ can be derived from the analysis of optical spectra at T_c[45].

The best fit of the slope-difference optical constants for Bi2223 is shown by the solid curves in Fig.3.29. From this we also calculate the slope-difference integrated spectral weight $\Delta_s W(\omega) = \int_0^{\omega} \Delta_s \sigma_1(\omega')d\omega'$ as shown in Fig.3.29(a). At $\Omega_c = 1$ eV we obtain the value of $\Delta_s W \approx +1100\ \Omega^{-1}\text{cm}^{-2}\text{K}^{-1}$ which corresponds to the superconductivity-induced increase of spectral weight, in agreement with the previous analysis.

To check that the value of $\Delta_s W$ is well defined by the present set of experimental spectra we repeated the fitting routine while forcing $\Delta_s W(\Omega_c = 1eV)$ to be equal to some imposed value $\Delta_s W(\Omega_c)_{imposed}$. We did this for different values of $\Delta_s W(\Omega_c)_{imposed}$ and monitored the quality of the fit, as expressed by the mean-squared error χ^2. In Fig. 3.30 we plot χ^2 as a function of $\Delta_s W(\Omega_c)_{imposed}$. The best fit quality is, of course, achieved for the mentioned value $\Delta_S W(\Omega_c)_{imposed} \approx 1100$ $\Omega^{-1}\text{cm}^{-2}\text{K}^{-1}$. It is evident that the fit quality deteriorates rapidly as $\Delta_S W(\Omega_c)_{imposed}$ is dragged away from this value. For example, the value of χ^2 for the case $\Delta_S W(\Omega)_{imposed} = 0$ (which would be the full recovery of the sum rule at 1 eV) is about 10 times larger than the optimal value; the corresponding data fit should be regarded as unacceptable. As it was discussed in Ref.[45] and in this section, this is due to the fact that any change of the low-frequency spectral weight inevitably affects the value of $\epsilon_1(\omega)$ and $R(\omega)$ at higher frequencies.

To compare the approach described in this Section and the one from previous Section, we derive from the curve $W(T)$, plotted in Fig. 3.23 $\Delta_s W(\Omega_c{=}1\text{ eV})\approx 1500$ $\Omega^{-1}\text{cm}^{-2}\text{K}^{-1}$. This is not far from the aforementioned value of 1100 $\Omega^{-1}\text{cm}^{-2}\text{K}^{-1}$ which quantitatively confirms the central assertion of this section, namely that the low frequency spectral weight increases below T_c.

As it was discussed in Ref.[45], the 'normal-state corrected' spectral weight difference of the superconducting state relative to the normal state, $W_{SC}-W_N$ can be estimated from the slope-difference conductivity spectra:

$$W_{SC}-W_N \approx \alpha T_c \Delta_s W, \tag{3.20}$$

where α is a dimensionless coefficient. The choice of α is suggested by the temperature dependence of $W(\Omega_c)$[45]. Since we observe in both normal and superconducting state a temperature dependence close to T^2 then we choose $\alpha = 1/2$. The corresponding curve $W_{SC}-W_N$ is shown as a dotted line in Fig.3.28. One can see that it is slightly smaller than the direct difference $W(\omega, 25K) - W(\omega, T = 110K)$. The latter fact is not surprising since the spectral weight in the normal state is increasing as a function of temperature.

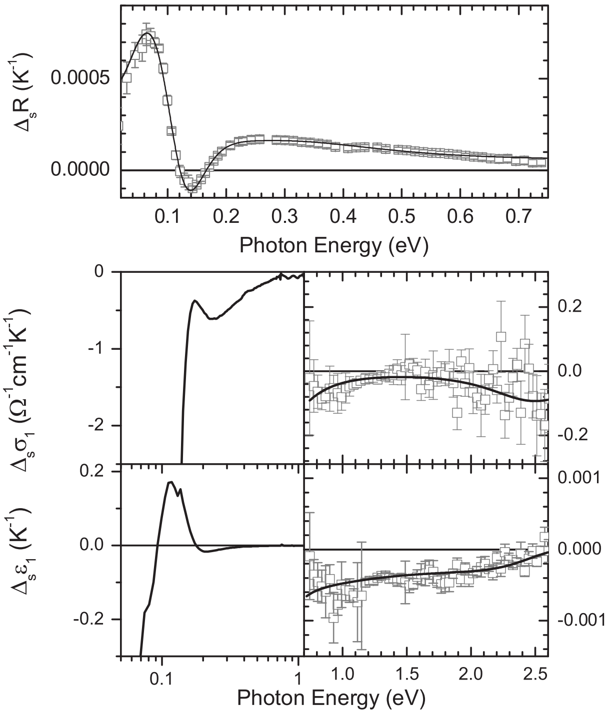

Figure 3.29: Slope-differential spectra of the complex dielectric function, obtained experimentally (open symbols) together with the multi-oscillator fitting curves (solid lines) as described in the text.

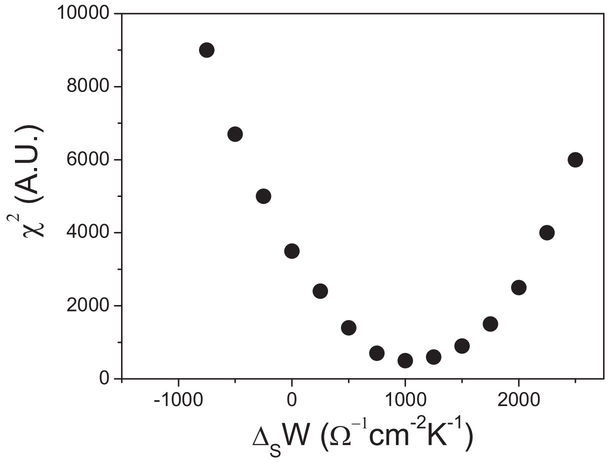

Figure 3.30: The demonstration that $\Delta_s W(\Omega_c)$ is well defined by the available data (Ω_c=1 eV). The mean squared error χ^2 for the total fit of $\Delta_s R(\omega)$, $\Delta_s \epsilon_1(\omega)$ and $\Delta_s \sigma_1(\omega)$ (shown in Fig.3.29) as a function of $\Delta_s W(\Omega_c)_{imposed}$. More description is given in the text.

3.6 The doping dependence of the spectral weight transfer in BSCCO

3.6.1 Optical properties of Bi2212 as a function of doping

In this section we concentrate on the properties of single crystals of Bi2212 at 4 different doping levels, characterized by their superconducting transition temperatures. The preparation and characterization of the underdoped sample (UD66K), an optimally doped crystal (OpD88) and an overdoped sample (OD77) with T_c's of 66, 88 K and 77 K respectively, have been given in Ref. [19]. The crystal with the highest doping level (OD67) has a T_c of 67 K. This sample has been prepared with the self-flux method. The oxygen stoichiometry of the single crystal has been obtained in a PARR autoclave by annealing for 4 days in oxygen at 140 atmospheres and slowly cooling from 400 °C to 100 °C. The infrared optical spectra and the spectral weight analysis of samples UD66 and OpD88 have been published in Refs. [19, 45]. The phase of $\sigma(\omega)$ of sample OD77 has been presented as a function of frequency in a previous publication[52]. Here we present the optical conductivity of the samples OD77 and OD67 for a dense sampling of temperatures, and we use this information to calculate $SW(\Omega_c, T)$. The samples are large ($4 \times 4 \times 0.2$ mm^3) single crystals. The crystals were cleaved within minutes before being inserted into the optical cryostat.

The spectra were measured with a combination of visible light ellipsometry and infrared reflectivity, as described together with the procedure to get the optical conductivity, in section 2.4.1.

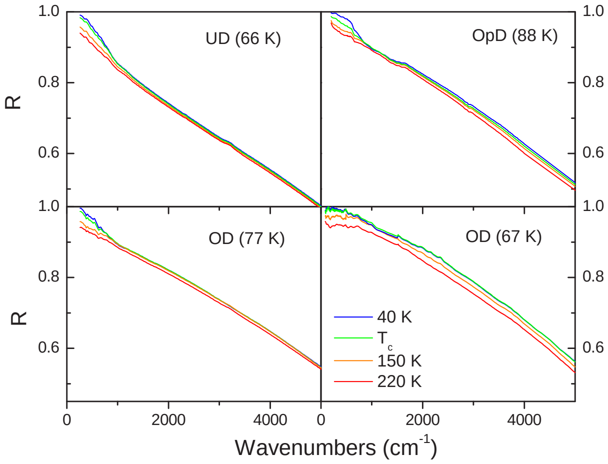

Figure 3.31: Reflectivity spectra of Bi2212 at selected temperatures for different doping levels, described in the text.

The infrared reflectivity is displayed for all the studied doping levels in Fig. 3.31. The absolute reflectivity increases with increasing doping, as expected since the system becomes more metallic. Interestingly, the curvature of the spectrum also changes from under to overdoping; this is reflected in the frequency dependent scattering rate as has been pointed out recently by Wang *et al.* [53].

In Fig. 3.32 we show the optical conductivity of the two overdoped samples of Bi2212 with $T_c = 77$ K and $T_c = 67$ K at selected temperatures. Below 700 cm^{-1} one can clearly see the depletion of the optical conductivity in the region of the gap at low temperatures (shown in the inset). The much smaller absolute conductivity changes at higher energies, which are not discernible at this scale, will be considered in detail below.

One can see the effect of superconductivity on the optical constants in the temperature dependent traces, displayed in Fig. 3.33, at selected energies, for the two overdoped samples. In comparison to the underdoped and optimally doped samples [19, 54] where reflectivity is found to have a further increase in the superconducting state at energies between 0.25 and 0.7 eV, in the overdoped samples the reflectivity decreases below T_c or remains more or less constant. In the strongly overdoped sample one can clearly see, for example at 1.24 eV, that at low temperature ϵ_1 increases while cooling down, opposite to the observation on the optimally and underdoped samples. These details of the temperature dependence of the optical constants influence the integrated SW trend as we will discuss in the following sections.

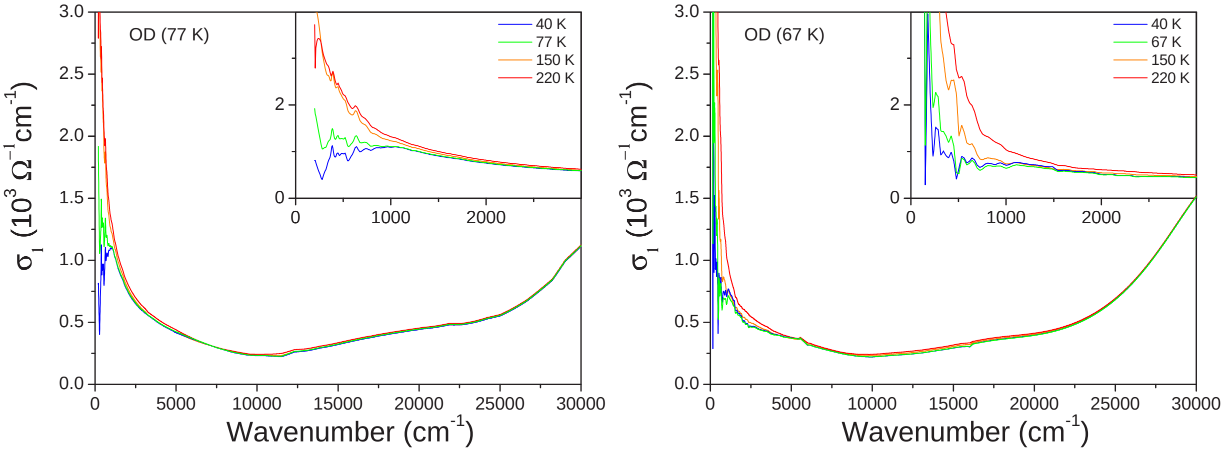

Figure 3.32: In-plane optical conductivity of slightly overdoped (T_c= 77 K, left panel) and strongly overdoped (T_c= 67 K, right panel) samples of Bi2212 at selected temperatures. The insets show the low energy parts of the spectra.

3.6.2 The spectral weight transfer

As we discussed in the previous chapter, using the knowledge of both σ_1 and ϵ_1 we can calculate the low frequency SW without the need of the knowledge of σ_1 below the lowest measured frequency[39, 54, 45]. When the upper frequency cut off of the SW integral is chosen to be lower than the charge transfer energy (around 1.5 eV), the SW is representative of the free carrier kinetic energy in the t-J model [14, 54, 55]. Here we set the frequency cut-off at 1.25 eV and compare the results with the predictions of BCS theory and CDMFT calculations based on the t-J model. In Fig. 3.34 we show a comparison between $SW(T)$ for different samples with different doping levels. One can clearly see that the onset of superconductivity induces a positive change of the SW(0-1.25 eV) in the underdoped sample and in the optimally doped one[19]; in the 77 K sample no superconductivity induced effect is detectable for this frequency cut off and in the strongly overdoped sample we observe a decrease of the low frequency spectral weight. In the righthand panel of Fig. 3.34 we also display the derivative of the integrated SW as a function of temperature. The effect of the superconducting transition is visible in the underdoped sample and in the optimally doped sample as a peak in the derivative plot; no effect is detectable in the overdoped 77 K sample, while in the strongly overdoped sample a change in the derivative of the opposite sign is observed.

The frequency ω_p^* for which $\epsilon_1(\omega_p^*) = 0$ corresponds to the eigenfrequency of the longitudinal oscillations of the free electrons for $k \rightarrow 0$. ω_p^* can be read off directly from the ellipsometric spectra, without any data-processing. The temperature dependence of ω_p^* is displayed in Fig. 3.35. The screened plasma-frequency has a red shift as temperature increases, due to the bound-charge polarizability, and the inter-

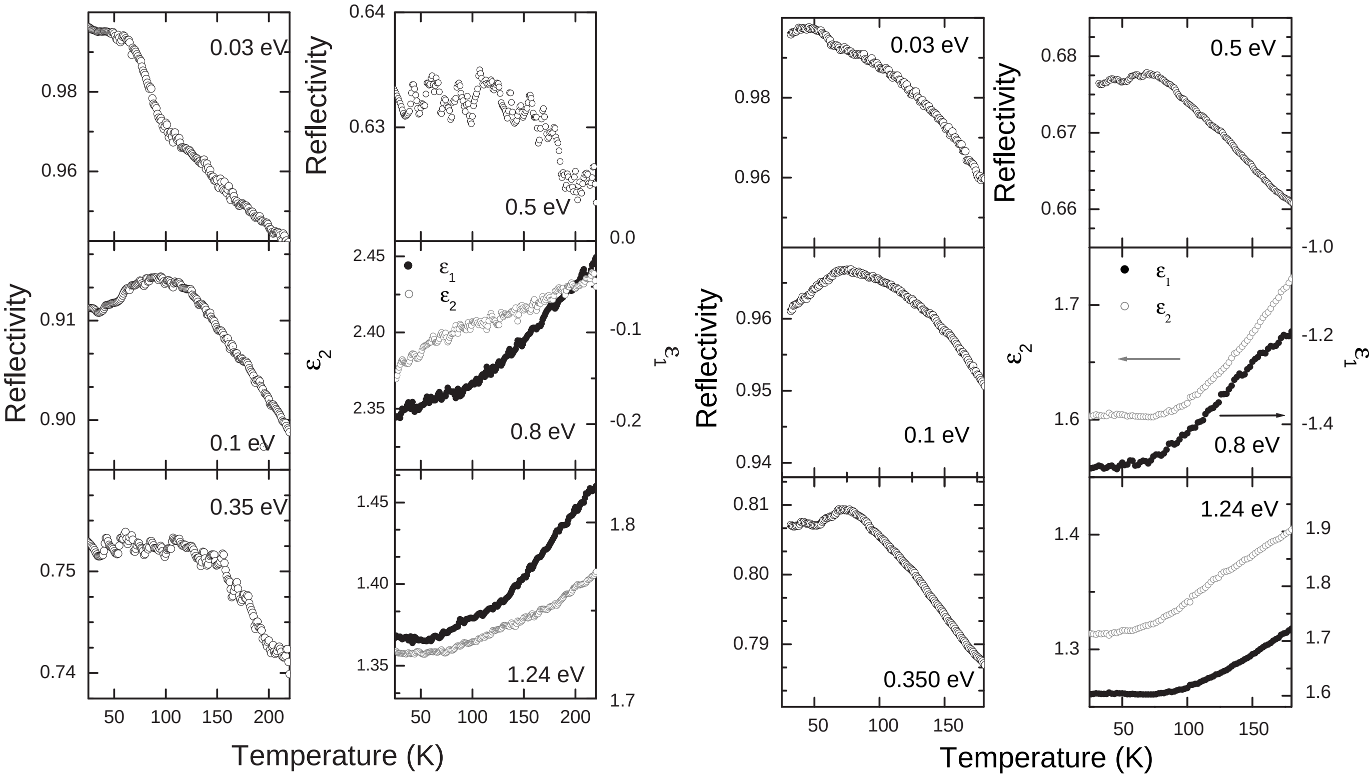

Figure 3.33: Leftmost (rightmost) two columns: reflectivity and dielectric function of sample OD77 (OD67) as a function of temperature for selected photon energies. The corresponding photon energies are indicated in the panels. The real (imaginary) parts of $\epsilon(\omega)$ are indicated as closed (open) symbols.

band transitions. Therefore its temperature dependence can be caused by a change of the free carrier spectral weight, the dissipation, the bound-charge screening, or a combination of those. This quantity can clarify whether a real superconductivity-induced change of the plasma frequency is already visible in the raw experimental data. In view of the fact that the value of ω_p^* is determined by several factors, and not only the low frequency SW, it is clear that the SW still has to be determined from the integral of Eq. 3.5. It is perhaps interesting and encouraging to note, that in all cases which we have studied up to date, the temperature dependences of $SW(T)$ and $\omega_p^*(T)^2$ turned out to be very similar.

One can clearly see in the underdoped and in the optimally doped sample that superconductivity induces a blue shift of the screened plasma frequency. In the 77 K sample no effect is visible at T_c while the 67 K sample shows a red shift of the screened plasma frequency. The behavior of the screened plasma frequency also seems to exclude the possibility that a narrowing or a shift with temperature of the interband transitions around 1.5 eV is responsible for the observed changes in the optical constants. If this would be the case then one would expect the screened

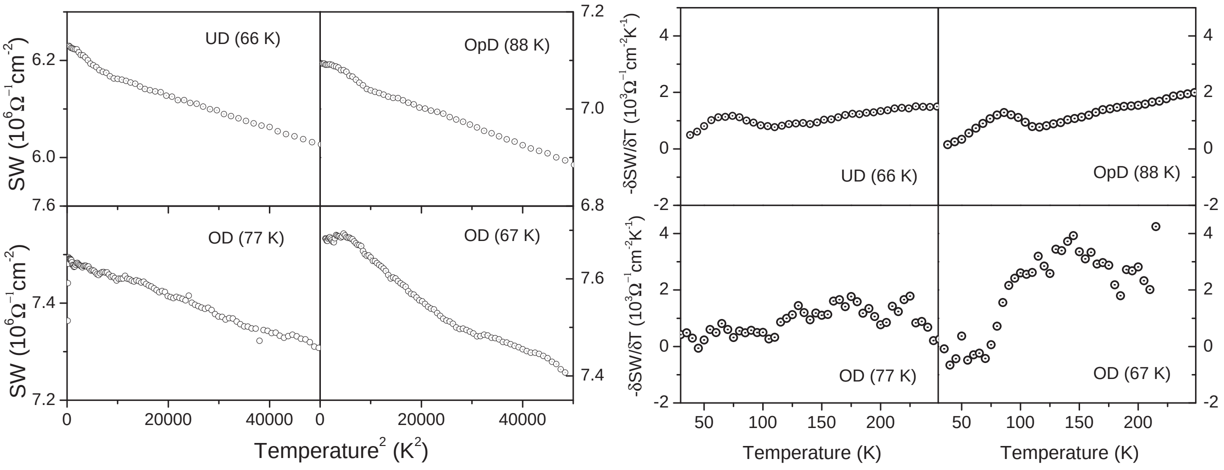

Figure 3.34: Left panel: spectral weight $SW(\Omega_c, T)$ for $\Omega_c = 1.24$ eV, as a function of temperature for different doping levels. Right panel: the derivative $(\frac{-\partial SW(\Omega_c,T)}{\partial T})$ as a function of temperature for different doping levels. For the derivative curves the data have been averaged in 5 K intervals in order to reduce the noise.

plasma frequency to exhibit a superconductivity-induced shift in the same direction for all the samples.

3.6.3 Predictions for the spectral weight using the BCS model

In order to give an interpretation of these data we compare these experiments to the SW calculated within the BCS model using an experimentally determined band structure parametrization. As discussed in section 3.3, the band structure can have a dramatic influence on the SW temperature dependence. In this paragraph we verify that for the samples we measured optically, the relation between SW and kinetic energy holds. Figures 3.12 and 3.13 make clear that, taking the ARPES-determined band structure seriously, then the observed doping dependence of the optical spectral weight change below T_c [56, 54, 37] *cannot* be explained by BCS theory. In this respect the observations may be indicative of physics beyond BCS theory. This remains true even if the hole doping is shifted by a small amount, that is, if the measured samples actually have hole concentrations that are larger than $0.09 < \delta < 0.21$; then the spectral weight anomaly calculated here has almost the opposite doping dependence compared with experiment [37].

On the other hand the band structure is a parametrization, and is reliant on a very surface sensitive probe. As an example of what we consider a remote possibility, Fig. 3.13 indicates that if the doping levels for BSCCO are *not* as indicated, but rather lie in the regime *between* the two van Hove singularities (i.e. approximately between

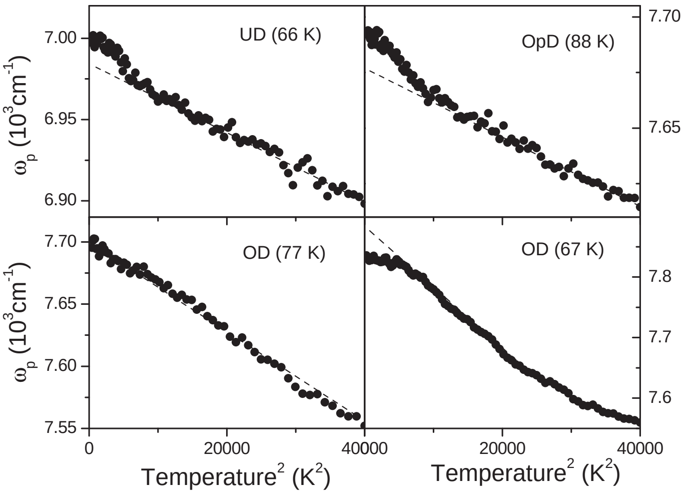

Figure 3.35: Screened plasma frequency as a function of temperature for different doping levels.

$n = 0.5$ and $n = 0.7$), then the results will be very different. Then 'underdoped' would have a positive change below T_c (near $n \approx 0.7$) while 'overdoped' would exhibit a negative change (compatible with experiment, and with expectations based on the negative of the kinetic energy) (near $n \approx 0.6$). The corresponding slope above T_c would, however, be *inconsistent* with experiment (not shown), but the slope is a purely normal state property, and, like all other normal state properties, undoubtedly requires electron correlations for a proper understanding. We view this possibility as remote, however, since many studies have established this band structure and the low doping scenario.

A more reasonable explanation comes from including effects considered in Ref. [29], along with the Kordyuk et al. band structure. The proposal there was to include the effect first observed in microwave measurements [57, 58], that the inelastic scattering rate decreases significantly below T_c. This has the effect of shifting the blue points in Fig. 8, for example, upwards. Thus, the anomaly below T_c would agree with experiment [56, 37], including a crossover from positive change for underdoped samples to a negative change for overdoped samples. Furthermore, the slope above T_c would always be negative, as observed. Finally, the magnitude of the slope would increase as the anomaly becomes more BCS-like, also in agreement with experiment. This was also found in the DMFT calculations [37], and further theoretical work and experiments would be required, however, to disentangle band structure effects from strong correlation effects. For example, the phenomenology of a collapsed scattering rate is generally indicative of an electronic scattering mechanism being responsible for superconductivity, so the DMFT calculations may be reconstructing the same phenomenology; it would be interesting to examine the interplay between strong correlation an band structure effects in these calculations. We should also remark that very early on Norman and Pépin [59] found that using a frequency dependent scattering rate extracted from optical data gave rise to a crossover as a function of doping very similar to what has been observed in experiment. Further work is required to distinguish between these various scenarios.

3.6.4 Superconductivity induced transfer of spectral weight: experiment and cluster DMFT calculations

In order to highlight the effect of varying the doping concentration, we have extrapolated the temperature dependence in the normal state of $SW(\Omega_c, T)$ of each sample to zero temperature, and measured it's departure from the same quantity in the superconducting state, also extrapolated to T=0: $\Delta SW_{sc} \equiv SW(T=0) - SW_n^{ext.}(T=0)$ In Fig. 3.36 the experimentally derived quantities are displayed together with the recent CDMFT calculations of the t-J[55] model and those based on the BCS model explained in the previous subsection. While the BCS-model provides the correct sign only for the strongly overdoped case, the CDMFT calculations based on the t-J model are in qualitative agreement with our data and the data in Ref [25], insofar both the experimental result and the CDMFT calculation give $\Delta SW_{sc} > 0$ on the underdoped side of the phase diagram, and both have a change of sign as a function of doping when the doping level is increased toward the overdoped side. The data and the theory differ in the exact doping level where the sign change occurs. This discrepancy may result from the fact that for the CDMFT calculations the values $t' = t'' = 0$ were adopted. This choice makes the shape of the Fermi surface noticeably different from the experimentally known one, hence the corresponding fine-tuning of the model parameters may improve the agreement with the experimental data. This may also remedy the difference between the calculated doping dependence of T_c and the experimental one (see righthand panel of Fig. 3.37). We also show, in Fig. 3.38, the doping dependence of the plasma frequency and effective mass compared to the CDMFT results. One can see that a reasonable agreement is achieved for both quantities.

3.6.5 Normal state trend of the spectral weight

The persistence of the T^2 temperature dependence up to energies much larger than what usually happens in normal metals has been explained in the context of the Hubbard model [47], showing that electron-electron correlations are most likely responsible for this effect. Indeed, experimentally we observe a strong temperature dependence of the optical constants at energies as high as 2 eV. In most of the temperature range, particularly for the samples with a lower doping level, these temperature dependencies are quadratic. Correspondingly, $SW(T)$ also manifests a quadratic temperature dependence. For sample OD67 the departure from the

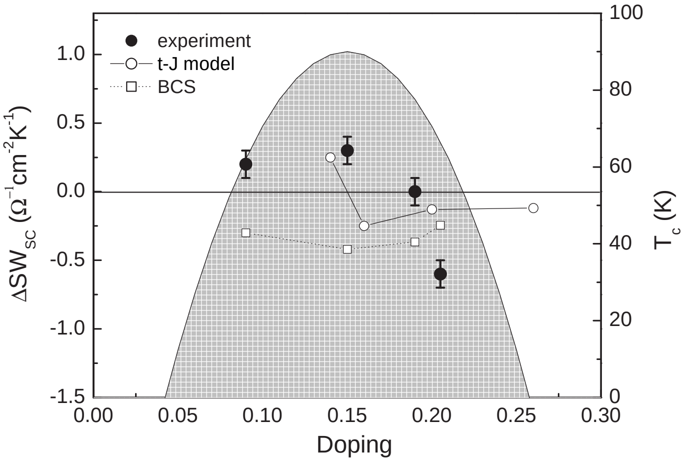

Figure 3.36: Doping dependence of the superconductivity induced SW changes: experiment vs. theory. Two theoretical calculations are presented: d-wave BCS model and CDMFT calculations in the framework of the t-J model.

quadratic behavior is substantial; the overall normal state temperature dependence at this doping is also much stronger than in the other samples.

In Fig. 3.37 the experimental $SW(T)$ is compared to the CDMFT calculations for the same doping concentration. Since the T_c obtained by CDMFT differs from the experimental one, (see Fig. 3.37) it might be more realistic to compare theory and experiment for doping concentrations corresponding to the same relative T_c's. Therefore we also include in the comparison the CDMFT calculation at a higher doping level, at which $T_c/T_{c,max}$ corresponds to the experimental one (see the right panel of Fig. 3.37). We see that the experimental and calculated values of $SW(T)$ are in quantitative agreement for the temperature range where they overlap. It is interesting in this connection that, at high temperature, the curvature in the opposite direction, clearly present in all CDMFT calculations, may actually be present in the experimental data, at least for the highly doped samples. These observations clearly call for an extension of the experimental studies to higher temperature to verify whether a cross-over of the type of temperature dependence of the spectral weight really exists, and to find out the doping dependence of the cross-over temperature. The experimental data, as mentioned before, show a rapid increase of the slope of the temperature dependence above optimal doping. This behavior is qualitatively reproduced by the CDMFT calculations.

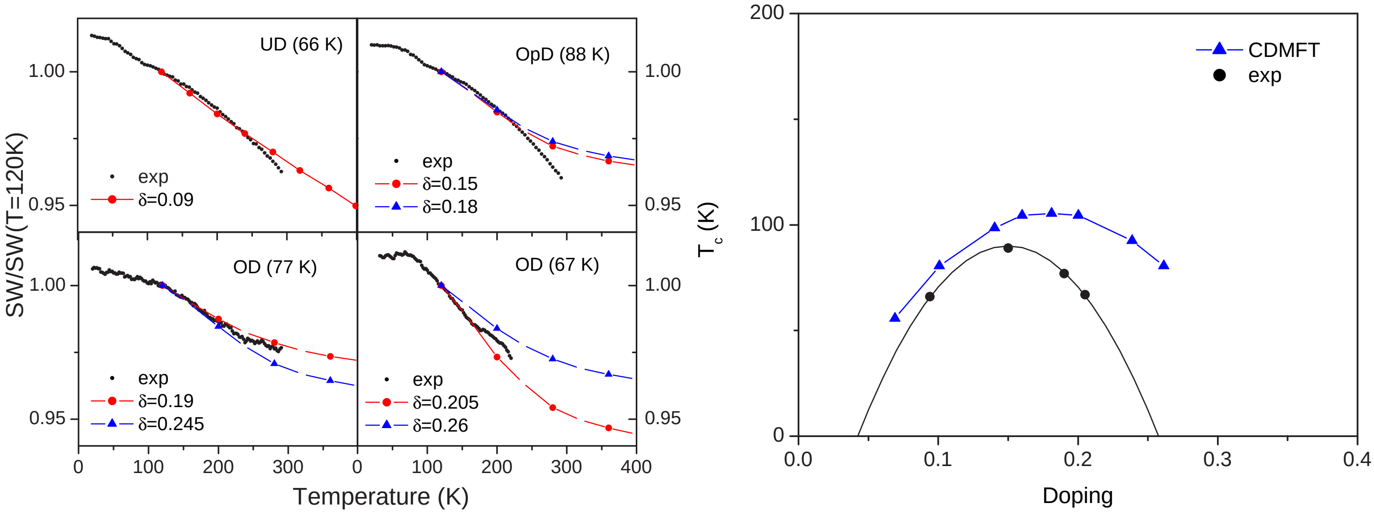

Figure 3.37: Left panel: Comparison between the experimental and the theoretical $SW(T)$ in the normal state for different doping levels. Right panel: comparison between the 'dome' as derived from theory and the experimental one.

3.7 The implications of the experimental observations

The superconductivity-induced increase of low-frequency spectral weight, which implies the opposite to the BCS type lowering of the electronic kinetic energy, was previously observed in the under-doped and optimally doped bi-layer $Bi_2Sr_2CaCu_2O_8$ [19, 20, 45]. Recent studies[25, 37] show that this effect changes sign for strongly over-doped samples of Bi2212, which then follows the trend of the BCS model. Hence the 'unconventional' superconductivity induced increase of low energy spectral weight appears to be a property characteristic of the Bi-based multi-layer cuprates at and below optimal doping, but not of the entire cuprate family for all doping levels.

3.7.1 Phenomenological implications of the effect

On the phenomenological level, recently an intriguing connection has been pointed out between the superconductivity induced increase of $W(T)$ on the one hand, and the drop of scattering rate on the other hand [29]. Since the former involves a spectral weight integral over 1 eV, whereas the latter is measured at microwave frequencies, these two experimental observations are seemingly unrelated. However, decreasing the scattering results in sharpening of the occupation distribution in k-space. Hence a decrease of scattering automatically implies a decrease of the average kinetic energy, which in turn is observed as an increased $W(T)$ when the sample turns from normal to superconducting. Since the standard BCS model (without a change in scattering)

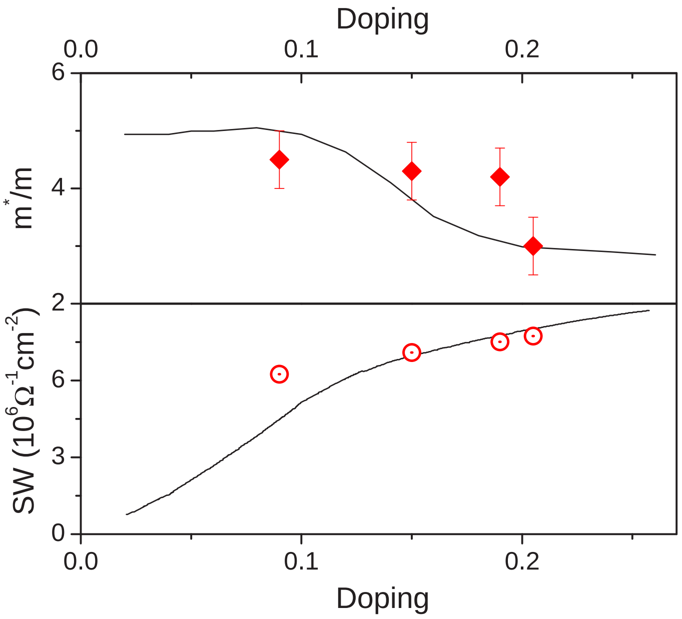

Figure 3.38: Comparison between the integrated SW and effective mass and the experimental values.

already predicts a superconductivity induced increase of the kinetic energy, the net result of both effects (scattering rate change and intrinsic BCS effect) will depend on the relative magnitude of these two effects. This explanation successfully relates two classes of experiments, without directly relating either one of these experiments to a particular pairing mechanism. The starting assumption of an anomalous drop in scattering is at this stage a phenomenological one, and still requires a microscopic explanation.

3.7.2 The dependence on the number of Layers per unit cell

Having data on both two layered and tri-layered materials we can verify whether the SW transfer depends on the dimensionality of the material in any way. We observe that the increase of spectral weight below T_c in Bi2223 is larger than in Bi2212[19]. We believe that this can be quite generally understood. It is well known that in the BCS theory

$$\Delta E_{kin} \sim \Delta_{SC}^2 \sim T_c^2. \tag{3.21}$$

The first equality holds generally for situations where the electronic occupation numbers $\langle n_k \rangle$ are redistributed in an energy range Δ around E_F, whereas the second is suggested simply by a dimensional analysis. Recent STM studies [42] indicate that the SC gap is indeed larger in Bi2223 than in Bi2212 at a similar doping level.

Assuming that Eq. (3.21) is also valid in Bi2212 and Bi2223 at optimal doping, and Eq. (3.5) is exact, we obtain $\Delta W_{Bi2223}/\Delta W_{Bi2212} = T^2_{c,Bi2223}/T^2_{c,Bi2212} \approx 1.6$. This ratio value matches the experimental observation, supporting the idea that the spectral weight transfer is intimately related to the SC-induced redistribution of the occupation numbers.

3.7.3 The doping dependence of the effect

Considering our BCS calculations, one notices that the single band optical spectral weight may behave very differently from the kinetic energy, both in the normal state, and in the superconducting state. This occurs when one uses a band structure more complicated than one involving nearest neighbour (nn) hopping only, since, with nn hopping only, the two are identical. Thus, one cannot use the phrase, 'BCS-like' behaviour for the optical spectral weight, but one can continue to use that phrase for the kinetic energy. This means that a wide variety of dependency on doping is in principle possible, due to band structure effects alone. This has a significant impact on the interpretation of experimental results, as doping dependence due to correlation effects, for instance, would have to be separated out either experimentally or theoretically. On the other hand, if one accepts the band structure for, say, BSCCO, as determined by ARPES, then the spectral weight observations [19, 60, 45, 54, 56, 37] remain anomalous, i.e. cannot be explained by BCS theory alone. We have advanced a number of possibilities, and many others have been proposed in the literature: doping levels may be shifted slightly compared to what we think they are, in which case strong correlations well beyond BCS theory are required to explain the observed trend with doping. A much stronger shift in doping actually reproduces the observed trends in the superconducting anomaly, but not in the normal state behaviour. Finally, including a scattering rate collapse below T_c also qualitatively accounts for the data.

On a microscopic level regarding the connection between SW and kinetic energy, it was shown that in the presence of strong electronic correlations this basic picture has to be extended to take into account that at different energy scales materials are described by different model Hamiltonians, and different operators to describe the electric current at a given energy scale [4, 61]. In the context of the Hubbard model, Wrobel *et al.* pointed out[14] that if the cutoff frequency Ω_c is set between the value of the exchange interaction $J \simeq 0.1$ eV and the hopping parameter $t \simeq 0.4$ eV then $SW(\Omega_c)$ is representative of the kinetic energy of the holes within the t-J model in the spin polaron approximation and describes the excitations below the on-site Coulomb integral $U \simeq 2$ eV not involving double occupancy, while $SW(\Omega_c > U)$ represents all intraband excitations and therefore describes the kinetic energy of the full Hubbard Hamiltonian. A numerical investigation of the Hubbard model within the dynamical cluster approximation[50] has shown the lowering of the full kinetic energy below T_c, for different doping levels, including the strongly overdoped regime. Experimentally, this result should be compared to the integrated spectral weight where the cutoff frequency is set well above $U = 2$ eV in order to take into account all the transitions into the Hubbard bands. However, in the cuprates this region also contains interband transitions, which would make the comparison rather ambiguous.

Using Cluster Dynamical Mean Field Theory (CDMFT) on a 2×2 cluster Haule and Kotliar [55] recently found that, while the total kinetic energy decreases below T_c at all doping levels, the kinetic energy of the holes exhibits the opposite behavior on the two sides of the superconducting dome: In the underdoped and optimally doped cuprates the kinetic energy of the holes, which is the kinetic energy of the t-J model, decreases below T_c. In contrast, on the overdoped side the same quantity increases when the superconducting order is switched on in the calculation. This is in agreement with the observations of Ref. [25] as well as the experimental data in the present thesis. The good agreement between experiment and theory in this respect is encouraging, and it suggests that the t-J model captures the essential ingredients, needed to describe the low energy excitations in the cuprate, as well as the phenomenon of superconductivity itself.

The Hubbard model and the t-J model are based on the assumption that strong electron-electron correlations rule the physics of these materials. Based on these models an increase of the low frequency SW in the superconducting state was found in the limit of low doping [14] in agreement with the experimental results [19, 54]. The optical conductivity of the t-J model in a region of intermediate temperatures and doping near the top of the superconducting dome has been recently studied using CDMFT [55]. The CDMFT solution of the t-J model at different doping levels suggests a possible explanation for the fact that the optical spectral weight shows opposite temperature dependence for the underdoped and the overdoped samples. It is useful to think of the kinetic energy operator of the Hubbard model at large U as composed of two physically distinct contributions representing the superexchange energy of the spins and the kinetic energy of the holes. The superexchange energy of the spins is the result of the virtual transitions across the charge transfer gap, thus, the optical spectral weight integrated up to an energy below these excitations is representative only of the kinetic energy of the holes. The latter contribution to the total kinetic energy was found to decrease in the underdoped regime while it increases above optimal doping, as observed experimentally. This kinetic energy lowering is however rather small compared to the lowering of the superexchange energy. Upon overdoping the kinetic energy of the holes increases in the superconducting state, while the larger decrease of the super-exchange energy makes superconductivity favorable with a still high value of T_c. In the CDMFT study of the t-J model, a stronger temperature dependence of $SW(T)$ is found on the overdoped side. This reflects the increase in Fermi Liquid coherence with reducing temperature.

At this point the most plausible explanation seems to be the one based on the cluster DMFT calculations and the $t - J$ model. In this respect we like to point out that while for the normal state temperature dependence of the SW, a direct comparison between the experiments and the calculations could be done; this is because the theoretical SW was calculated integrating the optical conductivity given by the solution of the $t - J$ model, and the comparison to the experiment in this case is quite direct. For technical issues though, the same kind of procedure could not be applied in the superconducting state, therefore the changes in kinetic energy were estimated by calculating the spectral function with and without superconductivity. This is indeed less direct and several assumptions have to be made in the definition of kinetic energy in order to compare to the experimental quantities. This does not mean that the result cannot be taken seriously of course, but stresses the fact that the kinetic energy we are referring to in these pages is not the real kinetic energy of the particles but a sort of "restricted kinetic energy" which neglects the contribution of some higher energies processes. In this sense we claim that the optical experiments combined with the $t-J$ model calculations can capture the essence of the low energy physics in cuprates, but for a confirmation of these result experimental data at energies higher than 4 eV combined with the full Hubbard Hamiltonian are desirable.

Bibliography

[1] E. Giannini, V. Garnier, R. Gladyshevskii, and R. Flükiger, Supercond. Sci. Technol. **17**, 220 (2004).

[2] S. Uchida *et al*, Phys. Rev. B**43**, 7942 (1991).

[3] F.C. Zhang and T.M. Rice. Phys. Rev. B **37**, 3759 (1988).

[4] H. Eskes, A. M. Oles, M.B.J. Meinders, W. Stephan. Phys. Rev. B **50**, 17980 (1994).

[5] P.Horsch and W. Stephan, in "Eletcronic properties of high temperature superconductors" edited by H. Kuzmany, M. Mehring and J. Fink, Springer Series in Solid-State Science **113** (Springer, Berlin, 1993). p. 351.

[6] P.W. Anderson, Science **235**, 1196 (1987).

[7] B. T. Thole, R.D. Cowan, G.A. Sawatzky, J. Fink, and J.C. Fuggle, Phys. Rev. B **31**, R6856 (1985).

[8] A. Fujimori *et al* Phys. Rev. B **35**, 8814 (1987).

[9] L.H. Tjeng *et al* Phys. Rev. Lett **67**, 501 (1991).

[10] M. Qvarford *et al* Phys. Rev. B **51**, 410 (1995).

[11] P.W. Anderson, P.A. Lee, M. Randeria, T.M. Rice, N. Trivedi, and F.C. Zhang, J. Phys.: Condens. Matter **16**, R755 (2004).

[12] J.E. Hirsch, Physica C **201**, 347 (1992).

[13] T. Eckl, W. Hanke and E. Arrigoni, Phys. Rev. B **68**, 014505 (2003).

[14] P. Wrobel, R. Eder, and P. Fulde, J. Phys.: Condend. Matter **15**, 6599 (2003).

[15] R.E. Walstedt, Jr and W.W. Warren, Science **248**, 1082 (1990).

[16] M.R. Norman *et al.* Nature **392**, 56 (1993).

[17] A.V. Puchkov, D.N. Basov, and T. Timusk, J. Phys.: Condens. Matter **8**, 10049 (1996).

[18] D.J. Van Harlingen, Rev. Mod. Phys. **67**, 515 (1995).

[19] H. J. A. Molegraaf, C. Presura, D. van der Marel, P. H. Kes, and M. Li, Science **295**, 2239 (2002).

[20] A. F. Santander-Syro, R. P. S. M. Lobo, N. Bontemps, Z. Konstatinovic, Z. Z. Li, and H. Raffy, Europhys. Lett. **62**, 568 (2003).

[21] D. van der Marel, H. J. A. Molegraaf, C. Presura, and I. Santoso, in *Concepts in electron correlation*, edited by A. Hewson and V. Zlatic, Kluwer (2003); cond-mat/0302169.

[22] C. Proust, E. Boaknin, R.W. Hill, L. Taillefer and A.P. Mackenzie, Phys. Rev. Lett. **89**, 147003 (2002).

[23] Z.M. Yusof, B.O. Wells, T. Valla, A.V. Fedorov, P.D. Johnson, Q. Li, C. Kendziora, Sha Jian, and D. G. Hinks, Phys. Rev. Lett. **88**, 167006 (2002).

[24] A. Junod, A. Erb, and C. Renner, Physica C **317**, 333 (1999).

[25] G. Deutscher, A.F. Santander-Syro, and N. Bontemps, Phys. Rev. B **72**, 092504 (2005).

[26] P.F. Maldague, Phys. Rev. B **16**, 2437 (1977).

[27] R. Kubo, J. Phys. Soc. Japan **12**, 570 (1957).

[28] A.A. Kordyuk, S.V. Borisenko, M. Knupfer, and J. Fink, Phys. Rev. B**67**, 064504 (2003).

[29] F. Marsiglio, Phys. Rev. B**73**, 064507 (2006).

[30] L. Benfatto, S. G. Sharapov, N. Andrenacci, and H. Beck, Phys. Rev. B **71**, 104511 (2005).

[31] M.R. Norman, M. Randeria, H. Ding, and J.C. Campuzano, Phys. Rev. B**52**, 615 (1995).

[32] Note that in the case of LSCO, doping can move the chemical potential through the van Hove singularity; see A. Ino, C. Kim, M. Nakamura, T. Yoshida, T. Mizokawa, A. Fujimori, Z.-X. Shen, T. Kakeshita, H. Eisaki, and S. Uchida, Phys. Rev. B **65**, 094504 (2002).

[33] Note that the labels of Fig. 3 of Ref. [29] were inadvertently interchanged. Thus, δT_D and δK_D should be switched, and similarly for δT_S and δK_S.

[34] N.W. Ashcroft and N.D. Mermin, In: *Solid State Physics* (Saunders College Publishing, New York 1976).

[35] More than just the doping dependence is contrary to experiment: the slope above T_c has a magnitude which is correlated with the magnitude of the anomaly, but not a sign change, as we have here.

[36] These curves differ roughly by a factor of 2 from those presented in Ref. ([37]) because of a difference in definition.

[37] F. Carbone, A.B. Kuzmenko, H.J.A. Molegraaf, E. van Heumen, V. Lukovac, F. Marsiglio, D. van der Marel, K. Haule, G. Kotliar, H. Berger, S. Courjault, P.H. Kes, and M. Li. Phys. Rev. B **74** 064510 (2006).

[38] A. Kaminski, S. Rosenkranz, H.M. Fretwell, M.R. Norman, M. Randeria, J.C. Campuzano, J-M. Park, Z.Z. Li, and H. Raffy, Phys. Rev. B **73**, 174511 (2006).

[39] A.B. Kuzmenko, Rev. Sci. Instrum. **76**, 083108 (2005).

[40] I. Bozovic, Phys. Rev. B **42**, 1969 (1990).

[41] M.A. Quijada, D.B. Tanner, R.J. Kelley, M. Onellion, H. Berger, and G. Margaritondo, Phys Rev B **60**, 14917 (1999).

[42] M. Kugler *et al.* J. Phys. Chem. Solids, in press.

[43] N. Petit, V. Garnier, V. Ta Phuoc, R. Caillard, A.M. Frelin, A. Ruyter, I. Laffez, J.C. Soret, A. Maignan, F. Gervais, Eur. Phys. J. B **25**, 423 (2002).

[44] D.E. Aspnes, J. Opt. Soc. Am. **70**, 1275 (1980).

[45] A.B. Kuzmenko, H.J.A. Molegraaf, F. Carbone and D. van der Marel, Phys. Rev. B, **72**, 144503 (2005).

[46] M. Ortolani, P. Calvani, and S. Lupi, Phys. Rev. Lett. **94**, 067002 (2005).

[47] A. Toschi, M. Capone, M. Ortolani, P. Calvani, S. Lupi, and C. Castellani, Phys. Rev. Lett. **95**, 097002 (2005).

[48] A.E. Karakozov and E.G. Maksimov, cond-mat/0511185.

[49] L. Benfatto, J.P.Carbotte, and F. Marsiglio, private communication.

[50] Th. A. Maier, M. Jarrell, A. Macridin, and C. Slezak, Phys. Rev. Lett. **92**, 027005 (2004).

[51] A.B. Kuzmenko, N. Tombros, H.J.A. Molegraaf, M. Grüninger, D. van der Marel, and S. Uchida, Phys. Rev. Lett. **91**, 037004 (2003).

[52] D. van der Marel, H.J.A. Molegraaf, J. Zaanen, Z. Nussinov, F. Carbone, A. Damascelli, H. Eisaki, M. Greven, P.H. Kes, M. Li. Nature **425** 271 (2003).

[53] J. Wang, T. Timusk, G.D Dung. Nature **427** 714 (2004)

[54] F. Carbone, A.B. Kuzmenko, H.J.A. Molegraaf, E. van Heumen, E. Giannini, D. van der Marel. Phys. Rev. B. **74** 024502 (2006).

[55] K. Haule and G. Kotliar cond-mat/0601478.

[56] N. Bontemps, R.P.S.M. Lobo, A.F. Santander-Syro, and A. Zimmers, cond-mat/0603024.

[57] M.C. Nuss, P.M. Mankiewich, M.L. O'Malley, E.H. Westerwick, and P.B. Littlewood, Phys. Rev. Lett. **66**, 3305 (1991).

[58] Y. Kuroda and C.M. Varma, Phys. Rev. B **42**, 8619 (1990).

[59] M.R. Norman and C. Pépin, Phys. Rev. B **66**, 100506 (2002).

[60] A.F. Santander-Syro, R.P.S.M. Lobo, N. Bontemps, Z. Konstantinovic, Z.Z. Li, H. Raffy, Europhys. Lett. **62**, 568 (2003); A.F. Santander-Syro, R.P.S.M. Lobo, N. Bontemps, W. Lopera, D. Girata, Z. Konstantinovic, Z.Z. Li, H. Raffy, Phys. Rev. B **70**, 134504 (2004).

[61] M. J. Rozenberg, G. Kotliar, H. Kajueter. Phys. Rev. B **54**, 8452 (1996).

Chapter 4

The scaling properties of the optical conductivity in the cuprates superconductors

The electronic dynamics of the high-T_c cuprates is invariably featured by a large optical spectral weight located in the mid-infrared range (~ 0.5 eV), which coexists with a relatively sharp Drude peak at low frequencies. The origin of this 'MIR band' has been a subject of a long-lasting debate [8, 9, 4]. Since the band theory does not predict strong optical interband transitions in this range [10, 11], it is commonly assumed that the band represents a portion of the intraband electronic spectral weight, which is pushed up to remarkably high energies by strong electron-electron interactions or scattering on some bosonic excitations. In this section we will discuss the nature of high-T_c electronic structure performing comparative analysis of the normal state optical response of two Bi-based cuprates: Bi2212 and Bi2223.

We performed a detailed analysis of the scaling properties of the optical conductivity and demonstrate that the experimental data do not support completely the quantum critical scenario.

The power-law dependence of the optical conductivity $\sigma(\omega) \sim (-i\omega)^{-\alpha}$ was indeed observed in the cuprates near optimal doping in a certain range of frequencies (from 0.1 to 0.7 eV) [14, 12, 2]. The exponent α, however, turned out to be 0.65 - 0.7, rather different from 0.5, as given by the 'cold spot' model[6] and more close to the predictions of the Luttinger Liquid model by Anderson [13]. In a recent paper [2] it was suggested, that a universal power-law behavior of optical conductivity for $\omega > T$ may be due to the proximity of a quantum critical point (QCP), where the electronic system becomes scale-invariant. This behavior is not observed for the underdoped and strongly overdoped samples of Bi2212. It is interesting to check whether or not this tendency is preserved in the cuprates with different number of CuO_2-planes per unit cell.

In a recent publication, we pointed out two peculiar aspects of the infrared optical conductivity in the normal state[2]:

- In the far infrared range the optical conductivity of optimally doped cuprates is characterized by a universal ω/T scaling function of the form

  $$\sigma(\omega) = T^{-1} g(\omega/T) \tag{4.1}$$

  where the function $g(x)$ is to very good approximation given by $g(x) = C/(1 - ix)$ for $x = \omega/T < 1.5$. A consequence of this behavior is a collapse of the spectra when $T\sigma_1(\omega, T)$ is plotted as a function of ω/T for different temperatures.

- At $\omega/T \approx 1.5$ a cross-over appears to take place to a power law behavior, previously pointed out in Refs. [14, 12, 13]. For $\omega/T > 1.5$ a collapse of the spectra plotted versus ω/T required that the conductivity is multiplied no longer with the temperature T, but with either $T^{0.5}$ or $\omega^{0.5}$. This change of behavior is also evident from a plot of the phase of the optical conductivity ($\arctan(\sigma_2/\sigma_1)$), which displays a plateau with a phase angle of approximately 60 degrees for all temperatures and frequencies in access of $k_B T$. In the same frequency range the absolute value of the conductivity, $\mid \sigma(\omega) \mid$, follows a power law behavior,$|\sigma(\omega)| \propto \omega^{-2/3}$. Both the frequency dependence of $\mid \sigma(\omega) \mid$ and of the phase angle are manifestations of the fact that the optical conductivity follows approximately a power law for frequencies in the range $T < \omega < 0.7eV$.

The exponent $\alpha = 2/3$ is rather different from 0.5, as given by the 'cold spot' model[6] and closer to Anderson's result based on the concept of spin-charge separation[13]. Experimentally the ω/T scaling and constant phase angle are most closely obeyed for samples close to optimal doping, as displayed in Fig.4.1, 4.2 where the modulus of the optical conductivity and its phase is plotted for Bi2212 and Bi2223 at different doping levels. As such they appear to be a direct manifestation of quantum critical behavior when the doping is tuned to match exactly a quantum phase transition. However, it remained unclear whether a single scaling function could be defined covering both aspects 1) and 2) of the optical conductivity.

Here we extend the analysis of Ref. [2] by introducing a novel transformation, allowing us to obtain the ω/T scaling function for all frequencies. The relations for this transformation rely on the derivative with respect to temperature of the real and imaginary part of the dielectric function. For such a procedure it is important to have a dense sampling of temperature, excellent signal-to-noise ratio, and a very small spurious time-dependent drift of the data, in particular in the frequency range below 1 eV. We will perform this analysis on the Bi2223 data discussed in the previous chapter.

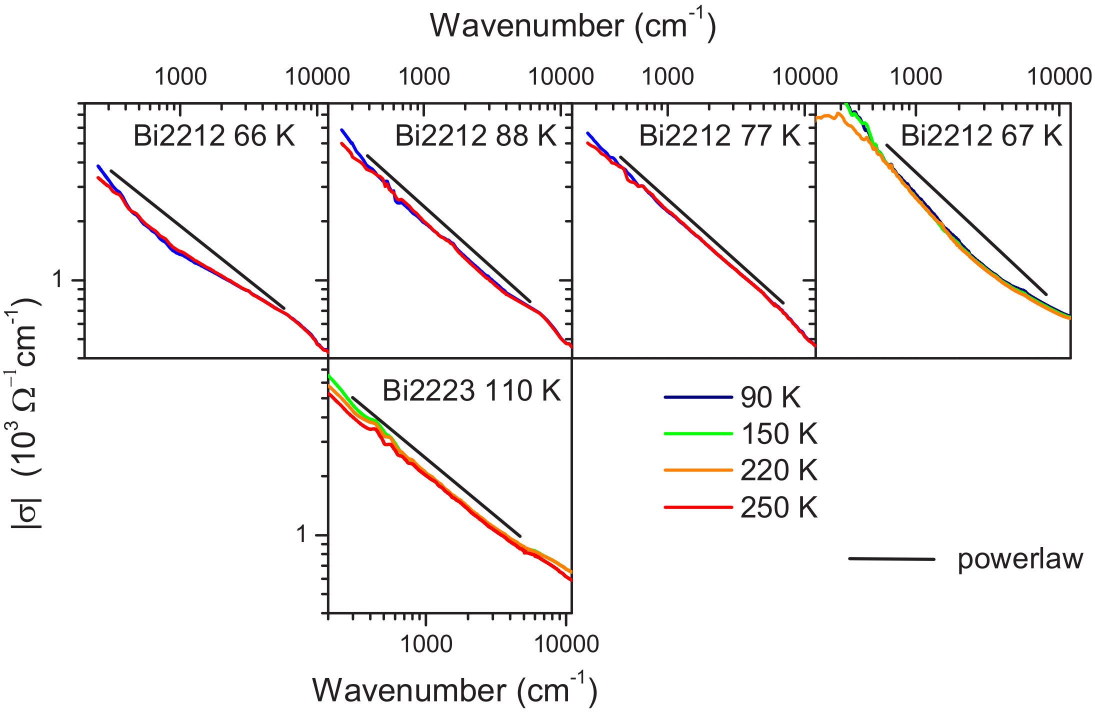

Figure 4.1: The absolute value of the optical conductivity as a function of frequency is plotted in a Log-Log graph. The power law behavior of the optical conductivity is evidenced by a linear frequency dependence in a Log-Log scale. This is visible in Bi2223 and Bi2212 close to optimal doping only

4.1 Novel transformation to obtain ω/T scaling function

The basic assumption which we will investigate is whether the optical conductivity representing the free charge carriers follows a universal scaling relation of the form[17]:

$$\sigma(\omega, T) = \frac{1}{T^{\nu}} g\left(\frac{\omega}{T}\right) \; ; \nu \equiv \frac{z}{2-d} \tag{4.2}$$

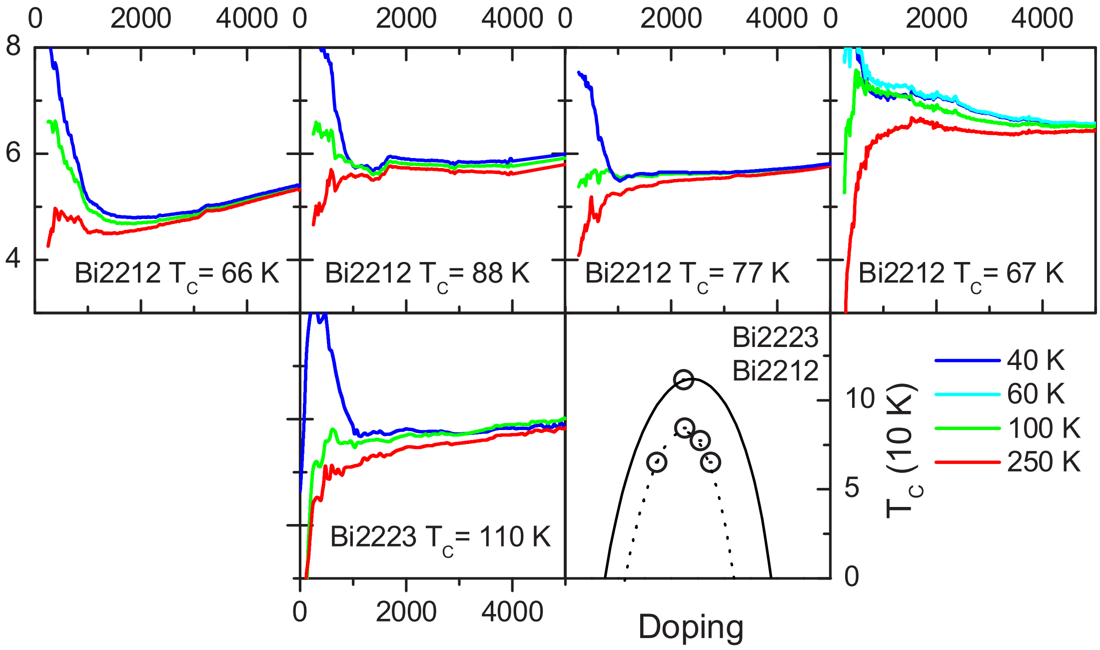

Figure 4.2: The Phase of the optical conductivity $(arctang(\sigma_2/\sigma_1(\omega)))$ at different temperatures of Bi2223, Bi2212 is plotted. In the region where the powerlaw is observed one expects to find a constant phase as a function of frequency. This is observed close to optimal doping only.

where d is the relevant dimension and z the dynamical exponent [3]. As pointed out by Philips and Chamon, T-linear resistivity requires the unphysical assumption that the dynamical exponent z is negative. Consequently, no consistent account of T-linearity is possible if the quantum critical modes carry the electrical charge. Apparently, either the T-linear resistivity is not directly linked to a quantum phase transition, or "quantum critical scenarios must relinquish the simple single scale hypothesis to explain the resistivity law in the cuprates."[17] Despite this deficiency we will treat ν as an adjustable scaling parameter, which can have the value $\nu = 1$. It is clear that it is no longer justified in this case to assume that $\nu = z/(2-d)$.

Before continuing we wish to make one general observation about the part of the optical conductivity described by $g(\omega/T)$: The integrated optical spectral weight is proportional to $T^{1-\nu}$. We already know that in the case of interest for this discussion $\nu = 1$, because at optimal doping the resistivity, $\rho \propto T^{\nu}$, is a linear function of the temperature. Hence taken together ω/T-scaling and T-linear resistivity imply that the integrated spectral weight presented by $g(\omega/T)$ has a constant value for all temperatures. Experimentally this is confirmed by the collapse of $T\sigma(\omega,T)$ plotted as a function of ω/T. Upon closer inspection, a few percent spectral weight variation between T_c and 300 K is not excluded. The optical conductivity integrated between 0 and 1.25 eV is known to exhibit a temperature dependence proportional to $1-bT^2$, with $b \approx \cdot 5 \cdot 10-7K^{-2}$. In previous papers it has not yet been investigated how this temperature dependence is distributed within the free-carrier contributions in the far and mid-infrared. We will revisit this point in more detail at the end of this chapter. We do note, however, that in order to include the possibility that the integrated free carrier weight has a correction proportional to T^2, we have to multiply $g(\omega/T)$ with a factor $1-bT^2$.

According to Ref. [2] the function $g(\omega/T)$ obeys a Drude form, at least for $\omega/T < 1.5$, but here we are interested to find out more about the continuation beyond this range of ω/T. One possible obstacle is, that at higher frequencies the scaling behavior becomes overshadowed by 'regular' (*i.e.* unrelated to quantum critical behaviour) contributions to the optical conductivity, notably in the range above about 1 eV where interband transitions dominate the optical conductivity. Because interband transitions present a fixed energy scale, for those high frequencies there is no shadow of doubt that the temperature is not the only relevant scale in the optical conductivity. For frequencies below 1 eV, but still above $k_B T$ the situation is less clear: Interband transitions are negligible in this range, but the optical conductivity in this range strongly exceeds the values obtained by extrapolating the Drude behaviour seen in the far-infrared range. The observed $\sigma(\omega)$ below 1 eV therefore appears to be an intrinsic part of the free carrier response. Yet, it needs to be established from the experimental data whether this part is described by the same $g(\omega/T)$ function which is found for $\omega/T < 1.5$. Experimentally[15, 18] the optical conductivity in the mid-infrared and visible part of the spectrum of optimally doped samples has a temperature dependence of the form $\sigma(\omega,T) = \sigma^{(0)}(\omega) + \sigma^{(2)}(\omega)T^2$. In Fig. 4.3 of the temperature dependence of $\sigma_1(\omega) = \omega/(4\pi)\mathrm{Im}\epsilon(\omega)$ and $\mathrm{Re}\epsilon(\omega)$ are shown. The non-monotonous temperature dependence in the normal state for frequencies below 1500 cm^{-1} is an immediate consequence of the fact that in this range the optical conductivity is dominated by a Drude peak the width of which varies linearly as a function of temperature. On the other hand the observed temperature dependence up to $2 \cdot 10^4$ cm^{-1} vastly exceeds that of the extrapolated Drude peak, and moreover has the wrong exponent: For $\omega \gg T$ the Drude function becomes $\sigma_1 \propto T/(\omega^2+T^2)$ crosses over to a T-linear temperature dependence. Indeed this is seen for example at 1200 cm^{-1}, but at higher frequencies the temperature variation becomes dominated by a T^2 term. Although this correction remains small relative to σ_1 in all cases, its presence in the experimental data motivates us to explore the following

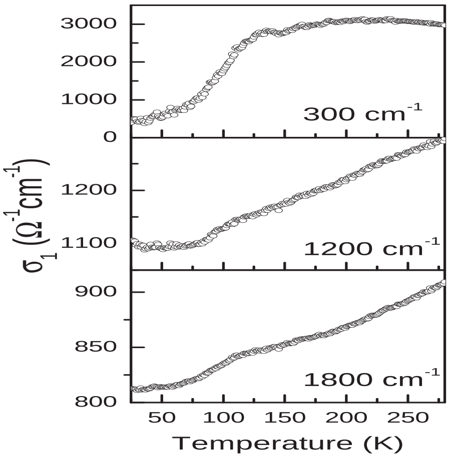

Figure 4.3: Temperature dependence of the ab-plane optical conductivity Bi2223 for three selected frequencies.

decomposition of the optical conductivity

$$\sigma(\omega,T) \;=\; \frac{1-bT^2}{T^\nu} g\left(\frac{\omega}{T}\right) + \sigma^{(0)}(\omega) + \sigma^{(2)}(\omega)T^2 \tag{4.3}$$

4.1.1 Temperature independent regular conductivity

Because the T^2 corrections b and $\sigma^{(2)}(\omega)$ are small, we will first work out the consequences in the limit where they are zero. Since here we are interested in the behavior near optimal doping, where the resistivity is T-linear, we consider the case where $\nu = 1$. Then Eq.4.3 reduces to

$$\sigma(\omega,T) = T^{-1}g\left(\omega/T\right) + \sigma^{(0)}(\omega) \tag{4.4}$$

In order to eliminate the temperature independent term $\sigma^{(0)}(\omega)$, we start by taking the temperature derivative of this expression. For the evaluation of $dg/d\omega$ and dg/dT we use the fact that the function g depends only on a single variable x, defined as the ratio $x = \omega/T$.

$$\frac{\partial\sigma(\omega,T)}{\partial T} \;=\; -\frac{1}{T^2}\left\{g + \frac{\omega}{T}g'\right\} = -\frac{1}{T^2}\frac{d}{dx}(xg) \tag{4.5}$$

Because xg is a function the ω and T dependence of which enters only as the ratio $x = \omega/T$, we are allowed to substitute ω for x in taking the derivative. Thus, using the chain-rule: $d(xg)/dx = -T^{-1}d(xg)/d\omega$. Inserting this for the righthand side of Eq.4.5 we obtain $-Td\sigma/dT = d(xg)/d\omega$. The integration of both sides of this equation results in an expression which relates xg(x) on one side of the expression to the frequency-integral of $d\sigma(\omega)/dT$ on the other side. Multiplying both sides with $1/x = T/\omega$ finally gives the following transformation of the complex optical conductivity function

$$g(\omega, T) = -\frac{T^2}{\omega}\int_o^\omega \frac{d\sigma(\omega', T)}{dT}d\omega' \tag{4.6}$$

In the above an important starting assumption was, that $g(\omega, T)$ depends on the ratio ω/T. It may therefore look somewhat strange that in Eq.4.6 we write it as a function of frequency and temperature. However, we want to feed the experimentally measured optical conductivity into the righthand side of the above transformation, providing g on output. *A priori* there is no guarantee that the experimental optical conductivity is of the form assumed in Eq. 4.3. In fact this is the model we like to test by plotting the output of the transformation, $g(\omega, T)$, as a function of ω/T for different temperatures.

4.1.2 Temperature dependent spectral weight of the scaling function

If $\sigma^{(2)}(\omega)$ is different from zero in Eq.4.3 and $b \neq 0$, we have no analytical expression for the transformation. However, it is possible, to perform a least-square fit of the reflectivity and ellipsometry data for all temperatures and frequencies at once, inserting in Eq.4.3 a multi-oscillator Kramers-Kronig consistent composition [19] for the three terms $g\left(\frac{\omega}{T}\right)$, $\sigma^{(0)}(\omega)$ and $\sigma^{(2)}(\omega)$.

4.2 Results

One can find the optical conductivity of Bi2223 in the previous chapter. Using the extended Drude formalism, we can obtain the frequency-dependent scattering rate:

$$\tau^{-1}(\omega) = \frac{\omega_p^2}{4\pi}\mathrm{Re}\left[\frac{1}{\sigma(\omega)}\right], \epsilon^\infty = 4.5, \tag{4.7}$$

The result, shown in Fig.4.4, indicates that the scattering rate has a power law type frequency dependence $\tau^{-1} \propto \omega^\eta$ with $\eta \approx 2/3$ as for optimally doped Bi2212. The plasma frequency ω_p was taken to be 20600 cm^{-1}, which gives $m^*(\omega)/m \approx 1$ at 1 eV.

The phase of the optical conductivity, shown for a few temperatures in Fig. 4.2 is close to 60 degrees and almost constant, which is also similar to the phase of Bi2212 at optimal doping.[2].

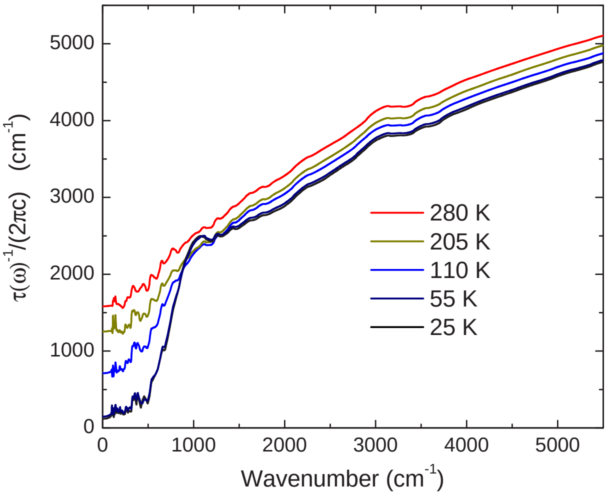

Figure 4.4: In-plane frequency-dependent scattering rate of Bi2223.

We have applied Eq. 4.6 to the full set of spectra in the normal state (140-260 K in 1 K steps). The output for the $g(\omega, T)$ is shown in Fig. 4.5. We see, that for a broad range of values of $\hbar\omega/k_BT$ the scaling-function is to a very good approximation given by the expression

$$g(\omega, T) = \frac{g(0)}{1 + iA\hbar\omega/k_BT} \tag{4.8}$$

where $A = 0.83$ and $g(0) = 1.67 \cdot 10^6 K\Omega^{-1}cm^{-1}$. This is also borne out by the frequency dependent phase of this function, displayed in Fig. 4.6, which asymptotically approaches 90 degree for $\omega/T \to \infty$. The curves for the different temperatures now show a good scaling collapse, also for $\hbar\omega/k_BT > 1.5$, where in the analysis of Ref. [2] the curves started to separate. Note, that the imaginary part of $g(\omega, T)$ has more scatter than the real part, which is due to the fact that for low frequencies the reflectivity spectra depend in in leading order only on σ_1. This is the so-called Hagen-Rubens limit, where for a frequency independent $\sigma_1(\omega)$ the optical reflectivity has a $\omega^{0.5}$ departure from 1.

The good collapse of our scaling function for large $\hbar\omega/k_BT > 1.5$ is clearly due to the fact, that in our analysis we have removed a part of the optical conductivity spectrum which is essentially independent of the temperature. This background, which is obtained by subtracting $Tg(\omega, T)$ from the experimental conductivity curves for the temperatures indicated, $\sigma^{(0)}$, is displayed in Fig. 4.7. If the decomposition in

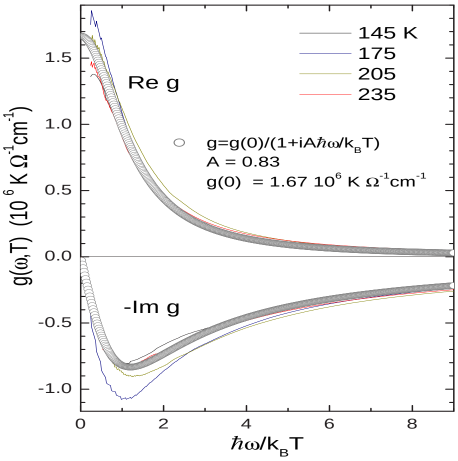

Figure 4.5: Real and imaginary parts of the scaling function $g(\omega, T)$ of Bi2223, calculated for 4 different temperatures from the experimental data using Eq. 4.6.

a T-independent part and an $g(\omega/T)$ term would be perfect, these curves would lie exactly on top of each other. In fact, we see that this works quite well, but a few significant changes remain. If we make instead the full decomposition using Eq. 4.3 as discussed in section4.1.2, we obtain almost identical result for $g(\omega/T)$ and $\sigma^{(0)}$. These results are presented in in Figs. 4.8,4.9,4.10.

The decomposition of the infrared spectra of the cuprates in a Drude-peak and a so-called mid-infrared band has a long history, dating back to the beginning of the high T$_c$ era. In a series of papers it has been pointed out by Tanner, that if one splits up the optical spectra this way, one finds that about one quarter of the spectral weight below 1 eV resides in the Drude peak, the rest is in the temperature dependent background. Although our analysis is different in detail, the experimental data do lead us to make an even stronger conclusion: If we try to fit the data to a function of the general form $Tg(\omega/T)$ plus a constant background, the result returned for $Tg(\omega/T)$ is a simple Drude function with a T-linear scattering rate. That about one third of the spectral weight or less resides in the Drude peak, is borne out by Fig. 4.12, where we display for T=245 K the spectral weight function

$$\hbar^2\omega_p^2(\omega) = 8\int_0^{\omega} Re\sigma(\omega)d\omega \qquad (4.9)$$

for the two components.

This analysis leads to the following conclusions:

- Our result indicates that the constant value of the phase above 1000 cm^{-1} is not a manifestation at high frequencies of the same $g(\omega/T)$ function which dominates the low frequency optical conductivity of the normal state.

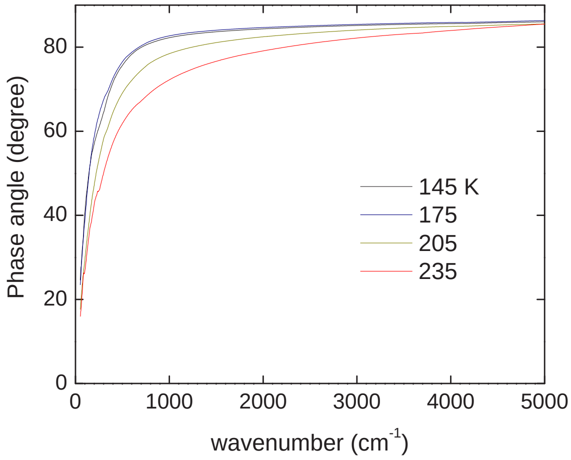

Figure 4.6: Phase of $g(\omega, T)$ shown in Fig. 4.5

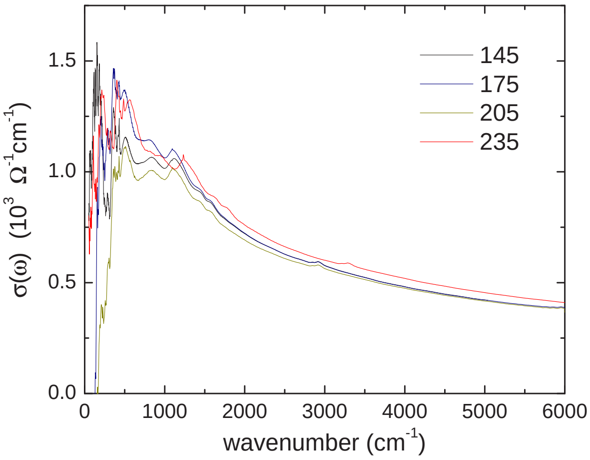

Figure 4.7: Regular contribution of the optical conductivity $\sigma^{(0)}(\omega, T)$, calculated by subtracting $Tg(\omega, T)$ shown in Fig. 4.5 from the experimental spectra.

- Our result does *not* imply that the optical spectra of the cuprates should be regarded as a sum of two independent terms, one of which is essentially a constant of temperature and the other a Drude term.
- If the $g(\omega/T)$ scaling collapse has something to do with quantum criticality, then the constant phase above 1000 cm^{-1} has a different origin, and vice versa.
- Our result does *not* imply that there is no frequency dependence in the scattering rate.

The different terms in Eq.4.3 are necessary to provide a continuation of $g(\omega/T)$ for large ω/T. However, it seems overwhelmingly natural to interpret the entire spectrum below 1 eV as the response of the free charge carriers. In this view, the

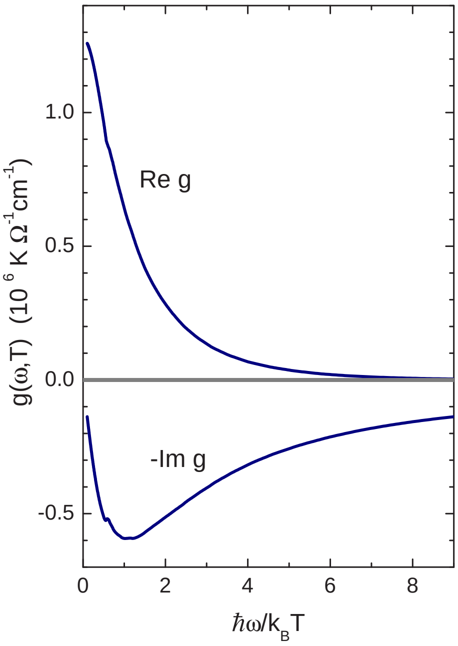

Figure 4.8: Real and imaginary parts of the scaling function $g(\omega, T)$ of Bi2223, from a fit to the optical spectra at all temperatures between 140 K and 280 K from the experimental data using Eq. 4.3.

mid-infrared peak would then correspond to the incoherent part of the optical response, reflecting excited states which, on a lower energy scale, condense into the superconducting state. From a conventional point of view $1/\tau(\omega)$ then reveals the 'glue' which binds electrons into Cooper pairs[20]. A more radical view is that the power law frequency dependence of the optical conductivity reveals an unconventional state of matter on an energy scale in excess of the scale where coherent transport is possible[21].

4.2.1 Anisotropic scattering rate model

Another possible explanation for the powerlaw observed in the optical conductivity is the anisotropic scattering rate model. The determination of ϵ_∞ necessary for the previous analysis is somewhat ambiguous; since the first interband transitions reside at rather low energies ($\sim$ 2 eV). Therefore, in addition to the simple conductivity phase analysis, it is instructive to fit the full set of our optical data (reflectivity in the far- and mid-infrared and ellipsometrically-obtained ϵ_1 and ϵ_2 at higher frequencies) with a causal (Kramers-Kronig consistent) dielectric function including the response

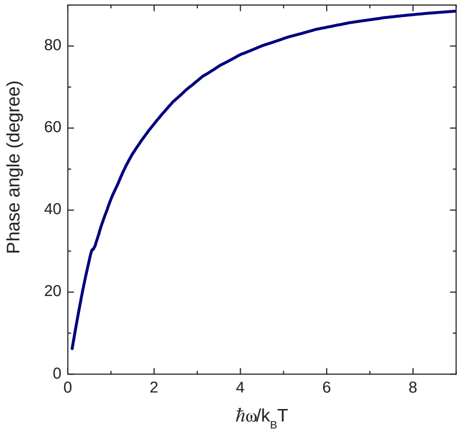

Figure 4.9: Phase of $g(\omega, T)$ shown in Fig. 4.8

of the core electrons ϵ_∞, the low-lying interband transitions ϵ_{inter} and an intraband conductivity σ_{intra}, which shows a power-law dependence in a certain frequency range:

$$\epsilon(\omega) = \epsilon_\infty + \epsilon_{inter}(\omega) + \frac{4\pi i}{\omega}\sigma_{intra}(\omega). \tag{4.10}$$

The powerlaw function

$$\sigma(\omega) = A(-i\omega)^{-\alpha}. \tag{4.11}$$

taken literally, is not suitable for σ_{intra}, since it diverges at low frequencies and is not integrable at high frequencies. The latter fact even precludes the determination of the plasma frequency. Therefore, we need to introduce physically sensible low- and high-frequency cutoffs in a Kramers-Kronig consistent fashion. A simple example of a function which satisfies these requirements, was given in Ref.[5]; initially, it has been derived in the context of the anisotropic scattering rate model, but proposed to be of a more general use, especially in cases of a non-Fermi-liquid behavior:

$$\sigma(\omega) = \frac{\omega_p^2}{4\pi} \frac{i}{(\omega + i\gamma_{min})^\alpha (\omega + i\gamma_{max})^{1-\alpha}} \tag{4.12}$$

(in order to match formula (4.11), we used a two times larger α than in the original paper [5]). Here we shall elaborate on a different expression for the optical conductivity, which, however, has very similar analytical properties to (4.12). Since at this point we do not stick to any microscopic theory and only assume a power-law behavior, our derivation will be rather phenomenological.

In the following we shall use the fact that *a power-law optical conductivity can be represented as a power-law scattering-rate distribution of Drude functions*:

$$(-i\omega)^{-\alpha} = \frac{\sin\pi\alpha}{\pi} \int_0^\infty f(\gamma) d\gamma \frac{i}{\omega + i\gamma}, \text{ where } f(\gamma) = \gamma^{-\alpha}. \tag{4.13}$$

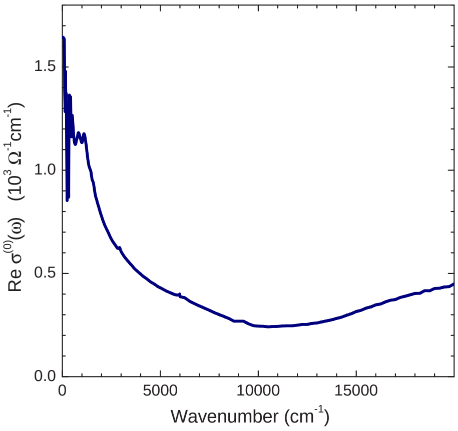

Figure 4.10: Regular contribution of the optical conductivity $\sigma^{(0)}(\omega, T)$, calculated by fitting the optical spectra at all temperatures between 140 K and 280 K from the experimental data using Eq. 4.3.

We begin with the low-frequency cutoff. It has to provide a finite value of the DC conductivity. Obviously, $\sigma(\omega)$ given by (4.13) diverges as $\omega \to 0$ because the integration goes over arbitrarily small scattering rates. On the other hand, the minimum scattering rate (Planckian dissipation) is given by the temperature:

$$\gamma_{min}(T) \approx k_B T/\hbar. \tag{4.14}$$

The breakdown of the power law at low frequencies can be also caused by the self-energy effects, due to the interaction of electrons with phonons or (and) with the spin-resonance mode. Therefore, as a first approximation we should start the integration from γ_{min} and replace γ with $\gamma - \gamma_{min}$ in the distribution function $f(\gamma)$. Since γ_{min} can be larger than the value (4.14), we should treat it as a free fitting parameter.

An upper estimate of the high-frequency cutoff is given by the bandwidth, which is of the order of 2 eV. The easiest way to introduce it is to limit the integration in (4.13) to $\gamma < \gamma_{max}$, also treated as a model parameter. This leads us to the following expression for the intraband conductivity:

$$\begin{aligned} \sigma_{intra}(\omega) &= A\frac{\sin\pi\alpha}{\pi}\int_{\gamma_{min}}^{\gamma_{max}}(\gamma-\gamma_{min})^{-\alpha}d\gamma\frac{i}{\omega+i\gamma} \\ &= \frac{\omega_p^2}{4\pi}\frac{i}{\omega+i\gamma_{min}}F(1,1-\alpha,2-\alpha,\frac{\gamma_{max}-\gamma_{min}}{i\omega-\gamma_{min}}), \end{aligned} \tag{4.15}$$

where $F(a, b, c, z)$ is the hypergeometric function. Here ω_p is the usual plasma frequency: $\omega_p^2 = 8\int_0^\infty \sigma_{1,intra}(\omega)d\omega$.

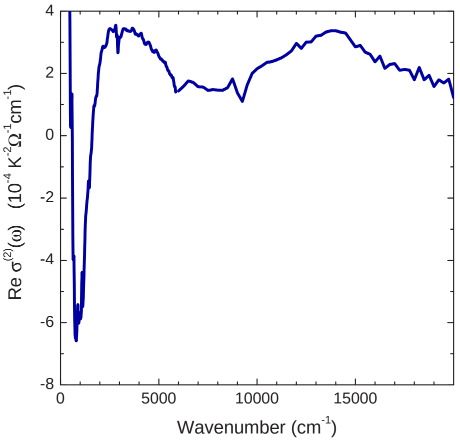

Figure 4.11: The term in the decomposition of the optical conductivity presented in Eq. 4.3 which has a temperature variation proportional to T^2.

Although formula (4.12) and (4.15) look rather different, they can be easily compared in terms of the scattering-rate distribution function $f(\gamma)$. One can show that (4.12) corresponds to $f(\gamma) = (\gamma - \gamma_{min})^{-\alpha}(\gamma_{max} - \gamma)^{\alpha-1}$ for $\gamma_{min} < \gamma < \gamma_{max}$ and $f(\gamma) = 0$ elsewhere, while (4.15) corresponds to $f(\gamma) = (\gamma - \gamma_{min})^{-\alpha}$ for $\gamma_{min} < \gamma < \gamma_{max}$ and $f(\gamma) = 0$ elsewhere. The difference is only in the extra multiplier $(\gamma_{max} - \gamma)^{\alpha-1}$, which diverges at γ_{max} and supplies an 'enhanced weight' to scattering rates close to γ_{max} in case of formula (4.12). Since, generally speaking, we do not see obvious reasons for such an enhancement, the expression (4.15) seems to be slightly more justified, although both formulas remain purely phenomenological.

Let us briefly discuss properties of the introduced conductivity (4.15), assuming that $\gamma_{min} \ll \gamma_{max}$. They are essentially the same as the ones of ([2]), which are described in [5]. In the Hagen-Rubens regime $\omega \ll \gamma_{min}$ the standard behavior of reflectivity $R = 1 - (2\pi\omega/\sigma_{DC})^{1/2}$ is observed with the DC conductivity :

$$\sigma_{DC} \approx \frac{\pi(1-\alpha)}{\sin \pi\alpha} \frac{\omega_p^2}{4\pi\gamma_{max}} \left(\frac{\gamma_{min}}{\gamma_{max}}\right)^{-\alpha}, \tag{4.16}$$

Well within the cutoff interval ($\gamma_{min} \ll \omega \ll \gamma_{max}$) the conductivity (4.15) is a powerlaw:

$$\sigma_{intra}(\omega) \approx \frac{\pi(1-\alpha)}{\sin \pi\alpha} \frac{\omega_p^2}{4\pi\gamma_{max}} \left(\frac{-i\omega}{\gamma_{max}}\right)^{-\alpha}. \tag{4.17}$$

At high frequencies $\omega \gg \gamma_{max}$ again a Drude form is recovered:

$$\sigma_{intra}(\omega) \approx \frac{\omega_p^2}{4\pi} \frac{i}{\omega + i\gamma_{eff}}, \text{ where } \gamma_{eff} = \frac{1-\alpha}{2-\alpha}\gamma_{max} \approx 0.25 - 0.3\gamma_{max}. \tag{4.18}$$

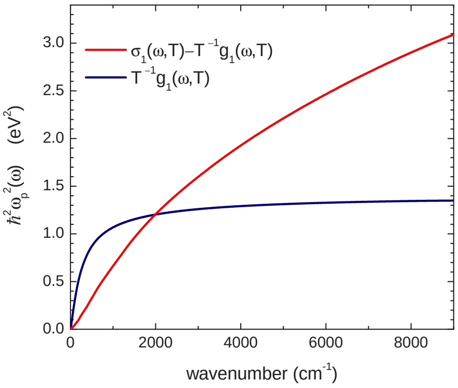

Figure 4.12: Comparison of the spectral weight function at 235 K of the regular term (red curve)$\sigma^{(0)}(\omega,T)$ and $Tg(\omega,T)$

Table 4.1: Parameters, obtained by fitting optical data with formulas (4.10) and (4.15) for Bi2223 at 260 K. All values, except the ones for α and ϵ_∞, are given in cm^{-1}. ϵ_∞ is found to be 2.5 for both equations.

	ω_p	α	γ_{min}	γ_{max}	ω_1	ω_{p1}	γ_1	ω_2	ω_{p2}	γ_2
eq. 11	22200	0.6	76	31500	19000	8700	7770	36500	37500	19000
eq. 14	24700	0.58	71	91200	19150	8200	7370	36340	36500	18000

We modeled optical spectra of Bi2223 and Bi2212 using the dielectric function (4.10) with expression (4.15) for the intraband response. The interband response was modeled with two Lorentz oscillators. The fitting parameters for the optimally doped samples are presented in Table 4.1; the quality of the fit in the infrared region is depicted in figure 4.13, together with the temperature dependence of the model parameters for both formula 4.12 and 4.15. The quality of the fit is at least as good as the one achieved in the two component scenario; there is hardly any difference between the fitting quality using equation 4.12 or 4.15.

This model has several advantages over the previous models reported; it gives the best fit to the data with the minimum number of free parameters and it is possible from this model to calculate the exponent of the power-law conductivity: $\sigma = C\omega^{-\alpha}$. The exponent α is found to be around 0.63, in optimally doped samples, in very good agreement with the value extracted from the quantum critical analysis of the data. In Fig. 4.13 one can see the infrared reflectivity together with the best multicomponent fit for samples with different doping levels. Remarkably, the fitting quality using this model decreases moving away from optimal doping and it is particularly bad in the

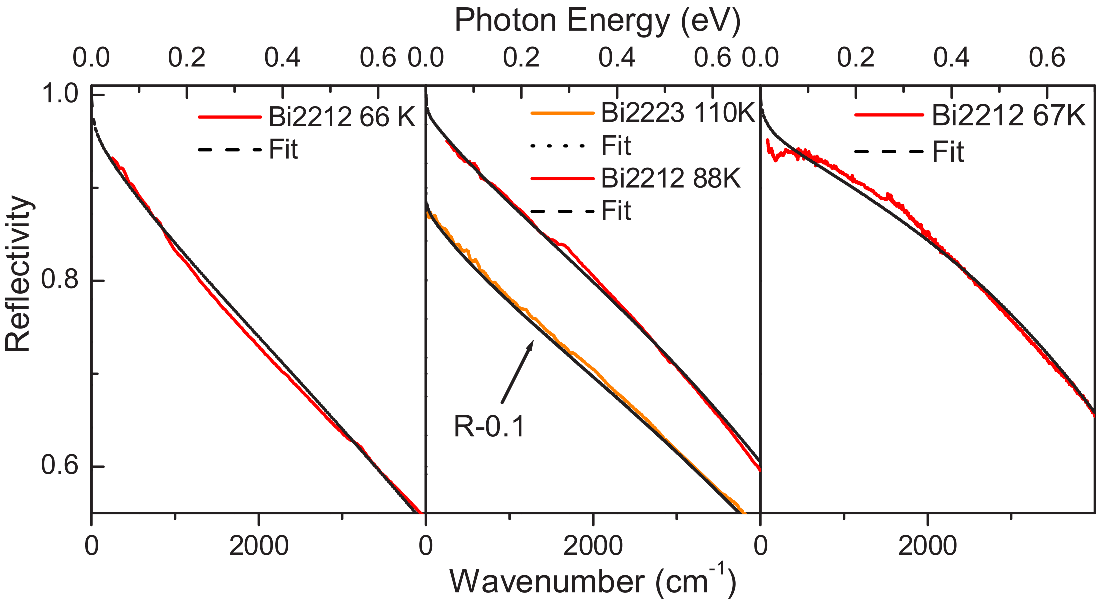

Figure 4.13: The infrared reflectivity of Underdoped Bi2212, Optimally doped Bi2212 and Bi2223 and overdoped Bi2212 is displayed together with the best fit based on the anisotropic scattering rate model.

strongly overdoped sample. This observation suggests that the powerlaw behavior of the optical conductivity and the anisotropy of the scattering rate on the Fermi surface are intimately related; we shall point out a close connection between these results and very recent ARPES measurements [1] in the discussion.

Bibliography

[1] A. Kaminski *et al.* Phys Rev B **71**, 014517 (2005).

[2] D. van der Marel *et al.* Nature **425** (2003).

[3] S. Sachdev Quantum phase transitions (Cambridge Univ. Press, Cambridge, 1999).

[4] M.A. Quijada *et al.* Phys Rev B **60**, 14917 (1999).

[5] D. van der Marel, Phys Rev. B **60**, 765 (1999).

[6] L. B. Ioffe and A. J. Millis, Phys Rev. B **58**, 11631 (1998).

[7] For instance, the physical meaning of the extracted $1/\tau(\omega)$ and $m^*(\omega)$ in the case of two independent conductivity bands becomes much less clear.

[8] T. Timusk and D. Tanner, *Optical properties of high temperature superconductors III*, ed. by D.M.Ginsberg (World Scientific, Singapore, 1992), Chap. 5.

[9] T.Timusk *et al*, J. Phys. Chem. Solids, **59** 1953 (1998).

[10] O. K. Andersen *et al*, J. Phys. Chem. Solids, **56** 1573 (1995).

[11] O. K. Andersen *et al*, Phys. Rev. B **49**, 4145 (1994).

[12] C. Baraduc, A. El Azrak, N. Bontemps, J. of Supercond **9**, 3 (1996).

[13] P. W. Anderson, Phys. Rv. B **55** 11785 (1997).

[14] Z. Schlesinger *et al*, Phys. Rev. Lett. **65**, 801 (1990).

[15] H. J. A. Molegraaf, C. Presura, D. van der Marel, P. H. Kes, and M. Li, Science **295**, 2239 (2002).

[16] The opposite statement is also valid: the scale invariance neccesarily requires the power-law behavior of the response functions.

[17] P. Phillips and C. Chamon, Phys. Rev. Lett. **95**, 107002 (2005).

[18] A. Toschi, M. Capone, M. Ortolani, P. Calvani, S. Lupi, and C. Castellani, Phys. Rev. Lett. **95**, 097002 (2005).

[19] A.B. Kuzmenko, Rev. Sci. Instr. **76**, 083108 (2005).

[20] M. R. Norman and A.V. Chubukov. cond-mat/0511584.

[21] P. Anderson. cond-mat/0512471

Chapter 5

The strange case of MnSi

Traditionally, MnSi is considered as a weakly itinerant ferromagnet[1, 2], *i.e.* the spin-polarization is modeled as a relative shift of bands of delocalized Bloch-states for the two spin-directions. At ambient pressure MnSi orders heli-magnetically below T_C=29.5 K, and becomes ferromagnetic in a magnetic field exceeding 0.6 Tesla. The Hall effect and the negative magneto-resistance[3] in the ferromagnetic phase agree well with the theory of spin-fluctuations in itinerant ferromagnetism[1]. Also the inelastic neutron scattering data have been interpreted in this framework[4, 5, 6, 7, 8]. The saturation moment of the magnetically ordered phase is 0.4 μ_B per Mn atom. On the other hand, *ab initio* calculations based on the Local Density Approximation (LDA) indicate a tendency of the Mn-atoms to form a moment close to 1 μ_B if the real lattice constant for MnSi (4.558 Å) is used[19, 20]. A fit of the susceptibility in the paramagnetic phase to a Curie-Weiss law gives 2.2 μ_B per Mn atom[30].

Recently, several properties of MnSi have been discovered which had not been anticipated on the basis of the itinerant model and which remain to be fully understood: Above 14.6 kbar the material enters a phase with partial heli-magnetic order along the (1,1,0) direction[31], where the resistivity is proportional to $\mathrm{T}^{3/2}$ in contradiction to standard notions of a Landau Fermi liquid[32]. A further indication of anomalous low energy scale properties follows from the non-Drude infrared optical conductivity at ambient pressure[33], proportional to $(i\omega)^{-1/2}$. The resistivity suggests that the magnetic scattering is the main source of scattering in MnSi [33]. MnSi shows an itinerant ferromagnetic behavior with a low ordering temperature and it is the ideal playground to investigate in detail the microscopic nature of band magnetism. I will show that difficulties can be encountered already in the description of its ground state. What behaves as a common metal hides important correlations effects.

5.1 Overview on the B20 crystal structure in nature

The geometrical properties:

The B20 crystal structure attracted our attention because of its peculiar geometric characteristics. In fact, we will show that this space group has a marked tendency to give frustrated geometry, in particular when the stoichiometry is 1:1, but also in other cases. The crystal structure of MnSi belongs to the T^4 P_{2_13} space group[34, 35]. Together with MnSi several other compounds involving a transition metal and a Si atom have been found to have the same crystal structure[35]. The unit cell contains 4 Mn atoms at crystallographically equivalent positions.

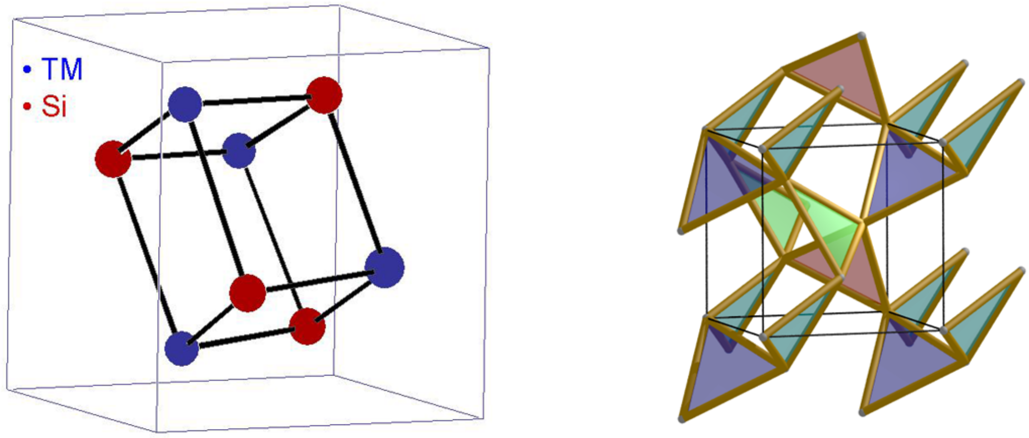

Figure 5.1: Left panel: The T^4 P_{2_13} crystal structure for TM-mono silicides. Right panel: Mn sublattice of MnSi. The corners of the triangles, all of which are equilateral, correspond to the positions of the Mn-atoms.

The sub-lattice of transition metal atoms, displayed in Fig. 5.1, reveals that the basic structural element is an equilateral triangle of 3 Mn atoms. The structure is corner-sharing: Each Mn-atom connects 3 triangles, which occur with 4 different orientations along the body-diagonals of the cubic unit cell. The singly connected loops of the structure shown in Fig. 5.1 contain an odd number of bonds. The structural similarity to the pyrochlore[36, 37], Kagome[38, 39], Gadolinium Gallium Garnet[40], and the β-Mn lattices[41, 42] is a peculiarity that has been overlooked so far.

Geometric frustration:

As far as geometric frustration is concerned, there is a remarkable similarity between the Mn sublattice in MnSi and the Mn^{2+} sublattice in β-Mn (β-Mn is a Mn crystal in which two sublattices of respectively Mn^{2+} and Mn^{3+} ions are intercalated). The latter has been found to be a frustrated quantum magnet by means of transport and magnetic measurements[41, 42, 43]. Taking a closer look (the Mn^{2+} sublattice of β-Mn is displayed in Fig. 5.2) one realizes that while for MnSi, in Fig. 5.1, the first bonds loop connecting one atom with itself is made of three bondings, the next is made of 5, then 7, etc. In β-Mn the second shortest loop is already made of an even number of bondings, 4. This means that this particular structure, the P4132 (213), is less frustrated than the P213 of MnSi, according to a definition of the degree of frustration based on similar arguments[44].

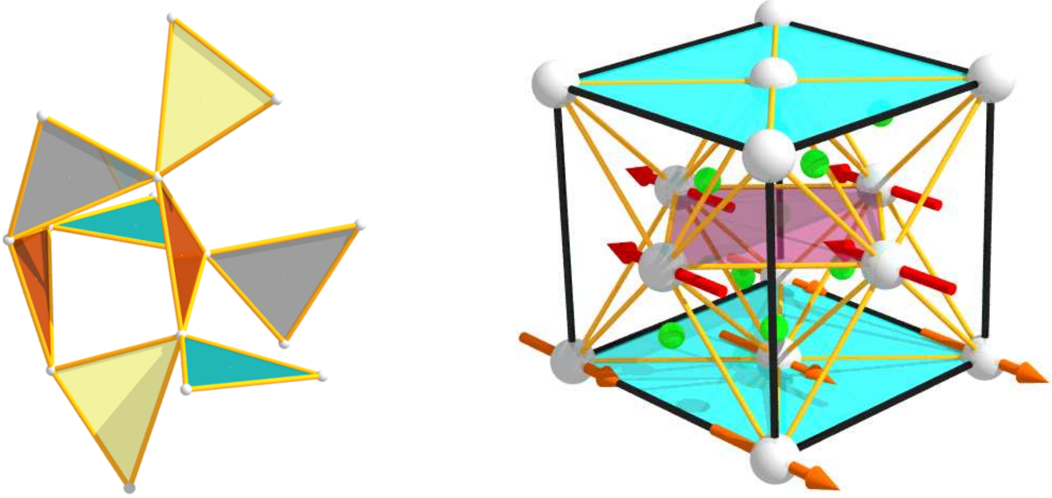

Figure 5.2: Left panel: The Mn^{2+} sublattice of β-Mn. Right panel: the unit cell of PdF2, gray balls are Pd ions, the green ones are Fluorine. The magnetism of PdF2 is depicted with red arrows.

As mentioned above, MnSi orders helimagnetically below 30 K. In MnSi helimagnetism has been explained in terms of the Dzyaloshinskii-Moryia interaction. However, this interaction is known to be small in the system. While we do not want to question this interpretation, we would like to point out that, since the ordering temperature is so low, many different effects could play a role in the magnetism of MnSi. On general grounds, the exchange interaction in MnSi gives an energy scale around 300 meV, the transition temperature is about 30 K (2-3 meV, comparable to the value of the Stoner boundary), and the local moment is strongly reduced in the ordered state (0.4-0.5μ_B) with respect to the paramagnetic state (2.2 μ_B). These observations evidence that a competition between different processes is taking place. Different exchange interactions in different directions is a plausible scenario. This anisotropy combined with the spin-orbit interaction leads to the Dzyaloshinskii-Moryia interaction; both the anisotropy and the spin orbit interaction are found to be small but not negligible in MnSi, see the discussion of the NMR experiments in section 5.5.1. Geometric frustration could also play a role, however, given the three dimensionality of the B20 structure, its investigation is complicated. It is difficult to find a smoking gun indicating that frustration plays a role, because the aforementioned triangles are oriented in four different directions. In a scattering experiment, one would like to use a geometry that allows to look at the response of the triangles lying in a certain direction, since four orientations are found in 3 dimension this is not possible. There will always be an admixture of the response coming from triangles oriented in other directions not perpendicular to the considered one. Moreover, the itinerant character of MnSi complicates the theoretical analysis of this aspect.

An overview of other B20 materials:

Given the complexity of the magnetism observed in MnSi, it is interesting also to take a look at other materials that share this peculiar crystal structure. Some indications of what is relevant for MnSi's magnetism could come from the behavior of related materials. B20 binary compounds have not been investigated much so far, for this reason we report the Density of States of some of them in order to have a rough idea whether something unexpected emerges form these other materials or not. Here we focus on those which are composed by just two elements in the ratio 1/1. This is because in this case the sublattice of each element will have the frustrated geometry discussed above. It has been found [45] that for two elements in order to crystallize in the $P_{2_1 3}$ space group a condition on the ratio between the atomic radii has to be satisfied. In particular the ratio r_A/r_B has to be larger than 0.77 and smaller than 1.365. We list all known $P_{2_1 3}$ binary compounds, and one can see that they all satisfy this rule.

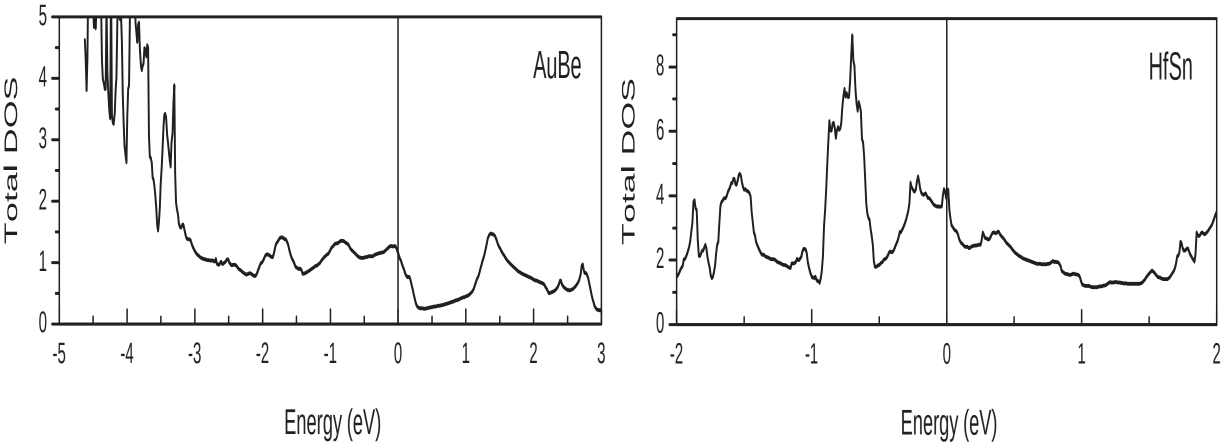

Figure 5.3: Left panel: The density of states of AuBe. Right panel: The density of states of HfSn.

Compound	a (Å)	r_A/r_B
HfSn	5.594	1
CrSi	4.629	0.96
CrGe	4.789	0.92
MnSi	4.557	0.98
TcSi	4.775	1.02
ReSi	4.775	1.04
FeSi	4.488	0.96
FeGe	4.7	0.98
RuSi	4.703	0.24
RuGe	4.846	1.01
OsSi	4.729	0.97
CoSi	4.447	1.02
RhSi	4.675	0.94
RhSn	5.132	1.01
NiSi	4.446	0.85
PdGa	4.89	0.94
PtAl	4.864	0.91
PtGa	4.91	0.97
PdHg	5.22	0.915
PtMg	4.863	0.94
AuBe	4.668	1.25

The interatomic distance for these compounds is between 2.2 and 3 Å, which means that when this structure is formed the bond length is rather small. Consequently, the orbitals of the elements involved in the bonding hybridize strongly, and these compounds usually have a very covalent nature. In the case of transition metal mono silicides, for example, one has elements with the tendency to localize electrons, transition metals, forming rather covalent bonds with silicon. This unusual interplay between localization and covalency, together with the geometrical frustration of the transition metal sublattice, leads to several unexpected phenomena as will be discussed in the following sections. In the list of compounds above, there are many systems whose electronic structure is unknown, besides the elementary electron counts that one can do knowing the formula unit. On the other hand, among the studied ones, some transition metal mono-silicides have shown non Fermi Liquid behavior[3, 33]. In Fig. 5.4 one can see a classification of several non-octet binary compounds in terms of their density-functional radii[69]. Non-octet compounds are those whose outer electronic shell is not composed by filled s and p orbitals (octet). The B20 binary compounds are found all in a confined region of this plot, except for AuBe, which is a metal with low density of states close to the Fermi level, see Fig. 5.3. In Ref. [69] a theoretical motivation is discussed for the fact that the B20 binary compounds are formed when the ratio between the radii discussed above is satisfied. Different crystal structures are found to form preferentially when similar conditions on the relative radii are satisfied, giving the possibility to find systematics among them.

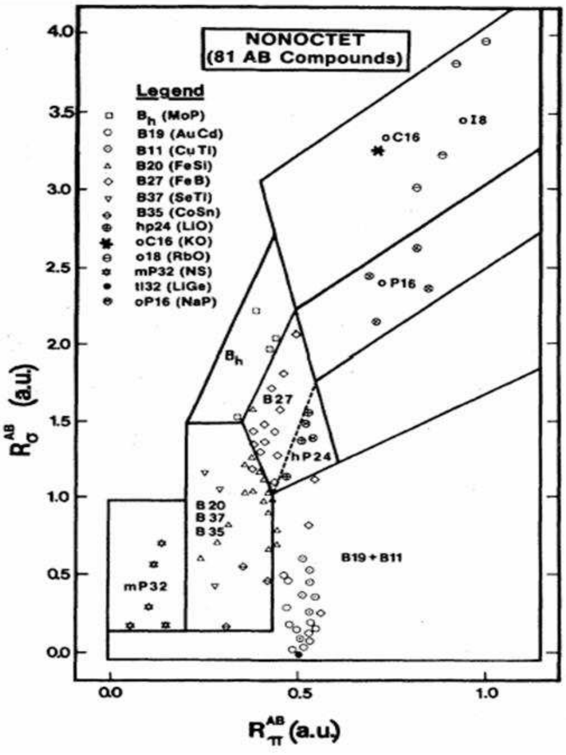

Figure 5.4: Structural separation plot for the 81 binary nonoctet compounds. This graph has been taken from Ref. [69]

In Fig. 5.5 one can see the effect of the chemical pressure on the transition metal ion in the density of states predicted by LMTO calculations for RSi, where R = Mn, Tc, Re. MnSi is found to be ferromagnetic, while TcSi and ReSi are not. The gap in the density of states, which causes FeSi to be an insulator, is found to be larger in TcSi than in MnSi; accordingly, a similar gap has been observed in RuSi [70], which is exactly one element below Fe in the periodic table. This observation supports the idea that FeSi and RuSi are band insulators, stressing the importance of the itinerant character of the Transition-Metal mono-silicides. In Fig. 5.5 the effect of the chemical pressure on the Si ion in the density of states predicted by LMTO calculations for MnR, where R = Si, Ge, Sn, is displayed. MnGe and MnSn are also ferromagnetic, while the aforementioned gap in the density of states disappears. MnGe and MnSn have never been grown to the best of my knowledge, but given the systematic classification given above they could exist. At last, we report the density of states of HfSn which is the only B20 binary compound known which contains a transition metal of the fourth group, in Fig. 5.3. This material is metallic according to LMTO calculations, it is not spin polarized and has the Fermi energy exactly in a peak of the DOS.

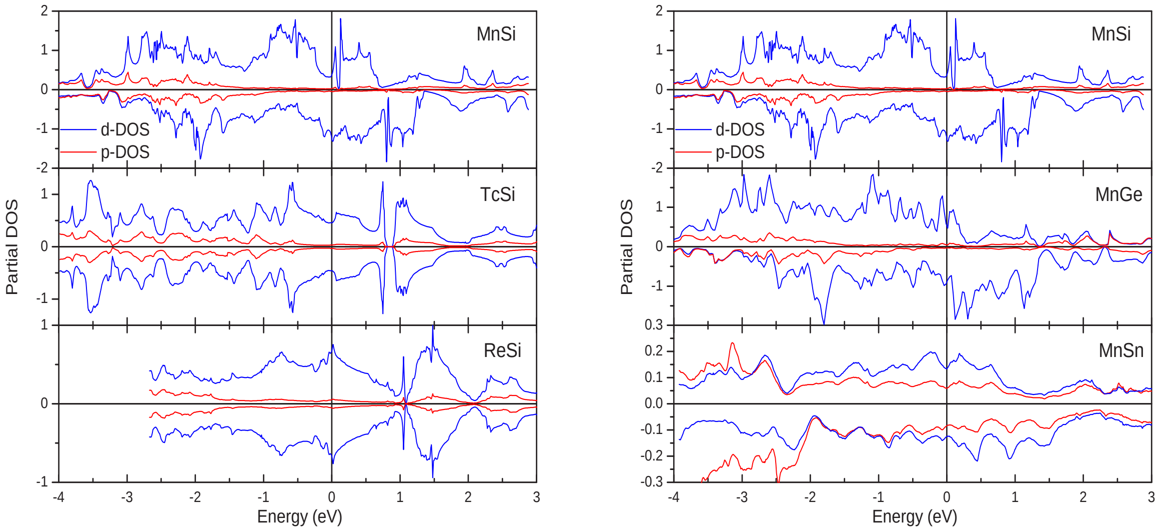

Figure 5.5: Left panel: The spin polarized TM - d-density of state and the Si p-density of state for MnSi, TcSi and ReSi. Right panel:The spin polarized Mn - d-density of state and the Si,Ge,Sn p-density of state for MnSi, MnGe and MnSn.

One may go further and ask what happens relaxing the condition, for example, on the stoichiometry being 1:1. The overall point of view I proposed above required an inspection of the periodic table, it is easy to imagine how many more compounds one can find considering also formulas of the kind AB_2 AB_3 etc. We do want to point out a few more interesting examples of the B20 crystal structures found in nature: Following the simple argument about the bond length, one can intuitively think that in the case of magnetic elements these materials should have fairly large exchange energies. This is true in MnSi, while the magnetic ordering temperature is much lower than the exchange value would suggest. This has been interpreted as a signature of weak itinerant magnetism. However, the same effect could be due to geometric frustration or competing ordering mechanisms. In the high pressure phase of PdF_2, one observes the B20 crystal structure again; this time though, due to the stoichiometry 1:2 between the transition metal and the F atom, the transition metal sublattice is not a corner sharing triangular network. One can see in Fig. 5.2 that the palladium sublattice (gray balls) forms an edge sharing equilateral triangles network (much less frustrated then the corner sharing one). In this compound neutron scattering experiments revealed an antiferromagnetic ordering, as depicted in Fig. 5.2, perpendicular to Pd planes which are ferromagnetically ordered squares. The Neel temperature of this material is around 200 K, which is fairly high. My suggestion is that here frustration does not lower the magnetic ordering temperature considerably because of the edge sharing network geometry. I want to stress that this is just a speculation, PdF_2 to my best knowledge has been studied very little so far [1].

5.2 Transition Metal mono-silicides Phase diagram

The transition metal mono silicides family crystallizes in the B20 structure. CrSi, MnSi, FeSi, CoSi and NiSi belong to this family. CrSi has not been studied exhaustively while NiSi stabilizes in the B20 structure only when small fractions of Al are substituted on the Ni site[45]. In the lower panel of Fig. 5.6, we show the phase diagram for the compositions ranging from Mn to Fe to Co silicide[3]. Depending on the substitution ratio of the transition metals one can find helimagnetism, in MnSi, in $Fe_xCo_{1-x}Si$ around x = 1/2 and $Mn_xFe_{1-x}Si$ around x = 0.9. The magnetism in these compounds has been described in the framework of weak itinerant ferromagnetism[1]. FeSi is a small gap semiconductor and CoSi is a diamagnet. In this thesis we will focus our attention on the stoichiometric compound MnSi, and I will discuss some related issues in FeSi and CoSi. For this purpose, in the topmost panel of Fig. 5.6, I display the phase diagram of MnSi as obtained by transport measurements [32]. In MnSi the helimagnetic ordering is found at ambient pressure below 30 K. This ordered state is destroyed above 14 kbar of hydrostatic pressure. In the high pressure region a non Fermi Liquid behavior is found in transport; this region corresponds to a particular magnetic phase observed with neutron diffraction in recent experiments under pressure[31]. These experiments have shown that the magnetic ordering is not suppressed by pressure, but a new state is formed with peculiar characteristics: while in the ordered phase the axis of the helixes, which have a 180 Å pitch, are all oriented among each other, above 14 kbar the helixes still exist but their orientation is random. MnSi shows a negative magnetoresistance, which can be explained by a suppression of spin fluctuations in magnetic fields in the context of Moriya's spin fluctuation theory for weak itinerant ferromagnets[1]. On the other hand, very similar magnetic properties are observed in $Fe_{1-x}Co_xSi$ where magnetoresistance is shown to be positive[3]. Later in this chapter, some data measured in very high magnetic field, where also MnSi shows a positive magnetoresistance, will be presented.

5.3 MnSi electronic structure

Nascimur uno modo, multis morimur. Transition metal mono silicides share the same band structure, but because of the different position of the Fermi energy they show very different properties. For example MnSi is a good metal, FeSi is a semiconductor and CoSi is a bad metal. In this section the electronic structure responsible for this

---

[1] I would like to mention that solid CO and NH_3 are also B20 compounds

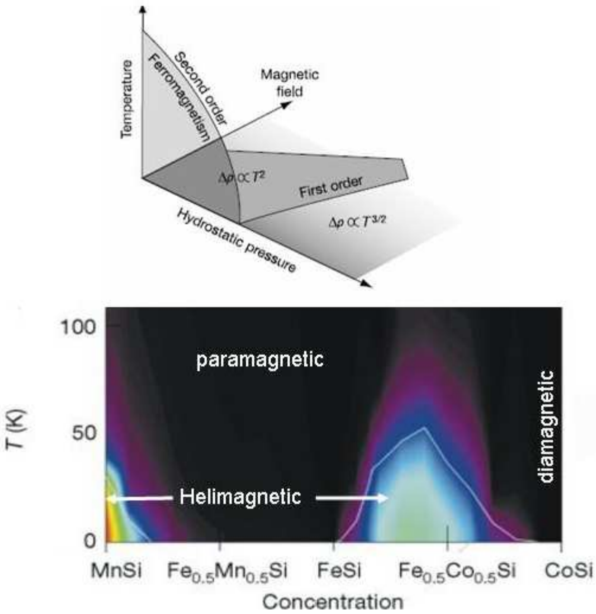

Figure 5.6: Upper panel: phase diagram for MnSi, taken from Ref. [32]. Lower panel: phase diagram for the silicides series, taken from Ref. [3]

variety of behaviors is discussed.

5.3.1 Band structure calculations

The band structure for MnSi, FeSi, $Fe_xCo_{1-x}Si$ and CoSi has been reported by Nakanishi in Ref. [48]; I display these results in Fig. 5.7. One can see that MnSi and $Fe_xCo_{1-x}Si$ have several bands crossing the Fermi level and behave as good metals, while FeSi has a small gap of 130 meV and it is a semiconductor; CoSi has a low density of states at the Fermi level and is a bad metal. In MnSi the minimum for the LDA energy is found for a moment around $1\mu_B$ per Mn atom, far too high with respect to the experimental value of 0.4. Usually LDA calculations are performed changing the lattice parameter in order to match the experimental value for the ordered moment[20]. A detailed study of the Fermi surface of MnSi has been reported in Ref. [19]. In the range between -11 and 4 eV one can see the 36 bands present in the unit cell of MnSi: a unit cell contains four formula units of MnSi, each Si atom contributes 4 electrons ($3s^2$, $3p^2$) to the valence band, each Mn atom contributes 7 electrons ($4s^2$, $3d^5$) to the valence band. These 11 states × 4 formula units /2 spins give 22 bands. Together with the Si and Mn empty states one has 36 valence-conduction bands. The Si 3s bands are found between -11 and -6.5 eV, the Si 3p ones are between -6.5 and -3 eV below the Fermi energy and over 1 eV above the Fermi level. The 3d bands are confined between -3.5 and 1 eV, the width of

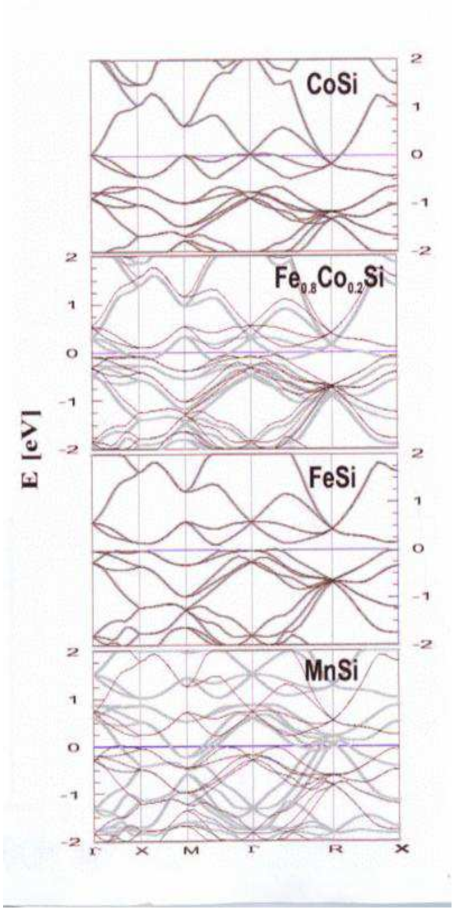

Figure 5.7: The band structure of MnSi, FeSi, $Fe_xCo_{1-x}Si$ and CoSi. Graph taken from Ref.[48].

the 3d bands has been estimated to be around 2 eV, performing a band calculation excluding the Si atoms from the crystal. A remarkable feature observed in this study is that because of the particular symmetry of the B20 structure, the bands tend to stick together at certain symmetry points. In Fig.5.8 one can see that at the X, M and R point several bands merge into a degenerate one. The B20 structure can be thought of as a deformation of the rocksalt one. This simple cubic structure becomes the B20 when distorted along the [1,1,1] direction. One can calculate the band structure for a rocksalt MnSi in order to see the effect of the particular B20 deformation on the electronic structure. Usually in cubic crystals flat bands are observed, as seen in the rocksalt MnSi; this effect is due to the cancelation of some $d-d$ hopping processes in a cubic environment, and is a cause of localization. In the rocksalt structure the degeneracy at the X and M point is also lifted while at the R point no splitting is observed; the dispersionless bands are modified by the B20 deformation and a more conventional dispersion for a metal is found, even if some tendency to flatten is observed around the high symmetry points. This particular band sticking around high symmetry points has consequences on the Fermi surface topology. Once the spin polarized Fermi surface is calculated for the majority and

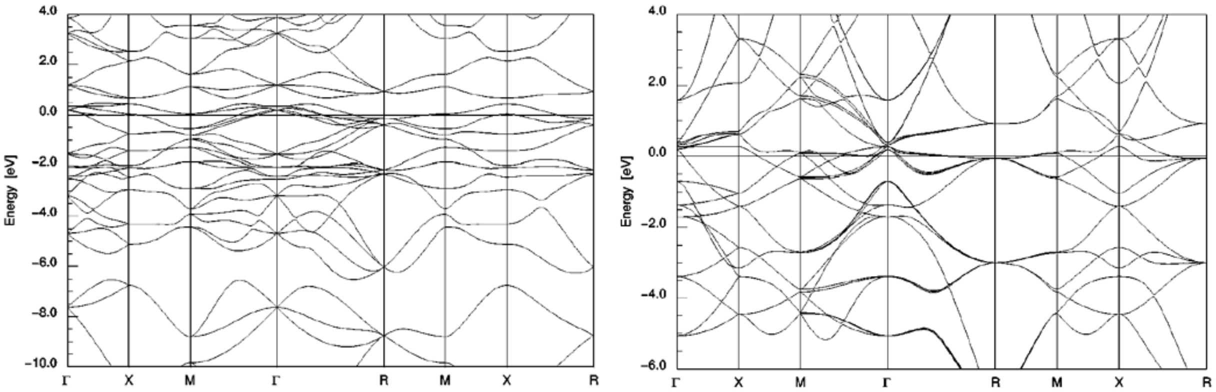

Figure 5.8: The band structure of MnSi in its B20 symmetry (left panel) and in the rocksalt symmetry(right panel). Graph taken from [19]

minority spin bands, one can plot the corresponding Fermi surfaces. In Fig. 5.9 we show the two spin polarized Fermi surfaces which are given by three bands each, these graphs are taken from Ref. [19]; the three contributions are plotted separately. One can see two main features: for the majority spin surfaces one has two "jungle gym" type of surfaces which do not intersect the zone faces perpendicularly; the normal situation is restored when one considers the summation of these surfaces. In fact, as one can see in the graph the two jungle gym surfaces have opposite curvatures at the zone faces. This though, could have effects on the cyclotron orbits observed in the de Haas van Alphen measurements, which I will discuss in the next paragraph. In the minority spin surfaces one observes strong nesting phenomena, the authors suggest that this could have an impact on the scattering processes[19].

5.3.2 De Haas van Alphen measurements, Positron Annihilation Spectroscopy, Optics

Experimental studies of MnSi Fermi surfaces have been carried out by means of low energy and high energy probes. In this section I will discuss the main results obtained by means of the low energy experiments. The Positron Annihilation Spectroscopy (PAS) data have been obtained very recently and allow an extensive comparison between the theoretical Fermi surface and the experimental one. In 1986 Taillfer, Lonzarich and Strange reported the de Haas van Alphen spectra (dHvA) of MnSi[2]. They identified three main dHvA frequencies and compared them to the predicted orbits around the Fermi surface. In table 5.1 I show the comparison between the experimental cyclotron frequency and masses and the calculated values. One can see that while the frequency of the orbits is in good

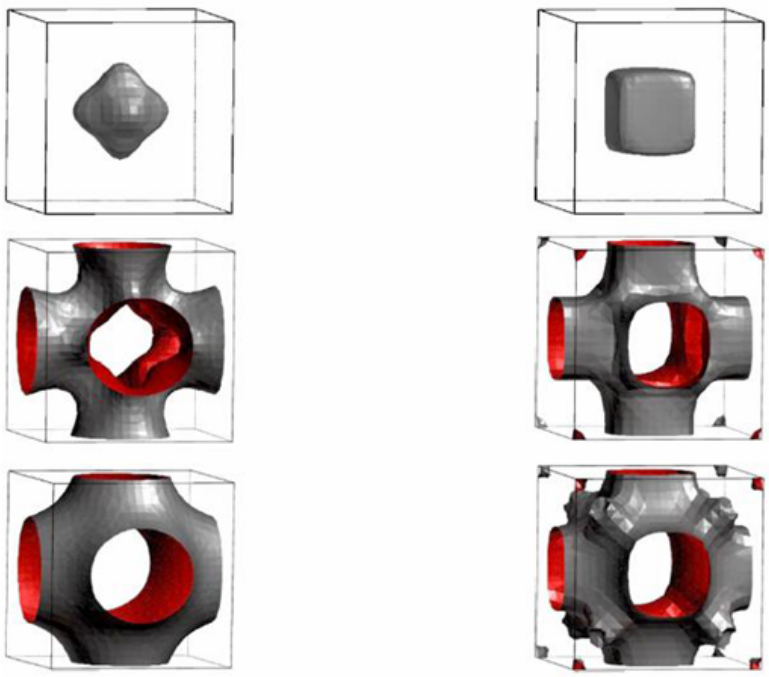

Figure 5.9: The spin polarized Fermi surfaces of MnSi. In the left panel the majority spin bands and in the right panel the minority spin bands. Graph taken from [19]

Table 5.1: The dHvA experimental orbits together with the predictions of LDA calculations

	Frequency (MG)		Cyclotron masses (m_0)	
orbit	Exp.	Calc.	Exp.	Calc.
α	0.7	0.3	2.4	0.5
η	29	30.7	8	2.4
μ	64	68	14.5	3

agreement with the theory, the masses are far higher than the theory could predict and are the highest cyclotron masses reported for a transition metal, as the authors point out. The average mass enhancement factor is found to be around 4, in agreement with the enhancement factor of the linear coefficient of specific heat[49] and optical measurements[33]. Moreover in order to interpret these experiments a rigid shift of the bands was needed in order to match the experimental observations.

The experimental investigation of MnSi Fermi surface has been carried out by means of Positron Annihilation Spectroscopy (PAS) by J. Laverock and S. Dugdale in Bristol. PAS is a well established technique that is particularly suitable for 3D materials where large high quality single crystals are available. In particular, while the dHvA

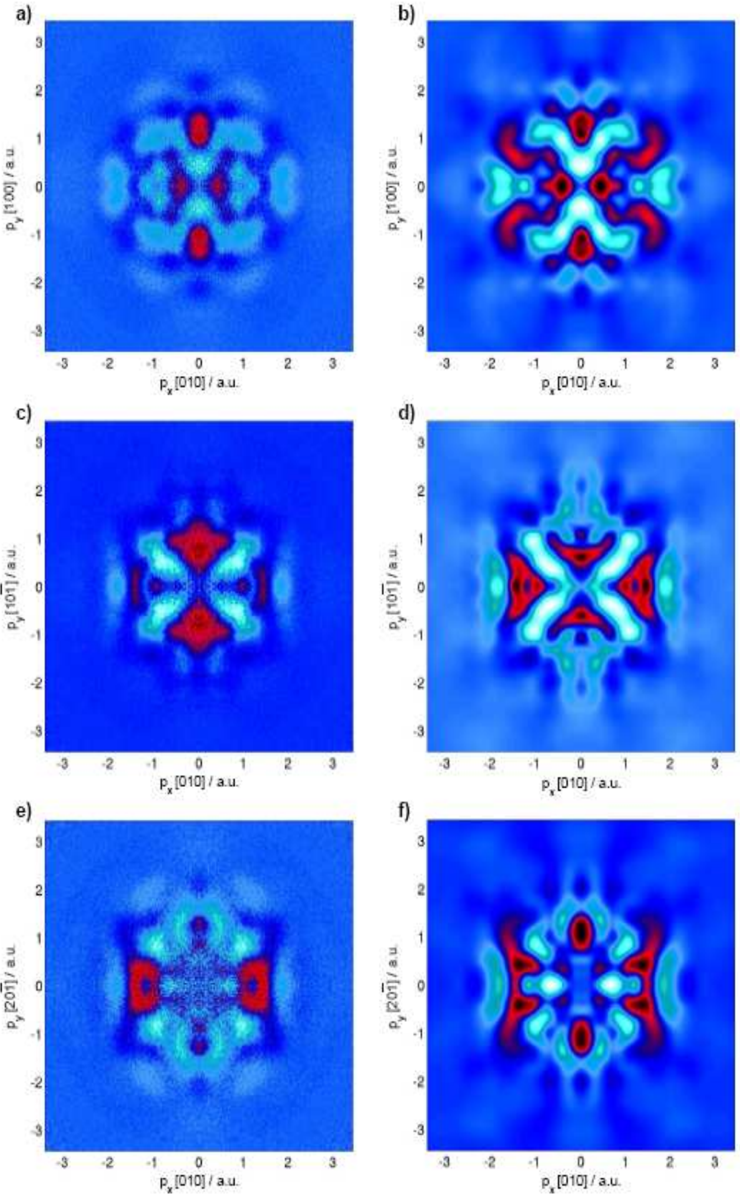

Figure 5.10: The theoretical (right panel) and experimental (left panel) radial anisotropy of the momentum density for the (a,b) [001] direction, (c,d) [101], (ef) [102]. Data measured by J. Laverock and S. Dugdale in Bristol, obtained in private communications.

technique is very sensitive to impurities, PAS is relatively unaffected by impurities as long as they do not cause the formation of vacancies or other open-voulme type of defects. MnSi is a very good candidate since large single crystals can be grown with residual resistivity as low as a few $\mu\Omega$/cm. For a detailed description of this technique I suggest reference [50] and references therein. First, we show a comparison between the experimentally determined momentum density and the calculated one, Fig. 5.10. Due to the effect of the particular B20 symmetry, the [100] and the [001] directions are not equivalent. The B20 structure arises from a set of point group operations which are simple rotations about the [111] direction. Because of this, the usual reflection plane that maps $(p_x, p_y, p_z) \to (p_x, p_y, -p_z)$ is no longer there. This happens even if in the paramagnetic state time-reversal restores the inversion center in the reciprocal space[2], $(p_x, p_y, p_z) \to (-p_x, -p_y, -p_z)$. The agreement between the theoretical anisotropy of the momentum density and the experimental one is qualitatively good, however, some deviations are observed especially in the relative intensities of the prominent features. The radial anisotropy of the momentum density, displayed in Fig. 5.10, has components coming from both filled and unfilled bands. Some of these components are coming from the Fermi surface, therefore it is possible to recover the shape of the Fermi surface from the momentum density distribution. The results of this procedure are shown in Fig. 5.11 together with the LMTO paramagnetic calculation performed for a lattice constant of 4.39 Å. One can see that the experimental Fermi surface is significantly different from the theoretical one. It is remarkable that the experimental Fermi surface is almost identical to the minority spin Fermi surface in the ferromagnetic state reported in Ref.[19]. An agreement between the LMTO result and the experiment is obtained considering a rigid shift of the bands of 0.2 eV. However, this approach does not conserve the number of particles.

The purpose of this short report on the PAS experiment, is to show that band calculations can capture some of the features of the electronic structure of MnSi. However, consistent with previous XAS and XPS results, some important deviations are present.

By means of optical spectroscopy it has been shown [33] that the low frequency (10-100 meV) reflectivity does not obey the Hagens-Ruben dependence usually observed in metals. Accordingly the scattering rate shows a non Fermi-liquid frequency dependence and the low temperature effective mass is enhanced by a factor of 4, in agreement with the dHvA experiments.

---

[2] This anisotropy is due to the way in which positrons probe the electronic structure in this peculiar symmetry. No electronic anisotropy is observed.

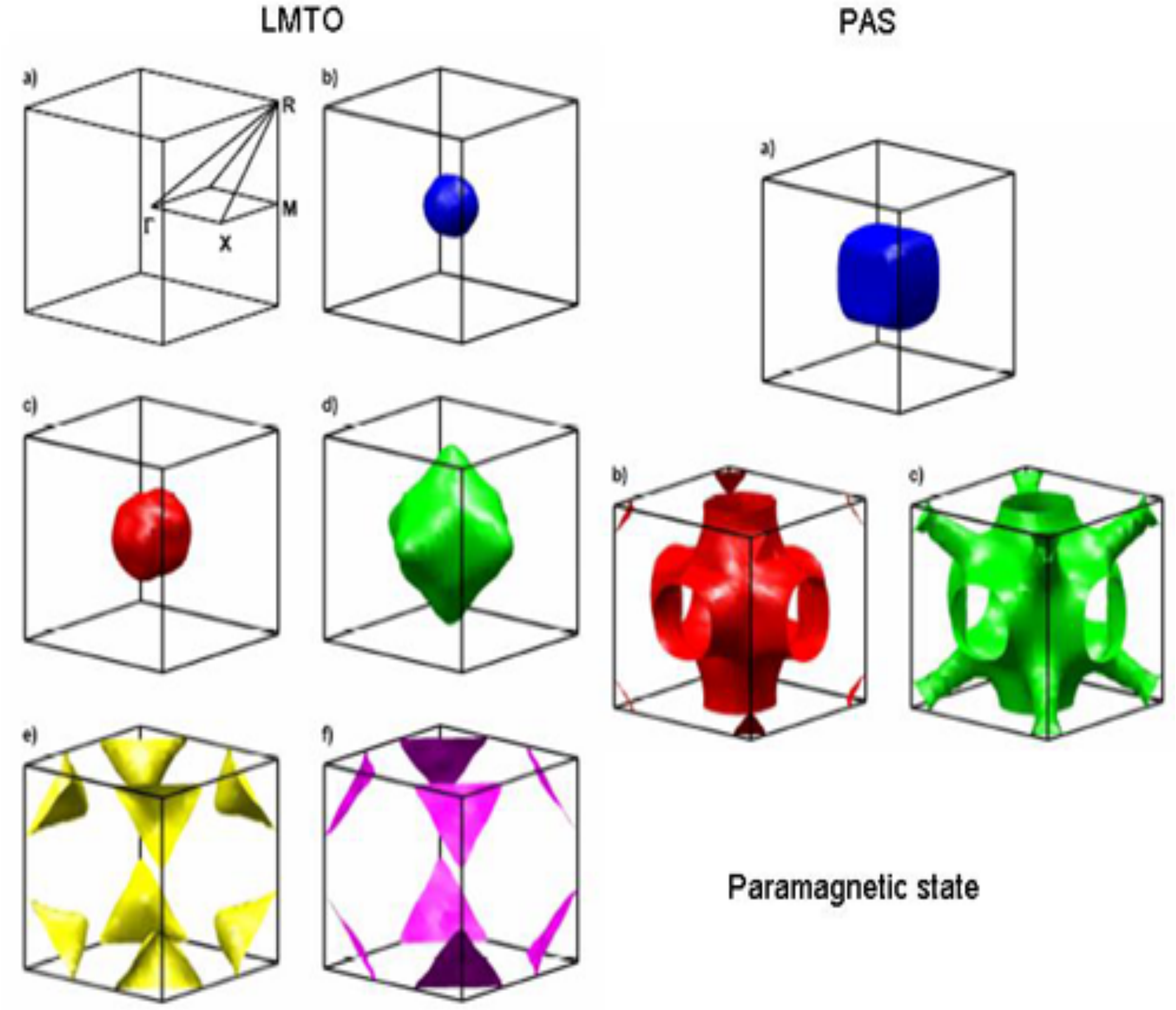

Figure 5.11: Left panel: The Fermi surface originating from the different bands crossing the Fermi level calculated with LDA. Right panel: The experimentally derived Fermi surfaces. Both data and experiments are obtained from J. Laverock and S. Dugdale in Bristol, private communications.

5.3.3 X-ray Absorption Spectroscopy, Core level photoemission and Valence band photoemission,

In this section we investigate the electronic structure of MnSi by means of high energy probes. We will show results obtained by X-ray Absorption Spectroscopy (XAS), core level photoemission (XPS) and valence band photoemission (VBP). While the low energy properties of MnSi have been seen to match fairly well with the single particle picture, although an indication of correlation effects already come from the optics experiments, we will show that on a higher energy scale the electron-electron correlation effects manifest themselves dramatically. In order to substantiate these findings we will show a systematic study of the family MnSi, FeSi and CoSi. The last has never shown any unexpected property and accordingly we succeed describing the spectra measured on CoSi by means of the single particle approximation. We will show that the correlation effects are evident in MnSi and FeSi while they are absent in CoSi.

MnSi, FeSi and CoSi high quality single crystals were measured. All samples were characterized by x-ray diffraction, EDX elemental analysis and electrical resistivity. The residual resistivity of all MnSi samples was less than 2 $\mu\Omega cm$. We will describe in detail the experimental procedure for the MnSi samples. All other compounds have been measured in the same conditions.

The experiments were performed at the BACH beam line [51] of the ELETTRA synchrotron in Trieste. XAS was performed in total electron yield (TEY), measuring roughly the first 50 Å of the surface, and total fluorescence yield (TFY), measuring down to 200 nm in the bulk. The XAS spectra were normalized to the incident photon flux, the resolution in TEY was 150 meV and 400 meV in TFY. The fluorescence experiments were done recording the fluorescent decay of Mn $3d \longrightarrow 2p$ and $2p \longrightarrow 3s$ levels on a CCD detector.

Large single crystals were cleaved in situ prior to the measurements in order to obtain clean surfaces; the surface quality was checked with XPS, shown in Fig. 5.12. The base pressure in the measurement chamber was $1 \cdot 10^{-10}$ mbar. XAS and XPS spectra were recorded at room temperature within minutes after cleaving. The contamination of the surface before and after cleaving was checked by oxygen and carbon $1s$ photoemission. The cleaved surface of the sample was scanned spatially with steps of 100 μm and XPS was recorded at each position. This analysis showed that a significant carbon contamination is present on the border of the sample. This contamination affects dramatically the shape of the TEY XAS. Only at least 150 μm away from the sample's border, where the XPS reveals a very clean surface, we could have a TEY spectrum in agreement with the TFY one, representative of the bulk properties of the material. In the XPS spectra, recorded in the middle of a cleaved sample, the oxygen and carbon $1s$ lines are completely suppressed with respect to the non cleaved sample, as shown in Fig. 5.12. The analysis of the surface revealed

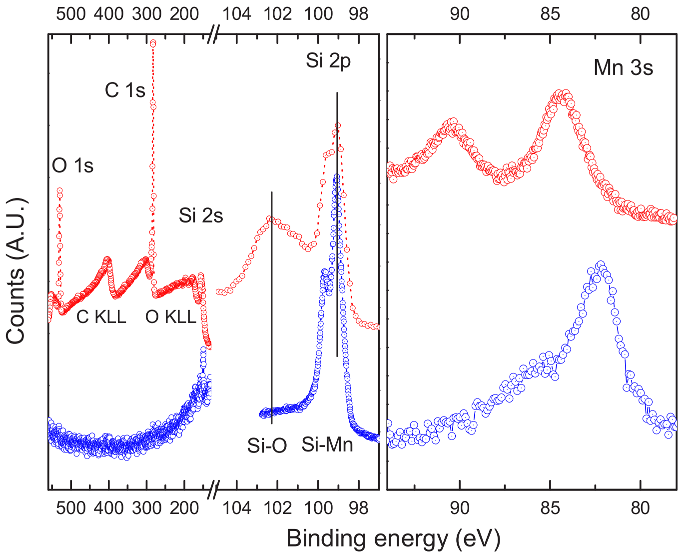

Figure 5.12: XPS spectra of MnSi before and after cleaving. In the right part of the figure one can see the high resolution spectra of the Mn 3*s* levels measured with an incident photon energy of 418 eV and the Si 2*p* levels measured with an incident photon energy of 196 eV before cleaving and 142 eV after cleaving; in the left part a survey from the Si 2*s* to the O 1*s* is displayed measured at 655 eV incident photon energy. The blue curve represents the spectrum after cleaving, the red curve was recorded before cleaving. After cleaving the high binding energy component of the Si 2p line is suppressed , the Mn 3s level splitting diminishes and the C and O 1*s* lines are also suppressed.

that carbon, MnO and SiO_2 are the main contaminants. The XPS of Si 2p levels shows a component around 102 eV associated to SiO_2; the Mn 3s splitting on the sample before cleaving was 6.3 eV, in agreement with earlier reports for MnO [52]. In the cleaved sample the high binding energy peak of the Si 2p level is suppressed, the Mn 3s levels splitting diminishes to a much smaller value and the carbon and oxygen 1*s* lines are suppressed.

In Fig. 5.13 we display the Mn $L_{2,3}$ XAS spectrum of MnSi measured both in TEY and TFY; one can see that the two spectra are almost identical, indicating that we are probing indeed the bulk. The two main peaks correspond to the $2p_{1/2}$ (642 eV) and $2p_{3/2}$ (653 eV) spin-orbit split components of the 2p core level. In a one particle picture these two edges have the same spectral shape, as illustrated by a first principles calculation using the Local Density Approximation (LDA, black line in Fig. 5.13). Self consistent LDA-LMTO (Local Density Approximation - Linear Muffin Tin Orbital) calculations have been performed for 64-atom supercells; one of the Mn atoms has a core hole. The groundstate of the calculation was ferromagnetic, adopting three different states of magnetic polarization characterized by local moments of 0.4, 0.8 and 1 μ_B, labelled as such in Fig. 5.13. The XAS spectrum

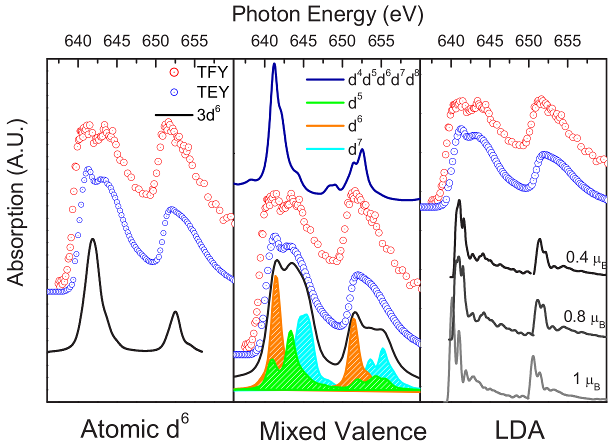

Figure 5.13: Left panel: Mn $L_{2,3}$ edge measured XAS together with atomic multiplet calculation for a $3d^6$ ground state. The TFY experiment has a resolution of 0.4 eV (red open symbols); the TEY experiment has a resolution of 0.2 eV (blue open symbols). Middle panel: the experimental spectra are plotted together with the Mn mixed valence atomic multiplets calculations in a cubic crystal field (black line); below this line is possible to see the contribution from the different configurations. The dark blue line represents the superposition of the d^4, d^5, d^6 and d^7 configurations with the weights given by the binomial distribution in table 5.2, which correspond to the non interacting particle picture. Right panel: the LDA calculations are plotted for 3 different value of the lattice parameter together with the experimental spectra.

corresponds to a broadened sum of the unoccupied local spin Mn-d DOS functions. A known problem of band calculations in MnSi is the predicted value of the local moment on the transition metal atom [20]. This quantity is strongly dependent on the unit cell dimension and tends to be higher then the measured one when the lattice constant has the experimentally determined dimension of 4.558 Å. We checked the influence of this effect on the XAS spectrum in 3 cases, changing the lattice constant: the local moment of Mn is 0.4 μ_B (the experimentally measured value) for a lattice parameter $a = 4.36$, 0.8 for $a = 4.5$ and 1 μ_B for the measured lattice constant $a = 4.55$. This is shown in the right panel of Fig. 5.13; this effect weakly modifies the XAS spectrum and cannot explain the strong departure from the measured one. It is evident that LDA calculations are narrower and cannot replicate the XAS spectra for MnSi. In the middle panel of Fig. 5.13 we compare the experimental spectra with atomic model calculations performed with a standard computer program [53]. We calculate the XAS spectra for several different configurations: Mn $3d^4, 3d^5, 3d^6, 3d^7$ and d^8 in a cubic crystal field environment of 2.4, 2.6 and 3 eV. Furthermore least mean square fits to the data of the weighted superposition of 4 single valence spectra, d^4, d^5, d^6, d^7 and d^5, d^6, d^7, d^8 were performed. The least mean square routine tends to give a negligible weight to the d^4 and d^8 configurations. We estimate the error bars of this approach as the maximum spread of values obtained for the d^5, d^6, d^7 configurations in the two cases for the 3 mentioned values of the crystal field. The crystal field is estimated from the band splitting observed in the high symmetry points of the band calculations [19]. In the best fit the relative weights of the different valences are found to be: $0\% d^4, 21\% d^5, 55\% d^6, 24\% d^7$, $0\% d^8$ in a crystal field of 2.6 eV. In Fig. 5.14 we plot the inverse of the χ^2 obtained fitting the experimental data to the combination of $d^4 + d^5$, $d^5 + d^6$, $d^6 + d^7$ and $d^7 + d^8$ respectively. This calculation shows that the fitting quality is peaked around the d^6 configuration and supports the conclusion that a large contribution to the XAS spectrum comes from the $3d^6$ configuration.

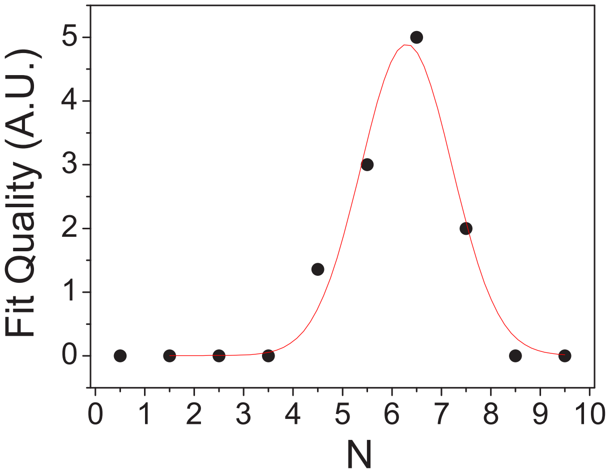

Figure 5.14: We display the inverse χ^2 for the fits to the experimental data of the superposition of $d^4 + d^5$, $d^5 + d^6$, $d^6 + d^7$ and $d^7 + d^8$ respectively.

In the left panel of Fig. 5.13 we display a calculation for an atomic $3d^6$ ground state; this simple calculation also does not represent satisfactorily the experiments. The better agreement between the experiments and the atomic multiplet mixed valence calculation emphasizes two important properties of the electronic configuration of MnSi: (i) the dominant configuration is $3d^6$; (ii) experimentally, the valence fluctuations are given by:

$$p(N) = P(N_0) \cdot exp[-(\frac{N - N_0}{\delta N})^2] \tag{5.1}$$

where $\delta N_{exp} = 0.92$ and $N_0 = 6$. For non interacting particles distributed over 10 $3d$ bands, having the average occupation of 6 electrons ($N_0 = 6$), P(N) is given by the binomial equation:

$$P_{NI}(N) = 0.6^N 0.4^{10-N} 10! \frac{1}{N!(10 - N)!} \tag{5.2}$$

(NI = non interacting), which is to a very good approximation given by Eq. 5.1 with $N_0 = 6$ and $\delta N_{NI} = 2.3$. Thus the value $\frac{\delta N_{NI}}{\delta N_{exp}} = 2.5$ gives a measure of the valence suppression in the ground state. In table 5.2 we show the probability of having N electrons on an ion as a function of the occupation number in a LDA picture, together with the experimental findings. In Fig. 5.16 one can see the fit to Eq. 5.1 for the experimentally derived P(N) and the theoretical ones. The sharp suppression of valence fluctuations in the ground state of Mn observed experimentally is likely the consequence of the on-site Coulomb interaction in the 3d shell of Mn. For the d^6 configuration of Mn $U_{eff} = F_0 - J - C = 1eV$ [54], where F_0 is the intra-shell Coulomb repulsion, J is the intra-shell exchange interaction and C takes into account all the multipole contributions of the Coulomb and exchange interaction. The overall 3d band-width of MnSi is about 6 eV, but this value in part reflects a relative shift of the different group of bands, representing the crystal field splitting. The width of each of the sub-bands is approximatively 2.5 eV, hence U = 0.4W in this compound. This value implies that MnSi has to be considered as an itinerant system. On the other hand the valence fluctuations should be strongly suppressed as compared to the non interacting picture, and this indeed corresponds to what we observed experimentally.

The same procedure is applied to the XAS spectra of FeSi and CoSi. A weighted superposition of $3d^6, 3d^7, 3d^8$ for Fe and $3d^7, d^8, d^9$ configurations for Co, in a cubic crystal field environment of 2.4 eV is fitted to the data. The resulting spectra are shown in Fig. 5.15. One can see that while in MnSi and FeSi the LDA calculations do not reproduce the measured XAS spectra, CoSi data are in good agreement with the single particle calculations. Accordingly, in CoSi the superposition of the different valence configurations closely resembles the LDA calculation. We display in Fig. 5.16 the theoretical and experimental P(N) for all the three compounds, the full-width half maximum of these distributions are displayed in Fig. 5.17. One can see that while in the non-interacting particles scenario the valence fluctuations distribution is narrowing moving toward higher d-occupancy, experimentally we observe the opposite trend. The result of this is that in CoSi the experimental and the theoretical curve are rather close. This is consistent with the fact that the non-interacting particle approach can reproduce very well the XAS spectra of CoSi.

This approach is not an exact treatment of the XAS process, because it neglects the so called interference effects [55]. In fact, we calculate the XAS process for the single configurations d^5, d^6, d^7 etc..which represent the spectra associated to the transitions: $2p^6\,3d^5 \longrightarrow 2p^5\,3d^6$, $2p^6\,3d^6 \longrightarrow 2p^5\,3d^7$, $2p^6\,3d^7 \longrightarrow 2p^5\,3d^8$, etc... Strictly speaking, a linear combination of these spectra does not represent the process $2p^6$ ($3d^5$, $3d^6$, $3d^7$) $\longrightarrow$ $2p^5$ ($3d^6$, $3d^7$, $3d^8$). In the presence of a core hall in fact, the energy of the different states are shifted, causing the interference effects, as such that the relative weights of the different configurations in the overall process are going to be different than what one would estimate starting from the single valence scenario. On the other hand, this effect is not going to modify the shape of the single valence

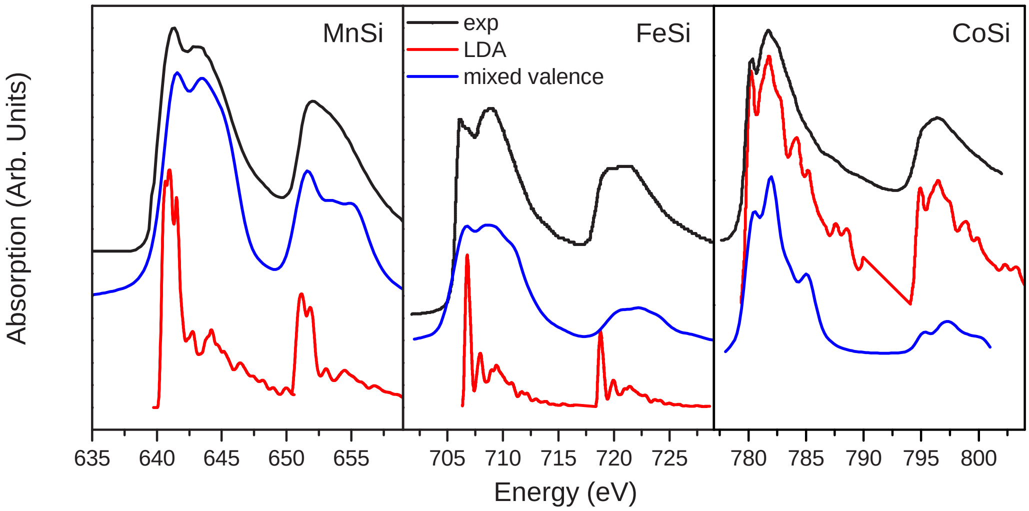

Figure 5.15: The XAS spectra of Mn, Fe and Co are displayed together with cluster LMTO calculations and mixed valence calculations based on the Cowan code[53]. The configurations mixed are d^5,d^6,d^7 in Mn, d^6,d^7,d^8 in Fe and d^7,d^8,d^9 in Co

spectra themselves; we know that the XAS spectra for different configurations have spectral weight at different energies, for example the $3d^4$ configurations has spectral weight between the two spin-orbit split components which is not present in the $3d^5$ spectrum [62]. For this reason, it is improbable that the interference effects can cause other configurations to be relevant component of the superposition of states that we consider. We believe that these effects could certainly cause somewhat different numbers for the weights of the configurations without affecting our main conclusions. On the other hand, our approach allows one to fit the data to the multiple valence calculations with a small number of fitting parameters, 6 in the case of 3 valences.

In Fig. 5.18 we present the photoemission spectrum of the Mn 3s core level measured at an incident photon energy of 418 eV and the fluorescence spectrum measured at a photon energy of 660 eV; since photoemission is a very surface sensitive technique, we cross check our results acquiring the corresponding fluorescence spectrum when possible. The Mn 3s photoemission shows a shoulder on the high energy side of the spectrum. Most likely, the mixed valence ground state we discussed before is responsible for this weak shoulder visible in the 3s spectrum. The asymmetry of the 3s photoemission in insulating Mn compounds, such as MnO, MnF_2 or manganites, has been shown to be caused by the many-body interaction between the core-hole and the localized 3d electrons [52, 57]. In this case the role of the exchange interaction is predominant and, when the orbital moment does not contribute to the

Table 5.2: Theoretical P(N) assuming non interacting particles, [$P_{NI}(N)$], experimental P(N) obtained from the mixed-valence fit to the XAS spectrum, [$P_{exp}(N)$]. The values of $\Delta(N)$ correspond to the shift of the energies $E(2p \longrightarrow 3d^{N+1})$, with respect to the output of the Cowan code, of the final state multiplets; the cubic crystal field parameter was 2.6 eV for all configurations.

N	$P_{NI}(N)$	$P_{exp}(N)$	$\Delta(N)$
0	0.0001	-	-
1	0.0015	-	-
2	0.011	-	-
3	0.042	-	-
4	0.111	-	-
5	0.193	0.21	2
6	0.251	0.55	0.38 eV
7	0.215	0.24	3.72 eV
8	0.121	-	-
9	0.04	-	-
10	0.006	-	-

total magnetic moment of the charge carriers, a direct relation between the 3s level splitting and the spin magnetic moment is valid. On the other hand, it is well known that this relation doesn't hold any longer in more metallic systems [58]. When the electronegativity of the ligand atom decreases, the charge transfer satellites and the screening of the final state become more important, as a result it is not possible any longer to attribute the peaks in the 3s spectra to pure spin states. Usually, in more covalent systems, the 3s levels splitting is smaller than what one would expect in the localized scenario because of these effects. We believe that this is the case in MnSi, whose metallic behavior reflects the covalent nature of the Mn-Si bonding. On the other hand, if one crudely uses the knowledge that the 3s level splitting is proportional to (S+1) where S is the Spin local moment, one finds a local moment between 1.9 and 2.5 μ_B which is in good agreement with the measured paramagnetic moment of MnSi. This, together with the new NMR data (discussed in section 1.5.1), might as well suggest that a localization is indeed taking place among the 3d electrons in MnSi.

In Fig. 5.18 and 5.19 we compare the experimental valence band photoemission spectra with the LDA calculations. The calculations includes the radial matrix elements but ignores the k-conservation between initial and final states. This is a reasonable approximation in the limit of large photon energy[59]. In MnSi, in the calculation a peak is evident around 2.8 eV away from the Fermi edge, a similar feature is visible in the experimental spectrum, although its position is only 1.8 eV away from the Fermi edge. The valence band photoemission spectra have been collected using three incoming photon energies: 86 eV, 104 eV and 196 eV and no appreciable changes

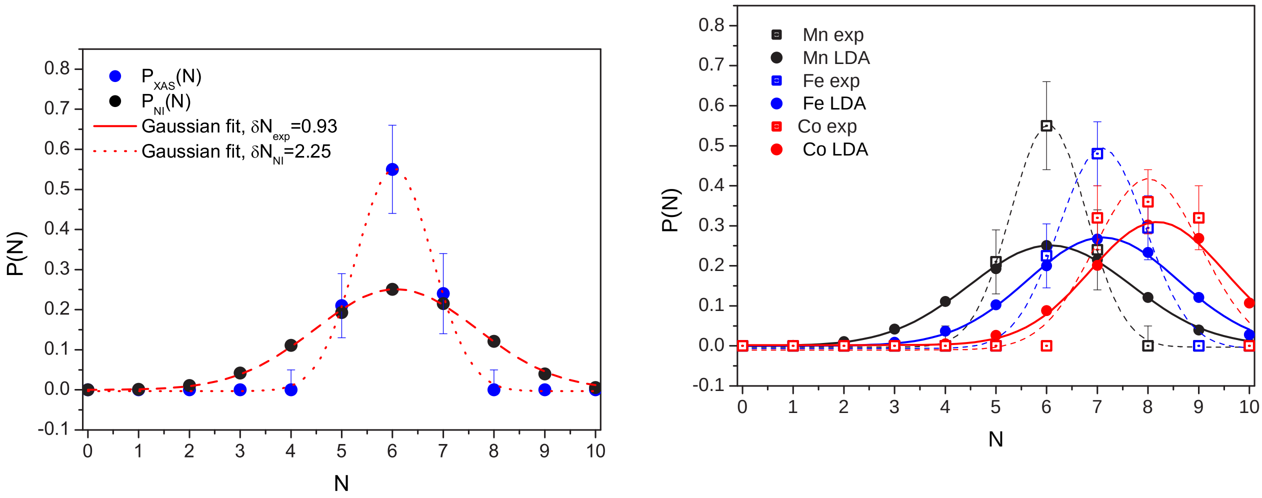

Figure 5.16: (Left panel: The theoretical and experimentally derived values of P(N) are plotted together with the fit to Eq. 5.1. From these fits we extract the values for δN and thus $\frac{\delta N_{NI}}{\delta N_{exp}} = 2.6$. Right panel: The theoretical and experimentally derived values of P(N) are plotted together with the fit to Eq. 5.1 in MnSi, FeSi and CoSi.

where observed. Also in this case the agreement between the calculation and the experiment is not satisfactorily. The valence band photoemission on MnSi has already been reported together with the LDA calculation in Ref. [60]. The authors point out that the major deviations from the raw spectra and the calculations are ascribable to the on site Coulomb repulsions, in agreement with our conclusion. In FeSi the agreement with band calculations is also poor, while for CoSi a good match is found.

Our observations evidence the fact that in this class of materials it is not justified to neglect completely the electron electron correlations. The discrepancy between the single particle scenario and the experiment is corroborated by the comparison in Fig. 5.13 (a) of the LDA-prediction of the XAS spectrum to the experimental data. It would be tempting to attribute this discrepancy to the fact that XAS is a high energy probe, and that the observed spectra correspond to the final state with an extra core-hole present. However, (i) both in the band-calculation as well as in the atomic multiplet calculations shown in Fig.5.13 (a) the presence of the core-hole has been taken into account, (ii) theoretically these spectra are expected to be a very sensitive fingerprint of the initial state electronic configuration, (iii) the same concerns would apply to the transition metal oxide family, where XAS has been quite successful probes of the magnetic properties [62, 63, 64, 65]. Moreover, also valence band photoemission, where no core hole is present, is inconsistent with the LDA approach. The cross check of the results by means of different techniques, electron counting and photon counting techniques, make us confident that we are indeed probing the

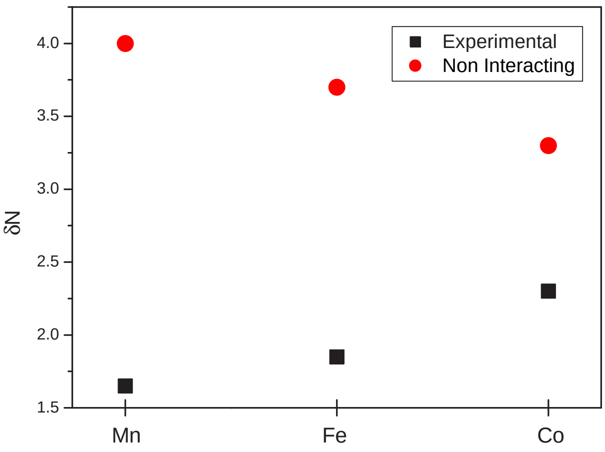

Figure 5.17: The values for δN for Eq. 5.1 and the experiments are displayed for MnSi, FeSi and CoSi

electronic structure of bulk MnSi. Our estimated value for U/W around 0.4 classifies MnSi in a class of materials where none of the two approximations is particularly good: completely neglecting the electron-electron interactions or considering them as dominant. The helical magnetic structure of MnSi has been explained in terms of the Dzyaloshinskii-Moryia interaction; the interplay between spin-orbit coupling and exchange interaction can result in an anisotropic exchange interaction, responsible for the helical magnetic structure in low symmetry crystals. For this to happen the motion of the conduction electrons must have a finite orbital component, for example a $3d^5(^6S)$ ground state would be rather unfavorable in this context, having a null orbital moment. Our observations are compatible with this picture, providing an experimental support to the microscopic model.

The occupation of the Mn d-orbitals in MnSi is somewhere between 6 and 7, close to what one would expect in the LDA scenario. Accordingly, adding one more electron to the system would imply an occupancy between 7 and 8 for FeSi and between 8 and 9 for CoSi, as experimentally confirmed. This is indeed visible in Fig. 5.17, where one can see that the experimental distributions P(N) get narrower moving from Mn to Co and becomes closer to the non interacting ones. Simultaneously, one observes also that the non interacting distributions are slightly narrowing moving from Mn toward Co. The combination of these two effects is such that in CoSi both the mixed valence calculation and the cluster LMTO give very similar results. One should realize also that moving toward the right of the periodic table the difference in electronegativity between the transition metal ion and Si becomes smaller. This implies that the TM d orbital is more hybridized by the Si 2p in CoSi than it is in MnSi. This, together with the previous observations, suggests that LDA is a more correct model than the

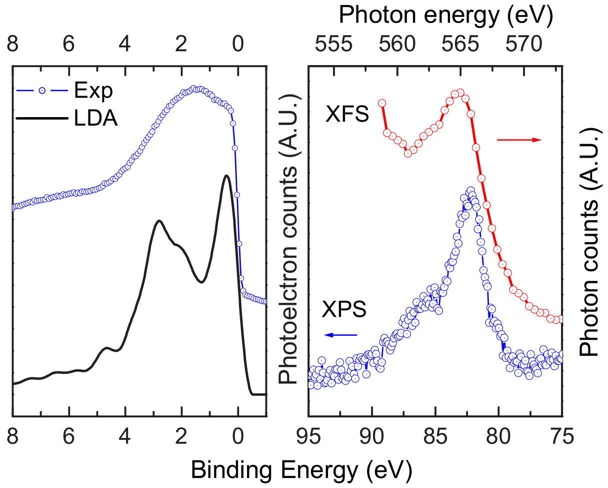

Figure 5.18: Left panel: Valence Band photoemission measured at an incident photon energy of 104 eV together with LDA calculations. Right panel: Photoemission (blue open symbols) measured at 418 eV incident photon energy and fluorescent (red open symbols) spectra of Mn 3s levels measured at 660 eV incident photon energy.

atomic multiplets based calculations for CoSi. All these observations, together with the bulk of other evidences for TM mono-silicides to be rather itinerant systems, show that Coulomb repulsion are likely to be a perturbation of the non interacting particle scenario. Still it is remarkable to notice that such a perturbation can have a very profound effect on the XAS and VBP spectra in MnSi and FeSi.

5.4 MnSi transport, magneto-transport and thermoelectric properties

5.4.1 Resistance and magneto-resistance

The phase diagram of MnSi has been investigated widely by resistivity measurements[30, 3, 32]. Above T_C the resistivity is described by the formula[33] $\rho = \rho_{sat} T/(T_0 + T)$ which for $T \gg T_0 = 180K$ approaches the Mott-Ioffe-Regel limit, ρ_{sat} =287$\mu\Omega$cm. The rapid rise towards saturation corresponds to a strong dissipation of the charge transport. The abrupt drop of the electrical resistivity when the material is cooled through T_C suggests that this dissipation is due to a coupling to magnetic fluctuations, see Fig. 5.20. The magnetoresistance of MnSi has been measured in Ref. [3] together with the magnetoresistance of Fe$_x$Co$_{1-x}$Si, displayed in Fig. 5.20. The commonly used description of MnSi in terms of a weak itinerant ferromagnet, suggests that the electrons contributing to the charge transport and to magnetism are the same. In this scenario a negative magnetoresistance is expected

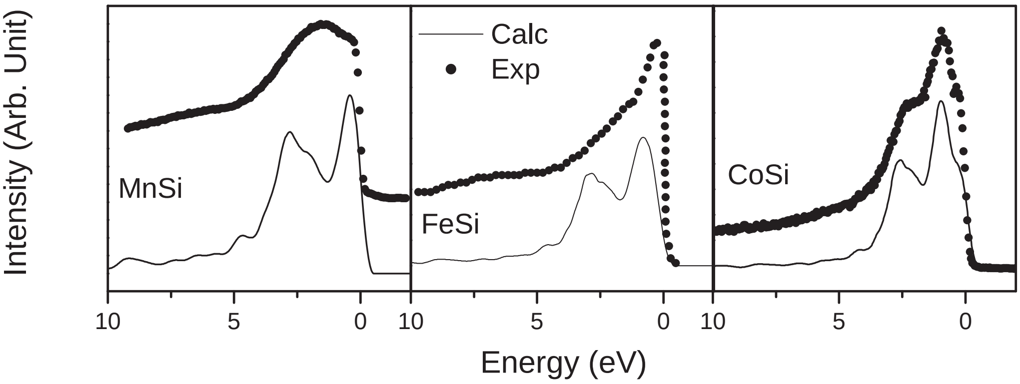

Figure 5.19: (The valence band photoemission spectra for MnSi, FeSi and CoSi together with the cluster LMTO calculations. The data on FeSi are taken from Ref [61]

because of the suppression of spin fluctuations by the magnetic field, which are one of the scattering channels for electrons and sometimes the most important one. In colossal magnetoresistance Manganites, the carriers contributing to the transport and those contributing to the magnetism are different and the scattering of the itinerant electrons on the localized ones gives rise to a positive magnetoresistence. In the low carrier density compound $\mathrm{Fe}_x\mathrm{Co}_{1-x}\mathrm{Si}$ it has been argued that positive magnetoresistance is caused by a combination of disorder and correlation effects. The parent compound of $\mathrm{Fe}_x\mathrm{Co}_{1-x}\mathrm{Si}$ is an insulator, FeSi, known to have local moments. Upon Co doping the system becomes metallic and eventually orders helimagnetically below 35 K. The presence of local magnetic moments in this system has been confirmed by neutron scattering experiments[66], even if strong similarities to the weak itinerant ferromagnets are observed. In this framework the positive magnetoresistance observed in $\mathrm{Fe}_x\mathrm{Co}_{1-x}\mathrm{Si}$ is explained by correlation and localization effects. Recently, we investigated the magnetoresistence of MnSi up to very high magnetic fields, 28 T. A rectangular sample of 4×1×0.2 mm was prepared starting from a large single crystal grown with the floating zone technique. The contacts were soldered with Indium in a typical 4 point geometry and the sample was attached to the cold finger of a dilution He cryostat. The magnetic field of a dissipative magnet was swept between 0 and 28T in the temperature region between 90 and 4 K. In Fig.5.21, we show the results of these measurements. In the top left panel one can see the resistivity as a function of temperature for magnetic fields ranging between 0 and 28 T with a step of 1.75 Tesla. One can see that our data are in very good agreement with those measured earlier in Ref. [3] where 4K and 5 T was the limiting condition, shown in Fig. 5.20. In the right panel of Fig. 5.21, one can see that at

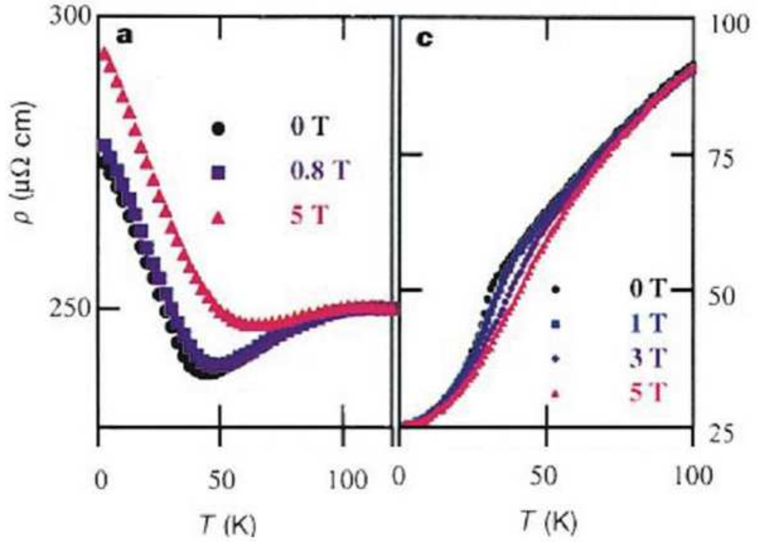

Figure 5.20: The magnetoresistance of $Fe_xCo_{1-x}Si$ (left panel) and MnSi (right panel). Graph taken from Ref. [3]

low temperature and very high field the magnetoresistance changes sign and becomes positive, *i.e.* resistivity increases when increasing the magnetic field, the very same behavior has been observed both for the geometry with the current parallel and perpendicular to the external magnetic field. In the lower left panel I show the derivative with respect to magnetic field of the resistivity which shows a pronounced minimum where the magnetoresistance changes concavity and a zero crossing at the lowest temperatures. In the lower right panel we show the field of the zero crossing of magnetoresistance with respect to temperature. This last graph may suggests the presence of a transition between different behaviors at zero temperature as a function of magnetic field.

5.4.2 Specific heat and thermal expansion

Specific heat measurements have been carried out on MnSi in Ref. [49] in the temperature range between 1.4 and 40 K and magnetic fields up to 3.5 T. These measurements show a second order phase transition occurring around 29 K, which is the magnetic ordering phase transition. In Fig. 5.22 I show the specific heat versus temperature taken from Ref. [49]. From these measurements the authors estimated a value for $\gamma = 85 \times 10^{-4} calK^{-2}$. The values for γ in pure Mn are found to be around $\gamma = 40 \times 10^{-4} calK^{-2}$, while the value estimated within a free electron approximation for Mn is $\gamma = 1.5 \times 10^{-4} calK^{-2}$. In transition metals the large discrepancy between the free electron γ and the measured value is due to the fact that their Fermi surface can be very different than the one given by the free electron approximation. In fact,

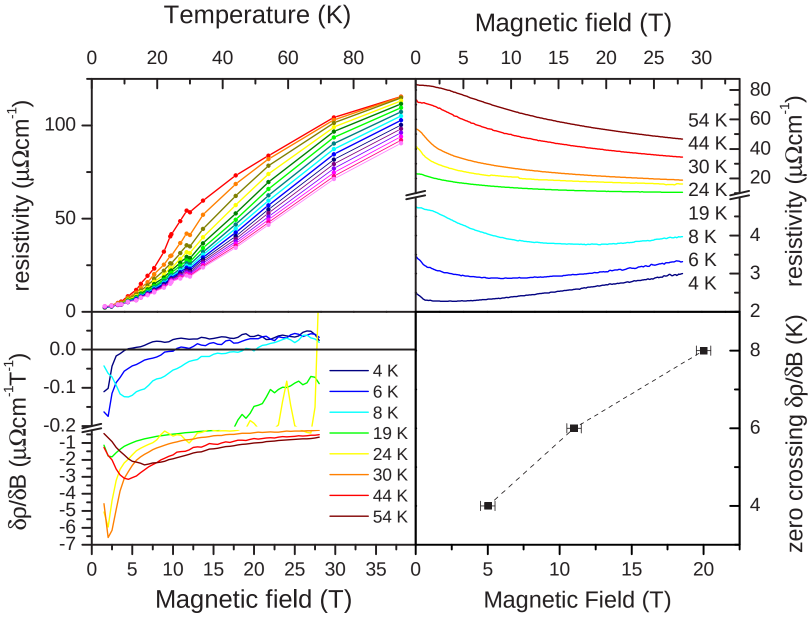

Figure 5.21: The high field magnetoresistance of MnSi: in the top left panel one can see the resistivity as a function of temperature for different fields. In the top right panel one has the resistivity as a function of field for different temperatures. In the bottom left panel we display the field derivative of the resistivity as a function of field and we show that a sign change happens at low temperature and high magnetic field. In the bottom right panel we display the zero crossing of the derivative as a function of magnetic field.

the d bands, which cross the Fermi level in transition metals, are much narrower than the usual free electrons conduction bands. Accommodating more electrons in a narrower energy region gives a higher density of states, which can explain the much higher value found for the γ coefficient, which is proportional to the density of states. This argument certainly applies also to MnSi where we have seen that the Fermi surface has mostly a 3d character, but electron-electron correlation effects are evident given the fact that γ for MnSi is twice as high as for pure Mn while the average bandwidth of the 3d bands is similar. The magneto-volume effect in MnSi has been interpreted in terms of the spin fluctuation theory, although discrepancies have been observed. Matsunaga *et al* show that the main contribution to the magnetovolume effect are coming from the Stoner excitations. The value for the magneto-elastic coupling constant is found to be around KC$_H$ = 1.49, rather close to the one measured in other weak itinerant ferromagnets, such as ZrZn. These data are interpreted in the framework of the spin fluctuation theory, but I would like to point out some important discrepancies: (i) the magnetovolume effect in spin fluctuation theory is

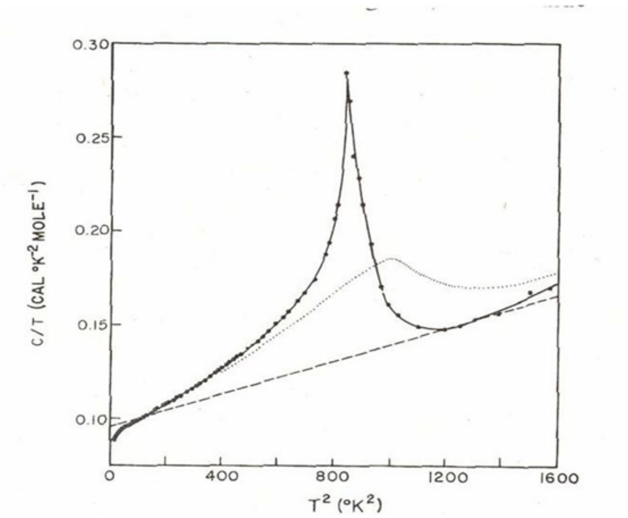

Figure 5.22: Specific heat measurements on MnSi from Ref. [49]

explained by the large temperature dependence of the spin density in weak itinerant magnets. Such a strong temperature dependence in the spectrum of the spin wave has not been unambiguously observed ([8] and related references) and there are even theoretical arguments against it [68]. (ii) the magnetization dependence of the volume changes predicted by the spin fluctuation model strictly speaking is not respected[67], but is in surprising agreement with the plain Stoner theory. This suggest that the magnetovolume effect is mostly due to the band polarization, while on the other hand, the contribution of the spin fluctuation below the Stoner boundary is not clear. More details about the connection between the magnetovolume effect and the Stoner excitations will be given in the following section where I will discuss very recent neutron scattering experiments carried out to study in detail the paramagnetic scattering of MnSi, and therefore the dumped spin waves in the Stoner continuum.

5.5 MnSi magnetic properties

MnSi orders helimagnetically below 29.5 K. The helical spin arrangement is similar to the one observed in other compounds, MnO_2, Tb, Dy, Ho, but its periodicity is much longer, around 180 Å. This magnetic structure has been investigated by means of small angle neutron scattering, polarized inelastic neutron scattering [9, 10, 11], NMR [12], and neutron scattering under pressure [31]. The helixes in MnSi are observed below an applied magnetic field of 0.6 T and are oriented along the [111] direction with a q vector of 0.035 $\mathring{A}^{-1}$. The magnetic ordering becomes ferromagnetic for higher magnetic fields. The crystal structure discussed in section 5.1 of MnSi has a screw axis which for all known samples is left-handed; the magnetic chirality is found to be also left handed [10], leading to the positive sign of the antisymmetric exchange interaction in MnSi. The origin of this magnetic structure has been explained in terms of the Dzyaloshinskii-Moriya interaction[13]; the anisotropic antisymmetric exchange interaction resulting from the interplay between spin-orbit coupling and exchange interaction in low symmetry crystals has been observed in MnSi by means of Electron Spin Rotation experiments [14]. Under an applied pressure of 14 kbar the net magnetization is found to vanish [30], and a partially ordered phase is observed with neutron scattering [31] for which several theoretical explanations have been proposed [15, 16, 18]. This very interesting phenomenon will not be discussed in further detail. We will focus our attention on the paramagnetic scattering of MnSi, which is of great interest for the description of the band magnetism. MnSi in fact, is considered to be a weak itinerant ferromagnet, in which the magnetic ordering is driven by the spin polarization of the electronic bands. Such a kind of magnetic behavior can be described by the Stoner model and presents many differences with respect to the usual Heisenberg picture for localized magnets. The Curie-Weiss behavior of the magnetic susceptibility in the paramagnetic state, which originates naturally from the Heisenberg model, is also observed in weak itinerant ferromagnets and it is not predicted by the standard Stoner model. This model also fails in estimating the Curie temperature of these materials. Several proposal have been made to circumvent these problems, among which the spin fluctuation theory by Moriya[1] has been the most successful in describing the magnetism of MnSi. The aim of the following section is to extensively test this model and verify its microscopical implications.

5.5.1 Magnetic susceptibility NMR and μSR

The usual fingerprints of weak itinerant ferromagnetism are (I) a low ordering temperature (29.5 K for MnSi), (II) a strong reduction of the magnetic moment from the paramagnetic to the ordered phase (in the paramagnetic phase MnSi shows a moment of 2.4 μ_B while in the ferromagnetic phase the ordered moment is only 0.5 μ_B, according to the most recent estimates.), (III) the lack of saturation in the magnetization under applied magnetic field, (IV) a Curie-Weiss temperature dependence of the paramagnetic susceptibility and (V) a temperature dependence of the NMR relaxation rate ($1/T_1$) of the magnetization which resembles that of a localized Heisenberg magnet but with a much smaller absolute value. The magnetic susceptibility of MnSi has been reported by Wernick et al [30] in high magnetic field. There is lack of saturation even for fields as high as 8 T. The Curie-Weiss law of the susceptibility has also been reported up to temperatures as high as 500 K [12] and explained in the context of the spin fluctuation theory. We will discuss this point later in the section dedicated to the neutron scattering experiments.

MnSi has already been studied in the paramagnetic phase by means of ^{55}Mn NMR

[12], nevertheless only few relaxation rate data have been obtained. A report based on μSR measurements of $1/T_1$ showed that the spin fluctuation model could explain both the high temperature NMR data and the divergence of $1/T_1$ close to T$_c$, a large gap in the experimental data however existed between 200 and 50 K [21]. Recently it has been claimed that below T_c the μSR data do not follow the spin fluctuation theory [22]. Here we cover the gap in the earlier data of $1/T_1$ by means of ^{29}Si NMR measurements. The problem is that in these metallic compounds one has to work on powder samples to allow a suitable irradiation with the RF field. ^{55}Mn NMR powder spectra are very broad owing to the sizeable anisotropy in the hyperfine coupling and the measured relaxation rates strongly depend on which part of the spectrum is irradiated. ^{29}Si nuclei, on the other hand, are characterized by a dominant hyperfine coupling which is isotropic. Hence, even in a powder the spectrum remains rather narrow and allows a more accurate determination of the nuclear spin-lattice relaxation rate. Only upon decreasing the temperature towards Tc the rapid increase in the spin susceptibility yields a broadening of the line and eventually causes the disappearance of the signal. Hereafter we present a study of the temperature dependence of the local static uniform spin susceptibility and of the low-energy excitations in MnSi, by means of ^{29}Si NMR spectra and nuclear spin-lattice relaxation rate measurements.

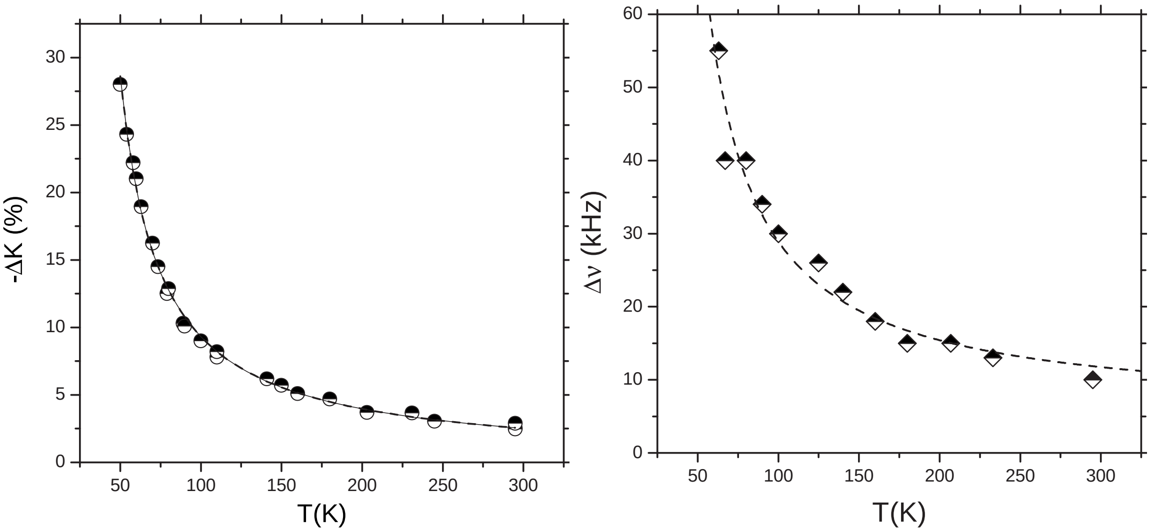

Figure 5.23: Left panel: Temperature dependence of ^{29}Si NMR paramagnetic shift in MnSi powders for $H = 1.57$ Tesla. Right panel:Temperature dependence of ^{29}Si NMR linewidth in MnSi powders for $H = 1.57$ Tesla.

The same crystals described in the XAS experiments were crushed and grinded into powders in order to allow a better penetration of the radiofrequency (RF).

NMR measurements were performed by using standard RF pulse sequences. ^{29}Si NMR powder spectra were obtained from the Fourier transform of half of the echo signal after a $\pi/2-\tau-\pi$ pulse sequence. Only at low temperature the line broadening prevented the full irradiation of the spectra. In this case the spectra were obtained by recording the echo amplitude upon sweeping the irradiation frequency. The spectra were observed to be nearly Gaussian and to sizeably shift to lower frequencies on cooling, indicating a strong and negative hyperfine coupling (Fig. 5.23). Also a sizeable increase in the linewidth was detected on decreasing the temperature (Fig. 5.23), suggesting a non-negligible anisotropy in the hyperfine coupling. Eventually, below 50 K the broadening is so strong to prevent the observation of the NMR signal. As the broadening is associated with the paramagnetic shift anisotropy it is convenient not to work at high fields. In fact, all measurements were performed at $H = 1.57$ Tesla. It is noted that both the shift and the linewidth follow the same temperature dependence of the static uniform susceptibility, measured with a MPMS-XL7 SQUID magnetometer (Fig. 5.24). The susceptibility $\chi_0 = M/H$, with M the magnetization, was observed to follow a Curie law above the ordering temperature, with a $T_c = 29.5$ K and a Curie constant consistent with a magnetic moment of $2.46\mu_B$ per Mn atom, namely the one expected for localized $S = 1$ spins.

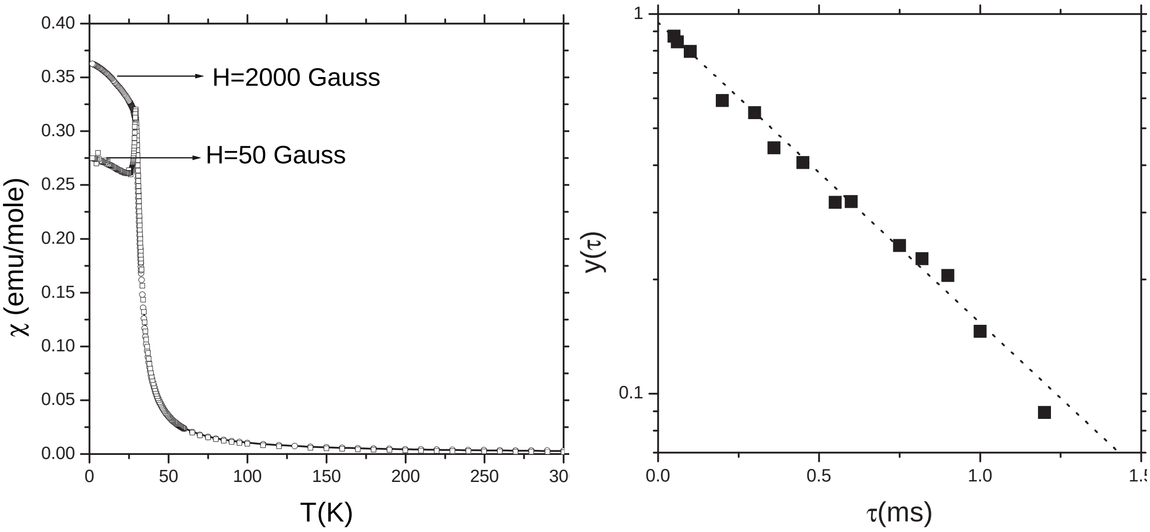

Figure 5.24: Left panel: Temperature dependence of the static uniform molar susceptibility $\chi_0 = M/H$ in a MnSi single crystal, where M is the magnetization measured with a SQUID magnetometer. Right panel: Recovery of ^{29}Si nuclear magnetization after a saturating pulse sequence, at $T = 90$ K. The dashed line is the best fit according to a single-exponential recovery.

The nuclear spin-lattice relaxation rate $1/T_1$ was estimated from the recovery of nuclear magnetization $m(t)$ after a saturating RF pulse sequence. The recovery law was a single exponential (Fig. 5.24), namely $y(\tau) = 1 - [m(\tau)/m(\infty)] = exp(-(\tau/T_1))$, as expected for an ensemble of $I = 1/2$ nuclei in a homogeneous system. The corresponding temperature dependence of $1/T_1$ is reported in Fig. 5.25. One notices that $1/T_1$ progressively increases upon cooling. Also the characteristic decay rate of the echo amplitude $1/T_2$, after a $\pi/2 - \tau - \pi$ pulse sequence was observed to be nearly exponential, suggesting that the relevant dephasing processes are associated with fast fluctuations, as the ones involved in nuclear spin-lattice relaxation.

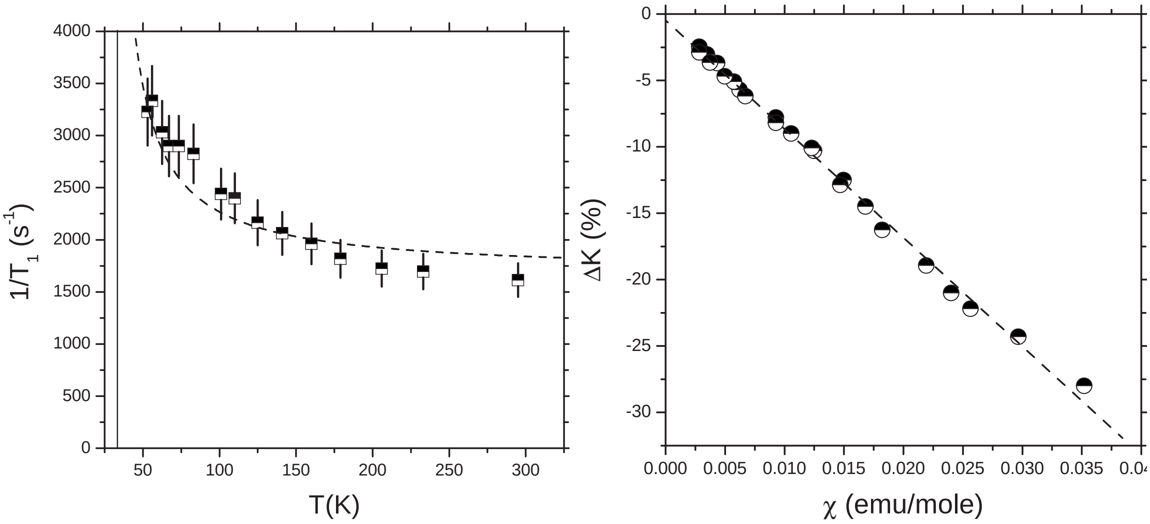

Figure 5.25: left panel: Temperature dependence of ^{29}Si nuclear spin-lattice relaxation rate in MnSi for $H = 1.57$ Tesla. The dashed line is the best fit according to Eq. 5.9 in the text. The vertical line indicates the ordering temperature. Right panel: ^{29}Si paramagnetic shift plotted versus the macroscopic susceptibility. The slope directly yields the hyperfine coupling.

The hyperfine hamiltonian can be written in the form $\mathcal{H} = -\gamma\hbar\vec{I}A\vec{S}$, with I and S the nuclear and electron spin, respectively. The paramagnetic shift of the NMR line $\Delta K = (\omega_R/\omega_L) - 1$ (ω_R the resonance frequency and ω_L the reference resonance frequency of the nucleus) can be written in terms of the macroscopic static uniform spin susceptibility χ_0

$$\Delta K = \frac{A\chi_0}{g\mu_B N_A} + \delta \tag{5.3}$$

where A is the ^{29}Si hyperfine coupling and δ the chemical shift, which is expected to be almost negligible here. Hence, by plotting ΔK vs. χ_0, leaving the temperature as an implicit parameter, it is possible to determine A and δ (see Fig. 5.25). It was found that $A = -91.3 \pm 1.5$ kOe and $\delta = 0 \pm 30$ ppm. It is noticed that A is twice the corresponding value in kOe/μ_B, i.e. 45.65 kOe/μ_B. Such a hyperfine coupling is quite strong for ^{29}Si and indicates a sizeable hybridization of Si p and Mn d orbitals. The magnitude of A and its negative sign put severe constraints on MnSi electronic band structure. According to LDA calculations the hyperfine field on Si is found to be -34 kOe, when the lattice parameter is 4.39 Å(the same used for the simulation of the positron spectra), which gives the experimental value of the local moment, 0.5 μ_B; if a = 4.5 Å, closer to the experimental value of 4.55 Å, the hyperfine field is found to be around -57 kOe and the local moment is 0.85 μ_B per Mn atom. The corresponding value per Bohr magneton is about 67 kOe. The hyperfine field on Si is therefore increasing when the moment on Mn is increased, as one would expect, but the absolute value is underestimated by the LDA calculation. In the right panel of Fig.5.26 we display the evolution of the hyperfine field according to LDA calculations as a function of the lattice parameter and the magnetic moment per Mn atom. One can see that the hyperfine field measured experimentally is approached when the lattice parameter is increased slightly above its experimental value and the magnetic moment approaches the paramagnetic moment given by the Curie-Weiss law of the magnetic susceptibility.

In the magnetically ordered phase, for $T \rightarrow 0$ ^{29}Si zero-field resonance frequency is known to reach $\nu_{low} = 20$ MHz [25, 26]. By taking the value estimated for the hyperfine coupling it is now possible to make a precise estimate of Mn magnetic moment for $T \rightarrow 0$. One finds that $<\mu>_{Mn} = 0.518 \pm 0.009\mu_B$. This value is sizeably reduced with respect to the magnetic moment estimated from the Curie constant; such a reduction has been interpreted in the framework of spin fluctuation theory, but it could also reveal a relevant role played by the geometric frustration discussed in the previous sections.

The broadening of the line on cooling is due to the shift anisotropy which yields a broadening proportional to χ_0. Again, by plotting the broadening of the line vs. the macroscopic spin susceptibility it is possible to estimate the anisotropic terms of the hyperfine coupling. It is found that $A_{aniso} \simeq 4.2$ kGauss. This anisotropy, even if small when compared to the main isotropic coupling, is too strong to be justified by a simple dipolar coupling with localized Mn spins and might be associated with an anisotropic transfer of the electron polarization to the nuclei through p electrons.

Now we turn to the discussion of the low-energy excitations in the light of the results obtained from $1/T_1$ measurements. In the presence of a relaxation mechanism driven by the fluctuations of the local field at the nuclei one can write

$$\frac{1}{T_1} = \frac{\gamma^2}{2} \int e^{i\omega_R t} < h_+(t) h_-(0) > dt \ , \tag{5.4}$$

where $h_\pm$ are the transverse components of the hyperfine field at the nucleus. Since for ^{29}Si the hyperfine hamiltonian is dominated by a transferred isotropic coupling, one can rewrite the previous equation in the form

$$\frac{1}{T_1} = \frac{\gamma^2 A^2}{2} \int e^{i\omega_R t} < S_+(t) S_-(0) > dt =$$

$$= \frac{\gamma^2 A^2}{2} \frac{k_B T}{\hbar} \frac{1}{N} \sum_{\vec{q}} \frac{\chi"(\vec{q}, \omega_R)}{\omega_R} \tag{5.5}$$

where the last equation arises from the low-frequency limit of the fluctuation-dissipation theorem. Following Ishikagi and Moriya [27] it is convenient to write the dynamical spin susceptibility in terms of two characteristic parameters T_0 and T_A which characterize the width of the spin excitations spectrum as a function of frequency and as a function of $\vec{q}$, respectively. For a ferromagnetically correlated system one has that[27, 28]

$$\chi(q,\omega) = \frac{\pi T_0}{\alpha_Q T_A}\frac{x}{k_B 2\pi T_0 x(y+x^2) - i\omega\hbar} \tag{5.6}$$

where $x = q/q_D$, with q_D a Debye-like cutoff wave-vector, α_Q is a dimensionless interaction constant, close to unity for strongly correlated systems, and $y = 1/2\alpha_Q k_B T_A \chi(0,0)$. Here the susceptibility is per spin and in $4\mu_B^2$ units and has the dimensions of the inverse of an energy, while T_A and T_0 are in Kelvin. From the previous expression one can derive $\chi"(\vec{q},\omega_R)/\omega_R$ by taking the limit $\omega_R \rightarrow 0$, since $\hbar\omega_R \ll k_B T_0$. Then, by integrating $\chi"(\vec{q},\omega_R)/\omega_R$ over $\vec{q}$, in a sphere of radius q_D, one derives

$$\frac{1}{T_1} = \frac{\gamma^2 A^2}{2} T \frac{3\hbar}{4\pi k_B T_A T_0}\frac{1}{\alpha_Q}\frac{1}{2y(1+y)} \tag{5.7}$$

Now, since $T_A \gg T$ [27, 28] in the T-range of interest $y \ll 1$ and one can simplify the previous expression in the form

$$\frac{1}{T_1} \simeq \gamma^2 A^2 \frac{3\hbar}{8\pi}(\frac{T}{T_0})\chi(0,0) \tag{5.8}$$

This expression is equivalent to the one derived by Ishikagi and Moriya if one takes into account that their hyperfine coupling constants are in kOe/μ_B. It should be noticed that since $\chi_0 = 4\mu_B^2\chi(0,0)N_A$, one can write $\Delta K = 2\mu_B A\chi(0,0)$ and hence

$$\frac{1}{T_1 T} \simeq \gamma^2 A \frac{3\hbar}{16\pi\mu_B}(\frac{1}{T_0})\Delta K \tag{5.9}$$

Hence by plotting $1/T_1T$ vs. ΔK a linear behaviour is expected and from the slope it is possible to derive T_0, which corresponds to a characteristic frequency for the spin fluctuations. Indeed (see Fig. 5.26) a linear behaviour is observed and a value for $T_0 \simeq 71 \pm 3$ K is derived. This value is much smaller than the one estimated by Ishikagi and Moriya in their previous analysis.

It is also noticed that in a magnetic field a flattening and eventually a decrease of $1/T_1$ is expected for $T \ll T_0$ [28, 23, 29]. The absence of this flattening seems to indicate that even at 50 K this temperature limit has not been reached in agreement with our estimate of T_0. The quantity T_0 is a characteristic energy of the spin fluctuations and should represent the energy scale in which most of the contribution

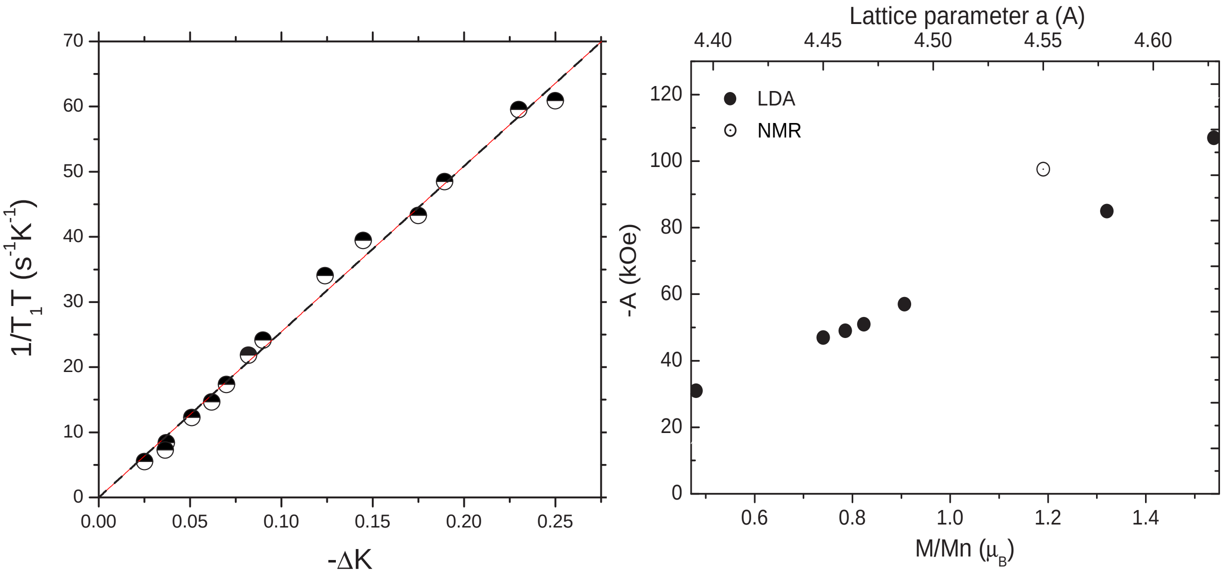

Figure 5.26: Right panel: the hyperfine field as a function of the lattice constant according to LDA calculations. Left panel: ^{29}Si $1/T_1T$ is plotted against the paramagnetic shift in order to evidence the validity of Eq. 5.9.

to the susceptibility due to the spin waves is contained. According to spin fluctuation theory:

$$T_0 = \Gamma_0 q_B^3 / 2\pi \tag{5.10}$$

Where $q_B^3 = (6\pi^2/v_0)$ and $v_0 = 23.7^3$ is the atomic volume for Mn. The parameter Γ_0 is determined by the width and dispersion of the spin waves and can be deduced from neutron experiments. According to previous estimates $\Gamma_0 = 50meV\text{Å}^{-3}$ while we estimate in our data a value of 70 meV meVÅ^{-3}, see Fig. 5.37 and related discussion. Given these numbers, T_0 should be around 230 K, somewhat higher than our estimate based on NMR experiments. Previously, the value of T_0 has been estimated from the theoretical formula 5.10 using Γ_0 derived from neutron experiments [8], while it has never been estimated directly from NMR measurements. In a previous NMR report on ^{55}Mn NMR [12], no value was estimated for T_0. In a later experiment[21], the qualitative temperature dependence of $1/T_1$ has been investigated by means of ^{55}Mn NMR and μSR experiments. The results have been interpreted in the framework of Moryia's spin fluctuation theory but an explicit value for T_0 has not been given. In spin fluctuation theory q_B is the average-zone boundary vector. In our view, it is more understandable to calculate it using the unit cell volume, rather than the atomic volume. If one uses a $\nu_0 = 90\text{Å}^3$ instead of $\nu_0 = 23.7\text{Å}^3$, used in spin fluctuation theory, $\mathrm{T}_0 = 70$ K and the consistency between neutron experiments and NMR is restored. If this is the case, the estimate of the ordering temperature given by spin fluctuation theory is not so good anymore. In fact, the transition temperature is estimated by means of the equation:

$$T_c = 1.419 p_s^{3/2} (\frac{A}{\alpha_0} \nu_0)^{3/4} \Gamma_0^{1/4} \tag{5.11}$$

which, with for $\Gamma_0 = 70$ meVÅ^{-3} and $\nu_0 = 90$Å^3, gives a T_c around 100 K. At this point it is relevant to discuss the role of the parameter q_B in the spin fluctuation model. The underlying idea in this model is that long wavelength (small q) and low energy spin waves play a major role. The inverse static susceptibility is obtained integrating over q in a sphere of diameter q$_B$ the dynamical susceptibility obtained from band theory. A Curie-Weiss law for χ_0 is found for small values of q$_B$. Increasing q$_B$ results in a curvature of the susceptibility versus temperature which departs from the C-W behavior. Therefore, in our opinion the C-W law emerging from the spin fluctuation model is less natural than believed and it is questioned by our experimental observations.

5.5.2 Neutron scattering

A very powerful probe for magnetic systems is neutron scattering. The cross section per unit of energy and solid angle for the electromagnetic interaction between the neutron magnetic moment and the magnetic moments present in a solid is given by the formula:

$$\frac{d^2\sigma}{d\Omega dE\prime} = \frac{k_f}{k_i} (\gamma r_0)^2 \mid \frac{g}{2} F(Q) \mid^2 \sum_{\alpha,\beta} (\delta_{\alpha,\beta} - Q_\alpha Q_\beta S^{\alpha,\beta}(Q,\omega)) \tag{5.12}$$

Where Q $= k_f - k_i$ and $\hbar\omega = E_f - E_i$ are the momentum and energy transfer. $\gamma = 1.913$ and $g \simeq 2$ are the spectroscopic g-factors of the neutron and magnetic atom. F(Q) is the magnetic form factor and depends on the atom present in the solid. In Eq. 5.12 the quantity S(Q,ω) contains the spin correlation function:

$$S^{\alpha,\beta}(Q,\omega) = \frac{1}{2\pi\hbar} \int dt e^{i\omega t} \frac{1}{N} \sum_{i,j} < S_i^\alpha(t) S_j^\beta(0) > e^{-iQ(R_i - R_j)} \tag{5.13}$$

Using the fluctuation-dissipation theorem one can relate the spin correlation function to the spin susceptibility by the formula:

$$S(Q,\omega) = \frac{1}{1 - e^{-\beta\hbar\omega}} \frac{\chi\prime\prime(Q,\omega)}{\pi (g\mu_B)^2} \tag{5.14}$$

with $\beta = 1/k_B T$. One can see from these equations that with a neutron scattering experiment it is possible to have direct information on the imaginary part of the spin susceptibility as a function of energy and momentum. In itinerant magnets,

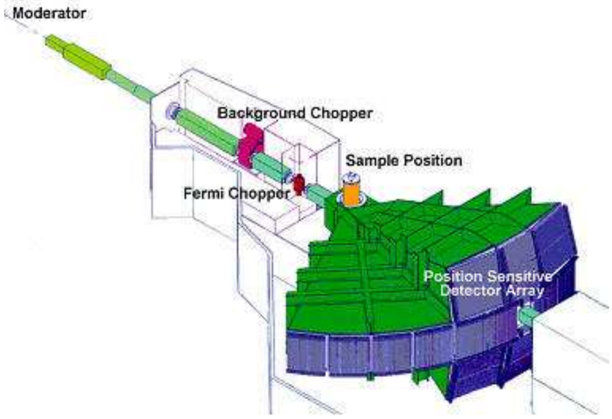

Figure 5.27: Experimental setup of the MAPS spectrometer

the spin susceptibility has been investigated by means of the RPA (random phase approximation) method. In this model the imaginary part of the spin susceptibility is given by:

$$\chi''(Q,\omega) = \frac{Im\chi_0(Q,\omega)}{[1 - IRe\chi_0(Q,\omega)]^2 + [IIm\chi_0(Q,\omega)]^2} \tag{5.15}$$

where I is the intra-atomic interaction and χ_0 is the susceptibility of the non interacting electron gas. χ_0 can be calculated analytically and well defined spin-waves with a quadratic dispersion are predicted by this model. A detailed comparison between this model and MnSi has been performed in Ref.[4]. In MnSi, one needs to go beyond this approach in order to explain the Curie-Weiss law of the magnetic susceptibility and the peculiar properties of the paramagnetic scattering. This is done by Moryia's spin fluctuation theory, where the spin susceptibility is given by the formula:

$$\chi(Q,\omega) = \frac{\chi_0(Q,\omega)}{1 - I\chi_0(Q,\omega) + \lambda(Q,\omega)} \tag{5.16}$$

The additional term with respect to the RPA formula $\lambda(Q,\omega)$ is producing the Curie-Weiss behavior observed experimentally.

This theory makes a number of predictions for the low energy spin-waves, which have been studied in detail in literature [4, 5, 6, 7], as well as for the Stoner excitations, which have been studied up to 20 meV energy transfer. We extend this study measuring the paramagnetic scattering of MnSi up to energy transfer as high as 400 meV in order to investigate the microscopic origin of the band magnetism of MnSi.

We performed inelastic neutron scattering experiments on a single crystal of MnSi on the MAPS time-of-flight spectrometer in ISIS[46]. The sample was the very same single crystal measured in Ref. [4], which has been largely characterized in the following 30 years.

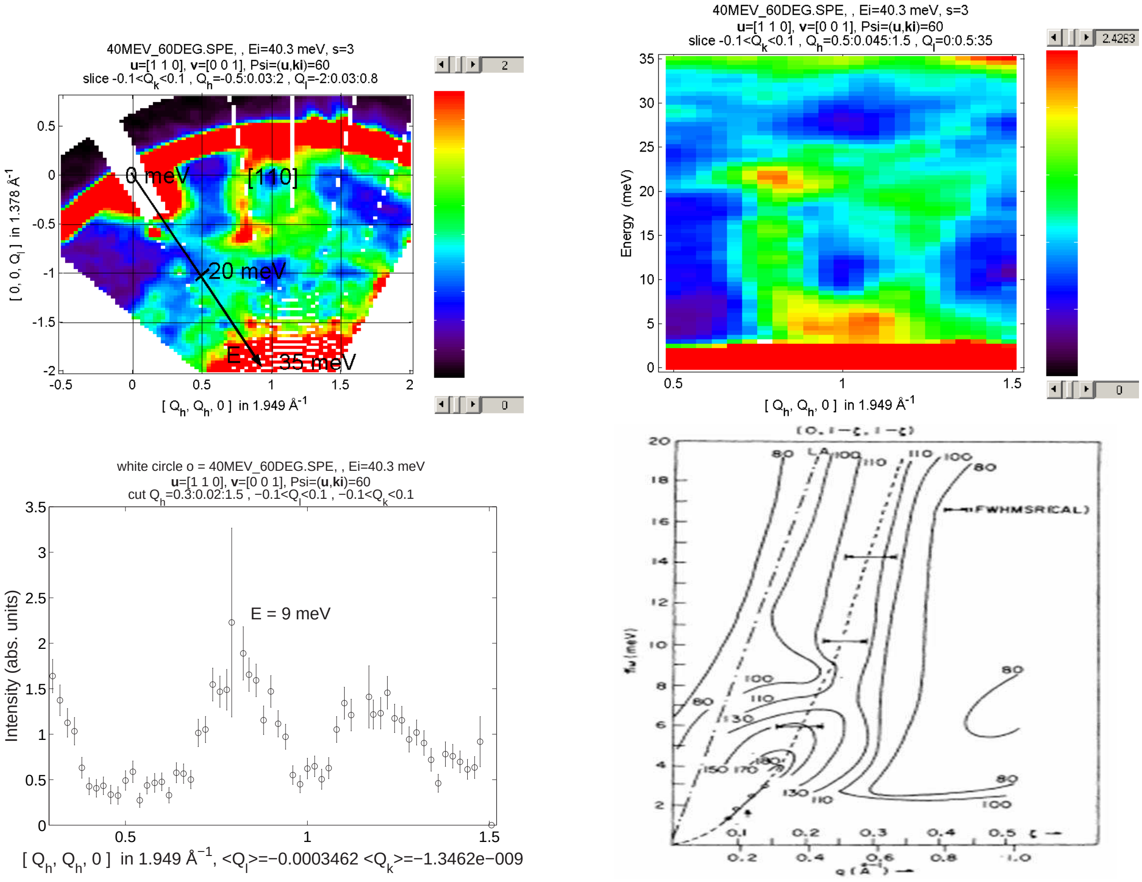

Figure 5.28: Top left: $S(Q,\omega)$ in the plane defined by the [110](Q_h) and [001](Q_l) directions with $\theta = 90^o$. Top right: the same cut is projected onto the energy and the Q_h axis. Bottom left: A cut in the Q_h direction at a constant Q_l gives a magnetic peak at an energy transfer of 9 meV. Bottom right: a contour plot taken from Ref. [4] shows the dispersion of the magnetic excitations in the Q_h direction.

The neutrons were delivered by a pulsed spallation source operating at 50 Hz repetition rate. Once the pulse is generated the phase of a Fermi chopper with respect to the pulse creation time selects the neutrons with a given kinetic energy, while the frequency of the chopping determines the energy resolution. The neutrons scattered by the sample impinge onto a 16 m^2 detector composed by 576 bars 1 m long and 2.5 cm in diameter filled with ^3He. The distance between the sample and the detector is 6 m. The temperature of the sample was controlled by a closed-cycle cryostat, all the experiments were performed at room temperature and 10 K. A pictorial representation of the experimental apparatus is depicted in Fig. 5.27 For a given sample orientation and incident neutron energy, the coordinates given by the position sensitive detector and the time of flight are mapped by a software into a portion of the four-dimensional space of momentum transfer (3 dimensions) and energy trans-

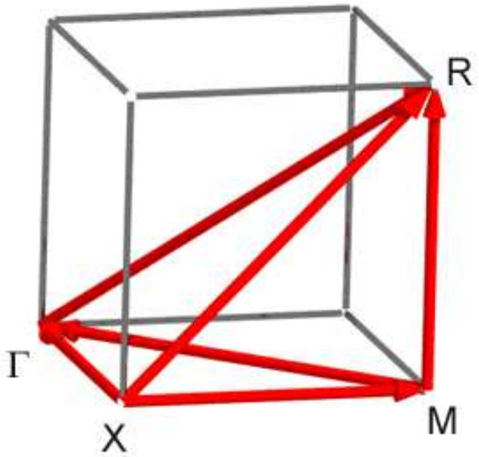

Figure 5.29: Top left: The directions in the reciprocal space in which we plot the dispersion.

fer (one dimension). In order to cover a larger part of this space different sample orientations and incident energies are used. In low dimensional systems the task of filling the momentum- transfer energy-transfer space is simplified by the possibility of neglecting the dispersion of the magnetic excitations in certain directions; this is not the case for MnSi, with the result that a total amount of data of 2.07 Gb needed to be collected in order to have a reasonable survey of the magnetic scattering. This data-set is composed of different scans where the incident neutron energy and the sample orientation are varied. The details of the performed scans are given in table 5.3:

In earlier neutron scattering reports[4, 5, 6, 7], it has been shown that the magnetic scattering has the highest structure factor around the points [110], [111] and [210] in reciprocal space[4]. This has been confirmed by the polarization analysis performed in a later publication [7], demonstrating that the scattering observed in these region is indeed magnetic in origin. In our experiment, when the incident beam is parallel to the [110] direction the magnetic scattering is in a favorable position for the detector, while rotating the sample by 90 degrees the acoustical phonons dominate the detected scattering. These are the two main orientations that we have chosen in order to characterize both the magnetic and the phonon scattering.

The measurements are corrected for the inhomogeneity of the detector sensitivity and other non ideality, by taking a reference run without the Fermi chopper on a vanadium sample. The software HOMER then converts the raw data into absolute units. The data are visualized with the aid of the software MSLICE which allows to plot 2D and 1D cuts in the momentum-energy space. We display in Fig. 5.28 an example of three slices performed on the data-set collected with incident neutron

Table 5.3: The largest part of the data were collected with the incident beam parallel to the [110] orientation of the sample. The angle θ is the angle with respect to this geometry.

θ (deg)	incident energy (meV)	temperature (K)
0	50	10
0	75	10
0	100	10
0	125	10
0	150	10
0	200	10
0	300	10
0	400	10
0	50	300
0	100	300
0	400	300
0	30	10
65	22	10
90	30	10
60	40	10
90	50	10
90	75	10
90	100	10
-35	100	10
-24	150	10

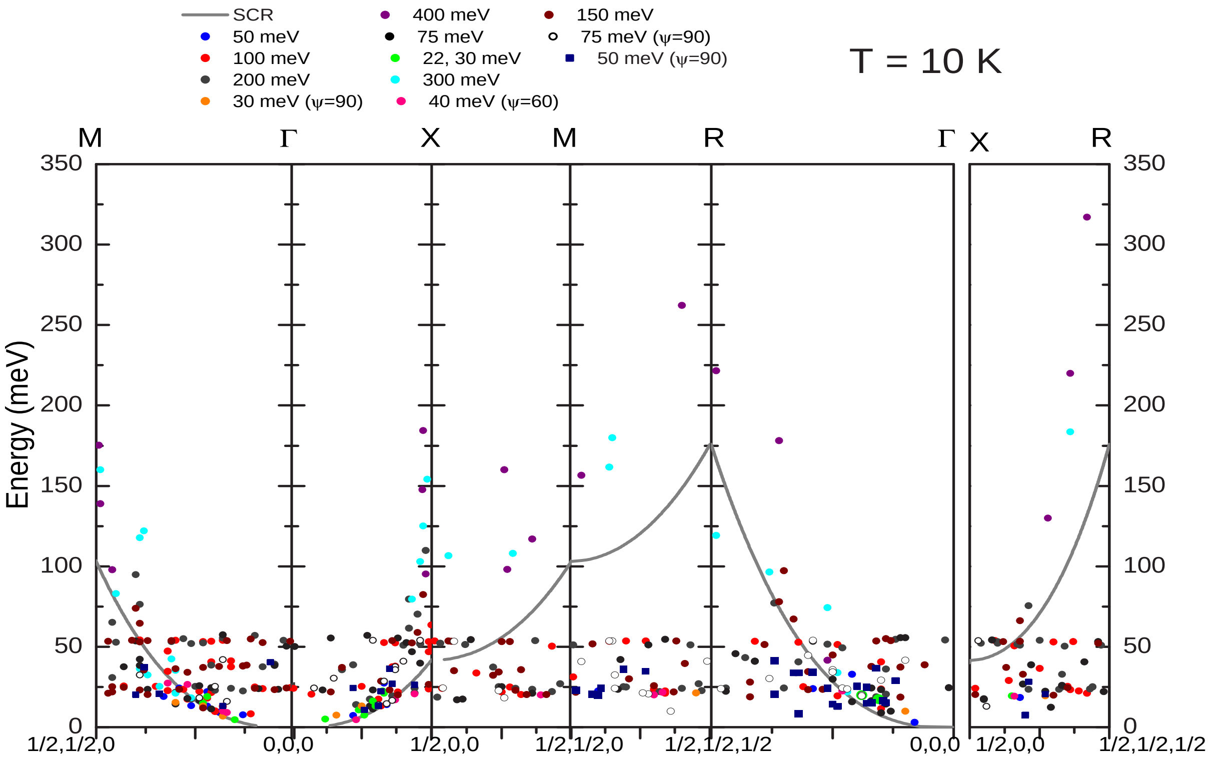

Figure 5.30: All the experimentally obtained peaks position are plotted together with the theoretical dispersion according to formula 5.17.

energy of 40 meV and the sample rotated by an angle of 60 degrees with respect to the [110] direction, in order to have the [110] point in the center of our detector array. In this particular slice the magnetic scattering around the [110] point is visible, therefor a direct comparison to the data reported in literature is very easy. In the top left panel of Fig. 5.28 the data are projected onto the axis [110][001][1-10] (named for simplicity Q_h, Q_l, Q_k) and a slice perpendicular to Q_k at the height $Q_k = 0$ is taken. Consequently, one can see a map of the scattering in the plane defined by the [110] and the [001] vectors. Given the geometry of this experiment, care has to be taken to the fact that the energy is varying throughout this 2D plot. In particular, the energy transfer is constant on concentric contours; the red contour labeled "0 meV" in the figure represents the elastic scattering from the sample (0 energy transfer), a contour labeled "20 meV" is given by the inelastic scattering on an almost dispersionless optical phonon. It is possible to project the data onto the energy axis as well, in this way one can plot a sort of dispersion, top right panel, keeping in mind that the 4th dimension, in this case the axis [001], is implicit in the graph. This results in a distortion of the dispersion, whenever the dispersion in the implicit direction is not negligible, as is the case for MnSi. In the bottom left panel of Fig. 5.28 one can see a cut parallel to the [110] direction performed in the plane Q_h, Q_l with $Q_l = 0$. The energy transfer at the peak position can be found by an appropriate software, given

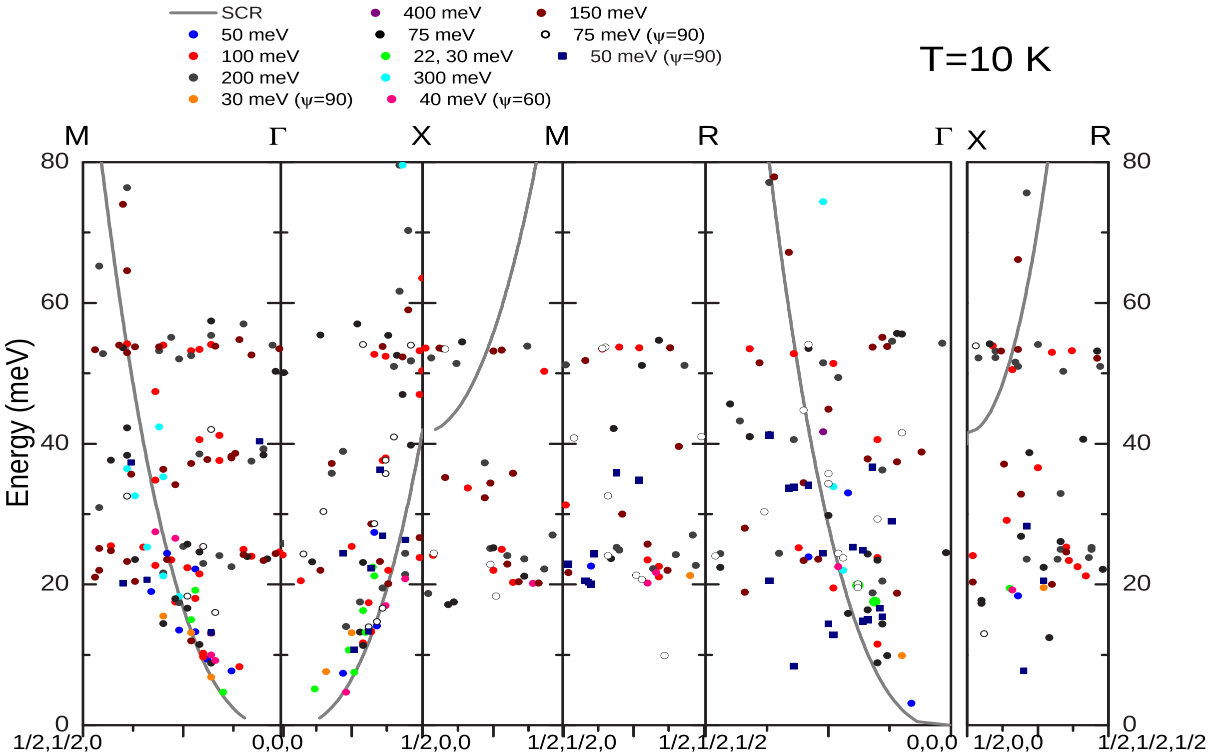

Figure 5.31: We show a zoom at low energy of the peaks in Fig. 5.30.

the geometry of the experiment and the 3 coordinate of momentum transfer. In this way one can get the dispersion of the magnetic excitations in the direction [ξ, ξ,0]. It has to be noted that the energy transfer is not constant along the cut plotted in the bottom left panel of Fig. 5.28. On the other hand, one can see that this particular cut is almost tangential to the constant energy circular contours visible in the top left panel of the figure. Furthermore, when the peaks are narrow, as in this case, the energy variations underneath the peak can be safely neglected. In general, not all the cuts performed in the data analysis are tangential to constant energy contours. Care has been taken in giving an errorbar on the width and position of these peak that takes into account this effect. In the bottom right panel of Fig. 5.28 one can see a contour plot of the scattering around the [110] point reported in Rf. [4]. One can visually compare this graph to the top right panel of the figure. For a more quantitative comparison, one should notice that the 1D cut reported in the bottom left panel of the figure shows a peak around the position (0.2,0.2,0), in reduced q units, at an energy transfer of 9 meV. Correspondingly, if one imagines a cut of the contour plot of the bottom right panel of the figure at an energy transfer of 9 meV a peak around $\xi = 0.2$ is expected. This comparison makes a good connection to the previous reports and is a good starting point for the following analysis. In the work in Refs. [4, 5, 6, 7] the low energy magnetic excitations have been studied. The onset of the Stoner continuum has been estimated around 3 meV and the scattering within

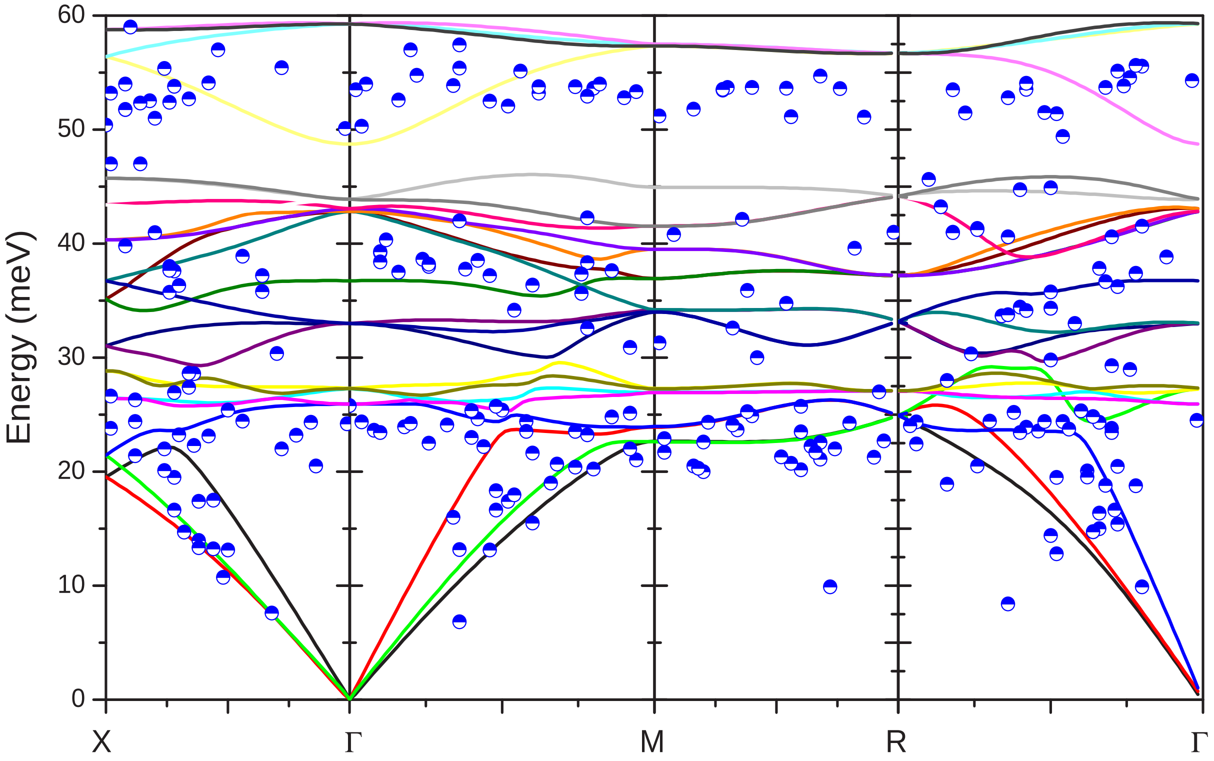

Figure 5.32: The peak positions obtained from the scans where the sample was rotated by 90 degrees with respect to having the [110] direction parallel to the incident beam and the peaks obtained from the other scans that could be addressed as phonons are displayed together with the phonon dispersion lines calculated by LDA on a 3×3×3 cluster.

this continuum could be studied only up to an energy transfer of 16 meV because of the presence of the optical phonons between 20 and 60 meV which complicate enormously the analysis. In our experiments we could reach energy transfer as high as 400 meV, allowing us to study the excitations in the Stoner continuum well above the phonon region.

Using the procedure described above we determined the peak position of the magnetic excitations as well as the phonons in the directions indicated in Fig. 5.29. In Fig. 5.30, 5.31 we display the dispersion of all the magnetic and phonon peaks obtained from the systematic analysis of the 20 data-sets aforementioned in the energy transfer range between 0 and 350 meV and 0 between 0 and 80 meV respectively. Together we plot the dispersion for the magnetic excitations as described by the eq. 5.17, obtained in the context of Moriya's spin fluctuation theory[7].

$$S(Q,\omega) = \frac{\hbar}{\pi}\frac{1}{1-e^{-\hbar\omega/kT}} \times \frac{C\imath\omega q}{\Gamma_0^2 q^2[k_0^2(T/T_c-1)+q^2]^2+\omega^2} \tag{5.17}$$

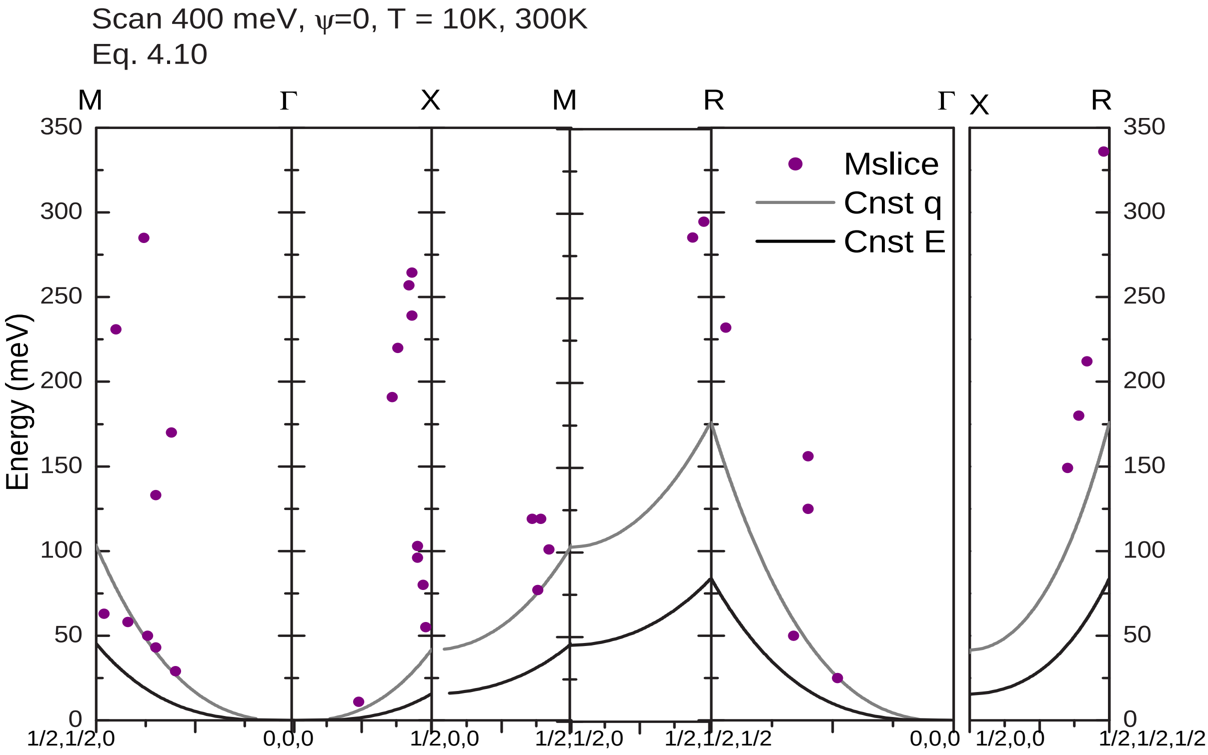

Figure 5.33: Comparison between the peak positions obtained by different trajectories of the cuts in the 4D space. The continuous black line is obtained cutting the scattering function at constant energy, the gray line is obtained from constant q cuts and the dots are obtained from cuts along trajectories which are neither constant energy nor constant q.

As one can see, many points in the dispersion graphs are originating from the acoustical and the optical phonons at low energy. In order to separate them from the magnetic scattering we use the same argument of Ref. [4], by orienting the crystal in such a way that either the magnetic scattering or the phonon scattering has a large structure factor in the region observed by the detector. In particular, as the sample is oriented with the [110] direction parallel to the incident beam, we are observing around high magnetic structure factor points in k-space. Otherwise, rotating the sample by 90 degrees, we observe high phonon structure factor points, (square symbols in the graphs). The optical phonons, visible as almost dispersionless lines in Fig. 5.30, 5.31, give very intense scattering in all points of the k-space and are difficult to distinguish from the magnetic scattering. Together with the considerations about the structure factor, we use calculations of the phonon dispersion made using plane-waves and ultrasoft pseudo-potentials on a $3 \times 3 \times 3$ atoms supercell. In this calculation the lattice parameter is 4.5 Åand gives a local moment around 0.8 μ_B per Mn ion. The results of these calculations are displayed in Fig. 5.32, where one can see that a reasonable match with the experiments is obtained. Some departures

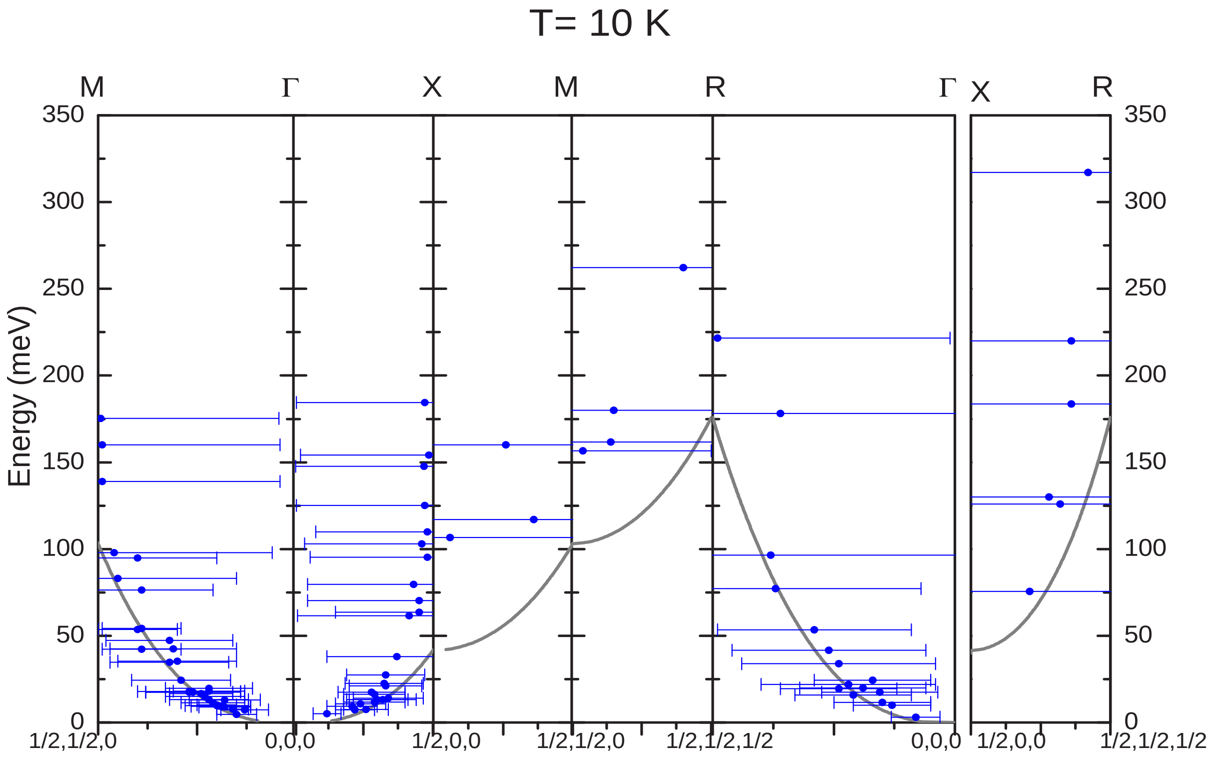

Figure 5.34: A selection of peak positions that we could attribute to magnetic excitations with their width in momentum transfer.

are observed, as was the case for the PAS spectra and the estimate of the Hyperfine field.

Below the optical phonon energies, the obtained magnetic scattering dispersion, displayed in Fig. 5.34, is in good agreement with previous reports, as already shown by Fig. 5.28. Due to the particular geometry of this experiment, at higher energy transfer where the peaks are much broader, the departure between the experiment and the analytical dispersion is significant. We verified that this is mostly due to the distorted trajectories of our cuts in the 4D space by projecting the formula 5.17 into a dataset similar to those experimentally acquired. This simulated dataset is than sliced with the software mslice in the very same way as the experimental data and in Fig. 5.33 one can see the result of this procedure: the two continuous lines correspond to the dispersion of the maxima in Eq. 5.17 taken analytically at constant q or constant energy respectively; the closed symbols are obtained with the software mslice. As one can see, close to the zone boundaries very broad scattering is observed and the peak position can have a very large spread in energy. One has to keep in mind that the intensities at these energies are very small, therefor the main contribution to the magnetic susceptibility is coming from the scatterig below 100 meV.

In Fig. 5.35 we show the width of these excitations in reduced q units; at low energy and low momentum transfer well defined spin waves are observable in the Stoner continuum, as already pointed out in Ref. [4], at higher energies and momentum transfer they broaden until they reach the width of one Brillouin zone around 100 meV.

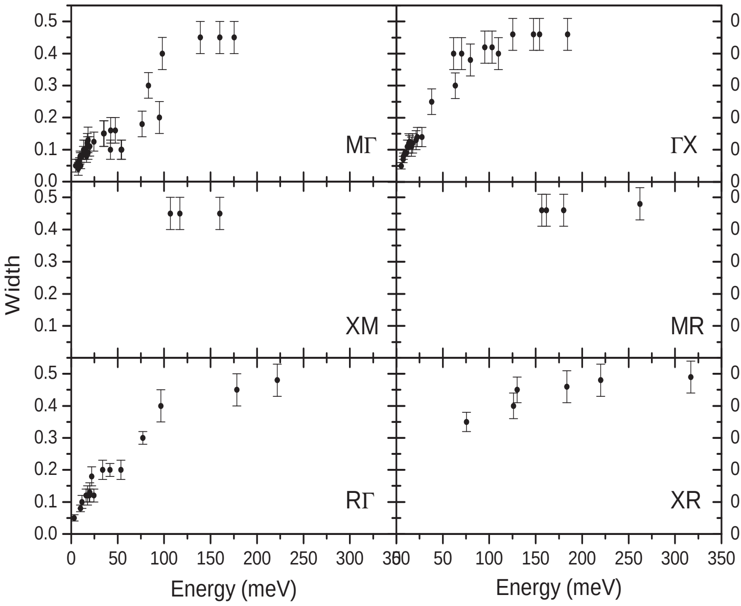

Figure 5.35: The width of the magnetic excitations in momentum transfer as a function of the energy transfer is plotted for different directions in the reciprocal space

The errorbar given on the width of the magnetic excitations takes into account the aforementioned problem that our cuts are not exactly constant energy nor constant q cuts. Since energy is varying throughout a cut like the one shown in the bottom left panel of Fig. 5.28, as the peaks broaden the error on the width increases, as shown by the errorbars in Fig. 5.35. In order to obtain the width in energy, we performed some cuts parallel to the energy transfer axis. This time the implicit quantity in the mono-dimensional plot is the momentum transfer along 1 axis. The energy width of the magnetic excitations is displayed in Fig. 5.36 for the directions ΓX and ΓM. In the left panel of the figure one can see the neutron counts as a function of energy for a particular point in the ΓM or ΓX direction; in the right panel the dispersion is displayed, and the vertical errorbar indicates the width of the peak. Once more, the high energy peaks are very broad in k-space, meaning that in this case the momentum transfer is somewhat ill defined.

In the context of the spin fluctuation theory, it has been predicted that the width of these magnetic excitations follows the law:

$$\Gamma = \Gamma_0 q[k(T)^2 + q^2] \qquad\qquad k(T)^2 = k_0^2(T - T_c) \tag{5.18}$$

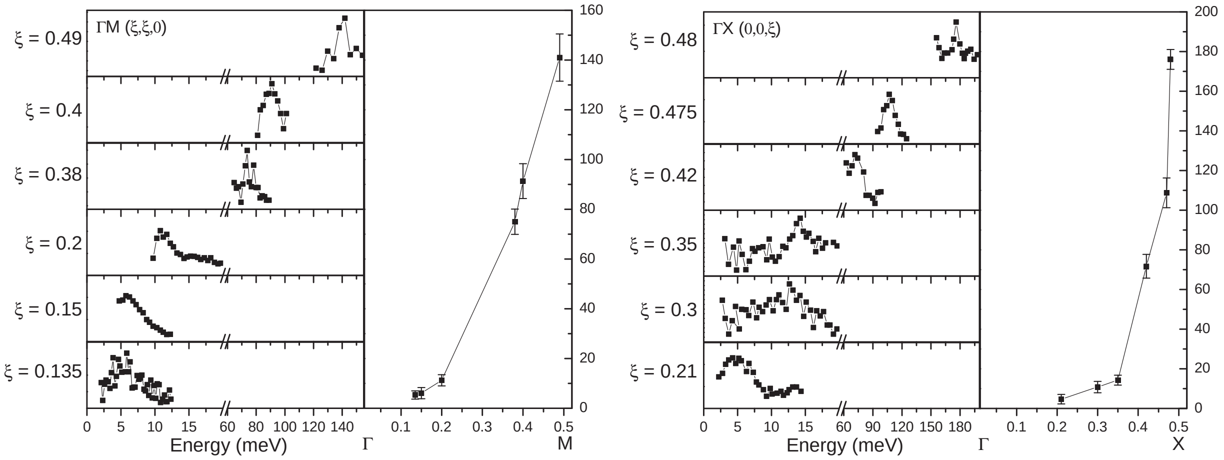

Figure 5.36: The width in energy of the magnetic excitations is estimated by performing cuts parallel to the energy transfer axis. The results are plotted along the ΓM direction (Left panel) and the ΓX direction (right panel).

This peculiar q-dependence has been observed in Ref. [7] with a $\Gamma_0 = 50meV^3$ and a $k_0^2 = 0.0325^{-2}$. Following Ref. [7], we plot the width of our magnetic excitations against $(k^2 + q^2)q$ in Fig. 5.37 for the data taken at 300 K. One can see that a good agreement is found with the previous report, even though we estimate a value for the parameter Γ_0 around 70 meV^3 rather than 50.

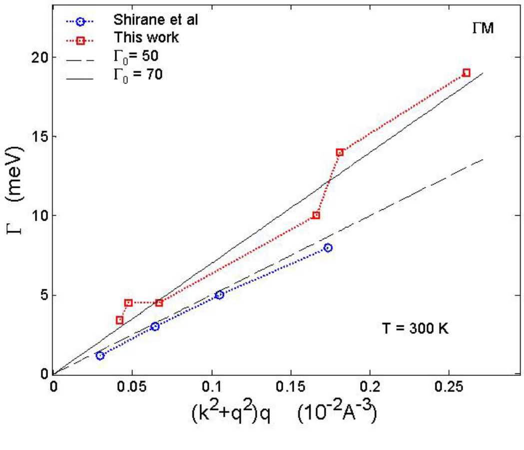

Figure 5.37: The line-width of the magnetic excitation is plotted against $(k^2 + q^2)q$ in order to compare our results to those of Ref. [7].

It has been argued that the temperature dependence of the low energy spin-waves, is responsible for the Curie Weiss law of the magnetic susceptibility. A Curie-Weiss like temperature dependence of these spin waves has been observed, but only in a limited temperature range [7]. The temperature dependence of the paramagnetic scattering in MnSi has been studied in Ref. [8]. In the energy range between 0 and 20 meV, no significant temperature dependence has been observed of the magnetic excitations in the Stoner continuum. This observation was in good agreement with the predictions of Moryia's spin fluctuation theory. In this framework, Eq. 5.17 represents a universal function able to describe the paramagnetic scattering even above T_c. In our experiments we could extend this study up to very high energy, we display in Fig. 5.38 the results obtained from 3 scans performed at room temperature with the incident beam parallel to the [110] direction. One can see that while at low energy it is difficult to see any significant difference with respect to the data at low temperature, simply because the changes are smaller than our experimental errobar, the high energy part of the spectrum is significantly different. In particular, the magnetic excitations at high momentum transfer moved to lower energy transfer with respect to the 10 K spectra.

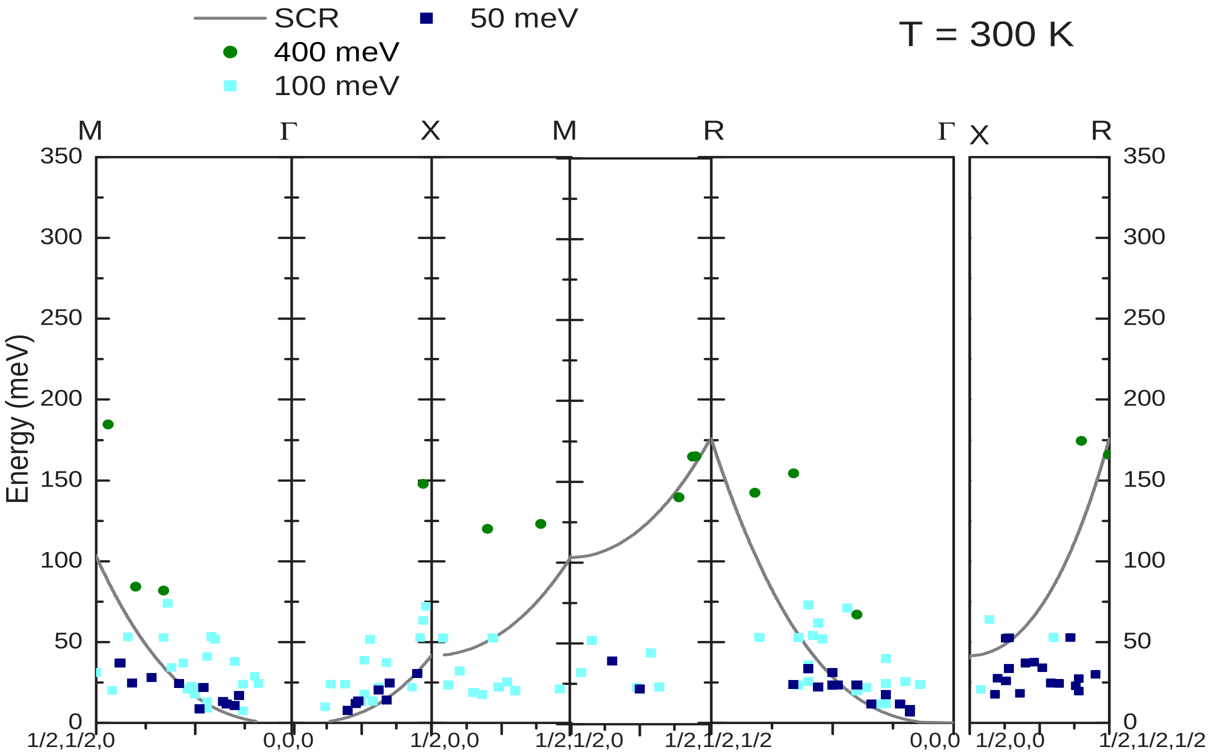

Figure 5.38: The peak positions obtained from the room temperature scans.

We display directly in Fig. 5.39the dispersion of the magnetic excitations at room temperature and 10 K together with the results obtained from the simulation based on eq. 5.17.

One can see that a significant temperature dependence is observed, especially around the R point (1,1,1) in the experiment. The theory however, predicts a weak temperature dependence of the Stoner spectrum, even of the opposite sign of the one

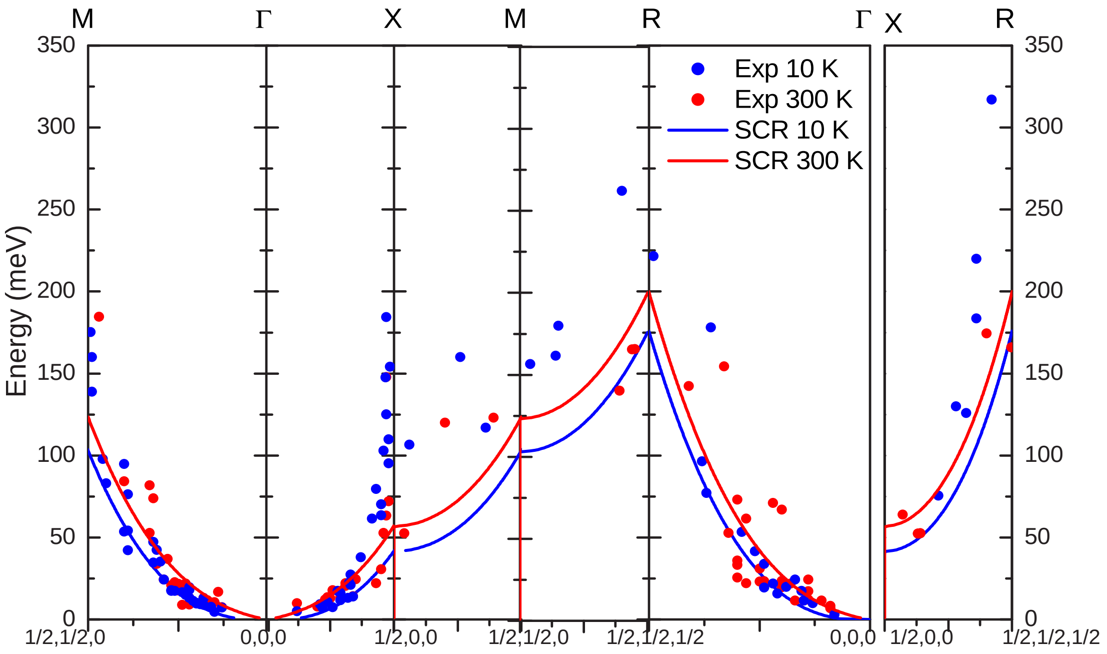

Figure 5.39: The dispersion of the magnetic excitations is plotted for two temperatures: 300 K (red) and 10K (blue). The continuous lines represent the predictions of Moryia's theory at the two temperatures, while the closed dots are the experimental points.

observed experimentally. It is remarkable that the strongest temperature dependence is observed around the (1,1,1) point, which is the easy axis of the magnetization in the ordered phase.

Our neutron scattering experiments extend the previous reports on the paramagnetic scattering of weak itinerant ferromagnets. We find a good experimental agreement with previous reports, especially considering the very different experimental set up. We find a reasonable agreement with the scattering function proposed in the context of Moryia's spin fluctuation theory, however, we point out that already in Ref. [4], a good representation of the experimental data was obtained by calculating the scattering function of a spin polarized electron gas within the Random Phase Approximation (RPA). The reason to refine the theoretical analysis was the need to explain the Curie-Weiss law of the magnetic susceptibility, which is typical of localized moments systems, and whose microscopic origin in itinerant magnets is hard to understand. The observation of a Curie-Weiss like temperature dependence of the spin waves strongly suggested that these are responsible for the behavior of the susceptibility, however, the large and positive magneto-volume effect above T_c[67] and the temperature dependence of the magnetization in an applied magnetic field [67] suggest that the Stoner excitations play a crucial role in the temperature dependence of the magnetization. Our observation of a large temperature effect on the Stoner scattering questions the ability of the spin wave model to account for the Curie-Weiss law of the susceptibility. In the spin fluctuation theory the spectrum of the Stoner continuum is supposed to be almost temperature independent, in contrast with our observations. The conclusion that band effects are important in the temperature dependence of the magnetic susceptibility, calls for a thorough investigation of the model proposed by Hirsch [68], where the Cuire-Weiss law of the susceptibility was explained assuming a temperature and magnetization dependent narrowing of the bands. We point out here, that a more extensive analysis of these data is still going on. In particular a thorough separation between cuts taken on different trajectories in the 4D space has to be done in order to have a better comparison to the theoretical models. As we discussed previously, in order to be able to put the data in absolute units and perform a detailed analysis of the magnetic moment as a function of energy, we need to reliably subtract the phonon background from the data; the preliminary results in this respect are rather encouraging, however the discrepancy observed in the phonons calculations might originate from the difficulty that LDA has describing MnSi electronic structure. As we discussed commenting the PAS data, the paramagnetic FS shows a close resemblance to the ferromagnetic FS, moreover, the very same shape of the FS is peculiar because it has several nesting vectors. This observation could have an impact on the phonon dispersion as well as on the spectrum of the magnetic excitations. Therefore, a theoretical modeling of the magnetic susceptibility that takes into account the real band structure of MnSi is very desirable.

5.6 Conclusions

This study aimed to understand the microscopic origin of the band magnetism observed in MnSi and some other compounds. To begin with, we have shown that the single particle description of MnSi is only partially valid, some deviations have been observed by means of low energy probes such as positron annihilation and De Haas van Alphen measurement; moreover, strong departures are observed in high energy spectroscopies like XAS or XPS. These deviations are ascribable to electron-electron correlation effects, which is not surprising considering the very same nature of Mn which is right in the middle of the transition metal series. What is more puzzling is to understand the microscopic nature of these deviations. If the description of MnSi as a weak itinerant ferromagnet would indeed be fully applicable, the d-electrons would be delocalized in bands and the typical effects of the interaction between the core-hole states and the conduction electrons (atomic multiplets or core level photoemission satellites) would be absent. A remarkable coincidence is also the fact that, if one treats the Mn 3s level photoemission spectrum as the result of the interaction between localized 3d states and the 3s core hole, one finds a localized moment of 2.4 μ_B. This is in very good agreement with the value obtained by a fit to the Curie-Weiss of the magnetic susceptibility. Based on previous neutron scattering observations, this behavior has been ascribed to spin fluctuations. However, our NMR and neutron scattering experiments suggest that the estimate of T_c given by spin fluctuation theory is higher than the experimentally observed one. A detailed estimate of some microscopic parameters also questions the origin of the C-W law predicted by this model. Moreover, we found that the temperature dependence of the Stoner excitations is not following the prediction of the spin fluctuation theory and questions the possibility that spin waves are responsible for the Curie-Weiss behavior of MnSi. Several suggestions have been made in order to provide a microscopic clue to these observations. It has been proposed that magnetization and temperature dependent band narrowing effects are playing a role in itinerant magnetism[68]; very recently, we proposed that frustration might play a role in the B20 crystal structure, and some theoretical investigation has been made on this aspect of the B20 structure [15]. Given the detailed description of the electronic structure that we can obtain experimentally from our study (PAS, XAS, XPS), together with the information about the magnetism obtained by means of NMR and inelastic neutron scattering, a definitive microscopic description of MnSi's magnetism should be possible.

We believe that this might be an ideal playground to study the properties of itinerant magnets in general, which are one of the less understood and yet more interesting materials.

Bibliography

[1] T. Moriya, and A. Kawabata, J. Phys. Soc. Jpn., **34**, 639 (1973).

[2] L. Taillefer, G.G. Lonzarich, and P Strange, J Magn. Magn. Mater. **54-57**, 957 (1986).

[3] N. Manyala, Y. Sidis, J.F. di Tusa, G. Aeppli, D.P. Young and Z. Fisk. Nature **404**, 581 (2000).

[4] Y. Ishikawa, G. Shirane, J.A. Tarvin and M. Khogi Phys. Rev. B **16**, 4956 (1977).

[5] J.A. Tarvin, G. Shirane, Y. Endoh and Y. Ishikawa. Phys. Rev. B **18**, 4815 (1978).

[6] Y. Ishikawa, Y. Noda, C. Fincher and G. Shirane, Phys. Rev. B **25**, 254 (1982).

[7] G. Shirane, R.Cowley, C. Majikrzak, J.B. Sokoloff, B. Pagonis, C.H. Perry and Y. Ishikawa. Phys. Rev. B **28**, 6251 (1983).

[8] Y. Ishikawa, Y. Noda, Y.J. Uemera, C.F. Majkrzak, and G. Shirane, Phys. Rev. B **31**, 5884 (1985).

[9] Y. Ishikawa, K. Tajima, D. Bloch and M. Roth. Solid State Commun. **19**, 525 (1976).

[10] M. Ishida *et al.* J. Phys. Soc. Jap. **54**, 2975 (1985).

[11] B. Roessli *et al.* Phys. Rev. Lett. **88**, 237204 (2002).

[12] K. Motoya *et al.* Solid State Commun. **19**, 529 (1976).

[13] T. Moriya. Phys. Rev. Lett. **4** 228 (1960).

[14] M. Date *et al.* J. Phys. Soc. Jap. **42**, 1555 (1977).

[15] J. M. Hopkinson *et al.* cond-mat/0608065.

[16] B. Binz *et al.* Phys. Rev. Lett. **96**, 207202 (2006).

[17] S. Tewari *et al.* Phys. Rev. Lett. **96**, 047207 (2006).

[18] B. Roessli *et al.* Phys. Rev. Lett. **88**, 237204 (2002).

[19] T. Jeong, and W. E. Pickett, Phys. Rev. B **70**, 075114 (2004).

[20] P. Lerch, and Th. Jarlborg, J. Magn. Magn. Mat. **131**, 321 (1994).

[21] R.S. Hayano *et al.* Phys. Rev. Lett. **41** 1743 (1978).

[22] A. Yaouanc *et al.* J. Phys. Condens. Matter **17** L129 (2005).

[23] T. Moriya, *Spin Fluctuations in Itinerant Electron Magnetism*, Springer, Berlin 1985

[24] H. Yasuoka, V. Jaccarino, R.C. Sherwood and J.H. Wernick, J. Phys. Soc. Jpn. 44, 842 (1978)

[25] K. Motoya, H. Yasuoka, Y. Nakamura, V. Jaccarino and J.H. Wernick, J. Phys. Soc. Jpn. 44, 833 (1978)

[26] W. Yu et al., Phys. Rev. Lett. 92, 086403(2004)

[27] A. Ishigaki and T. Moriya, J. Phys. Soc. Jpn. 67, 3924 (1998)

[28] A. Ishigaki and T. Moriya, J. Phys. Soc. Jpn. 65, 3402 (1996)

[29] I.M. Gat-Malureanu et al., Phys. Rev. Lett. 90, 157201 (2003)

[30] J.H. Wernick, G.K. Wertheim and R.C. Sherwood, Mater. Res. Bull. **7**, 1153 (1972).

[31] C. Pfleiderer, D. Reznik, L. Pintschovius, H. v. Lohneysen, M. Garst, A. Rosch, Nature **427**, 15 (2004).

[32] N. Doiron-Leyraud *et al.*, Nature **425**, 595 (2003).

[33] F.P. Mena,D. van der Marel, A. Damascelli, M. Faeth, A.A. Menovsky, J.A. Mydosh, Phys. Rev. B **67**, 241101 (2003)

[34] B. Borén, Ark. Kemi Min. Geol. **11**A, 1 (1933).

[35] D. van der Marel, A. Damascelli, K. Schulte, and A. A. Menovsky, Physica B **244**, 138 (1998).

[36] X. Obradors,A. Labarta, A. Isalgue, J. Tejada, J. Rodriguez, and M. Pernet, Solid State Commun. **65**, 189 (1988).

[37] A. P. Ramirez, G. P. Espinosa, and A. S. Cooper, Phys. Rev. Lett. **64**, 2070 (1990).

[38] C. Broholm,G. Aeppli, G.P. Espinosa, and A. S. Cooper, Phys. Rev. Lett. **65**,3173 (1990).

[39] J. T. Chalker, P.C.W. Holdsworth, and E. F. Shender, Phys. Rev. Lett. **68**, 855 (1992).

[40] P. Schiffer, A.P. Ramirez, D.A. Huse, P.L. gammel, U.Yaron, D.J. Bishop and A.J. Valentino. Phys. Rev. Lett. **74**, 2379 (1995).

[41] H. Nakamura,K. Yoshimoto, M. Shiga, M. Nishi, and K. Kakurai, J Phys. Condens. Matter. **9**, 4701-4728 (1997).

[42] B. Canals, and C. Lacroix, Phys. Rev. Lett **61**, 11251 (2000).

[43] J. Hafner and D. Hobbs. Phys. Rev. B **68** 014408 (2003).

[44] J. Hopkinson and H. Y. Kee. cond-mat/0509586.

[45] O. Schob and E. Parthé. Acta Cryst. **17** 452 (1964).

[46] T.G. Perring and C.D. Frost. Neutron News **15**, 30 (2004)

[47] V. Guritanu et al. Private communications.

[48] Nakanishi et al, J. Magn. Magn. Mat.15-18, 879 (1980)

[49] E. Fawcett, J.P. Maita and J.H. Wernick. Intern. J. Magnetism, **1** 29 (1970).

[50] "Positron studies of condensed matter" R.N. West, Taylor and Francis (1974).

[51] M. Zangrando,M. Finazzi, G. Paolucci, B. Diviacco, R.P. Walker, D. Cocco, F. Parmigiani, Rev. Scient. Instr. **72**, 1313 (2001).

[52] V. R. Galakhov,M. Demeter, S. Bartkowski, M. Neumann, N.A. Ovechkina, E.Z. Kurmaev, N.I. Lobachevskaya, Y.M. Mukovskii, J. MiTchell, D.L. Ederer, Phys. Rev. B **65**, 113102 (2002).

[53] R. D. Cowan, The Theory of Atomic Structure and Spectra (University of California press, Berkeley, 1981).

[54] D. van der Marel and G.A. Sawatzky. Phys. Rev. B **37**, 10674 (1988)

[55] J. Zaanen and G.A. Sawatzky Phys. Rev. B **33**, 8074 (1986).

[56] H. Ogasawara, A. Kotani and K. Okada Phys. Rev. B **43**, 854 (1991).

[57] L. Sangaletti, F. Parmigiani and P.S. Bagus Phys. Rev. B **66**, 115106 (2002).

[58] Gey-Hong Gweon, Je-Geun Park and S.-J. Oh Phys. Rev. B **48**, 7825 (1993).

[59] T. Jarlborg and P.O. Nilsson. J. Phys. C **12**, 265 (1979)

[60] J.Y. Son, K. Okazaki, T.Mizokawa, A. Fuimori, T. Kanomata and R. Note. J. Phys. Soc. Jap. **71**, 1728 (2002).

[61] T. Susaki, T. Mizokawa, A. Fujimori, A. Ohno, T. Tonogai, and H. Takagi. Phys. Rev. B **58**, 1197-1200 (1998)

[62] B. T. Thole, R.D. Cowan, G.A. Sawatzky, J. Fink, and J.C. Fuggle, Phys. Rev. B **31**, 10 (1985).

[63] G. van der Laan, and B. T. Thole, Phys. Rev. B **43**, 13401 (1991).

[64] B. T. Thole,P. Carra, F. Sette, G. van der Laan, Phys. Rev. Lett. **68**, 1943 (1992).

[65] P. Carra *et al.*,B.T. Thole, M. Altarelli, X. Wang, Phys. Rev. Lett. **70**, 694 (1993).

[66] K. Ishimoto et al. J. Phys. Soc. Jap. **61** 2503 (1992).

[67] M. Matsunaga et al. J. Phys. Soc. Jap. **51** 1153 (1982).

[68] J.E. Hirsch. Phys. Rev. B **44** 675 (1991).

[69] A. Zunger. Phys. Rev. B **22** 5839 (1980).

[70] V. Vescoli *et al* Solid State Comm. **105** 367 (1998).

Chapter 6

Conclusion and final remarks

We have investigated the properties of different strongly correlated electron systems. One of the milestones of solid state physics is the theory of Fermi liquids, which could account for several effects of the Coulomb repulsions in condensed matter systems. Nowadays, many new materials as well as new experiments on known systems, question the ability of this theory to properly account for electron-electron correlations. Among them, cuprates superconductors and transition metal mono-silicides have attracted much attention and are the subject of this thesis. When encountering "non Fermi-liquid" behavior one could ask himself what is the origin of the violation of the Fermi liquid "dictata". As we discussed in the introduction, the Fermi liquid theory assumes that very close to the Fermi surface, the Pauli principle limits the phase space for the electron-electron scattering processes and the dominant scattering is still the electron-lattice one. This scenario though is based on the starting point that the system can still be described by a set of single particle states. Clearly, Coulomb repulsions can lead to many-body effects that can invalidate this statement. This brings us to the second key point of the Fermi liquid theory, which says that if the new set of "something" states, have the same characteristics as a set of "single particle states" and obey the Pauli exclusion principle, then these "something" are called quasi-particles, and they behave as single particles with renormalized properties. In this work we have shown two systems where this picture appears to break down in different ways: in the case of MnSi, some discrepancies have been reported at high pressure between the single particle approximation and the experimental observations. On general grounds, LDA calculations can describe the main properties of the transition-metal mono-silicides, the electronic gap in FeSi and the ferromagnetic ground state of MnSi for example. However, a detailed description of MnSi magnetism, for which the role of Coulomb repulsions is crucial, is not yet satisfactorily achieved within this context.

In the cuprates instead, the very same description of the low energy physics by means of the $t-J$ model is a non Fermi liquid scenario, where the many-body entities (singlets) forming the RVB soup are clearly not quasi-particles as in a Landau Fermi Liquid. To conclude I like to point out my opinion that once one has established a violation of the standard Fermi liquid scenario it becomes very important to try to classify this violation and compare it to what happens in other systems. Finding systematics and trends could be useful for the theoretical task of classifying and characterizing "non-Fermi liquid" systems.

List of Publications

- "Temperature-modulation analysis of superconductivity-induced transfer of in-plane spectral weight in $Bi_2Sr_2CaCu_2O_8$" A.B. Kuzmenko, H.J.A. Molegraaf, **F. Carbone**, and D. van der Marel. Phys. Rev. B **72** 144503 (2005).

- " In-plane optical spectral weight transfer in optimally doped $Bi_2Sr_2Ca_2Cu_3O_10$" **F. Carbone**, A.B. Kuzmenko, H.J.A. Molegraaf, E. van Heumen, E. Giannini and D. van der Marel. Phys. Rev. B **74** 024502 (2006).

- "Model independent sum rule analysis based on limited-range spectral data". A.B. Kuzmenko, D. van der Marel, **F. Carbone**, F. Marsiglio. Submitted to Nature Physics.

- "Doping dependence of the redistribution of optical spectral weight in $Bi_2Sr_2CaCu_2O_8$". **F. Carbone**, A.B. Kuzmenko, H.J.A. Molegraaf, V. Lukovac, E. van Heumen, F. Marsiglio, P. Kes, M. Li, S. Corajault, H. Berger, K. Haule and G. Kotliar. Phys. Rev. B **74** 064510 (2006).

- "Intraband Optical Spectral Weight in the presence of a van Hove singularity: application to $\mathrm{Bi_2Sr_2CaCu_2O_{8+\delta}}$ ". F. Marsiglio, **F. Carbone**, A.B. Kuzmenko, D. van der Marel. Phys. Rev. B. in press. cond-mat/0606688

- "Quantum critical behavior in a High Temperature superconductor". D. van der Marel, H.J.A. Molegraaf, J. Zaanen, Z. Nussinov, **F. Carbone**, A. Damascelli, P. Kes, M. Li, M. Greven. Nature **425** (2003).

- "Scaling properties of the optical conductivity of Bi-based cuprates". D. van der Marel, **F. Carbone**, A.B. Kuzmenko, E. Giannini. Annals of Physics. **321** 1716 (2006).

- "Optical properties and specific heat of the high temperature superconductor $HgBa_2CuO_4$". E. van Heumen, R.Lortz, A.B. Kuzmenko, **F. Carbone**, D. van der marel, X. Zaho, G. Yu, Y. Cho, M. Greven, C.C. Homes, S. V. Dordevic. Submitted to Phys. Rev. B.

- "Optical study of the charge density wave system $Lu_5Ir_4Si_10$". R. Tediosi, **F. Carbone**, D. van der Marel, Maydosh. In preparation.

- " Optical properties of bcc transition metals in the range 0–40 eV ". P. Romaniello, P de Boejl, **F. Carbone** and D. van der Marel. Phys. Rev. B **73** 075115 (2006).

- "Electronic structure of MnSi: The role of electron-electron interactions". **F. Carbone**, M. Zangrando, A. Brinkman, A. Nicolaou, F. Bondino, E. Magnano, F. Parmigiani, A.A. Nugroho, D. van der Marel. Phys. Rev. B **73** 085114 (2006).

- "Valence fluctuations in Transition Metal mono-silicides". **F. Carbone**, M. Zangrando, A. Brinkman, A. Nicolaou, F. Bondino, E. Magnano, F. Parmigiani, A.A. Nugroho, D. van der Marel. In preparation.

- "Strong magnetic pair breaking in Mn-substituted MgB_2 single crystals". K. Rogacki, B. Batlogg, J. Karpinski, N. D. Zhigadlo, G. Schuck, S. M. Kazakov, P. Wagli, R. Puzniak, A. Wisniewski,**F. Carbone**, A. Brinkman, D. van der Marel. Phys. Rev. B **73** 174520 (2006).

- "Experimental investigation of the electronic structure of $Gd_5Ge_2Si_2$ by photoemission and X-ray Absorption Spectroscopy". F. Bondino, A. Brinkman, M. zangrando, **F. Carbone**, D. van der Marel, D.L. Schlagel, T.A. Lograsso. Submitted to Phys. Rev. B.

- "MnSi single crystals and films deposited on Si(111): a comparative spectroscopic study". E. Carleschi, E. Magnano, M. Zangrando, F. Bondino, A. Nicolaou, **F. Carbone**, D. van der Marel, F. Parmigiani. Submitted to Surface Science.

- "Si-NMR spectra of MnSi". M. Corti, **F. Carbone**, P.Carretta, Th Jarlborg, A.A. Nugroho, D. van der Marel. In preparation

Other publications and patents:

- I Cristiani, V. Degiorgio, L. Socci, **F. Carbone**, M. Romagnoli, "Polarization-insensitive wavelength conversion in a lithium niobate waveguide by the cascading technique", IEEE Photonics Technology Letters, 14, p. 669-671, 2002.

- L. Tartara, I. Cristiani, V. Degiorgio, **F. Carbone**, D. Faccio, M. Romagnoli, "Nonlinear propagation of ultra short laser pulses in a microstructured fiber", Journal of Nonlinear Optical Physics and Materials, 11, p.409-419, 2002..

- A. Tonello, **F. Carbone**, L. Socci, M. Romagnoli. "Carrier frequency hopping for optical pulse transmission in dispersion-managed fiber systems" Optics Comm. Vol 218, 273 Apr. 2003. "
- L. Tartara, I. Cristiani, V. Degiorgio, F. Carbone, D. Faccio, M. Romagnoli, W. Belardi, "Phase-matched nonlinear interactions in a holey fiber induced by infrared super-continuum generation", Optics Communications, 215, p. 191-197, 2003.
- Suche, H. Schreiber, G. Lee, Y.L. Quiring, V. Ricken, R. Sohler, W. Paoletti, A. **Carbone, F.** Caccioli, D. Schiffini, A. "Efficient Ti:PPLN multi-wavelength converter for high bitrate WDM-transmission systems". Optical Communication, Vol. 6, 42, 2001
- **F. Carbone**, L. Socci, M. Romagnoli, A. Tonello. EP1436920. "Optical transmission system comprising dispersion management system".
- **F. Carbone**, L. Socci, M. Romagnoli, A. Tonello. EP1430623. "Transmission of solitons on alternate sign dispersion optical fibers with phase conjugation".
- **F. Carbone**, L. Socci, M. Romagnoli EP1282247. "Wavelenght division multiplexing optical transmission system using a spectral inversion device".

Acknowledgements

Dirk, it is hard to be original, after many PhD students you had. The first thing that I want to say is that when I decided to start working at the university I expected something, which I could not express in words. I can say I was expecting......Dirk. I would have liked to work with somebody very motivating, with a volcano-like mind and a great personality for, it might be my defect, but I cannot separate the professional and the human aspects of people. I also expected a lot of freedom to express my ideas, and encouragement, and good discussions over good glasses of wine. I had way more than all this. I find still incredible the amount of time you spent discussing with me, and if you have the impression that I know something about solid state physics, you should consider that when I started, my knowledge stopped little further then the band structure of semiconductors. I learned a lot from you. You let me go after all my ideas, and accepted my nature of a "self scattering" person. I had hard times too, December 2004 after my last beam time in Trieste, but instead of disappointment you showed me comprehension and support. Glasses of wine, I can remember some of them, some maybe were followed by others and now I cannot remember them anymore, but we had great times and discussions also outside the university. There is one negative aspect in all this: now I am spoiled. How can I say just thanks to you, maybe "so long, and thanks for all the fish!". It's long time I decided that doing science must have been my way, after the university I started working as an engineer and one day I decided that I should have really pushed to do what I really liked to do: physics. Good or bad the choice might be, in order actually to accomplish your decision you need to meet the right people at the right moment. That indeed happened to me, a former professor of mine, **Giampiero Banfi**, took me in his lab for a short period while I was finding a PhD position. He introduced me to **Fulvio Parmigiani** who advised me to apply for a PhD with Dirk van der Marel. Giampiero, to whom I also dedicate this thesis, I will never forget the attention and time you dedicated to me in that period which was the hardest for you. How many students did you have in your life, and still the faith of a single one mattered so much, thank you. Fulvio Parmigiani once told me "you won't meet many other persons like Giampiero", but you were indeed the second, for you advised me as a father would do with his son. I even had the chance to work with you during my thesis, and I enjoyed a lot our scientific interaction.

Sometimes you can have an easy success, which is good, but sometimes you have to struggle a lot and if you succeed is even better. It is easy to be good when there are no problems, in difficult moments one can see the real value of a person, you have been always encouraging and positive to me. I am proud of the results we had in Trieste and I wish they will just be a starting point for future challenges. Fulvio has also the merit of introducing me to Dirk, which is not a negligible one. When I had to make up my mind my father told me: "I know a guy who could advise you, he was a very good football player at the high school...", I like to thank prof. **Enrico Bellone** for the attention you dedicated to me. I always read your precious comments on "Le Scienze", and I really appreciate the effort you put in promoting science in Italy. However, having married this year, I probably precluded myself the only well paid opportunity for a physicist in Italy: "La pupa e il secchione".
When you have pestered your professor for 3 years and you have one more year to go, the best thing that can happen to you as a PhD student is to have a fresh unpestered professor on sabbatical to pester. Would you believe it? I had that. We had the chance to have **Frank Marsiglio** for one year in Geneva and I really wish to thank you for all the time you spent discussing with me. I wish to thank **Thomas Jarlborg** who also very kindly dedicated lot of his time to me and my MnSi experiments. I am very pleased that I had your knowledgeable support on this subject. The years of the PhD have been really great especially for the great atmosphere that is in Dirk's group. Thank you **Alexey** for not killing me during our several and long interactions; I really appreciated the help you gave me and the comprehension you had even if our styles are so different. I think that together we made a good duo, if I won't write papers with you any more, I at least hope that you will keep on being the referee of all those I write. Endless thanks go to **Riccardo**, for being a true friend and a great experimentalist. It has been a fortune having you again as a colleague after the great experience in Pirelli. I hope that this won't be the last scientific adventure we share. A special thank goes to my guide to life in Holland, **Hajo**, without whom we would have certainly appreciated less the Netherlands. Moreover, you have a crucial part in this thesis since you inspired a large part of it and since you gave me your precious and thorough comments. Thanks **Eric** for being such a funny and stubborn guy, for sharing the passion of all that it is politically incorrect and for the many papers we made together. Thanks **Dook** for all the Drops you brought from Holland. Thanks to **Francesco**, who shares with his father a great human touch and a great knowledge of physics, I am happy to have had you as a colleague, I would have liked to have more interactions but one never knows, maybe in the future. I would like to remind to **Joachim** and **Jeremie** at this point that Luigi is world champion, thanks for being there right when Italy eliminated both Germany and France, without you it wouldn't have been so funny. Jeremie, thanks a lot also for your French consulting....Thanks **Violeta** for having shared with me the ISIS experience, I have just an advice to you: when you sit behind a neutron scattering experiment the right question to ask yourself is not "is there a peak or not?" but "with which Gaussian do I fit this

peak?". It has been a lucky chance to have **Alexander Brinkman** in our group for a while, and even better sharing the interest about MnSi and frustrated magnets. Thanks for all the smart comments you always had and thanks for sharing with me maybe the most difficult experience of the doctorate, my last beam time in Trieste, too bad we didn't demonstrate Riemann's theorem.... Thanks to **Pietro l'Eremita or Peter Armitage**, for all the advices I got from you on jobs, articles and books. All this people are good, but they are even better with their wives and girlfriends, **Elena, Sandra, Lucille, Nichole, Melida, Katrin, Marieke, Nicola and Ana**. Thanks for tolerating us talking about work even on Saturday evenings. All this work couldn't be possible without the help of **Cor Bos** and **Mehdi Brandt**, who have the non-trivial task of keeping a lab with 5 PhD students and 5 post docs working in it. A great thanks to a group of people which has been crucial for my work: sample growers. Thank you **Enrico** not only for the beautiful samples of Bi2223 you prepared, also for the mp3 of the pizzaiolo......Thanks also to **Romain and Agung**.

I would like to acknowledge also my previous colleagues in Groningen: **Patricio Mena and Anita**, the Italo-Equadorian restaurant "from Appenini to Ande" is still a great idea, **Michele, Sandra, Francesca, Pina** with whom I had a very pleasant scientific interaction, **Renate, Henk Bron** for the great "non ho l'età" singing, **Arjen, Daniele, Silviu and Paul**. I stayed only one year in Holland but you made it a special occasion.

I consider it as my other group, the team of the beam line BACH in Trieste. A great thanks goes to **Marco Zangrando** for his enormous experimental support, for his Triestinity and friendliness. Thanks to **Michele Zacchigna** for teaching me that "sguarare" is not really Italian. Thanks to **Federica, Elena, Alessandro, Tommaso and Manuela** as well. Coming to Trieste has always been great, not only scientifically. Thanks to **Stefania Pagliara** also in Brescia for her ultrafast course on how to use the Cowan code.

I would like to thank also **Tobey Perring**, for I really had great times in ISIS in the MAPS cabin. I really learned a lot from you, and I think it has been a great opportunity to collaborate with you on the MnSi project; Thanks also for the dinners in the pubs in the Oxford countryside, it really made my stay in the punishment block more enjoyable. In the neutron scattering project I have been sharing the MAPS cabin with prof. **John DiTusa**. Thanks for the very usefull scientific discussions, and for making 11 days of beam times also a moment of entertainment. I really enjoyed meeting you. A special thanks goes to prof. **Gabriel Aeppli** for supporting the project on MnSi and for accepting to be part of the Jury for my Doctorate. I feel very honored of having your attention on my work.

I would like to thank also the people in the DPMC for these very nice years. It is a very good environment to do science in. The door of professors offices is always open for students to discuss matters. I would like to thank **prof. Triscone, and Dr. Jaccard**. Thanks to **prof. Fisher** for reading this thesis and being a member of the Jury, it is very rewarding for a young scientist to have the attention

of somebody like you. Thanks also to prof. **Giammarchi**, not only for being a member of the Jury and for reading my thesis, but also for the magic sessions of cards tricks at the social dinners. I would like to thank also **Fabienne, Lilianne and Elisabeth** for only with your help we can survive bureaucracy, in particular myself. Thank you a lot **Céline** for helping me formatting the thesis.

I want to thank **Pietro Carretta and prof. Rigamonti** for their invitations to the university of physics in Pavia, and for their contribution to the MnSi project.

Thanks to **Stepehn Dugdale and Jude Laverock** in Bristol for your collaboration on the MnSi project.

I want to thank also **Andrea Damascelli** for: painting the house in Groningen where I went to live, inviting me to Vancouver, organizing such a fantastic visit to the UBC physics department and thanks for never let me win a foosball match. Working together would have been really great, I really hope that one day this can happen. I'd like to thank your family also for the hospitality, **Barbara, Matteo and Luca**. Matteo and Luca, thanks for teaching me the enormous possibilities of elasticity of the human stomach. From now on each time I'll sit behind the table of a sushi restaurant I will reconsider the amount of food I can introduce in myself. Thanks to **prof. George Sawatzkii** for the discussions on my work we had over my PhD and in Vancouver. Thanks also to **prof. Shen** for the hospitality in Stanford. I would also like to acknowledge very interesting discussions with **prof. Khomskii, prof. Zaanen, Matthias Schubert, Franco Vigliotti and Joel Mesot**.

At the thesis defense of **Filippo**, magico, I had the chance to meet **prof. Petra Rudolf**, thanks for your precious advice and support, I am looking forward to start our collaboration. **Maggico, Pippo, Rod Blazer** of course, you deserve a special thank, for being one of my best friend, my partner of insane dinners and for one of the best times in life: the life in via Flarer's cave. Thank you also, **Adelaide**, our landlord, for you always favored Filippo for no good reason. But you were always the best landlord we could have indeed.

I would like to thank my previous colleagues in Pirelli. **Marco Romagnoli, Luciano Socci and Pierluigi Franco**, you have been my first research advisors, I learned a lot from you, and it was a great time the one I spent in Pirelli. Thanks to **Giacomo**, it was great to work with you, and it is great to have you as one of my best friends. Thanks **Chiara** of course for tolerating Jaq. "Quel motel vicino alla palude" though is hard to forgive.... Thanks to **Daniele Faccio** for not calling his son "Faccio Casino", and for coming to visit me in Geneva. It is so good to see how friendship survives distance, time and commitments. Thanks to **Maurino and Marta, Matteo, Silvia, Allessandro, Arianna and Paola** for the great time we had together. **Giulia, Michele, and Paolo** you are another example of very good friends, you are always available for a diner when I come to visit Pavia, you cannot imagine how much I appreciate that. Thanks to **Davide, Paola and Francesco Setolone** for sharing the office in the 307 building, making fun of "the zia" was so good.

A very warm thank you goes also to **prof. Degiorgio**; it is always a great pleasure to visit you in Pavia, being your student and then working with you were beautiful experiences. I would like to thank also **prof. Malvezzi**, cause still a student, I was curious to see what was going on in a lab and you welcomed me allowing the waist of some of your time.
Thanks also to prof. **Cosso** and prof. Pelasso of the scientific Lyceum in Novi. Your passion in teaching is an example for me and part of what I do has roots in it.
A special thank goes to my friends in Novi. There is something special about them, and it is that whatever I do, wherever I go, I will always be the Carbo for them. Since calculating the speed of Matteo diving from the 3m platform I made an error converting m/sec into Km/h and got a crazy number, they have absolutely no faith in my physics whatsoever. Well, as a matter of fact as an experimentalist it wasn't any better since I blew up my class trying to distil beer when I was 13. Anyway, I love it, because there I am just what I used to be when we were growing up together, I am the devil getting Cristiano drunk to his end, the nerd hiding right where the hornets nested in Montebello and the unforgotten guitar player of the "Outsiders"....As for the postcard that I always send to one of you for everybody, do you really want all to be named here? What if I forget one of you? In the end, you know who I am talking about, that's: **Giulio, Matteo, Matteo, Gabry, Andrea, Ilenia, Alessandro, Francesca, Mema, Marc, Paola, Cristiano, Verne, Gozzo, Roby, Laura, Elena, Gianni, Marta**.
I would like to thank also **Rossella** for her help in my beginning years of the university. I seriously think that the fact that you did not finish the university of physics is very bad for physics. I owe my passion for physics to you, thank you, with my heart.
A special part of my stay in Geneva was the Veyrier Volleyball team. I would like to thank **Luc, Nico, Tarek, Robert, Pascal, Eric, Cristophe, Regis, Marc-André, Christian, Jorn**. You are such a pool of funny people, I will miss you all a lot. Even if we lost many times, almost all, I like to remember that some of these times we let the best teams sweat 5 sets. Thanks also for deciphering my French e-mails....
Thanks you **Franco** for your friendship and the great tennis matches we had. I will miss you as well.
Finally, the time for my family. I shouldn't forget to mention my sister **Sabrina** this time, making my homework at the high-school, I am not so sure though weather this contributed positively or negatively to my education....thanks anyway, also to **Julian**, for his English mother-tongue advices and the many great windsurfing sessions. No words can express a thank to my mother **Giovanna**, I wish I can always carry on your spirit of initiative and will in what I do. Thanks to the **Domenico** also for the most useful instruction he gave me: "The most important thing in life is knowledge". Thanks to **Giorgio, and Miranda** for the support you gave me and Milena when we got to Geneva. **Milena**, thank you for so many things that I cannot write down, I'll express it in private.

Living far from home.....: Quando ti metterai in viaggio per Itaca
devi augurarti che la strada sia lunga
fertile in avventure ed esperienze
Sempre devi avere in mente Itaca
Raggiungerla sia il pensiero costante.
Soprattutto non affrettare il viaggio;
fa che duri a lungo, per anni, e che da vecchio
metta piede sull'isola, tu, ricco
dei tesori accumulati per strada
senza aspettarti ricchezze da Itaca.
Itaca ti ha dato il bel viaggio,
senza di lei mai ti saresti messo
in viaggio: che cos'altro ti aspetti?

When you will leave to Itaca
You must hope that it will be a long way
Rich of adventures and experiences
You must keep in mind Itaca constantly
To reach it must be your goal.
However, do not hurry up
Let the journey last for years and you, old,
will get on the island together
with the treasures you found on the way.
Do not expect more from Itaca.
Itaca gave you the nice trip,
Without her you would never have left:
What more do you want?

Kostantinos Kavafis

All'ombra di cipressi e dentro l'urna
confortate di pianto è forse il sonno
della morte men duro?
..
..
Sol chi non lascia eredità d'affetti
Poca gioia ha dell'urna; e se pur mira
Dopo l'esequie, errar vede il suo spirito
Fra'l compianto de' templi acherontei,
o ricoverarsi sotto le grandi ale
del perdono d'Iddio ma la sua polve
lascia alle ortiche di deserta gleba
ove ne donna innamorata preghi,
ne passeggiar solingo oda il sospiro
che dal tumulo a noi manda Natura.

Ugo Foscolo. "Dei Sepolcri